STUDY AGEING IN BATTERY CELLS: FROM A QUANTUM MECHANICS, MOLECULAR DYNAMICS, AND MACRO-SCALE PERSPECTIVE

STUDY AGEING IN BATTERY CELLS: FROM A QUANTUM

MECHANICS, MOLECULAR DYNAMICS, AND MACRO-SCALE

PERSPECTIVE

By AMIRMASOUD LANJAN, M.Sc.

A Thesis Submitted to the in Partial Fulfillment of the Requirements

for

the Degree Doctor of Philosophy

DOCTOR OF PHILOSOPHY (2023)

(Mechanical Engineering)

TITLE: STUDY AGEING IN BATTERY CELLS: FROM A
                    QUANTUM MECHANICS, MOLECULAR DYNAM-
                    ICS, AND MACRO-SCALE PERSPECTIVE

AUTHOR: Amirmasoud Lanjan

                    Master of Science

SUPERVISOR: Dr.Seshasai Srinivasan

NUMBER OF PAGES: xxviii, 225

Dedicated to my beloved wife, Farnaz who has been my

constant source of support and inspiration throughout this

journey.

I would like to express my deepest gratitude to my
mother, father, and sister for their support.

Declaration of Academic Achievement

I, Amirmasoud Lanjan (born on June 11, 1994), declare that this thesis titled *"STUDY AGEING IN BATTERY CELLS: FROM A QUANTUM MECHANICS, MOLECULAR DYNAMICS, AND MACRO-SCALE PERSPECTIVE"* and the work presented in it are my own original work. All contributions made to this research have been appropriately acknowledged. This thesis has not been submitted for any other degree or qualification at any other university or institution.

This thesis represents my own intellectual work, and all sources of information and ideas have been cited and acknowledged appropriately. Any assistance received in the preparation of this thesis has been acknowledged, and all ethical considerations have been taken into account.

The research presented in this thesis has been conducted under the supervision of Dr.Seshasai Srinivasan, and the experimental and computational works have been carried out in the Mechanical Engineering Department of McMaster University.

I certify that the work in this thesis complies with the guidelines for the submission of theses set by *"McMaster University"* and that this thesis represents a significant contribution to the field of *"Batteries and Electric Vehicles"*.

Signed: Amirmasoud Lanjan

Date: June 2023

Acknowledgements

I would like to thank my supervisor Dr. Seshasai Srinivasan at McMaster, who provided me with this opportunity to work on this research topic and for supporting me throughout. He is the best guide anyone can have and I have always felt that I was under the right guidance throughout my research. I would also like to thank my supervisory committee members Dr. Amin Reza Rajabzadeh and Prof. Mohamed Abdelaziz Elbestawi for their valuable time and feedback for improving this work. My thanks also to the Natural Sciences and Engineering Research Council of Canada (NSERC) Canada for funding this project. I would like to thank the Department of Mechanical Engineering and W Booth School of Engineering Practices and Technology for providing all the resources. I would like to thank Zahra Moradi for having fruitful conversations on various parts of my research.

Lay Abstract

The limited lifespan of expensive batteries is the main obstacle to electrification of the transport sector, despite its necessity for addressing the current environmental issues. Li^+/electrolyte reduction on the electrode surface is responsible for more than 50% of capacity loss and the consequent ageing is a complex and fast-occurring phenomenon (few ns) that cannot be easily resolved using conventional experimental and computational techniques. This thesis presents the development of some computational frameworks and demonstrates their employment to investigate this phenomenon from a multi-scale perspective, i.e., from a few electrons to an entire battery length scale, with the operating cycles ranging from a few ps to several months, employing Quantum Mechanics, Molecular Dynamics, and Macro-Scale Modeling. The frameworks have been successfully validated with respect to experimental data from the literature and have been applied successfully to highlight the parameters that impact ageing in batteries. The findings presented in this thesis can be used as the base for further research on next-gen durable batteries with liquid and solid-state electrolytes.

Abstract

When an anode electrode potential is larger than the lowest unoccupied molecular orbital (LUMO) of the electrolyte, Li-ions and electrolyte molecules will participate in reduction reactions on the anode surface and form a solid electrolyte interface (SEI) layer. Active Li-ion consumption in the formation reactions is the main source of capacity loss ($> 50\%$) and ageing in Li-ion batteries (LIBs). Due to the fast-occurring and complex nature of the electrochemical processes, conventional experimental techniques are not a feasible approach for capturing and characterizing the SEI formation phenomenon. The lack of experimental data and consequently the absence of potential parameters for crystal structures in this layer makes molecular dynamics (MD) simulations inapplicable to it. Also, due to the multi-component multi-layer structure of the SEI, the smallest system representing an SEI layer is too large for employing the principles of quantum mechanics (QM), that traditionally work with much smaller system sizes. Addressing this, this thesis presents a novel computational framework for coupling QM and MD calculations to simulate a system with the size limits of MD simulations independent of the experimental data. The QM evaluates sub-atomic properties such as energy barriers against diffusion and employs seven new algorithms to estimate potential parameters as the input of the MD simulations. Then MD simulations forecast SEI's properties including density, Young's Modules, Poisson's Ratio,

thermal conductivity, and diffusion coefficient mechanisms. The output of the QM and MD calculations are employed to develop two macro-scale mathematical models for predicting battery ageing and battery performance, incorporating the impact of the SEI layer in addition to the cathode, anode, and separator parts. Finally, the results obtained have been validated with respect to the experimental data in different operational conditions.

Table of Contents

3 Combining Neuro-Computing Techniques with Quantum Mechanics and Molecular Dynamics to Determine the Nonbonded Potential Parameters   67

4 A Multi-Scale Investigation of Diffusion Mechanism Within the Solid-Electrolyte Interface Layer: Coupling Quantum Mechanics, Molecular Dynamics, and Macro-Scale Mathematical Modeling   109

5 Analysis of the Solid-Electrolyte Interface Layer in Li-ion Batteries Using Multi-Scale Modeling Techniques

6 An Enhanced Battery Aging Model Based on a Detailed Diffusing Mechanism in the SEI layer

List of Figures

List of Tables

xxiii

Notation, Definitions, and Abbreviations

Notation

Symbol	Description
a_{crd}	Proportionality factor
$A(m^2)$	Electrode surface area
$C(\frac{mol}{m^3})$	Reactant concentration of SEI formation
$C_{batt}(Ah)$	Relative capacity
$D_i(\frac{m^2}{s})$	Diffusion coefficient
$E_{eq,i}(\mathbf{V})$	Equilibrium potential
f	Lumped fitting parameter
$F(\frac{C}{mol})$	Faraday's constant, 96485
$I_0(\mathbf{A})$	Exchange current

$I_{1C}(\mathbf{A})$ 1C charge/discharge current, 2.3

$I_{kin}(\mathbf{A})$ Kinetic current

$I_{lim}(\mathbf{A})$ Limiting current

$I_{load}(\mathbf{A})$ Applied current on the battery

J Lumped fitting parameter

H Lumped fitting parameter

$Q_{batt.0}(\mathbf{C})$ Initial battery capacity, 2.3

$Q_{neg}(\mathbf{C})$ Charge stored in the negative electrode

$Q_{SEI}(\mathbf{C})$ Charge lost to SEI forming reactions

$R(\frac{J}{molK})$ Molar gas constant, 8.3145

$s(\mathbf{m})$ SEI layer thickness

$T(\mathbf{K})$ Temperature

$V(\frac{m^3}{C})$ Coulombic volume for forming the SEI

x Stoichiometric coefficient in $\mathrm{Li}_x[\mathrm{Electrode}]$

α Transfer coefficient

ϵ_i Porosity

$\eta_i(\mathbf{V})$ Over-potential

$\Phi_i(\mathbf{V})$ Potential of i phase

τ_i	Tortuosity

Index	Description
cov	Areas covered by a microporous SEI layer
crd	Areas where the SEI layer has cracked
ical	Intercalating reaction
neg	negative electrode
SEI	SEI layer or SEI layer forming reaction
s	Solid (Electrode) phase
l	Liquid (Electrolyte) phase

Abbreviations

CPU	Central Processing Unite
DFT	Density Function Theory
DNN	Deep Neural Network
DOS	Density of State
EB	Energy Barrier
ESS	Energy Storage System

MSD	Mean Square Displacement
LAMMPS	Large-scale Atomic/Molecular Massively Parallel Simulator
LIB	Lithium-Ion Battery
LUMO	Lowest Unoccupied Molecular Orbital
MD	Molecular Dynamics
ML	Machine Learning
MSMM	Macro-Scale Mathematical Modeling
NPT	Constant Temperature and Pressure Ensemble
NVT	Constant Temperature and Volume Ensemble
PBE	Perdew–Burke–Ernzerhof
QM	Quantum Mechanics
SEI	Solid Electrolyte Interface
SOC	State of Charge
XRD	X-Ray Diffraction

Chapter 1

Introduction

1.1 Environmental Issues and Electric Vehicles

Electric Vehicles (EVs) are gaining a lot of attention in the past decade in the wake of current issues relating to global warming, climate change, and other related environmental issues. Electrical motors were used in the vehicle's propeller in 1834 by T. Davenport and followed by others. Eventually, an EV as the "car" we know today was produced about 150 years ago, in 1851. This is while the internal combustion engines (ICEs) were introduced about 20 years after them in 1872 by G. Bryton [1]. Despite their higher efficiency, lower noise, simple design, zero greenhouse gas emissions, and many other advantages, EV vehicles were replaced by ICE vehicles during the world war due to the need for affordable, powerful, and long-range vehicles in poor economic conditions [1]. Until the 2000s, petroleum and its sub-products were known for their low price, and easy availability, making them a popular source of energy. However, after the 2000s, these beliefs are beginning to crack. Governments, people, and companies are realizing that though petroleum is cheap, it has many hidden costs such

as health problems due to climate change and environmental issues [1]. On the other hand, public awareness has been rising and people can easily see the consequence of their activities on the planet. Consequently, society now wants to control the amount of energy consumption, and GHG emissions, and implement some policies to stop or retard the climate change process.

Each year, the International Energy Agency (IEA) publishes data on energy consumption by different industries and services, all over the world. IEA energy usage and GHG emission shares for different sectors are indicated in Figure 1.1 a and b, respectively. The highest energy consumption is by the transportation sector which is 36% [2]. The transportation sector also has a significant share in GHG emissions.

(a)

(b)
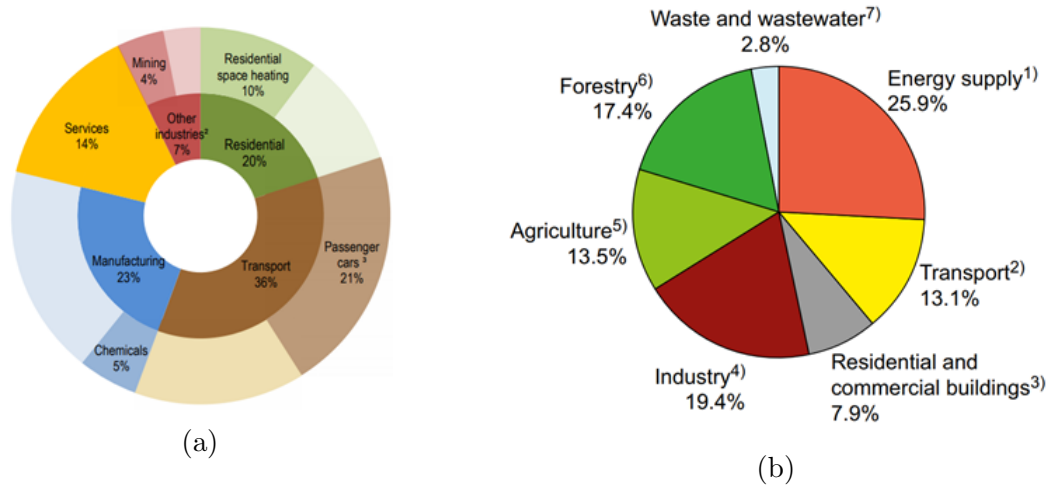
Figure 1.1: (a) Share of energy usage by different sectors published by IEA (Image source: [2]). (b) Share of GHG emission by different sectors (Image source: [3]).

With the challenges of limited fossil fuel supply, climate change and global warming, there is a large-scale consensus to undertake initiatives that will retard global warming. The different projections, estimated based on the contemporary GHG emission and energy consumption, are indicated in Figure 1.2. Governments all around

the world are trying to find a solution to the contemporary problem and achieving the 1.5^{o}C or 2°C target.

Annual global greenhouse gas emissions
in gigatonnes of carbon dioxide-equivalents

150 Gt

100 Gt

50 Gt

Greenhouse gas emissions
up to the present

0

No climate policies
4.1 – 4.8 °C
→ expected emissions in a baseline scenario
if countries had not implemented climate
reduction policies.

Current policies
2.8 – 3.2 °C
→ emissions with current climate policies in
place result in warming of 2.8 to 3.2°C by 2100.

Pledges & targets
2.5 – 2.8 °C
→ emissions if all countries delivered on reduction
pledges result in warming of 2.5 to 2.8°C by 2100.

2°C pathways
1.5°C pathways

1990 2000 2010 2020 2030 2040 2050 2060 2070 2080 2090 2100

Figure 1.2: Different global GHG emission scenarios and their impact on global warming and climate change (Image source: [4]).

High efficiency is the main reason for selecting EVs as an alternative for ICEs to control environmental issues in transportation systems. The efficiency of an electric motor (EMs) and an ICE versus motor speed and torque are indicated as an example in Figure 1.3. While the efficiencies for the ICE are below 36%, these values are higher than 90% for the EM.
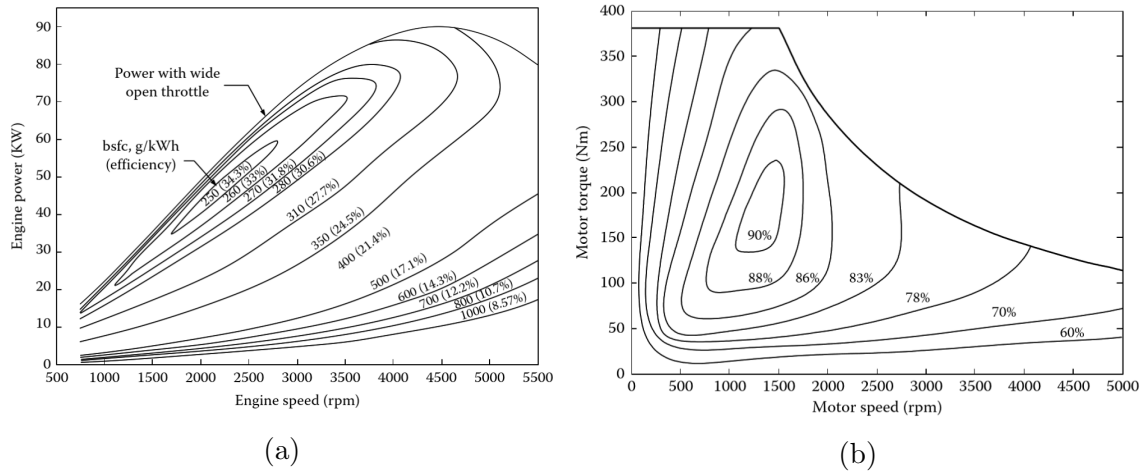
Figure 1.3: (a) Internal Combustion Engine and (b) Electrical motor efficiency for a range of motor torque and speed.

There are two ways for utilizing EMs in the vehicle's propulsion systems:

1. Employing EMs along with ICEs in the propulsion system (called hybrid) for producing electrical energy from gasoline. There are several architectural designs for hybrid systems. The purpose of a hybrid system is to keep the ICE efficiency at the highest possible value in different conditions, by running the ICE at a certain range of torque and speeds.

2. Full electric vehicles (EVs) in which only EMs are utilized in the propulsion systems.

Consequently, most hybrid vehicles can reach an efficiency below 36%, whereas the efficiency of a full EV is usually higher than 90%. Although a full EV has about three times higher efficiency than a hybrid vehicle, most commercialized EVs are hybrid due to the advantages in the energy storage systems (ESSs) of gasoline vehicles over Li-ion batteries (LIBs), which include the following:

- Theoretical energy density of gasoline is 12,200 (1,700 practically) Wh.Kg^{-1} which is much higher than that of electrical ESSs.

- Filling a fuel tank takes about five minutes which is much lower than the several hours that are required for charging a battery.

- A typical fuel tank price is below 1,000$ which is much lower than the several thousand dollars required for the electric ESSs of an EV.

- Fuel tanks have a long lifetime, more than a few decades, while electric ESSs usually last less than a decade.

1.2 Li-Ion Batteries

With the commercialization of LIBs in the 1990s, research is focused on developing this technology. Applications of LIBs range from small-size miniaturized portable electronic devices to large-size stationary versions that are used for storing the electricity generated from renewable sources such as green energies. Chief among these applications is the automotive sector where LIBs can play a key role in displacing the internal-combustion engine technology with EV technology. Their popularity is due to their advantages such as high working voltage, fast charge and discharge process, long lifetime, and no memory effect. Even considering the LIBs' capabilities, in the automotive sector, EVs face challenges with their ESS, limiting their practical utility. Nevertheless, there is still a lot of room to enhance LIBs' performance, efficiency, and durability. The ESS in internal combustion engines is durable for almost as long as the vehicle's lifetime. Also, on average, the cost of a gasoline tank for a passenger vehicle is typically a negligible fraction of the overall vehicle cost, ranging from just

5

a few hundred dollars to a few thousand dollars. However, on average, the cost of the battery pack accounts for a significant portion of the total vehicle cost, typically ranging from 20% to 50%. In recent years, the cost of batteries has been declining due to advancements in technology and economies of scale, but it remains one of the main costs for EV owners. Besides the costs, the durability of the batteries for EVs is 8 - 10 years which is much lower than the vehicle's lifetime. Also, in terms of waste material, a fuel tanks' average weight is around 12 kg while that of the battery pack is around 500 kg. So, massive amounts of mining and manufacturing energy are required for battery production due to their large mass and the requirement of specific elements. Therefore, ESS' replacement for EVs is the greatest concern for (I) the vehicle owner in terms of maintenance costs and (II) the environment due to the high waste of energy and materials.

1.3 Solid Electrolyte Interface (SEI) Layer

Studies on various components of LIBs, such as the anode, cathode, and electrolyte, have been conducted in recent years. However, one of the primary causes of battery aging is the buildup of solid-electrolyte interphase (SEI) on the electrode surfaces. SEI is a thin layer of solid electrolyte that forms on the electrode surfaces as a result of the electrolyte decomposition during the initial charging cycles. When the anode electrode potential (μ_a) is larger than the lowest unoccupied molecular orbital (LUMO) of the electrolyte and/or the cathode potential (μ_c) is smaller than the highest occupied molecular orbital (HOMO) of the electrolyte, electrolyte molecules will be reduced/oxidized and form a solid layer on the electrode/electrolyte interface called the "SEI Layer" [5], which introduced by Peled in 1979 [6].

The major challenge in creating durable LIBs is the lack of a comprehensive understanding of the SEI layer in LIBs. SEI layer formation reactions consume active Li-ions in the battery, resulting in capacity fade; even in a well-engineered LIB, the SEI formation is the main source (more than 50%) of capacity loss [7–9]. On the other hand, a desired SEI layer reduces electron tunneling that prevents further contact between electrons and electrolyte molecules, resulting in suppressing further formation reaction and battery ageing [9], but it also hinders the movement of lithium ions between the electrodes. The SEI layer is essential for the stable operation of Li-ion batteries, but it also contributes to the battery's aging. The SEI layer grows thicker over time, reducing the available active surface area of the anode, consuming active Li-ions, and slowing down their movements for transferring charges which leads to a decrease in the battery's capacity and performance.

Moreover, the SEI layer is not a perfect barrier and is a preamble to some electrolyte molecules which can cause further degradation of the anode, leading to a reduction in the battery's capacity and performance. The composition of the SEI layer also changes over time, leading to the formation of new species that can contribute to the battery's aging. The formation and composition of the SEI layer are influenced by various factors, including the electrolyte composition, temperature, and charging rate. For example, the SEI layer can form more quickly at high temperatures or with high charging rates, leading to faster battery aging. Therefore, understanding SEI formation reactions, Li-ions diffusion mechanisms, and material characteristics in this layer are critical for enhancing the electrochemical performance and durability of LIBs [10, 11].

The SEI layer has two subsections including (I) an organic outer sub-layer (near

the Electrolyte interface), which allows the transfer of both Li-ions and the electrolyte solvent molecules, and (II) an inorganic inner sub-layer (near the Electrode interface), which only preamble to the Li-ions [12]. While the SEI composition depends on the electrolyte molecules and the formation reactions, the outer sub-layer is mainly made up of three crystal structures including Li_2O, LiF, and Li_2CO_3 and some mostly unknown crystal structures in the inner sub-layer including $Li_2C_2O_4$, Li_2EDC, $LiOCO_2CH_3$, and $LiOCO_2C_2H_5$.

1.4   Drawbacks and Deficiencies of the SEI Layer Investigation

It is a challenge to directly capture the reaction at the SEI interface experimentally since some of the reactions could occur at the picosecond (ps) time scale. As a result, most experimental methods are incapable of accurately characterizing the SEI layer, particularly the thermodynamics and kinetic properties [13]. Due to the complexity of the SEI structure and the challenges in conducting experimental investigations, our understanding of the diffusion mechanism in this layer continues to remain unclear. The lack of precise knowledge of the diffusion coefficient results in disagreement between the mathematical models that predict the SEI-related properties, such as the capacity fading and internal resistance, from the experimental data.

Christensen and Newman [14] presented a mathematical model to predict SEI growth rate, film resistance, and irreversible capacity loss due to layer formation. In their work, due to the lack of knowledge about diffusion mechanisms in the SEI layer, they assumed that all the ions (Li^+ and PF_6) in all of the regions of the SEI

layer have the same diffusion coefficient, i.e., $5.0 \times 10^{-14}(\frac{m^2}{s})$. On the other hand, Deng et al. [15] found that SEI growth is a diffusion-limited process that is strongly impacted by the diffusion coefficient in this layer, stressing the importance of knowing the exact diffusion coefficient. Also, Liu et al. [16] presented a model proposing a spatially dependent growth of the SEI layer in LIBs. They indicated that in the diffusion-limited condition, by doubling the diffusion coefficient of Li-ions in the SEI layer, the thickness of the layer will increase from 4 to 20 nm (a 500% increase) [16]. However, due to the lack of insight into the diffusion mechanisms, they continued using the constant diffusion coefficient from Christensen and Newman [14], similar to other researchers (e.g., References [16–21]), due to the lack of detailed information on the diffusion mechanisms in the SEI layer. In 2015, Ekström and Lindbergh [22] derived a macro-scale mathematical continuum model to estimate the effect of SEI layer formation on the aging in LIBs that use a graphite anode material. The model is a combination of kinetic and transport control systems and uses a constant diffusion coefficient. In their model, the authors proposed three lumped fitting parameters which are substituted in the equations instead of some variables such as diffusion coefficient. Using these parameters improved the accuracy of their model with respect to the experimental data for different temperature and concentration values. However, employing these fitting parameters has resulted in the dependency of this model on the experimental data. **In general, almost all mathematical models predicting battery electrochemical performance have a significant deviation from experimental data or use some fitting parameters that restrict their performance for new unseen conditions/systems.**

Experimental techniques for studying SEI layers such as scanning and transition

electron microscope [23], focused ion beam [24], and atom probe tomography [25] are usually too expensive and time-consuming. Computational approaches involving QM and MD calculations are excellent alternatives to investigate particle-particle interactions at atomic and even sub-atomic time- and length-scales. By evaluating electron-electron interactions, the QM technique enables the characterization of material and elucidates phenomena with exceptional accuracy, independent of the experimental data. Applying QM simulations would require us to consider the interactions with the electron cloud as well as using the complicated Schrödinger equation ($\hat{H}\Psi = E\Psi$). As a result, QM calculations can only be employed at high computational costs, significantly restricting the size of the system that we can investigate. On the other hand, the MD simulations simplify the complex interactions between a cloud of electrons in a multi-particle system using five main types of interactions, namely, nonbonded[1], bonded[2], angle[3], dihedral[4], and improper[5], and employs a simple algebraic equation instead of the Schrödinger equation for each of them. With such formulations, the computational costs are significantly minimized, and the MD simulations can study systems with more than one million particles that are more than 1000 times larger than the size of the systems that can be investigated by QM simulations, for a much larger timescale than what is possible with the QM simulations [26]. However, MD simulations are dependent on the potential parameters that are often obtained from

---

[1]*Nonbonded:* Refers to the forces of attraction or repulsion between atoms or molecules that do not involve the formation or breaking of chemical bonds such as Van der Waals, Coulombic, and polarization.

[2]*Bonded:* Refers to the attractive and repulsive forces that hold atoms together in a molecule or compound, such as covalent bonds or ionic bonds.

[3]*Angle:* Refers to the forces that determine the spatial arrangement of atoms in a molecule or compound, based on the bond angles between them.

[4]*Dihedral:* Refers to the forces that determine the orientation of two connected bonds in a molecule, based on the angle between them.

[5]*Improper:* Refers to the forces that help maintain the correct orientation of a functional group or a specific atom in a molecule, by preventing unwanted rotation or inversion.

experimental studies. Nevertheless, SEI layers cannot be solely studied through experimental methods due to the rapid formation of the SEI layer in just a few picoseconds, or QM/MD due to the high computational cost of QM calculations, and the limited availability of experimental data for MD simulations.

1.5   Objectives

The main objective of this thesis is to develop a computational framework to study the ageing mechanisms in a battery by accurately accounting for the various electrochemical processes occuring at the various time and length scales in a battery. To accomplish this, the following sub objectives were pursued in this thesis:

1. Establish QM processes to determine the potential parameters for MD simulations.

2. Set up MD framework that accounts for the detailed chemistry within the SEI layer and which can be used to derive the various properties that impact the performance of the battery.

3. Set up a macro-scale model that enables us to study the ageing characteristics of a battery.

4. Validate the entire computational setup with experimental data

 Achieving the above objectives, in Chapter 2, a computational framework that combines QM and MD simulations was proposed. The proposed framework employs a geometric approach for designing the required crystal structures and running the QM calculations to evaluate the potential parameters, employing seven algorithms. The

first five algorithms have been developed for evaluating nonbonded, bonded, angle, dihedral, and improper potential parameters, respectively. The algorithms change the structure of the system for each interaction while keeping the other properties constant, to evaluate their energy employing QM calculations. There are two other algorithms for rotating a vector in the structure and evaluating the dihedral angle between four connected atoms, respectively.

The framework can simulate sufficiently large systems with the accuracy of QM calculations using speeds permissible within the MD simulations. This combination of accuracy and speed enables the simulation of a wide variety of applications such as designing novel cathode materials for batteries, new Nano-carbon drug deliverers, studying interfacial transference in the SEI layer, or characterizing the crystal structures of the Martian soil.

In addition to helping run MD simulations independent of the experimental data, this framework also supports the design and characterization of new materials even in hypothetical conditions and compositions, investigating chemical/physical phenomena that happen over very small time scales, undertaking doping investigations, simulating systems beyond the limits of QM calculations, and predicting system operating conditions dynamically as a function of time.

Overall, the proposed computational framework provides a valuable tool for the simulation of new and novel systems, enabling the investigation of materials and chemical phenomena that cannot be captured experimentally.

Now, the number of atoms that participate in a bonded, angle, dihedral, and improper interaction, are 2, 3, 4, and 4 atoms, respectively, and there are well-established algorithms for creating structural changes as the input of QM calculations

for them [27–31]. Since $\frac{N^2}{2}$ nonbonded interaction exists in a system with N atoms, each QM calculation will provide a $\frac{N^2}{2}$ vector as the input, and the energy of the system as the output. In other words, instead of a data set of (x, U) which can be fitted on a quadratic equation such as $U = K(x - x_0)$ to find K and x_0, we will have data set of $([r_1, ..., r_{\frac{N^2}{2}}], U)$ which must be fitted on nonbonded potential equations such as the Buckingham potential equation as follows:

$$U = \sum_{i=1}^{N} \sum_{j=i}^{N} A_{ij} exp(-\frac{r_{ij}}{B_{ij}}) - \frac{C_{ij}}{r_{ij}^6}, \tag{1.1}$$

where $A_{i,j}$, $B_{i,j}$ and $C_{i,j}$ are the nonbonded potential parameters, and $r_{i,j}$ is distance between the ith and j^{th} atoms. Thus, we will have $\frac{3N^2}{2}$ coefficients for a system of N atoms. This fitting process is not feasible with conventional mathematical methods. Hence, each atom type will be extracted from the system and studied under an isolated situation. Subsequently, a mixing rule will be employed to evaluate the analogous interaction between dissimilar atom types. However, there are some severe drawbacks to this approach:

1. Using mixing rules to estimate the interaction between dissimilar atom types negatively impacts the accuracy.

2. Electron cloud around each atom in a molecule is different from the single-atom situation. Studying the interaction between two atoms by neglecting the other atoms in the molecule will result in a deviation from the experimental data.

3. Polarization in atoms due to the presence of other molecules and atoms in the system is ignored in this approach.

While using a conventional mathematical modelling approach to fit large data sets

to equations with innumerable unknowns is very challenging, machine learning (ML) techniques, deep neural network (DNN) in particular, can make this task relatively easy. With this in mind, in a pioneering approach, a computational framework is introduced in Chapter 3 that combines QM, MD, and ML techniques that collectively overcome the drawbacks of the individual approaches and present a robust tool for the next-generation Nano-based computational investigations for characterizing, designing, developing, and studying a wide range of novel materials/phenomena.

These frameworks were employed to evaluate potential parameters for crystal structures in the SEI layer in Chapters 4 and 5. In these chapters, this new computational framework was employed for coupling QM, MD, and ML calculations for characterizing crystal structures in the SEI layer and estimating potential parameters for running MD simulations. Subsequently, the MD simulation utilized these potential parameters to predict the SEI's crystal properties including density, Young's Modules, Poisson's Ratio, thermal conductivity, and diffusion coefficient.

In Chapter 4, QM calculations and MD simulations were employed to prescribe an equation for the diffusion coefficient as a function of temperature and Li-ions concentration for each crystal structure in the outer part of the SEI layer. Subsequently, a single equation for the diffusion coefficient was integrated with the macro-scale mathematical model to accurately model the physics within the SEI layers.

In Chapter 5, employing SEI layer characteristics, a new macro-scale mathematical model has been developed to evaluate the electrochemical performance of LIBs. This model, as opposed to the previous conventional models, considers the SEI layer section in addition to the anode, cathode, and electrolyte. The SEI properties that were obtained were employed in the macro-scale model to evaluate the operating voltage

for a Li-ion battery and the results were compared with the previous models in the literature and experimental data.

In Chapter 6, the diffusion mechanisms in the SEI layer were used to introduce an enhanced version of the Ekström model with two lumped fitting parameters. The enhanced model was used to study SEI growth and capacity fading as a function of time and initial SOC for a wide range of temperatures and concentrations and the results were validated with respect to the experimental data and compared with the results obtained from the pristine model.

Finally, Chapter 7 summarizes the presented computational frameworks and mathematical models followed by a conclusion of this study on the SEI layer. Additionally, in the "Future Investigation" section in Chapter 7, the importance of solid-state batteries besides the SEI layer for producing durable batteries has been discussed. Finally, some of the applications of the introduced computational framework to overcome the challenges associated with the solid-sate batteries are presented.

Bibliography

[1] Ali Emadi. *Advanced Electric Drive Vehicles*. 2014.

[2] International Energy Agency. Key World Energy Statistics. *Statistics*, 33(August):740, 2011.

[3] Intergovernmental Panel on Climate Change. Working Group 3, Bert Metz, Ogunlade Davidson, Peter Bosch, Rutu Dave, and Leo Meyer. Climate Change 2007: Mitigation: Contribution of Working Group III to the Fourth Assessment Report of the Intergovernmental Panel on Climate Change: Summary for Policymakers and Technical Summary. Technical report, 2007.

[4] Our World Is Data. Greenhouse gas emissions - Our World in Data, 2020.

[5] John B. Goodenough and Youngsik Kim. Challenges for rechargeable li batteries. *Chemistry of Materials*, 22(3):587–603, 2010.

[6] E. Peled. The electrochemical behavior of alkali and alkaline earth metals in nonaqueous battery systems—the solid electrolyte interphase model. *Journal of The Electrochemical Society*, 126(12):2047–2051, dec 1979.

[7] A Naji, Jaâfar Ghanbaja, Bernard Humbert, Patrick Willmann, and Denis Billaud. Electroreduction of graphite in liclo4-ethylene carbonate electrolyte. characterization of the passivating layer by transmission electron microscopy and fourier-transform infrared spectroscopy. *Journal of power sources*, 63(1):33–39, 1996.

[8] Felix Joho, Beat Rykart, Roman Imhof, Petr Novák, Michael E Spahr, and Alain

Monnier. Key factors for the cycling stability of graphite intercalation electrodes for lithium-ion batteries. *Journal of power sources*, 81:243–247, 1999.

[9] Yubo Zhang, Daniil A Kitchaev, Julia Yang, Tina Chen, Stephen T Dacek, Rafael A Sarmiento-Pérez, Maguel AL Marques, Haowei Peng, Gerbrand Ceder, John P Perdew, et al. Efficient first-principles prediction of solid stability: Towards chemical accuracy. *npj Computational Materials*, 4(1):1–6, 2018.

[10] Franz Dinkelacker, Philipp Marzak, Jeongsik Yun, Yunchang Liang, and Aliaksandr S. Bandarenka. Multistage mechanism of lithium intercalation into graphite anodes in the presence of the solid electrolyte interface. *ACS Applied Materials & Interfaces*, 10(16):14063–14069, 2018. PMID: 29539259.

[11] Dong Zheng, Xiao-Qing Yang, and Deyang Qu. Stability of the solid electrolyte interface on the li electrode in li–s batteries. *ACS Applied Materials & Interfaces*, 8(16):10360–10366, 2016. PMID: 27045986.

[12] Aiping Wang, Sanket Kadam, Hong Li, Siqi Shi, and Yue Qi. Review on modeling of the anode solid electrolyte interphase (sei) for lithium-ion batteries. *npj Computational Materials*, 4(1):15, 2018.

[13] Review on Modeling of the Anode Solid Electrolyte Interphase (SEI) for Lithium-Ion Batteries. *npj Computational Materials*, 4(1):1–26, mar 2018.

[14] John Christensen and John Newman. A Mathematical Model for the Lithium-Ion Negative Electrode Solid Electrolyte Interphase. *Proceedings - Electrochemical Society*, 20:85–94, 2003.

[15] Jie Deng, Gregory J. Wagner, and Richard P. Muller. Phase field modeling of solid electrolyte interface formation in lithium ion batteries. *Journal of The Electrochemical Society*, 160(3):A487–A496, 2013.

[16] Lin Liu, Jonghyun Park, Xianke Lin, Ann Marie Sastry, and Wei Lu. A Thermal-Electrochemical Model that Gives Spatial-Dependent Growth of Solid Electrolyte Interphase in a Li-Ion Battery. *Journal of Power Sources*, 268:482–490, 2014.

[17] Xiankun Huang, Shaoyong Ke, Haichao Lv, and Yongzhong Liu. A Dynamic Capacity Fading Model with Thermal Evolution Considering Variable Electrode Thickness for Lithium-Ion Batteries. *Ionics*, 24(11):3439–3450, 2018.

[18] Andrew M. Colclasure, Kandler A. Smith, and Robert J. Kee. Modeling Detailed Chemistry and Transport for Solid-Electrolyte-Interface (SEI) Films in Li-Ion Batteries. *Electrochimica Acta*, 58(1):33–43, 2011.

[19] Githin K. Prasad and Christopher D. Rahn. Model Based Identification of Aging Parameters in Lithium Ion Batteries. *Journal of Power Sources*, 232:79–85, 2013.

[20] Saksham Phul, Abhishek Deshpande, and Balaji Krishnamurthy. A Mathematical Model to Study the Effect of Potential Drop Across the SEI Layer on the Capacity Fading of a Lithium Ion Battery. *Electrochimica Acta*, 164:281–287, 2015.

[21] Birger Horstmann, Fabian Single, and Arnulf Latz. Review on Multi-Scale Models of Solid-Electrolyte Interphase Formation. *Current Opinion in Electrochemistry*, 13:61–69, 2019.

[22] Henrik Ekström and Göran Lindbergh. A model for predicting capacity fade due to SEI formation in a commercial graphite/lifepo$_4$cell. *Journal of The Electrochemical Society*, 162(6):A1003–A1007, 2015.

[23] David B Williams and C Barry Carter. The transmission electron microscope. In *Transmission electron microscopy*, pages 3–17. Springer, 1996.

[24] John Melngailis. Focused ion beam technology and applications. *Journal of Vacuum Science & Technology B: Microelectronics Processing and Phenomena*, 5(2):469–495, 1987.

[25] Thomas F Kelly and Michael K Miller. Atom probe tomography. *Review of scientific instruments*, 78(3):031101, 2007.

[26] Ramavtar Tyagi, Amirmasoud Lanjan, and Seshasai Srinivasan. Co-doping strategies to improve the electrochemical properties of lixmn2o4 cathodes for li-ion batteries. *ChemElectroChem*.

[27] Hao Hu, Zhenyu Lu, and Weitao Yang. Fitting molecular electrostatic potentials from quantum mechanical calculations. *Journal of chemical theory and computation*, 3(3):1004–1013, 2007.

[28] Simone Di Micco, Maria Giovanna Chini, Raffaele Riccio, and Giuseppe Bifulco. Quantum mechanical calculation of nmr parameters in the stereostructural determination of natural products. *European Journal of Organic Chemistry*, 2010(8):1411–1434, 2010.

[29] Chuan Tian, Koushik Kasavajhala, Kellon AA Belfon, Lauren Raguette, He Huang, Angela N Migues, John Bickel, Yuzhang Wang, Jorge Pincay, Qin Wu,

et al. ff19sb: Amino-acid-specific protein backbone parameters trained against quantum mechanics energy surfaces in solution. *Journal of chemical theory and computation*, 16(1):528–552, 2019.

[30] Chengwen Liu, Jean-Philip Piquemal, and Pengyu Ren. Amoeba+ classical potential for modeling molecular interactions. *Journal of chemical theory and computation*, 15(7):4122–4139, 2019.

[31] Yudong Cao, Jhonathan Romero, and Alán Aspuru-Guzik. Potential of quantum computing for drug discovery. *IBM Journal of Research and Development*, 62(6):6–1, 2018.

Chapter 2

A Computational Framework for Evaluating Molecular Dynamics Potential Parameters Employing Quantum Mechanics

PRELUDE: This chapter is been re-produced from the following manuscript with permission of "The Royal Society of Chemistry" Publishing: *A. Lanjan, Z. Moradi, S. Srinivasan, "A Computational Framework for Evaluating Molecular Dynamics Potential Parameters Employing Quantum Mechanics", Mol. Syst. Des. Eng., 2023. DOI:10.1039/D3ME00007A*

Contributing Author: Amirmasoud Lanjan.

Copyrights holder: The Royal Society of Chemistry.

Abstract

Molecular dynamics (MD) and Quantum Mechanics (QM) calculations can be used to characterize novel materials and phenomena that experimental methods cannot

capture. While QM provides accurate results, it is at high computational costs and applicable only to small system sizes. On the other hand, MD can work with larger systems and has better computational efficiency but is incapable of studying novel material/phenomena due to the dependency on the experimental data in the literature. Therefore, complex systems such as solid-electrolyte interface (SEI) layer formation cannot be comprehensively investigated by (I) experimental methods due to small time scales, (II) MD simulations because of the absence of experimental data, and (III) QM calculations due to the relatively large system. Herein we report a suite of new nano-scale algorithms to facilitate studying complex material interphases and molecular systems with the accuracy and precision of the QM calculations and at the speed and system size permissible using the MD simulations. Our formulation addresses the most challenging aspect of performing an MD simulation, i.e., *finding accurate potential (force field) parameters* that are often derived from experimental methods. The computational framework presented in this work consists of seven main functions/algorithms that collectively help us account for the effects of nonbonded, bonded, angle, dihedral, and improper interactions in a system/molecule. It is now possible to use these simulations to design and study wholly new and novel materials and investigate phenomena at an atomic/molecular scale in different conditions without the need for prior experimental investigations. We have successfully validated our algorithms with respect to the experimental data of established materials such as H_2O (a polar molecule), $LiPF_6$ (an ionic compound), C_2H_5OH (ethanol), C_8H_{18} (a long chain molecule), and Ethylene Carbonate (EC) (a complex molecular system). The obtained results have an accuracy of over 90%.

2.1   Introduction

Nanotechnology, involving manipulating materials at the Nano-scale, near-atomic/molecular dimension, is a promising approach to designing new and novel materials with enhanced properties for energy, medicine, consumer products, and manufacturing [1–6]. However, capturing and studying particle-particle interactions at atomic/molecular scale with experimental techniques such as scanning and transition electron microscope [7], focused ion beam [8], and atom probe tomography [9] are usually too expensive and time-consuming. Additionally, many interfacial phenomena, such as solid electrolyte interface (SEI) layer formation, occur at a pico-second time scale inside the battery, making them inaccessible for current conventional experimental techniques [10].

Computational approaches involving Quantum Mechanics (QM) and Molecular Dynamics (MD) calculations are excellent alternatives to investigating particle-particle interactions at atomic and even sub-atomic scales. By evaluating electron-electron interactions, the QM technique enables the characterization of material and elucidates phenomena with exceptional accuracy, independent of the experimental data. Applying QM simulations would require us to consider the interactions with the electron cloud as well as using the complicated Schrödinger equation ($\hat{H}\Psi = E\Psi$). As a result, QM calculations can only be employed at high computational costs, significantly restricting the size of the system that we can investigate.

On the other hand, the MD approach reduces the complexity by simplifying the interactions between particles to just five main types of interactions, namely, (I) *Non-bonded:* Van der Waals, Coulombic, and polarization interactions between two particles, (II) *Bonded:* Repulsion and attraction of bond electron pair between two atoms

in a bond, (III) *Angle:* Interactions between bond pair and valance electrons in two neighbor bonds, (IV) *Dihedral:* Bond pair electron interactions in a sequential series of three bonds (four atoms), and (V) *Improper:* Interactions between bond electrons among three bonds connected to a single atom [11–13]. A simple algebraic equation is required for each interaction to estimate the system energy. For instance, Nonbonded interactions between two atoms, ignoring the polarization, can be obtained by the Buckingham and Coulombic potential equation ($U_{nonbonded} = Ae^{-\frac{r}{B}} - \frac{C}{r^6} + k\frac{q_1 q_2}{r}$), where A, B, and C are the constant coefficients called *potential parameters*, q_i is the partial charge of ith particle, and k is Coulomb's constant. With this formulation, the computational costs are significantly minimized, and the MD simulations can study systems with $\sim 10^6$ particles that are over 1000 times larger than permissible QM system sizes, and for a much longer duration [14–16].

Many phenomena, such as SEI layer formation in batteries, cannot be investigated exclusively by just experimental methods, or QM or MD. The SEI timescales are too fast for experimental investigations. QM is computationally very expensive and cannot handle large systems. MD simulations cannot be undertaken due to the absence of experimental data.

Most thermodynamic, structural, and transport properties of the material / phenomena are readily accessible using MD simulations. The *potential parameters* are essential for MD simulations, directly impacting the accuracy of the results [17, 18]. Given the abilities of MD simulations to characterize materials/phenomena and understand their fundamental properties and characteristics, a significant amount of research is invested in determining the potential parameters and potential equations

for various systems. A literature search reveals that most investigations provide little or even no details on validation of the potential parameters/equations used in their work, raising potential questions on the accuracy of the results [19–23]. Other groups [24–27] have developed potential parameters/equations specifically for a very small set of materials, and have validated it with respect to the experimental data. While they can provide a valuable understanding of those materials' properties, it is unclear whether the same potential parameters/equations can be employed for other materials that are composed of similar functional groups or have a slightly different combination. Effective utilization of MD simulations in the design of new materials heavily relies on accuracy, reliability, and more particularly, the transferability of the potential parameters/equations, which are largely untested and unproven for existing approaches. Very few groups, such as the ones led by Oleg Borodin, Padua - Canongia Lopes, Maginn, and Acevedo, have presented a consistent effort in constructing potential parameters/equations that are applicable beyond a few compounds of interest[28, 29]. However, even their approach applies only to ionic liquids.

The accurate potential parameters for the MD simulations can be obtained either using QM simulations or experiments. Besides the high costs, the main drawback of the experimental approach is that the data are only available for existing and well-investigated materials, making MD simulations inapplicable for new and novel systems [17, 18]. Therefore, QM calculation is the only feasible approach for evaluating the potential parameters for studying novel systems at an atomic scale.

In this approach, each interaction (e.g., a bond length) is investigated separately while others are maintained at the least possible changes from their minimum energy level. Afterward, QM calculation evaluates the system energy (U) as a function of

the single change (x) (e.g., the bond length). Finally, fitting the potential equation on these data sets (x, U) gives the *potential parameters*. These steps will be repeated for all interactions in the system. Therefore, for a system with just a single molecule type, such as ethylene carbonate (EC) with 40 types of interactions, we need around 400 different molecular structures and QM calculations. Thus, a computational framework that combines the QM and MD simulations will fill a large gap in the computational toolkit to study new and novel systems for which experimental data are unavailable.

To this end, we have introduced a novel computational framework containing seven algorithms for employing QM calculations in evaluating potential parameters for MD simulations. This framework employs a geometric approach for designing the required crystal structures and running the QM calculations to evaluate the potential parameters. The first five algorithms have been developed for evaluating nonbonded, bonded, angle, dihedral, and improper potential parameters, respectively. The algorithms change the structure of the system for each interaction such as the distance between two nonbonded atoms or the angle between two bonds, while keeping the other properties constant, to evaluate their energy employing QM calculation. There are two other algorithms for rotating a bond vector in the structure and evaluating the dihedral angle between four connected atoms, respectively. The flowchart and pseudo-code for these algorithms are presented in the ensuing sections. This framework present in this work can simulate sufficiently large systems with the accuracy of the QM calculations using the speeds permissible within the MD simulations. With this combination of accuracy and speed, the proposed framework can be used for a wide variety of applications such as designing novel cathode materials for batteries,

new Nano-carbon drug deliverers, studying interfacial transference in the SEI layer, or characterizing the crystal structures of the Martian soil [10, 14–16, 30]. In addition to helping run MD simulations independent of the experimental data, this framework supports the following investigations:

- Designing and characterizing new materials even in hypothetical conditions and compositions.

- Investigating chemical/physical phenomena that happen over very small time scales (e.g., at pico-second) that cannot be captured experimentally.

- Undertaking doping investigations, studying a variety of dopants that may not be experimentally feasible.

- Simulating systems beyond the limits of QM calculations.

- Predicting system operating conditions dynamically as a function of time.

In addition to presenting the algorithms in the ensuing sections, we also present a successful validation of the framework with respect to the experimental data on the density, viscosity, and dipole moment of established materials, including H_2O (a polar molecule), $LiPF_6$ (an ionic compound), C_2H_5OH (ethanol), C_8H_{18} (a long chain molecule), and EC (a complex molecular system).

2.2 Computational Methods

The atomic force field ($\mathbf{F}$) describes the system in an MD simulation. $\mathbf{F}$ is essentially a gradient of the effective potential (U) that is a combination of the five main types of

interactions, including bond length and angle deformation energies, the rotational energy of the atoms, the Van der Waals inter-atomic, polarizable forces, and Coulomb's electrostatic potential energy. For the ith atom in the system, $\mathbf{F}$ can be represented as:

$$\mathbf{F}_i = -\nabla_i U \left(\mathbf{x}_1, \cdots, \mathbf{x}_N\right), \tag{2.1}$$

where $\mathbf{x}_k$ represents parameters such as distance ($\mathbf{r}$) and angle (θ) of the kth particle. Numerical integration of Newton's equation characterized by this force field via schemes such as the Verlet algorithm will yield an updated position of every particle in the domain. Similarly, the velocity Verlet schemes can calculate the updated velocity. Thus, *QM calculations* can be used to obtain the force field (potential) parameters ($U(\cdot)$) in two steps: (I) Obtain the energy (U) of a system as a function of influential variables among the five main types of interactions, $\mathbf{x}$, (e.g., distance $\mathbf{r}$ and/or the angle θ). (II) Fit a force field (potential) equation on the $U(\mathbf{x})$ data series.

This work considers all of the five main types of interactions in an MD simulation: nonbonded, bonded, angle, dihedral, and improper interactions. A framework containing seven algorithms is developed to employ QM calculation to obtain all these force field parameters for a molecular system.

2.2.1 The Main Procedure

In employing QM calculations to obtain the potential parameters, the following procedure is adopted: **(I)** Initially, we create and optimize the geometry of the crystal structure using QM calculation by minimizing the system's energy. **(II)** Then the partial charge is evaluated for each atom in the system either by extracting it from the literature, or calculating it based on the electronegativity, or using the common

population analysis, such as Lowdin [31], Hirshfeld [32], and Mulliken [33]. It must be noted that since Lowdin and Mulliken's analysis are highly dependent on the basis set of QM calculations and have a significant deviation from experimental data, they can only be used when the other methods were not possible. **(III)** Different atom types are distinguished based on the type of elements and their orientations. For example, in the C_2H_5OH molecule, we have two types of hydrogen atoms, distinguished by their bond with Carbon and Oxygen. **(IV)** Next, we evaluate the nonbonded, bonded, angle, dihedral, and improper potential parameters using the Algorithm 1-7. **(V)** Finally, we run an MD simulation with the potential parameters obtained from these algorithms to characterize the material or phenomena. This sequence is summarized in Figure 2.1.
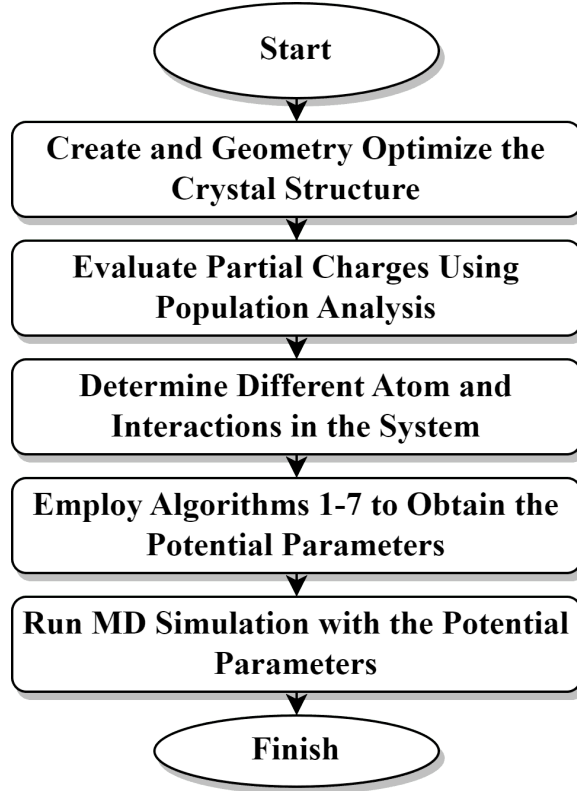
Figure 2.1: Schematic diagram of the main *framework*.

In the ensuing sections, we describe the seven algorithms for evaluating the potential parameters:

Algorithm 1: Nonbonded

Each atom pair in a system has polarization, Van der Waals, and Coulomb interactions, called nonbonded (Figure 2.2). In this work, we considered fixed charges and ignored the polarizing forces. The Coulomb potential energy is evaluated directly from the partial charges obtained in the previous step and Coulomb's law ($U_{Coulomb} = k\frac{q_1 q_2}{r}$).
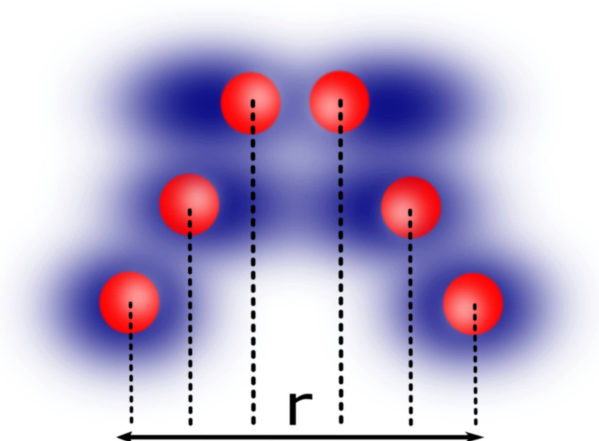
Figure 2.2: Schematic diagram of the *nonbonded* interactions in a molecular system. 3 atom pairs in three different distances (r), corresponding to the attractive, equilibrium, and repulsive states are shown in the schematic. Further, the electron clouds are in blue and the nucleus is in red.

Nonbonded interactions are evaluated by Algorithm 1, which determines the energy (E) of a system containing two atoms of the same type as a function of the distance (r) between them, neglecting the other atoms in the molecule/system to remove other interactions.
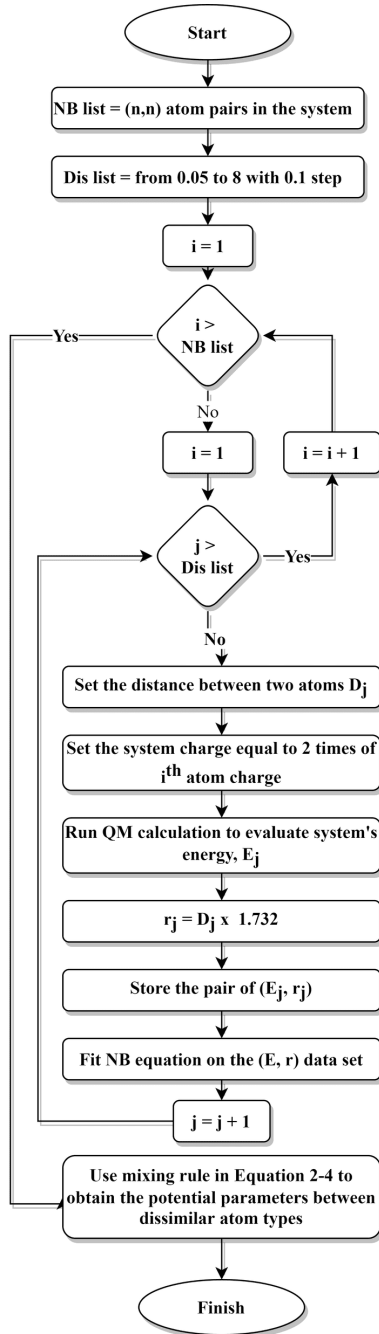
(a) Algorithm 1 Flowchart:
Nonbonded
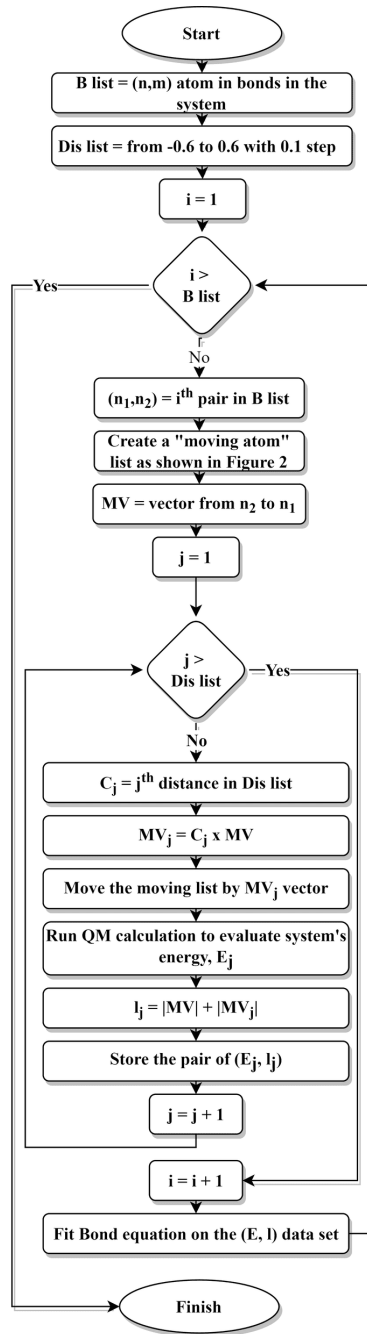
(b) Algorithm 2 Flowchart:
Bonded
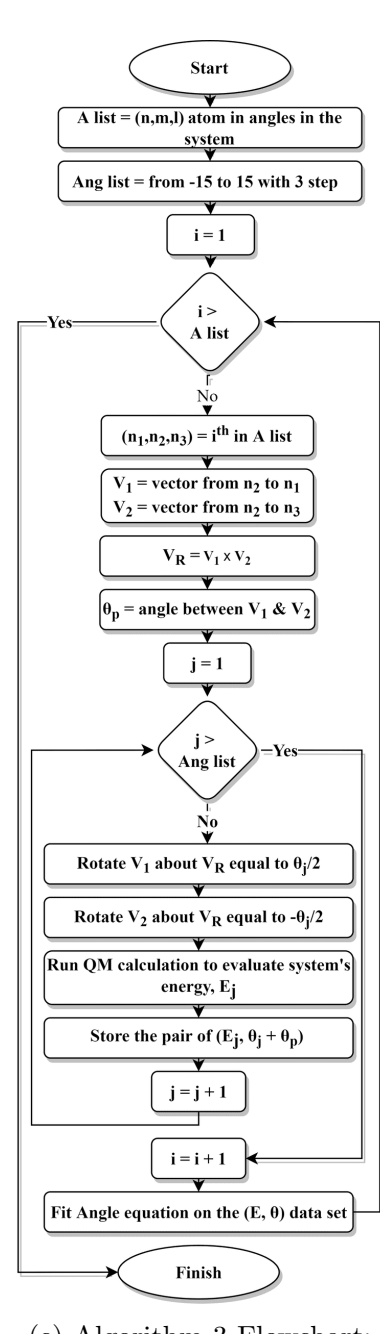
(c) Algorithm 3 Flowchart:
Angle

Figure 2.3

Subsequently, the nonbonded force field equation, Buckingham style in this work (Table 2.2), is fitted on this data sets (E,r) to find the potential parameters A, B, and C. These steps are repeated for each atom type to find the potential parameters of nonbonded interactions between the same atom type. Finally, we employ a mixing rule to calculate these coefficients for the nonbonded interactions between dissimilar atom types as follows:

$$A_{mn} = (A_{mm} * A_{nn})^{0.5}, \tag{2.2}$$

$$B_{mn} = \frac{1}{(\frac{1}{B_{mm}} * \frac{1}{B_{nn}})^{0.5}}, \tag{2.3}$$

$$C_{mn} = -(C_{mm}^{6} * C_{nn}^{6})^{\frac{1}{12}}, \tag{2.4}$$

where A, B, and C are the Buckingham potential parameters. Also, m and n represent the atom-type index in the system. The flowchart and pseudo-code for this algorithm are shown in Figure 2.3a and the Supporting Information (Appendix A), respectively.

Algorithm 2: Bonded Structure Production

This algorithm handles the situations wherein one or more electron pairs in a bond are under intensive repulsion and attraction from other electrons and nuclei, respectively. Bonded interactions result in a relatively strong force on the atom pairs participating in a covalent bond in addition to the nonbonded interactions.
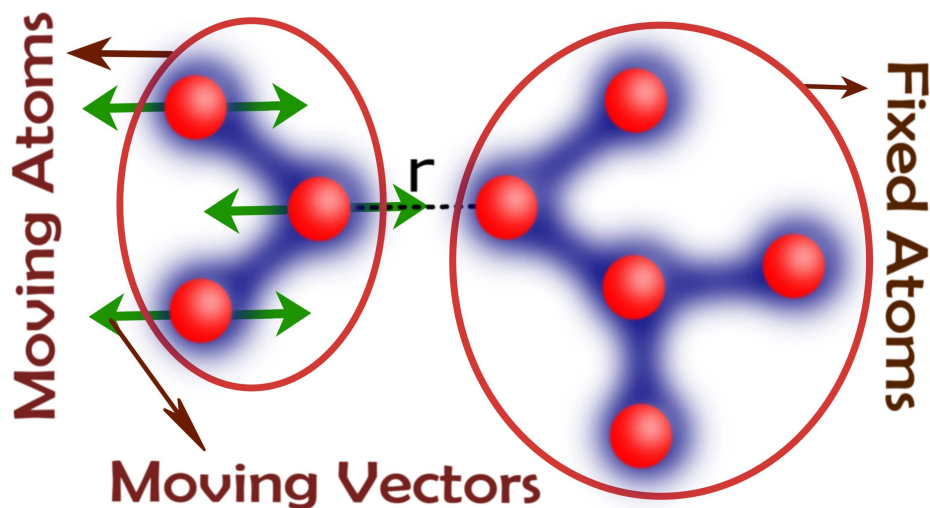
Figure 2.4: Schematic diagram of the *bonded* interactions in a molecular system. The atoms participating in a bond are indicated in orange color. The set of moving atoms and fixed atoms are identified.

Unlike the nonbonded interaction which can be investigated by simply keeping one atom fixed and moving the other, the bonded interaction must be investigated in relation to the entire molecular system. For this, we must evaluate the system's energy level as a function of change in each bond length while adjusting the other influential variables such as other bonds' length, angles, dihedrals, and impropers to maintain them at their minimum energy levels. To accomplish this, Algorithm 2 splits the molecule's structure into two parts. The two groups are connected by the bond under investigation (see the bond between the two orange atoms in Figure 2.4). Next, one group is kept fixed at their minimum energy level, and the other group is moved along the direction of this bond, varying the bond length. The system's energy is evaluated as a function of this bond length. A schematic of the bonded algorithm process is shown in Figure 2.4. Also, the flowchart and pseudo-code for this algorithm are shown in Figure 2.3b and the Supporting Information (Appendix A).

Algorithms 3 and 4: Angle Structure Production

Figure 2.5 shows a schematic of the atoms involved in an angle interaction. The electron pairs in these bonds have repulsive interactions with each other and the nonbonding electrons of the middle atoms (Figure 2.5). Therefore, changing this angle affects the system's energy and is categorized as an angle interaction.
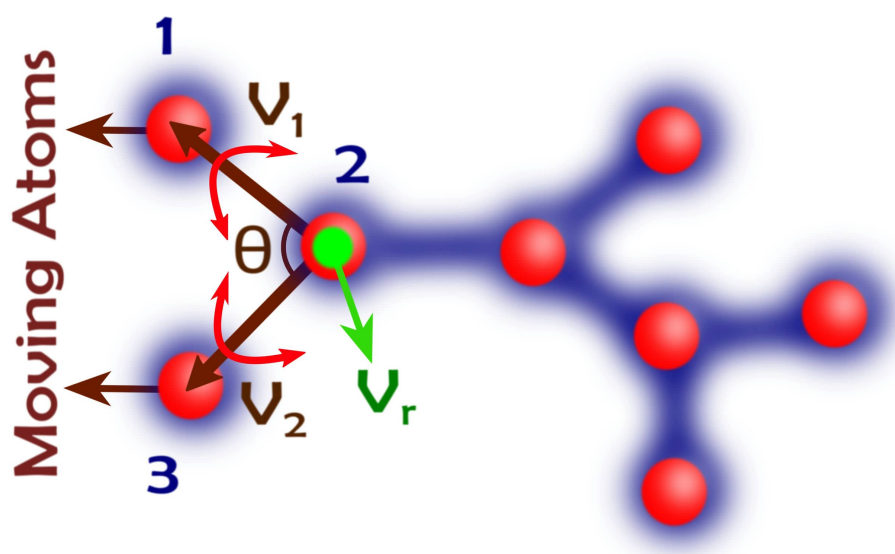
Figure 2.5: Schematic diagram of the *angle* interactions in a molecular system. The atoms participating in the angle are indicated in orange color. The vector $\vec{V_r}$ is orthogonal to the two legs, i.e, $\vec{V_1}$ and $\vec{V_2}$.

To evaluate the system's energy as a function of the angles, the Angle algorithm operates as follows: First, it determines all angle types that are present in the system. The algorithm identifies the two-leg vectors creating a specific angle between 3 atoms (see Figure 2.5). These vectors are then rotated using the "Rotator" function by an angle (θ) to evaluate the impact of a change in the angle on the system's energy. Following this, the energy of the system is calculated employing QM calculations. After creating a data set of the system's energy (E) as a function of an angle (θ), the

angle force field equation ($E = K(\theta - \theta_0)^2$) is fitted to find the potential parameters of the angle which is under investigation. This sequence of steps is repeated for all angle types. Algorithm 3 and its pseudo-code are presented in Figure 2.3c and the Supporting Information (Appendix A), respectively.

An integral part of this algorithm is a "Rotator" function (Figure 2.7a), which receives an angle (θ), a vector ($\vec{V}$), and a reference vector ($\vec{V_r}$) such that $\vec{V}$ makes an angle θ about $\vec{V_r}$. This function employs the following rotation matrix to accomplish this rotation [34]:

$$\vec{R} = \begin{bmatrix} \cos\theta + V_{r_x}^2(1-\cos\theta) & V_{r_x}V_{r_y}(1-\cos\theta) - V_{r_z}\sin\theta & V_{r_x}V_{r_z}(1-\cos\theta) + V_{r_y}\sin\theta \\ V_{r_y}V_{r_x}(1-\cos\theta) + V_{r_z}\sin\theta & \cos\theta + V_{r_y}^2(1-\cos\theta) & V_{r_y}V_{r_z}(1-\cos\theta) - V_{r_x}\sin\theta \\ V_{r_z}V_{r_x}(1-\cos\theta) - V_{r_y}\sin\theta & V_{r_z}V_{r_y}(1-\cos\theta) + V_{r_x}\sin\theta & \cos\theta + V_{r_z}^2(1-\cos\theta) \end{bmatrix}$$

$$(2.5)$$

In the above matrix, V_{r_x}, V_{r_y}, and V_{r_z} represent three vector components of the reference vector (V_r).

Algorithms 5 and 6: Dihedral Structure Production

A dihedral system is created when four atoms are sequentially connected to each other via three covalent bonds in a row. Figure 2.6 shows the schematic of a molecule containing a dihedral formed by atoms labeled 1-4. The electron pairs of these bonds have interactions with other electrons and the nucleus of the atoms, called dihedral interaction. The two bonds connecting 1st to 2nd and 3rd to 4th atoms are the legs for the dihedral angle which rotate about the middle bond that connects atoms 2 and 3. A change in this dihedral angle, while other nonbonded, bonded, and angle

interactions are held constant, affects the system's energy. Thus, this angle is included in a separate category named dihedral interaction.

This algorithm utilizes two essential functions for creating several dihedral structures with different angle values: the *Rotation* function defined in the previous algorithm and the *Angle-Finder* function.
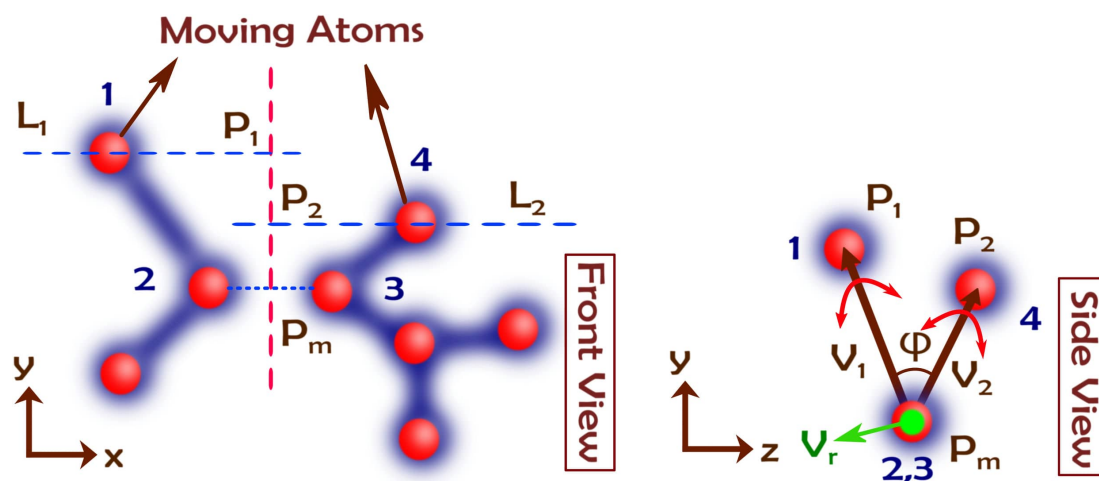
Figure 2.6: Schematic diagram of the *dihedral* interactions in a molecular system. The atoms participating in the dihedral are indicated in orange color.
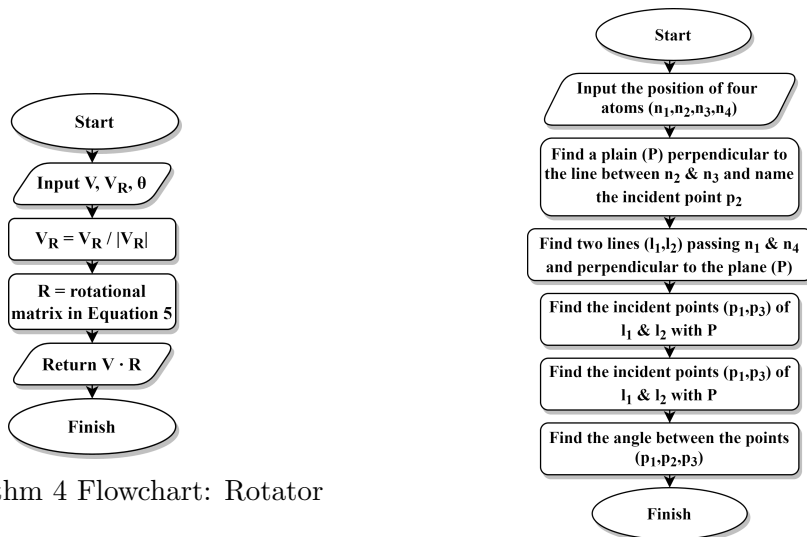
(a) Algorithm 4 Flowchart: Rotator

(b) Algorithm 5 Flowchart: Angle Finder

Figure 2.7: Flowcharts for the *rotator* and the *angle finder* algorithms.

The Angle Finder function is designed to project an image of all four atoms onto a plane that is perpendicular to the bond connecting atoms 2 and 3 (see Figure 2.6). Since these two atoms are projected onto a single point of this plane, we will have only three points on the plane (see Figure 2.6). The "Angle Finder" function will return the angle created by these three points as the dihedral angle. The flowchart and pseudo-code for this "Angle Finder" are presented in Figure 2.7b and the Supporting Information (Appendix A), respectively.

Finally, Algorithm 6 identifies the different dihedral structures, and for each structure, it determines the angle's two leg vectors: the first one connecting atoms 2 and 1, and the second one connecting atoms 3 and 4 (see Figure 2.6). Subsequently, these vectors are rotated around a reference vector connecting atoms 2 and 3, employing Algorithm 4, to create the different dihedral angles. The system's energy is then

evaluated for these different dihedral angles, and an appropriate dihedral interaction equation is used to fit the data to determine the potential parameters for each dihedral. These steps are repeated for all dihedral types present in the system to calculate their potential parameters. The related flow chart and pseudo-code for this are presented in Figure 2.8a and the Supporting Information (Appendix A).

Algorithm 7: Improper Structure Production

An improper angle is an angle between two planes P_1 and P_2 such that P_1 contains the atoms 1, 2, and 3, and P_2 contains the atoms 2, 3, and 4 (see Figure 2.9). As in the dihedral, bonded and nonbonded cases, electron-electron, and electron-nucleus interactions are the source of energy change in the improper interaction. However, the geometric shape of the improper is much different from the dihedral interaction, and hence it is specifically categorized.
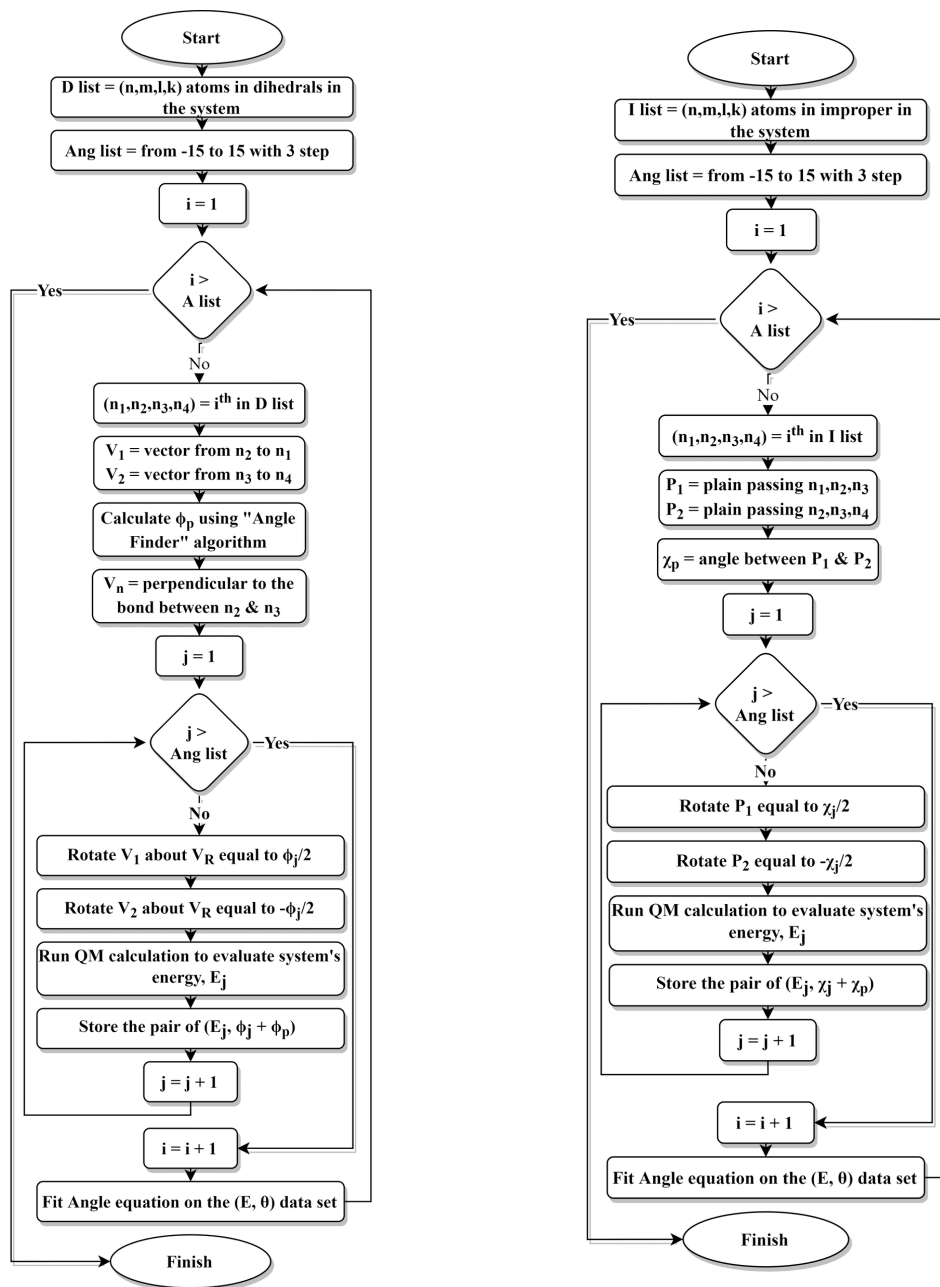
(a) Algorithm 6 Flowchart: Dihedral

(b) Algorithm 7 Flowchart: Improper

Figure 2.8: Flowcharts for the *Dihedral* and the *Improper* algorithms.
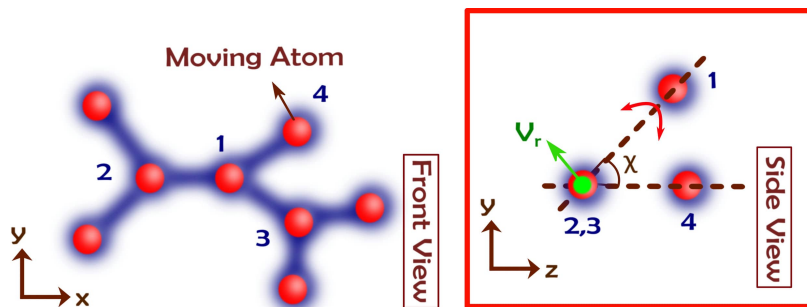
Figure 2.9: Schematic diagram of the *improper* interactions in a molecular system. The atoms participating in the improper are shown in orange color.

Algorithm 7 finds the improper angle and varies this angle to create different structures of the molecule for evaluating the system's energy as a function of the improper angle. Specifically, the algorithm finds the two planes, P_1, and P_2, and uses the "Rotator" algorithm (Algorithm 4), to rotate the plane's normal vector, creating various new improper angles. Finally, the system's energy as a function of such improper angles is calculated and fitted to the appropriate force field equations (Table 2.2). These steps are repeated for all the improper types determined in the system. The flowchart and pseudo-code for this algorithm are presented in Figure 2.8b and the Supporting Information (Appendix A).

2.2.2   Quantum Mechanics Calculations

Since this framework is focused on creating and preparing the molecular input structures for QM and MD calculations, almost all software packages and approximations can be used to evaluate the system's energy, based on the required accuracy and computational costs.

In this work, all QM calculations have been done using the "Quantum Espresso"

package [35, 36] and the following characterizations to make a balance between accuracy and computational costs. Since QM can be used only for systems with a few electrons, the density functional theory (DFT) [37–39] with Perdew Burke Ernzerhof (PBE) as its exchange-correlation function has been employed for QM calculations. Also, other QM approaches such as ab-initio can be employed in this framework for higher accuracy at higher computational costs. The key parameters characterizing the QM simulations are summarized in Table 2.1.

Table 2.1: The summary of the settings for QM calculations in this work.

Properties	Value/Method
XC Functional	PBE
Convergence tolerance	1.0×10^{-6} Ry
W.F. Cutoff	1.0×10^{2}
Charge Cutoff	1.0×10^{2} Ry
Maximum force	1.0×10^{-3} Ry/Bohr
Smearing factor	1.0×10^{-2} Ry

2.2.3   Molecular Dynamics Simulations

Since the system's energy as a function of x (where x is r, θ, ϕ, or χ) is evaluated, all potential styles (equations) and MD simulation software packages are applicable in this framework. In this work, we have employed the "LAMMPS" software package [40], along with the potential styles summarized in Table 2.2. The summation of Buckingham and Coulombs' potentials is considered for the nonbonded interactions. Also, the "Ewald" long-range solver is employed to compute long-range Coulombic interactions.

Table 2.2: The potential styles utilized in the MD simulations using the LAMMPS software package.

Interaction type	Potential Style	Equation
Nonbonded	Buckingham/Coulombic	$E = Ae^{-\frac{r}{B}} - \frac{C}{r^6}$
Bonded	harmonic	$E = K(r - r_0)^2$
Angle	harmonic	$E = K(\theta - \theta_0)^2$
Dihedral	quadratic	$E = K(\phi - \phi_0)^2$
Improper	harmonic	$E = K(\chi - \chi_0)^2$

Eliminating the close contacts between atoms and stabilizing the temperature, velocity, and pressure of the system, the energy is minimized in 20,000 steps followed by two stages of MD simulations under the NVT and NPT ensemble, each for 1 ns and 10 ns, respectively. Parrinello Rahman barostat [41] and Nosé Hoover thermostat [42, 43] were used to fix the simulations' pressure and temperature with damping relaxation times of 0.1 ps and 1 ps, respectively. Stoermer-Verlet integrator with a time step of 1 fs was used to integrate Newton's equations of motion. Dynamic load balancing [44] was employed to overcome the load imbalance on the CPU and minimize the execution time. The trajectories data were stored every 1,000 time steps to compute the time-averaged results for transport and structural properties. Detailed information on the MD characteristics is presented in Table 2.3. The current simulations were run on 11th Gen Intel i7-11700K and 16 GB memory. Around 16 h was needed for these three stages of simulations including energy minimization, equilibrium gain, and property estimation.

Table 2.3: The summary of the settings for MD simulations in this work.

Properties	Descriptions and specifications
Energy minimization	conjugate gradient for 2×10^4 steps
Equilibrium	1 ns NVT run and 10 ns NPT run
Production run	10 ns
Motions integrator	Stoermer-Verlet, 1 fs time-step
Temperature coupling	25^oC, Nose-Hoover thermostat
Pressure coupling	1 bar, Parrinello-Rahman barostat
Constraint solver	Constraining all bonds
Periodic Boundary	x, y and z directions
Long-range interactions	Ewald summation with 1.0×10^{-5} accuracy
Trajectory output	Every 1,000 time step (fs)
Neighbor list updating	Every 10 fs
Dynamic load balance	Yes

2.2.4   Employing the Framework

The algorithms proposed in the previous section have been used to obtain the potential parameters for Nonbonded, Bonded, Angle, Dihedral, and Improper interactions, and the results have been used as the input for the MD simulations. Specifically, in this work, we have studied the following molecules to evaluate the potential (force field) parameters: (i) H_2O, a simple molecule. (ii) $LiPF_6$, a larger molecule with ionic and valance bonds. (iii) $(CH_2O)_2CO$ Ethylene Carbonate (EC), a relatively complex molecule with a ring section. (iv) C_2H_5OH (ethanol), a short-length hydrocarbon. (v) C_8H_{18} (octane), a long chain molecule. Finally, MD simulations using

these parameters have been performed to estimate the different properties of the system, including Density, Viscosity, and Dipole Moment, and the results were validated with the experimental data from the literature.

Viscosity, Density, and Dipole Moment

While there are several models to predict viscosity employing MD simulations [45, 45–53], the Green-Kubo approach is the most widely utilized method [54]. Therefore, in this work, we have employed this method to estimate systems' viscosity using the obtained potential parameters as:

$$\eta(t) = \frac{V}{k_b\,T} \int_0^{\text{inf}} \left\langle P_{\alpha\beta}(t)\dot{P}_{\alpha\beta}(0) \right\rangle dt, \tag{2.6}$$

where V, k_b, and T are the system volume, Boltzman constant, and temperature, respectively. $P_{\alpha\beta}$ represents the elements of $\alpha\beta$ dimension of the pressure tensor. Also, the angle brackets denote the average ensemble.

The density of the system can be obtained using the following formula:

$$\text{Density} = \frac{\sum n_i M_i}{V_{\text{system}}}, \tag{2.7}$$

where n_i and M_i are the numbers and atomic weight of ith atom in the system, respectively. Also, V_{system} is the volume of the system.

The dipole moment is a vector quantity used to measure the separation of two opposite electric charges. The magnitude of the dipole moments is equal to the charge multiplied by the distances between the two charges, and their direction is

from negative to positive:

$$\mu = q\dot{r} \tag{2.8}$$

2.3   Results and discussion

A schematic of H_2O, $LiPF_6$, $(CH_2O)_2CO$ (EC), C_2H_5OH (ethanol) and C_8H_{18} (octane) molecules with an index number assigned to each atom are shown in Figure 2.10.

2.3.1   Evaluating Potential Parameters

The algorithms introduced in the previous section have been employed in conjunction with QM calculations to estimate the energy changes of the different atom types in each molecule as a function of r, θ, ϕ, and χ, and the results are summarized in Table A1-A4 of the Supporting Information (Appendix A). In this, *the same atom type* implies atoms with the same element and partial charge. For example, in the EC molecule shown in Figure 2.10, atoms numbered 2 and 5 are carbon. However, they have been placed in different conditions with different partial charges. Therefore, we have two carbon atom types in each EC molecule.
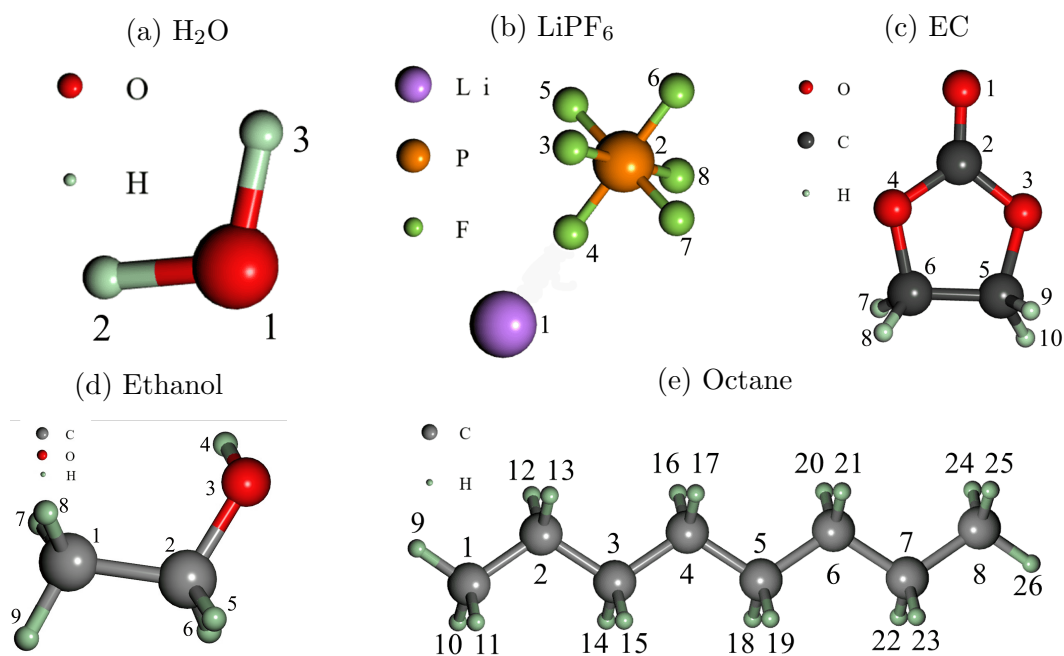
Figure 2.10: Schematic diagram of H_2O, $LiPF_6$, $(CH_2O)_2CO$ (EC), C_2H_5OH (ethanol), and C_8H_{18} (octane) molecules with numbers assigned to each atom for identification. (a) H_2O has two atom types: one bonded and one angle type interaction. (b) $LiPF_6$ molecule has two atom types: one bonded and two angle interactions. (c) For the EC molecule, five different atom types have been considered because each EC molecule has two different types of carbon and two different types of oxygen. Additionally, each EC molecule has five bonded, seven angles, ten dihedral, and three improper types of interactions. (d) Each ethanol molecule contains six atom types, five bonded, four angles, two dihedral, and one improper interaction. (e) The octane molecule has two atoms, bonds, dihedrals and impropers, and three angle interaction types.

In a H_2O molecule, oxygen with a larger atomic radius than hydrogen will experience repulsive forces at longer distances. The potential parameters for such non-bonded interactions have been evaluated by fitting the Buckingham equation (Table 2.2) on the obtained data points for each pair of the same atom type, and the results are summarized in Table A1 of the Supporting Information (Appendix A). Additionally, the potential parameters for all possible pairs were evaluated using the

mixing rules presented in Equations 2.2-2.4 in the previous section.

The R^2 values in fitting the Buckingham potential equation (Table A1 of the Supporting Information (Appendix A)) show an accuracy of nearly 99%. Therefore, it can be claimed that the Buckingham potential style (Table 2.2), which has three variables (A, B, C), is perfectly capable of predicting the trends in the data from QM.

The bonded interaction energy as a function of the bond length has been calculated for different bond types in the three molecules and is shown in Figure A2 of the Supporting Information (Appendix A). Similar to the atom type, the same pair of atoms could have two different bonds between them in a molecule. For example, as shown in Figure 2.10, the 1(O) - 2(C) bond and the 3(O) - 5(C) bond are between the same atoms but have different strengths and lengths. Similarly, as seen in Table A2 of the Supporting Information (Appendix A), the 3(O) - 5(C) bond has a lower length and higher strength compared to the 1(O) - 2(C) bond.

The harmonic style equation (see Table 2.2) is the most common force field style for bonded interaction in MD simulations. This equation has been fitted to the data from the QM simulations. The corresponding parameters for each fit are summarized in Table A2 of the Supporting Information (Appendix A). As seen in this table, the R^2 values are approximately between 85% and 95% (except for 2(P)-3(F) that has an R^2 of 78%), indicating an acceptable accuracy for using the harmonic potential to model the bonded interactions. The 1(O) - 2(C), 2(C) - 3(O), and 3(O) - 5(C) bonds are between carbon and oxygen atoms. However, each of these bonds has different bond lengths and strengths and are summarized in Table A2 of the Supporting Information (Appendix A). The bond between 1(O) - 2(C) (blue dashed line) is a double bond, and, as expected, it has the highest strength. 5(C), which is connected to two

hydrogen atoms, is fed by their electrons and therefore has a lower partial charge despite participating in a bond with an oxygen atom. As a result, the 3(O) - 5(C) bond (green dashed line) has the lowest partial charge difference and the weakest bond strength.

The results from the study of the Angle interactions using the algorithm developed in this work and the QM simulations are summarized in Table A3 of the Supporting Information (Appendix A). Specifically, one angle type for H_2O, two types for $LiPF_6$, seven types for EC, two types for octane, and five types for ethanol molecules have been considered in this work. By fitting the harmonic potential with two parameters to this data (see Table 2.2), we obtain the potential parameters for the Angle interactions. The R^2 values of 99% indicate an excellent accuracy of the harmonic potential equation in modeling the Angle interactions.

Finally, since there are no Dihedral or Improper in H_2O and $LiPF_6$ molecules, these interactions have been considered only for the EC, ethanol, and octane molecules, and the results are shown in Figure A4 in the Supporting Information (Appendix A). In this work, we have used quadratic and harmonic potential equations to model the Dihedral and Improper interactions, respectively. The evaluated potential parameters are summarized in Table A4 of the Supporting Information (Appendix A). Once again, the R^2 values of 99% present a strong validation of our algorithms and justify the use of quadratic and harmonic potential equations in modeling these interactions.

The average repulsive and attractive forces on the different atoms in the dihedral and improper interactions are relatively weak compared to the angle and bonded interactions. The bonded interactions experience the highest interaction forces. Therefore, it is expected that most of the atomic movements in a molecule are dictated by the

angle and bonded interactions instead of the dihedrals and the impropers.

2.3.2   Validating the Accuracy of the Potential Parameters

MD simulations were run for H_2O, $LiPF_6$, EC, ethanol, and octane molecules with the configuration outlined in the Methodology section to determine the density, dipole moment, and viscosity of these molecules. Density and viscosity are two main properties for validating all types of interaction in the system. However, they are susceptible to molecule-molecule interactions. Also, the dipole moment is more sensitive to the molecule structure and so the inter-atomic interactions within a molecule become relevant. Therefore, calculating these properties and demonstrating a good agreement with the experimental data presents a strong validation of our algorithms in determining the potential parameters for the internal and external molecular interactions in different materials. MD Simulations were conducted using the potential parameters obtained from these algorithms, summarized in Tables A1-A4 of the Supporting Information (Appendix A), and simulation characterization described in the previous sections.

Specifically, studying 200 H_2O molecules under 1 (atm) pressure and 25 (C^o) temperature within an MD simulation box, we estimated the density as 0.99 (g/cm^3). This is an accuracy of 99% with respect to the experimental value of 1.00 (g/cm^3) [55]. Similarly, the density for 200 molecules of $LiPF_6$ at atmospheric pressure and the room temperature was calculated as 2.71 (g/cm^3) which is a 4% deviation from the experimental value of 2.84 (g/cm^3) [55]. The same investigation carried out with 200 EC molecules at room temperature and atmospheric pressure predicted the density of the EC molecules as 1.37 g/cm^3. This is a deviation of just 3% from the experimental

value of 1.32 g/cm^3 [55]. Similarly, the density estimates of ethanol (0.73 g/cm^3) and Octance (0.66 g/cm^3) are in excellent agreement with the experimental data of 0.79 g/cm^3 and 0.70 g/cm^3, respectively. A summary of these results is presented in Table 2.4.

The viscosity values for these molecules at the same operating conditions, calculated via the MD simulations that use the potential parameters from our algorithms, are shown in Figure 2.12. The values calculated for H$_2$O, EC, ethanol, and octane systems are 0.99 cP, 1.7 cP, 1.09 cP, and 0.54 cP, respectively. Further, these are in excellent agreement with the experimental data from the literature, i.e., 1 cP, 1.9 cP, 1.09 cP, and 0.51 cP, respectively [55, 56]. A comparison of the estimates from our algorithm and the experimental data is presented in Table 2.4.
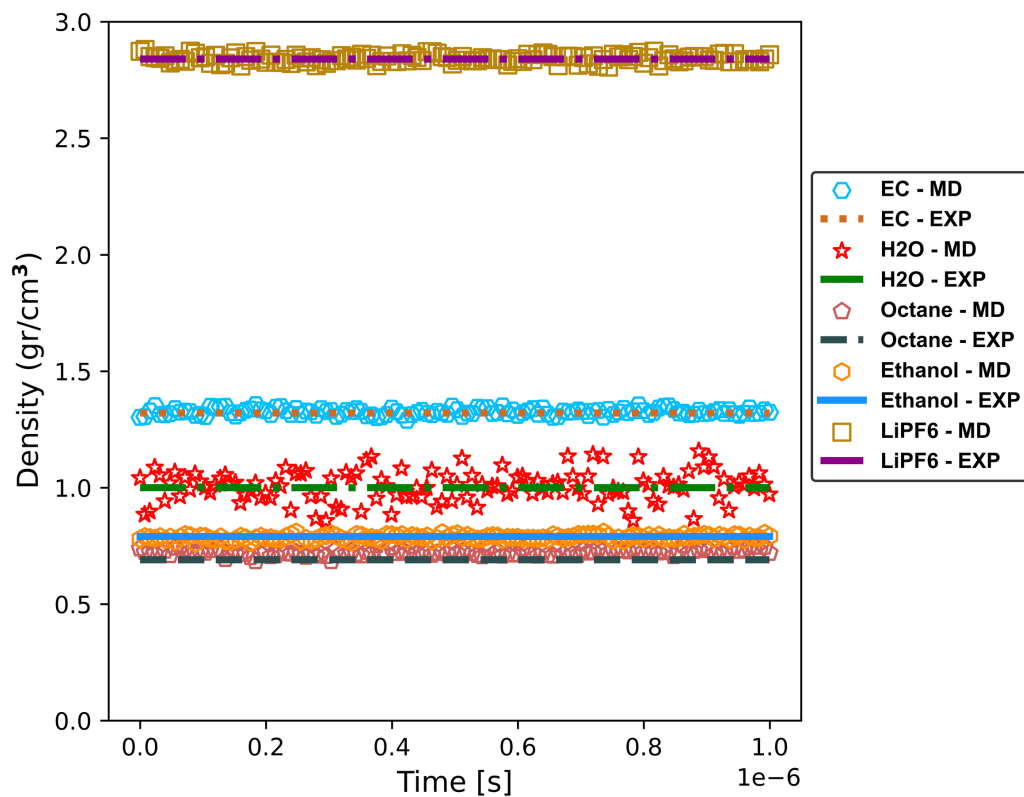
Figure 2.11: The estimated density of H_2O, $LiPF_6$, EC, ethanol, and octane molecules, from the MD simulations that employ the potential parameters from the algorithms presented in this work in comparison with experimental data from [57–61]
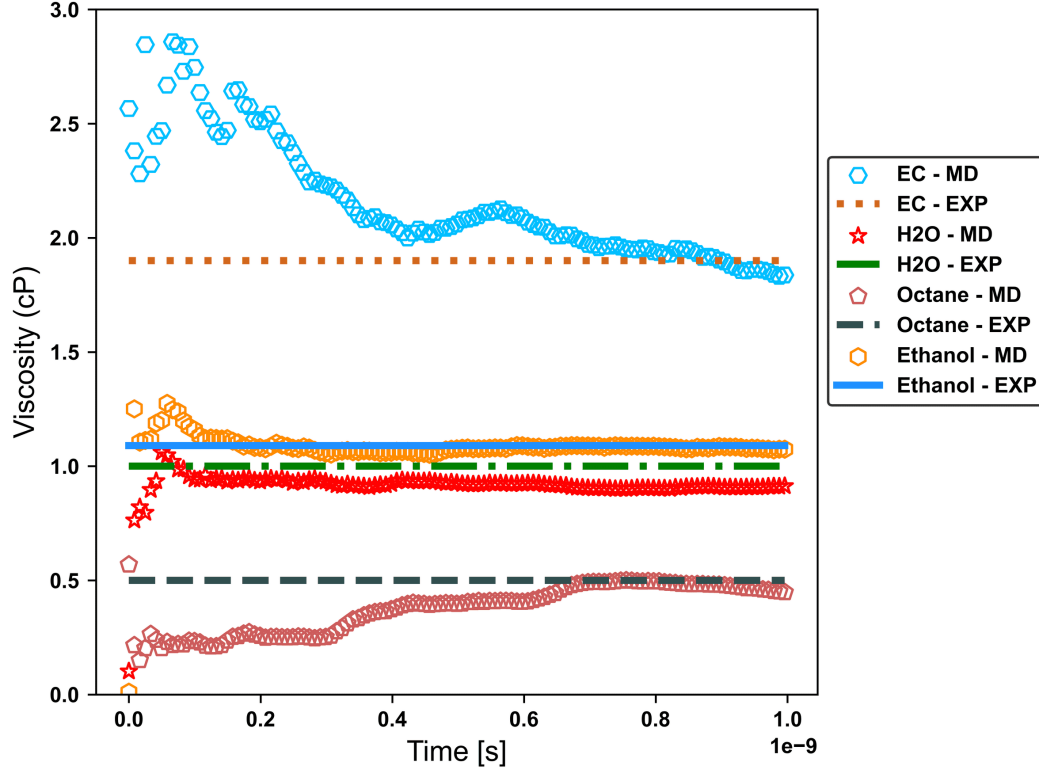
Figure 2.12: Viscosity as a function of time for H_2O, EC, ethanol, and octane molecules, from the MD simulations equipped with the potential parameters from the algorithms presented in this work. The *obtained viscosity* is from MD simulations and using Equation 2.6. The experimental viscosity is extracted from [57–61].

In addition to validating two properties that are governed by the inter-molecular distance and the interactions therein, namely, density and viscosity, we also investigated the dipole moment which represents an inter-atomic property. The dipole moment from the MD systems comprising 200 molecules of ES or H_2O or ethanol is shown in Figure 2.13. We found that the calculated dipole moment for EC (5.04 D), H_2O (2.01 D), and ethanol (1.40 D), has 2%, 8%, and 15% deviation from the corresponding experimental values. Additionally, we also calculated the dipole moment

of octane, a non-dipole molecule. As expected, the MD simulations predicted a small dipole moment of just 0.02 D.
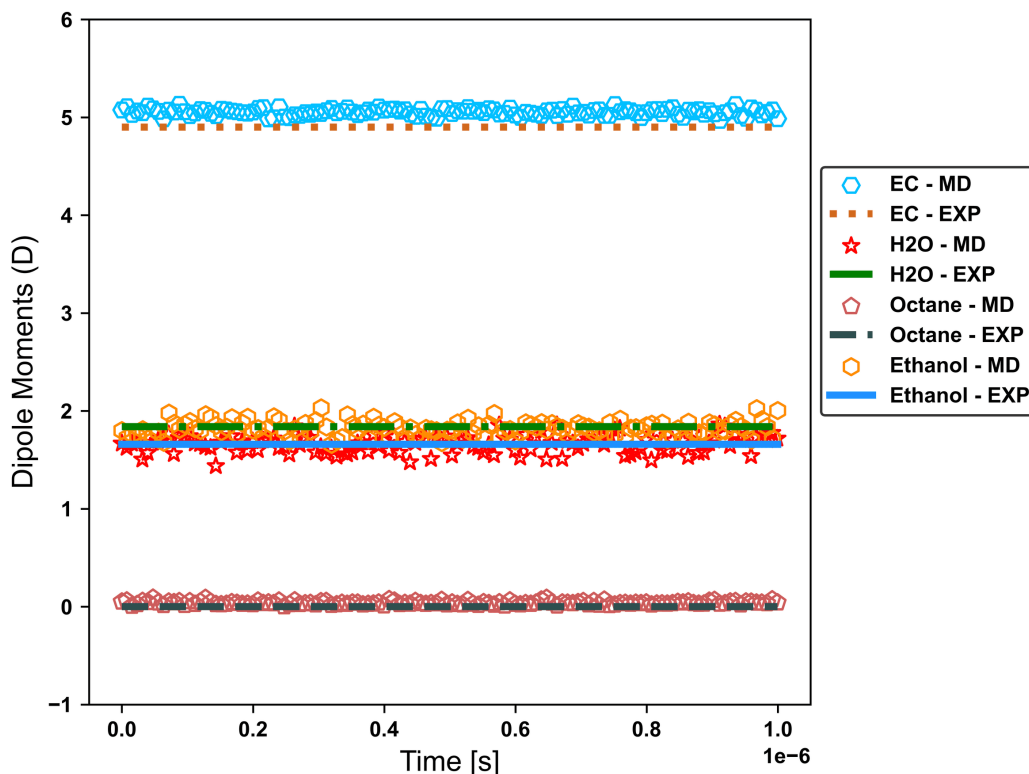
Figure 2.13: The dipole moments of H_2O, EC, ethanol, and octane molecules are calculated from the MD simulations that use the potential parameters from the algorithms presented in this work in comparison to experimental data in the litrature [57–61].

In summary, using the potential parameters generated from algorithms proposed in this work in the MD simulations enables an accurate prediction of multiple properties in a variety of molecules. This clearly establishes the validity and the performance of the suite of algorithms presented in this study, instilling confidence in determining and using the potential parameters of any molecule, including new and novel materials, for MD simulations.

54

Molecules	Properties								
	Density ($\frac{gr}{cm^3}$)			Viscosity (cP)			Dipole Moment (D)		
	This work	EXP	Err	This work	EXP	Err	This work	EXP	Err
H_2O	1.01	1.00	1%	0.93	1.00	7%	1.70	1.84	7%
$LiPF_6$	2.85	2.84	<1%	-	-	-	-	-	-
EC	1.32	1.33	<1%	1.84	1.90	3%	5.05	4.90	3%
ethanol	0.78	0.79	1%	1.07	1.09	2%	1.81	1.66	8%
octane	0.69	0.70	1%	0.46	0.50	8%	0.02	0.00	-

Table 2.4: Density, Viscosity, and Dipole Moment values for H_2O, $LiPF_6$, EC, ethanol, and octane molecules estimated by the introduced algorithm in this work and the experimental data in the literature [57–61].

2.4 Conclusion

MD simulations are a very reliable computational method in the areas of nanotechnology and biomedical sciences. However, the most challenging step for every researcher in this field is finding appropriate and accurate potential parameters. In fact, in the absence of prior experimental data on the materials' potential parameters, it is not possible to employ MD simulations to investigate new and novel materials. Overcoming this limitation, this work presents a suite of algorithms closely coupled with QM calculations to accurately determine the required potential parameters for any molecular configuration and thereby any material systems. Collectively, these algorithms help obtain the potential parameters for the nonbonded, bonded, angle, dihedral, and improper interactions.

The algorithms have been applied to obtain the potential parameters of five different types of molecules, and the values are subsequently used in the MD simulations to calculate the density, viscosity, and dipole moments of these molecules. In all

molecules, all three properties predicted by the MD simulations were in close agreement with the experimental data from the literature, establishing the validity and accuracy of the proposed suite of algorithms. In conclusion, these pioneering algorithms are unique and novel in this field, and we have conclusively established that they can be used to find the potential parameters for compounds for which experimental data is unavailable. Thus, the introduced framework coupling the MD and QM simulations is a next-generation computational tool to design and characterize novel materials and investigate elusive nano-scale phenomena that occur at very rapid time scales.

2.5   Acknowledgments

2.6   Conflicts of interest

There are no conflicts of interest to declare.

Bibliography

[1] Shan Jiang, Junyeob Song, Yujing Zhang, Meitong Nie, Jongwoon Kim, Ana Lopez Marcano, Kelly Kadlec, William A Mills III, Xiaodong Yan, Hefei Liu, et al. Nano-optoelectrodes integrated with flexible multifunctional fiber probes by high-throughput scalable fabrication. *ACS Applied Materials & Interfaces*, 13(7):9156–9165, 2021.

[2] Shan Yan, Dong K Dinh, Guojung Shang, Shan Wang, Wei Zhao, Xin Liu, Richard Robinson, Jack P Lombardi III, Ning He, Susan Lu, et al. Nano-filamented textile sensor platform with high structure sensitivity. *ACS applied materials & interfaces*, 14(13):15391–15400, 2022.

[3] Wei Hong, Yining Zhao, Yuru Guo, Chengcheng Huang, Peng Qiu, Jia Zhu, Chun Chu, Hong Shi, and Mingchun Liu. Pegylated self-assembled nano-bacitracin a: probing the antibacterial mechanism and real-time tracing of target delivery in vivo. *ACS applied materials & interfaces*, 10(13):10688–10705, 2018.

[4] Ramavtar Tyagi and Seshasai Srinivasan. Co-doping studies to enhance the life and electro-chemo-mechanical properties of the limn 2 o 4 cathode using multi-scale modeling and neuro-computing techniques. *Physical Chemistry Chemical Physics*, 24(31):18645–18666, 2022.

[5] Simran Sandhu, Ramavtar Tyagi, Elahe Talaie, and Seshasai Srinivasan. Using neurocomputing techniques to determine microstructural properties in a li-ion battery. *Neural Computing and Applications*, 34(12):9983–9999, 2022.

[6] R Tyagi and S Srinivasan. Molecular dynamics modeling of lithium ion intercalation induced change in the mechanical properties of lixmn2o4. *The Journal of Chemical Physics*, 153(16):164712, 2020.

[7] David B Williams and C Barry Carter. The transmission electron microscope. In *Transmission electron microscopy*, pages 3–17. Springer, 1996.

[8] John Melngailis. Focused ion beam technology and applications. *Journal of Vacuum Science & Technology B: Microelectronics Processing and Phenomena*, 5(2):469–495, 1987.

[9] Thomas F Kelly and Michael K Miller. Atom probe tomography. *Review of scientific instruments*, 78(3):031101, 2007.

[10] Amirmasoud Lanjan, Zahra Moradi, and Seshasai Srinivasan. Multiscale investigation of the diffusion mechanism within the solid–electrolyte interface layer: Coupling quantum mechanics, molecular dynamics, and macroscale mathematical modeling. *ACS Applied Materials & Interfaces*, 13(35):42220–42229, 2021.

[11] Amirmasoud Lanjan and Seshasai Srinivasan. An enhanced battery aging model based on a detailed diffusing mechanism in the sei layer. *ECS Advances*, 1(3):030504, 2022.

[12] Amirmasoud Lanjan, Behnam Ghalami Choobar, and Sepideh Amjad-Iranagh. Promoting lithium-ion battery performance by application of crystalline cathodes lixmn1- zfezpo4. *Journal of Solid State Electrochemistry*, 24(1):157–171, 2020.

[13] Zahra Moradi, Amirmasoud Lanjan, and Seshasai Srinivasan. Enhancement of

electrochemical properties of lithium rich li2ruo3 cathode material. *Journal of The Electrochemical Society*, 167(11):110537, 2020.

[14] Ramavtar Tyagi, Amirmasoud Lanjan, and Seshasai Srinivasan. Co-doping strategies to improve the electrochemical properties of lixmn2o4 cathodes for li-ion batteries. *ChemElectroChem*.

[15] Sheng Bi, Harish Banda, Ming Chen, Liang Niu, Mingyu Chen, Taizheng Wu, Jiasheng Wang, Runxi Wang, Jiamao Feng, Tianyang Chen, et al. Molecular understanding of charge storage and charging dynamics in supercapacitors with mof electrodes and ionic liquid electrolytes. *Nature Materials*, 19(5):552–558, 2020.

[16] Wujie Wang and Rafael Gómez-Bombarelli. Coarse-graining auto-encoders for molecular dynamics. *npj Computational Materials*, 5(1):1–9, 2019.

[17] Zahra Moradi, Amirmasoud Lanjan, and Seshasai Srinivasan. Multiscale investigation into the co-doping strategy on the electrochemical properties of li2ruo3 cathodes for li-ion batteries. *ChemElectroChem*, 8(1):112–124, 2021.

[18] Thijs Van Westen, Thijs JH Vlugt, and Joachim Gross. Determining force field parameters using a physically based equation of state. *The Journal of Physical Chemistry B*, 115(24):7872–7880, 2011.

[19] Mario G Del Pópolo and Gregory A Voth. On the structure and dynamics of ionic liquids. *The Journal of Physical Chemistry B*, 108(5):1744–1752, 2004.

[20] Tianying Yan, Christian J Burnham, Mario G Del Pópolo, and Gregory A Voth.

Molecular dynamics simulation of ionic liquids: The effect of electronic polariz-ability. *The Journal of Physical Chemistry B*, 108(32):11877–11881, 2004.

[21] Jones de Andrade, Elvis S Böes, and Hubert Stassen. Force field development and liquid state simulations on ionic liquids. ACS Publications, 2005.

[22] Yanting Wang and Gregory A Voth. Tail aggregation and domain diffusion in ionic liquids. *The Journal of Physical Chemistry B*, 110(37):18601–18608, 2006.

[23] Yanting Wang and Gregory A Voth. Unique spatial heterogeneity in ionic liquids. *Journal of the American Chemical Society*, 127(35):12192–12193, 2005.

[24] José N Canongia Lopes, Johnny Deschamps, and Agílio AH Pádua. Modeling ionic liquids using a systematic all-atom force field. *The journal of physical chemistry B*, 108(6):2038–2047, 2004.

[25] Xiaoping Wu, Zhiping Liu, Shiping Huang, and Wenchuan Wang. Molecular dynamics simulation of room-temperature ionic liquid mixture of [bmim][bf 4] and acetonitrile by a refined force field. *Physical chemistry chemical physics*, 7(14):2771–2779, 2005.

[26] José N Canongia Lopes and Agílio AH Pádua. Molecular force field for ionic liquids composed of triflate or bistriflylimide anions. *The Journal of Physical Chemistry B*, 108(43):16893–16898, 2004.

[27] Hui Li, Jerry A Boatz, and Mark S Gordon. Cation- cation π- π stacking in small ionic clusters of 1, 2, 4-triazolium. *Journal of the American Chemical Society*, 130(2):392–393, 2008.

[28] Aiping Wang, Sanket Kadam, Hong Li, Siqi Shi, and Yue Qi. Review on modeling of the anode solid electrolyte interphase (sei) for lithium-ion batteries. *npj Computational Materials*, 4(1):1–26, 2018.

[29] Oleg Borodin. Polarizable force field development and molecular dynamics simulations of ionic liquids. *The Journal of Physical Chemistry B*, 113(33):11463–11478, 2009.

[30] Amirmasoud Lanjan, Behnam Ghalami Choobar, and Sepideh Amjad-Iranagh. First principle study on the application of crystalline cathodes li2mn0. 5tm0. 5o3 for promoting the performance of lithium-ion batteries. *Computational Materials Science*, 173:109417, 2020.

[31] Per-Olov Löwdin. On the non-orthogonality problem connected with the use of atomic wave functions in the theory of molecules and crystals. *The Journal of Chemical Physics*, 18(3):365–375, 1950.

[32] Roman F Nalewajski and Robert G Parr. Information theory, atoms in molecules, and molecular similarity. *Proceedings of the National Academy of Sciences*, 97(16):8879–8882, 2000.

[33] Robert S Mulliken. Criteria for the construction of good self-consistent-field molecular orbital wave functions, and the significance of lcao-mo population analysis. *The Journal of Chemical Physics*, 36(12):3428–3439, 1962.

[34] Åke Björck and Clazett Bowie. An iterative algorithm for computing the best estimate of an orthogonal matrix. *SIAM Journal on Numerical Analysis*, 8(2):358–364, 1971.

[35] Giannozzi, P.; Baroni, S.; Bonini, N.; Calandra, M.; Car, R.; Cavazzoni, C.; Ceresoli, D.; Chiarotti, G. L.; Cococcioni, M.; Dabo, I.; Corso, A. D.; Gironcoli, S. D.; Fabris, S.; Fratesi, G.; Gebauer, R.; Gerstmann, U.; Gougoussis, C.; Kokalj, A.; Lazzeri, M.; Mauri, F.; Mazzarello, R.; Paolini, S.; Pasquarello, A.; Paulatto, L.; Sbraccia, C.; Scandolo, S.; Sclauzero, G.; Seitsonen, A. P.; Smogunov, A.; Umari, P.; Wentzcovitch, R. M. QUANTUM ESPRESSO: a modular and open-source software project for quantum simulations of materials. *Journal of Physics: Condensed Matter*, 21(39):395502, sep 2009.

[36] Giannozzi, P.; Andreussi, O.; Brumme, T.; Bunau, O.; Buongiorno Nardelli, M.; Calandra, M.; Car, R.; Cavazzoni, C.; Ceresoli, D.; Cococcioni, M.; Colonna, N.; Carnimeo, I.; Dal Corso, A.; De Gironcoli, S.; Delugas, P.; Distasio, R. A.; Ferretti, A.; Floris, A.; Fratesi, G.; Fugallo, G.; Gebauer, R.; Gerstmann, U.; Giustino, F.; Gorni, T.; Jia, J.; Kawamura, M.; Ko, H. Y.; Kokalj, A.; Kücükbenli, E.; Lazzeri, M. ; Marsili, M.; Marzari, N.; Mauri, F.; Nguyen, N. L.; Nguyen, H. V.; Otero-De-La-Roza, A.; Paulatto, L.; Poncé, S.; Rocca, D.; Sabatini, R.; Santra, B.; Schlipf, M.; Seitsonen, A. P.; Smogunov, A.; Timrov, I.; Thonhauser, T.; Umari, P.; Vast, N.; Wu, X.; Baroni, S., Advanced Capabilities for Materials Modelling with Quantum ESPRESSO. *Journal of Physics Condensed Matter*, 29(46), oct 2017.

[37] W. Kohn and L. J. Sham. Self-Consistent Equations Including Exchange and Correlation Effects. *Physical Review*, 140(4A):A1133, nov 1965.

[38] Ivan Novikov, Blazej Grabowski, Fritz Körmann, and Alexander Shapeev. Magnetic moment tensor potentials for collinear spin-polarized materials reproduce

different magnetic states of bcc fe. *npj Computational Materials*, 8(1):1–6, 2022.

[39] Yang Zhang, Qiunan Xu, Klaus Koepernik, Roman Rezaev, Oleg Janson, Jakub Železnỳ, Tomáš Jungwirth, Claudia Felser, Jeroen van den Brink, and Yan Sun. Different types of spin currents in the comprehensive materials database of non-magnetic spin hall effect. *npj Computational Materials*, 7(1):1–7, 2021.

[40] Steve Plimpton. Fast parallel algorithms for short-range molecular dynamics. *Journal of Computational Physics*, 117(1):1–19, 1995.

[41] Michele Parrinello and Aneesur Rahman. Polymorphic transitions in single crystals: A new molecular dynamics method. *Journal of Applied physics*, 52(12):7182–7190, 1981.

[42] William G Hoover. Canonical dynamics: Equilibrium phase-space distributions. *Physical review A*, 31(3):1695, 1985.

[43] Shuichi Nosé. A unified formulation of the constant temperature molecular dynamics methods. *The Journal of chemical physics*, 81(1):511–519, 1984.

[44] HJC Berendsen, B Hess, E Lindahl, D Van Der Spoel, AE Mark, and G Groenhof. Gromacs: fast, flexible, and free. *J. Comput. Chem*, 26(16):1701–1718, 2005.

[45] Yong Zhang, Derrick Poe, Luke Heroux, Henry Squire, Brian W. Doherty, Zhuoran Long, Mark Dadmun, Burcu Gurkan, Mark E. Tuckerman, and Edward J. Maginn. Liquid structure and transport properties of the deep eutectic solvent ethaline. *The Journal of Physical Chemistry B*, 124(25):5251–5264, 2020. PMID: 32464060.

[46] Alejandro Rodriguez, Stephen Lam, and Ming Hu. Thermodynamic and transport properties of lif and flibe molten salts with deep learning potentials. *ACS Applied Materials & Interfaces*, 13(46):55367–55379, 2021. PMID: 34767334.

[47] Nikhil V. S. Avula, Anwesa Karmakar, Rahul Kumar, and Sundaram Balasubramanian. Efficient parametrization of force field for the quantitative prediction of the physical properties of ionic liquid electrolytes. *Journal of Chemical Theory and Computation*, 17(7):4274–4290, 2021. PMID: 34097391.

[48] Shobha Sharma, Alexander S. Ivanov, and Claudio J. Margulis. A brief guide to the structure of high-temperature molten salts and key aspects making them different from their low-temperature relatives, the ionic liquids. *The Journal of Physical Chemistry B*, 125(24):6359–6372, 2021. PMID: 34048657.

[49] Junfang Zhang, Mojtaba Seyyedi, and Michael B. Clennell. Molecular dynamics simulation of transport and structural properties of co2–alkanes. *Energy & Fuels*, 35(8):6700–6710, 2021.

[50] Ivan M. Zeron, Miguel A. Gonzalez, Edoardo Errani, Carlos Vega, and Jose L. F. Abascal. "in silico" seawater. *Journal of Chemical Theory and Computation*, 17(3):1715–1725, 2021. PMID: 33533631.

[51] Srimayee Mukherji, Nikhil V. S. Avula, and Sundaram Balasubramanian. Refined force field for liquid sulfolane with particular emphasis to its transport characteristics. *ACS Omega*, 5(43):28285–28295, 2020. PMID: 33163812.

[52] Piotr Kubisiak and Andrzej Eilmes. Estimates of electrical conductivity from

molecular dynamics simulations: How to invest the computational effort. *The Journal of Physical Chemistry B*, 124(43):9680–9689, 2020. PMID: 33063509.

[53] Punyaslok Pattnaik, Shampa Raghunathan, Tarun Kalluri, Prabhakar Bhimala-puram, C. V. Jawahar, and U. Deva Priyakumar. Machine learning for accurate force calculations in molecular dynamics simulations. *The Journal of Physical Chemistry A*, 124(34):6954–6967, 2020. PMID: 32786995.

[54] Yong Zhang and Edward J. Maginn. Water-in-salt litfsi aqueous electrolytes (2): Transport properties and li+ dynamics based on molecular dynamics simulations. *The Journal of Physical Chemistry B*, 125(48):13246–13254, 2021. PMID: 34813336.

[55] William M Haynes, David R Lide, and Thomas J Bruno. *CRC handbook of chemistry and physics*. CRC press, 2016.

[56] Behnam Ghalami Choobar, Hamid Modarress, Rouein Halladj, and Spideh Amjad-Iranagh. Multiscale investigation on electrolyte systems of [(solvent+ additive)+ lipf6] for application in lithium-ion batteries. *The Journal of Physical Chemistry C*, 123(36):21913–21930, 2019.

[57] Marco Masia, Michael Probst, and Rossend Rey. Ethylene carbonate- li+: A theoretical study of structural and vibrational properties in gas and liquid phases. *The Journal of Physical Chemistry B*, 108(6):2016–2027, 2004.

[58] Kathie L. Dionisio, Katherine Phillips, Paul S. Price, Christopher M. Grulke,

Antony Williams, Derya Biryol, Tao Hong, and Kristin K. Isaacs. Data descriptor: The chemical and products database, a resource for exposure-relevant data on chemicals in consumer products. *Scientific Data*, 5, 7 2018.

[59] Octane — c8h18 - pubchem.

[60] FX Hassion and RH1955 Cole. Dielectric properties of liquid ethanol and 2-propanol. *The Journal of Chemical Physics*, 23(10):1756–1761, 1955.

[61] Philip G Hill. A unified fundamental equation for the thermodynamic properties of h2o. *Journal of Physical and Chemical Reference Data*, 19(5):1233–1274, 1990.

Chapter 3

Combining Neuro-Computing Techniques with Quantum Mechanics and Molecular Dynamics to Determine the Nonbonded Potential Parameters

PRELUDE: This chapter is been re-produced from the following manuscript which is under review in the "Neural Network Applications" journal: *A. Lanjan, Z. Moradi, S. Srinivasan, "Combining Neuro-Computing Techniques with Quantum Mechanics and Molecular Dynamics to Determine the Nonbonded Potential Parameters", Neural Computing and Applications.*

Contributing Author: Amirmasoud Lanjan.

Abstract

Quantum Mechanics (QM) calculation is the main computational alternative for evaluating potential parameters in Molecular Dynamics (MD) simulations when experimental techniques are inaccessible or too expensive. QM evaluates the system's energy

as a function of the nonbonded distances, and the resulting dataset is fit to a generic potential equation to obtain the fitting constants (potential parameters). However, fitting this massive dataset containing thousands of unknown parameters using traditional mathematical formulations is not computationally feasible. Hence, most of the frameworks in the literature utilize several simplifications, leading to a severe loss of accuracy. Addressing this deficiency, in this work, we employ neuro-computing techniques, Deep Neural Networks (DNN) in particular, to determine these potential parameters by interpreting the QM results. Further, we also present an enhanced computational framework combining QM, MD, and DNN to significantly enhance the prediction accuracy of the intrinsic properties such as density, boiling point, and melting point of five types of molecules, namely, polar molecule H_2O, ionic compound $LiPF_6$, ethanol (C_2H_5OH), long chain molecule C_8H_{18}, and the complex molecular system Ethylene Carbonate (EC). Our results establish the validity and accuracy of the novel computational framework that can be used to determine the potential parameters of new materials in the absence of experimental data. This in turn will help researchers design and develop novel materials for next-generation applications, and help us investigate molecular and nanoscale systems and phenomena.

3.1 Introduction

Nanotechnology, involving material characterization near the atomic/molecular level (Nano-scale), is the most promising technique in designing and developing the next generation of batteries, drug delivery systems, biosensors, and medicines [1–5]. Popular experimental approaches such as the atom probe tomography [6], focused ion beam [7], and scanning/transition electron microscope [8] that facilitate studying

inter-particle interactions are expensive and time-consuming, propelling the need for alternative methods. To this end, computational methods such as quantum mechanics (QM) and molecular dynamics (MD) calculations are significant since they help reduce the time and cost of research, minimize the wastage of materials, have negligible side effects, and most importantly can be employed without any restrictions to study new and novel materials.

QM calculations offer exceptional accuracy in characterizing materials and phenomena by evaluating electron-electron interactions, independent of experimental data [9–11]. However, this accuracy comes at a high computational cost, and QM simulations are usually done only for a very short duration and on small systems with just a few atoms. On the other hand, the MD simulations simplify the complex interactions between a cloud of electrons in a multi-particle system using five main types of interactions, namely, nonbonded[1], bonded[2], angle[3], dihedral[4], and improper[5], and employs a simple algebraic equation instead of the Schrödinger equation for each type. For instance, bonded interactions between two atoms in a bond can be obtained by harmonic potential equation ($U_{bonded}(l) = A(l - l_0)^2$), where A and l_0, the constant coefficients, are called the *potential parameters*, and l is the bond length. With such formulations, the computational costs are significantly minimized, and the MD simulations can study systems with $\sim 10^6$ particles that are more than 1000 times larger than the size of the systems that can be investigated by QM simulations, and for a much larger timescale than what is possible with the QM simulations [12–14].

---

[1]*Nonbonded:* Coulombic, Van der Waals, and polarization interactions between two atoms.
[2]*Bonded:* Attractive and repulsive forces among bonded electron pairs in a bond between two atoms.
[3]*Angle:* Attractive and repulsive interactions of valance electrons and bond pair for two neighbour bonds.
[4]*Dihedral:* Interaction of bonded pair electrons in three bonds in sequential series of four atoms.
[5]*Improper:* Interactions of bonded electron pairs in three bonds group connected to a single atom.

However, MD simulations are dependent on the potential equations/parameters that are often obtained from experimental studies.

In general, important underlying phenomena, such as solid electrolyte interface (SEI) layer formation in batteries, that impact the macroscale behavior of the system, cannot be investigated by the conventional methods by employing one of experimental, MD, or QM techniques, exclusively. This is because experimental approaches cannot capture phenomena that occur at very small timescales (pico-second). QM simulations can only be employed with small systems with a few atoms. MD simulations cannot be done without the experimental data on the potential parameters [15, 16]. To overcome this bottleneck in computational Nano-based techniques, a combination of QM and MD simulations are often employed [13, 17–20].

In our recent work [13], we have developed a comprehensive framework for coupling the QM and MD calculations for evaluating potential parameters as an alternative for experimental techniques. This approach selects a tiny sample of the main system and evaluates its energy as a function of a structural change (e.g., bond length) while other effective parameters are maintained at their minimum energy level. Subsequently, these data sets (e.g., (l, U)) are fitted on the generic potential equations (e.g., $U_{bonded}(l) = A(l - l_0)^2$) to obtain the potential parameters (e.g., A, l_0). These potential parameters are employed in the MD simulations to study the main system's properties. Thus, we can study a system with the accuracy of QM calculations, and at the size and speed permissible with MD simulations, completely independent of experimental techniques.

Now, the number of atoms that participate in a bonded, angle, dihedral, and

improper interaction, are 2, 3, 4, and 4 atoms, respectively, and there are well-established algorithms for creating structural changes as the input of QM calculations for them [17–21]. Since $\frac{N^2}{2}$ nonbonded interaction exists in a system with N atoms, each QM calculation will provide a $\frac{N^2}{2}$ vector as the input, and the energy of the system as the output. In other words, instead of a data set of (x, U) which can be fitted on a quadratic equation such as $U = K(x - x_0)$ to find K and x_0, we will have data set of $([r_1, ..., r_{\frac{N^2}{2}}], U)$ which must be fitted on nonbonded potential equations such as the Buckingham potential equation as follows:

$$U = \sum_{i=1}^{N} \sum_{j=i}^{N} A_{ij} exp(-\frac{r_{ij}}{B_{ij}}) - \frac{C_{ij}}{r_{ij}^6}, \tag{3.1}$$

where $A_{i,j}$, $B_{i,j}$ and $C_{i,j}$ are the nonbonded potential parameters, and $r_{i,j}$ is distance between the ith and j^{th} atoms. Therefore, we will have $\frac{3N^2}{2}$ coefficients for a system of N atoms. This fitting process is not feasible with conventional mathematical methods. Hence, each atom type will be extracted from the system and studied under an isolated situation. Subsequently, a mixing rule will be employed to evaluate the analogous interaction between dissimilar atom types. However, there are some severe drawbacks to this approach:

1. Using mixing rules to estimate the interaction between dissimilar atom types negatively impacts the accuracy.

2. Electron cloud around each atom in a molecule is different from the single-atom situation. Studying the interaction between two atoms by neglecting the other atoms in the molecule will result in a deviation from the experimental data.

3. Polarization in atoms due to the presence of other molecules and atoms in the

system is ignored in this approach.

While using a conventional mathematical modeling approach to fit large data sets to equations with innumerable unknowns is very challenging, machine learning (ML) techniques, deep neural network (DNN) in particular, can make this task relatively easy. With this in mind, in a pioneering approach, we have introduced a computational framework that combines QM, MD, and ML techniques that collectively overcome the drawbacks of the individual approaches and present a robust tool for the next-generation Nano-based computational investigations for characterizing, designing, developing, and studying a wide range of novel materials/phenomena. The ensuing sections present the details of this strategy. The key highlights of the computational framework proposed in this work can be summarized as follows:

- The entire interaction range, from the pairs' Van der Waals radius to the cutoff blue radius, is covered for all atoms that are required for the DNN training data set.

- Herein, a series of atomic coordinates are produced for each atom pair to investigate their interaction with each other while other types of interactions are minimized. Therefore, the produced dataset will be physics-informed which provides higher accuracy and lower computational cost in comparison to a dataset obtained from randomly produced coordinates.

- The algorithm produces coordinates with minimized (almost zero) interactions of the other types such as Bonded, Angel, Dihedral, and Improper interactions, to reduce the deviation from the experimental data.

- The produced distances and energies follow a nonlinear trend to prevent over- or under-fitting in the DNN training step.

- The dataset is large enough for training and testing a proper DNN model.

3.2   Computational Methods
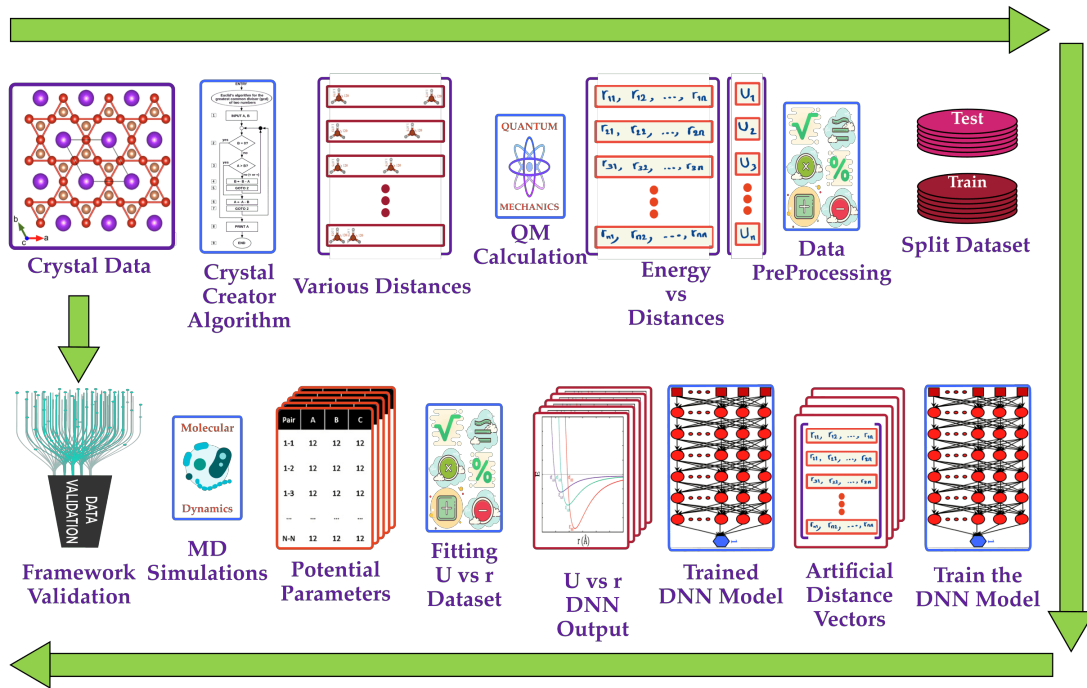
Figure 3.1: Schematic procedure for creating a database and training the DNN model from a crystal structure as the input.

A schematic of the procedure to train the DNN model from the input crystal structure is presented in Figure 3.1. As an initial step, this framework needs to extract position vectors ([element, x, y, z]) of the atoms from the input crystal structures. While the order of listing of the atoms does not affect the system's energy from a physical perspective, it is an influential parameter for training and using the DNN model.

Therefore, in this work, we chose to sort the N atoms of the crystal based on their distance from the center of the crystal (0,0,0). Also, atoms with the same distance from the center point are sorted based on their x positions and then their y value. This sorted list of atomic positions is used as the input for the "Crystal Creator" algorithm.

3.2.1   Crystal Creator Algorithm

After defining a molecule or crystal structure, to find its nonbonded potential parameters, we need to evaluate the system's energy (U) for a wide variety of distances ($r_{i,j}$) between each atom pair. For this, different crystal structures must be produced and QM calculations must be made to evaluate their energy values. Since each QM simulation is time intensive, the sample space of the feasible atomic coordinates (input data) must be carefully defined. More precisely, the sample space must cover a wide range of nonbonded distances for all atom pairs without any repetition. Since randomly produced input structures will result in numerous redundant simulations that not only miss key coordinate structures but also result in an enormous computational cost, we developed the "Crystal Creator" algorithm to create a physics-informed dataset for training a DNN model. This not only helps maintain accuracy but is also computationally efficient.

To begin with, in this algorithm, we run a geometry optimization simulation, employing the QM calculation, to find the system's relaxed coordinates. Next, a list of different atom types in the system is created. Now, for each atom type, one relaxed molecule is put at the center of the system and a second molecule of the same type is rotated and placed near this molecule such that the corresponding atoms are at

the closest distance (see Figure 3.2). Finally, the distance between the two atoms is varied from a few angstroms to the cutoff radius, and for each distance value, the system's energy is obtained using QM calculations. A detailed pseudo code for this algorithm is presented in Algorithm 1.
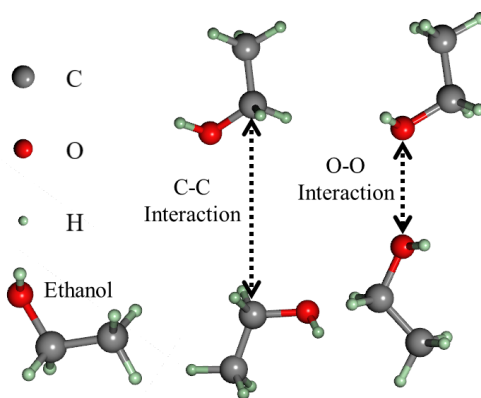
Figure 3.2: Coordinates of an Ethanol molecule for oxygen-oxygen and carbon-carbon interactions, generated using Algorithm 1.

Algorithm 1 Crystal Creator

0: Start
0: Optimize the molecule geometries to find the relaxed molecule's
   coordinates
0: Create a list of different atom types present in the system
0: Define the list of distance values between two atoms as: [0.5, 9.0] (in
   steps of 0.2)
0: for (F_i, S_i) in the list of atom pair types do
0:   for A_j in the list of all atoms in the molecule do
0:     Create and append the $[x_{A_i} - x_{F_i}, y_{A_i} - y_{F_i}, z_{A_i} - z_{F_i}]$ vector to the
   vector list (V_{list}).
0:   end for
0:   Add the molecule in the system in a way that ($x_{F_i} = 0$, $y_{F_i} = 0$, and
   $z_{F_i} = 0$).
0:   Find the geometric center (x_c, y_c, z_c) of the molecule
0:   Create the main vector as: $\vec{V_m} = [x_{F_i} - x_c, y_{F_i} - y_c, z_{F_i} - z_c]$
0:   Find the main vector angle with respect to the vector [1,1,1] as: $\theta = \cos^{-1} \frac{[1,1,1].\vec{V_m}}{|\vec{V_m}|}$
0:   Create a reference vector as: $\vec{V_{ref}} = [1,1,1] \times \vec{V_m}$
0:   Normalize the reference vector's length to unity: $\vec{V_{ref}} = \frac{\vec{V_{ref}}}{|\vec{V_{ref}}|}$
0:   for V_j in the V_{list} do
0:     Rotate V_j by $-\theta$ with respect to $\vec{V_{ref}}$
0:   end for
0:   Find the new positions for this molecule with these new vectors
0:   for D_j in the list of distances do
0:     Add another molecule in the system in a way that ($x_{S_i} = \frac{D_j}{\sqrt{3}}$, $y_{S_i} = \frac{D_j}{\sqrt{3}}$,
   and $z_{S_i} = \frac{D_j}{\sqrt{3}}$)
0:     Create the main vector for the second molecule as: $\vec{V_m} = [x_{F_i} - x_c,$
   $y_{F_i} - y_c, z_{F_i} - z_c]$
0:     Find the main vector's angle with respect to the vector [-1,-1,-1]
   as: $\theta = \cos^{-1} \frac{[-1,-1,-1].\vec{V_m}}{|\vec{V_m}|}$
0:     for V_j in the V_{list} do
0:       Rotate V_j by $-\theta$ with respect to $\vec{V_{ref}}$.
0:     end for
0:     Find the new positions for the second molecule using these vectors
0:     Set the system's charge equal to two times a single molecule charge
0:     Run QM simulation to evaluate the total system energy, E_j
0:     for i = 1 to N do
0:       for j = i to N do
0:         $r_{i,j} = \sqrt{(x_i - x_j)^2 + (y_i - y_j)^2 + (z_i - z_j)^2}$
0:       end for
0:     end for
0:     Store the energy and a vector of distances as ($[r_{1,1}, ..., r_{N,N}]$,E_j)
0:   end for
0: end for
0: Finish =0

3.2.2 Quantum Mechanics

Several crystal structures are created using the "Crystal Creator" algorithm. The energy of the system with this atomic arrangement within the crystal can be obtained via QM simulations using any software package. In this work, we have used "Quantum Espresso" package [22, 23], which provides a great balance between accuracy and computational costs to run the QM calculations. Since QM can be used only for systems with a few electrons, the density functional theory (DFT) [24–26] with Perdew Burke Ernzerhof (PBE) as its exchange-correlation function are employed. Also, higher accuracy can be achieved at the expense of higher computational costs using other QM approaches such as ab-initio. The parameters for the QM simulations in this research are summarized in Table 3.1.

Table 3.1: The summary of the settings for QM calculations in this work.

Properties	Value/Method
XC Functional	PBE
Convergence tolerance	1.0×10^{-6} Ry
W.F. Cutoff	1.0×10^{2}
Charge Cutoff	1.0×10^{2} Ry
Maximum force	1.0×10^{-3} Ry/Bohr
Smearing factor	1.0×10^{-2} Ry

3.2.3 Deep Neural Network Model

Several ML model architectures such as decision tree [27], random forest [28], support vector regression [29], and DNN models [30], are applicable for finding the correlation

between the system's energy and the distances vector. However, the most appropriate model should have the best prediction accuracy and the least computational time for the training and testing processes. With this benchmark, the linear regression, random forest, and decision tree have the least computational processing time but have poor accuracy levels. Further, between the support vector regression and the DNN model, both with very high accuracy, the latter has the lowest training time. Hence, in this work, we have preferred to use the DNN.

DNN Architecture

A DNN model combines mathematical and associative operations to decipher the relationship between the input distance vector ($[\frac{1}{r_{1,1}^k}, \ ..., \ \frac{1}{r_{N,N}^k}]$) and output energy ($U$). A schematic of a DNN with $N^2/2$ neurons in the input layer, one neuron in the output layer, and six intermediate layers, each with a specific number of neurons, is shown in Figure 3.3. A neuron at layer k receives a vector of inputs ($y_i^{(k-1)}$) from the previous layer ($k-1$) and produces an output $y_j^{(k)}$. This output is a function of the weighted sum of the input vector and a bias value ($B_j^{(k)}$). Further, $y_j^{(k)}$ is relayed to every neuron in the subsequent layer. More precisely, the output y_j^k of a neuron is calculated as:

$$y_j^{(k)} = f^{(k)} \left(B_j^{(k)} + \sum_{i=1}^{I} y_i^{(k-1)} w_{ij}^{(k)} \right), \tag{3.1}$$

78
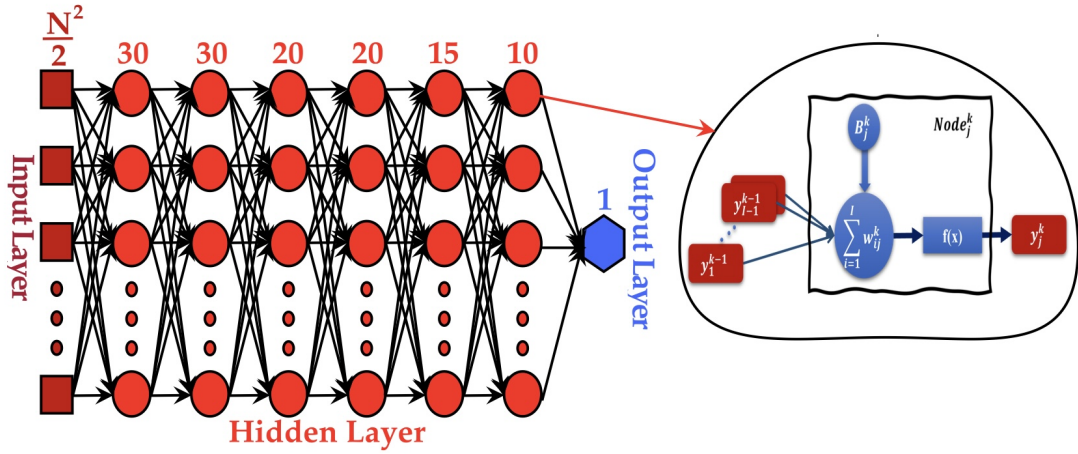
Figure 3.3: Schematic of the DNN model and the function of jth neuron in the kth layer (Equation 3.1).

where $w_{ij}^{(k)}$ is the weight for the jth neuron in layer k. $f(x)$ is the transfer function determining the final alteration of the output. Commonly used transfer functions include *sigmoid, tanh, softmax*, and *rectified linear unit* (ReLU). In this work, we have employed the ReLU function [31] ($f(x) = max(0, x)$) due to its efficiency, accuracy, and ease of implementation. The first fully connected (FC) layer with $\frac{N^2}{2}$ neurons for the input and thirty output neurons is followed by the six FC layers with 30, 30, 20, 20, 15, 10 neurons, respectively. This architecture is inspired by the work of Li et al. [32], forcing the layer to engage features of different scales by reducing the neurons. Finally, the output of the DNN model is a single node that is fed to the linear activation function for estimating the continuous variable, i.e., the system's energy.

Data Pre-Processing

The dataset for the DNN comprises of the distance vectors $[r_{1,1}, r_{1,2}, ..., r_{1,N}, ..., r_{N,N}]_i$ and systems energy (U_i) data that are extracted from the input and output

files of the QM calculations, respectively. This dataset needs pre-processing before feeding to the DNN model. It is well known that U is inversely related to the distance r. More precisely, U is related to r as $U \propto \frac{1}{r^k}$. In this work, to ensure faster and more accurate training of the DNN, we have employed this relationship. Specifically, based on our experience, using $k = 6$, we have defined the input/output pairs as ($[\frac{1}{r_{1,1}^k}, ..., \frac{1}{r_{N,N}^k}]_i, U_i$).

Also, in order to avoid any significant bias emanating from any input parameter, to minimize the training time, and to increase the accuracy and compatibility with the selected ReLU transfer function, the input vectors and output energy values were normalized in the range $[0, 1]$ and standardized with a mean value of 0.5 employing StandarScaler and MinMaxScaler methods in the Scikitlearn [33]. Thus, normized distance $(\hat{r}_{ij})$ can be written as:

$$\frac{1}{\hat{r}_{ij}^k} = \frac{\frac{1}{r_{ij}^k} - min(\frac{1}{r^k})}{max(\frac{1}{r^k}) - min(\frac{1}{r^k})}. \tag{3.2}$$

Also, the standardized value $\frac{1}{r^{*}{}_{ij}^{k}}$ for the ith input vector is equal to:

$$\mu_i = \frac{\sum_{j=0}^{N} \frac{1}{\hat{r}_{ij}^k}}{N}, \quad \sigma_i = \sqrt{\frac{\sum_{j=0}^{N}(\frac{1}{\hat{r}_{ij}^k} - \mu_i)^2}{N}}, \quad \frac{1}{r^{*}{}_{ij}^{k}} = \frac{\frac{1}{\hat{r}_{ij}^k} - \mu_i}{\sigma_i}, \tag{3.3}$$

where $1/r^{*}{}_{ij}^{k}$ is the standardized value of the jth array in the ith vector. μ_i and σ_i are the mean and standard deviation of ith vector, respectively.

DNN Initialization

The performance of a neural network is greatly influenced by the initial values of the weights. In this work, we found that starting with randomly initialized weights does not result in a DNN with high accuracy during the training[34–36]. To address this issue, a pre-training was carried out with a small sample size from the database using the Adam optimizer [37, 38], to minimize the mean squared error (MSE) of the output.

DNN Training

To improve the accuracy and efficiency of training, we used much smaller intervals to investigate shorter inter-atomic distances and used somewhat larger intervals to study cases with larger inter-atomic distances. More precisely, for the inter-atomic distances in the range $[1.5\mathring{A}, 4\mathring{A}]$, we considered 10 distance values. Similarly, just 10 points were considered for the inter-atomic distances in the range $[4\mathring{A}, 8\mathring{A}]$, i.e., we used a much larger interval. This is because we found that DNNs have a larger MSE in the non-linear short inter-atomic distance cases whereas they are more accurate in the larger inter-atomic distance cases where there is more linearity. This is based on the fact that the DNNs have a tendency to estimate the intermediate variables of distinct input values through interpolation. Thus, a total of $20\frac{N^2}{2}$ data points are fed to the system during the training step.

3.2.4   Calculate Potential Parameters

After training, the DNN model is ready to be employed to investigate the interaction between two specific atoms. For this, we define a set of distance vectors as the input of

the DNN model. Through this sequence of vectors, the distance between two atoms is varied while the other distances are kept at the largest possible value to remove their impact on the output energy value. Thus, the change in the energy of the system, obtained as the output of the DNN, is solely a function of the interaction between the two atoms of interest. For instance, the input distance vectors for evaluating the 1-1 interaction is defined as $[\frac{1}{r^6}, \frac{1}{r_c^6}, ..., \frac{1}{r_c^6}]$ where r is varied in a range $[2\mathring{A}, 8\mathring{A}]$ with a step size of $0.1\mathring{A}$ and $r_c = 8\mathring{A}$ is the cutoff distance. The DNN predicts the energy values as a function of the distances $(r_{i,j})$. This data can be used to fit a nonbonded potential equation, Buckingham $(U_{i,j} = A_{i,j}exp(-\frac{r_{i,j}}{B_{i,j}}) - \frac{C_{i,j}}{r_{i,j}^6})$ in this work, to find the potential parameters $(A_{i,j}, B_{i,j}, \text{ and } C_{i,j})$.

3.2.5   Molecular Dynamics

After determining all potential parameters using the DNN, a MD simulation can be run to estimate systems properties and compare the results with the experimental data in the literature for validating the methodology introduced in this work. Since the system's energy is evaluated as a function of r, all potential equations and MD simulation software packages are applicable within this framework. In this work, we have employed the "LAMMPS" software package [39], along with the potential styles summarized in Table 3.2. The nonbonded interactions are modeled using the summation of Buckingham and Coulombs' potentials. Also, the "Ewald" solver is employed to effectively calculate the long-range Coulomb interactions.

Table 3.2: The potential styles utilized in the MD simulations using the LAMMPS software package.

Interaction Type	Potential Style	Equation
Nonbonded	Buckingham/Coulombic	$E = Ae^{-\frac{r}{B}} - \frac{C}{r^6}$
Bonded	harmonic	$E = K(r - r_0)^2$
Angle	harmonic	$E = K(\theta - \theta_0)^2$
Dihedral	quadratic	$E = K(\phi - \phi_0)^2$
Improper	harmonic	$E = K(\chi - \chi_0)^2$

Eliminating the close contacts between atoms and stabilizing the system's temperature, pressure, and velocity, the energy of the system is minimized in 20,000 steps. This is followed by two stages of MD simulations under the NPT and NVT ensemble, for 10 ns and 1 ns, respectively. Parrinello Rahman barostat [40] and Nosé Hoover thermostat [41, 42] were used to fix the simulations' pressure and temperature with damping relaxation times of 100 fs and 1000 fs, respectively. Stoermer-Verlet integrator with a time-step of 1 fs was employed to integrate Newton's equations of motion. Dynamic load balancing [43] was employed to overcome the load imbalance on the CPU and minimize the execution time. The trajectories system data were stored every 1 ps to estimate the time averaged results for structural and transport properties. Additional information on the MD characteristics is presented in Table 3.3. The current simulations were run on 11th Gen Intel i7-11700K and 16 GB memory. Around 16 h was needed for these three stages of simulations including energy minimization, equilibrium gain, and property estimation.

Table 3.3: The summary of the settings for MD simulations in this work.

Properties	Descriptions and specifications
Energy minimization	conjugate gradient for 2×10^4 steps
Equilibrium	1 ns NVT run and 10 ns NPT run
Production run	10 ns
Motions integrator	Stoermer-Verlet, 1 fs time-step
Temperature coupling	25^oC, Nose-Hoover thermostat
Pressure coupling	1 bar, Parrinello-Rahman barostat
Constraint solver	Constraining all bonds
Periodic Boundary	x, y and z directions
Long-range interactions	Ewald summation with 1.0×10^{-5} accuracy
Trajectory output	Every 1,000 time step (fs)
Neighbor list updating	Every 10 fs
Dynamic load balance	Yes

3.3   Results and Discussion

A schematic of H_2O, $LiPF_6$, $(CH_2O)_2CO$ (EC), C_2H_5OH (Ethanol) and C_8H_{18} (Octane) molecules is shown in Figure 3.4.   The parameters for bonded, angle, dihedral, and improper interactions were determined using the pristine algorithm, introduced in our previous work [13]. Additionally, two sets of nonbonded potential parameters were obtained for each atom type using the pristine algorithm as well as the enhanced algorithm introduced in this study to compare the accuracy of the results obtained from these two frameworks.   Here, different *"atom type"* implies different elements

and conditions in a molecule. For instance, each ethanol molecule has a combination of oxygen, carbon, and hydrogen atoms. However, it has six different atom types because the hydrogen atom connected to a carbon atom is a different atom type compared to the hydrogen atom that is connected to an oxygen atom.
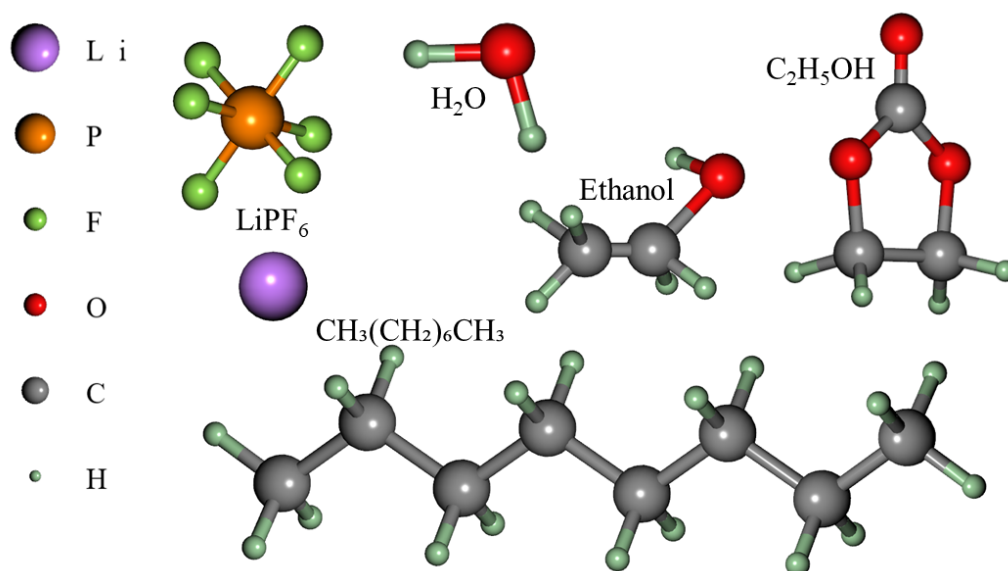
Figure 3.4: Schematic diagram of $LiPF_6$, H_2O, $(CH_2O)_2CO$ (EC), C_8H_{18} (Octane), and C_2H_5OH (Ethanol) molecules. C_8H_{18}, $LiPF_6$ and H_2O that have two, three, and two atom types, respectively. Since each EC molecule has two different carbon and two different oxygen types, this molecule has five different atom types. Finally, each ethanol molecule contains six atom types.

3.3.1   Evaluating Nonbonded Potential Parameters

In an Ethanol molecule, we have considered six different types of atoms for nonbonded interactions. On the other hand, H_2O and Octane molecules contain only two atom types. Finally, $LiPF_6$ and EC molecules have three and five-atom types, respectively. The predicted nonbonded energies were fitted on the Buckingham potential equation and the results are reported in Table B1 of the Supporting Information (Appendix B).

It is important to note that the $R^2 > 99\%$ for almost all parameters demonstrates the high accuracy of the DNN model in predicting the energy trend for nonbonded inter atomic interactions.

Density of a system in MD simulation is defined by the distance between atoms/molecules of that system which is directly governed by the nonbonded interactions. Atoms/molecules are located where the nonbonded interaction is the least (energy well), which has contributions from the Van der Waals and Coulombic interactions. The density of the five molecular systems is calculated using MD simulations and the potential parameters obtained in this work. The evolution of the results is shown in Figure 3.5 and the final density estimates are summarized in Table 3.4. The density values obtained for the five molecules were in close agreement with the experimental data, with a high level of accuracy (greater than 93%) using the pristine algorithm as well as the enhanced algorithm (greater than 95%) proposed in this work. In other words, the framework proposed in this work is fairly accurate in predicting the system's density, validating the algorithm to study nonbonded interactions and the energy well distance.

Table 3.4: Density [g/cm^3] of EC, Ethanol, H$_2$O, LiPF$_6$, and Octane predicted by the pristine and enhanced algorithms, compared with the experimental data from the literature.

Molecule	Enhanced Algorithm (This work)		Pristine Algorithm [13] (previous work)		Experimental Data*
	Density	Error	Density	Error	
EC	1.35	0%	1.34	1%	1.35[44]
Ethanol	0.78	1%	0.75	5%	0.79[45]
H$_2$O	1.02	2%	1.03	3%	0.99[46]
LiPF$_6$	2.50	5%	2.84	7%	2.65[47]
Octane	0.71	1%	0.71	1%	0.70[48]

*The reference for each experimental value is mentioned in the brackets.

(a) H_2O

(b) $LiPF_6$

(c) EC
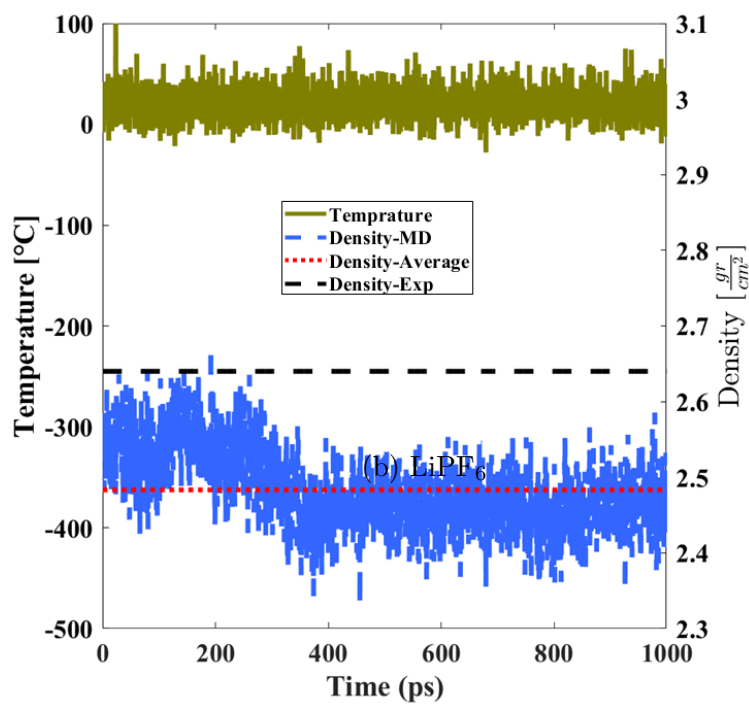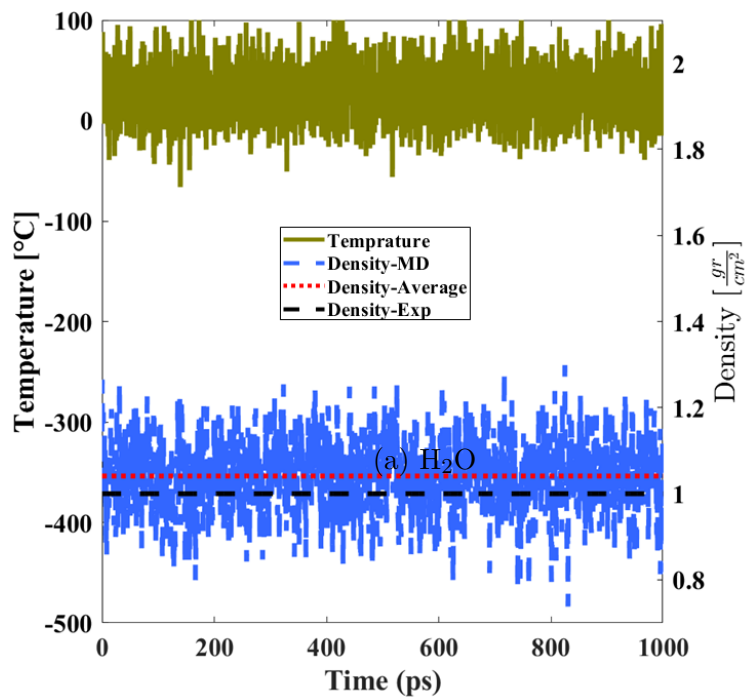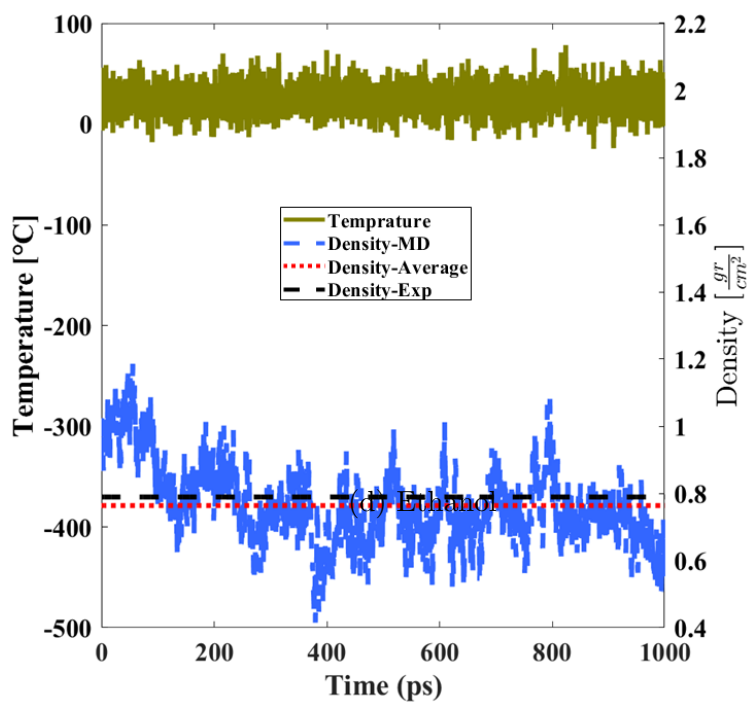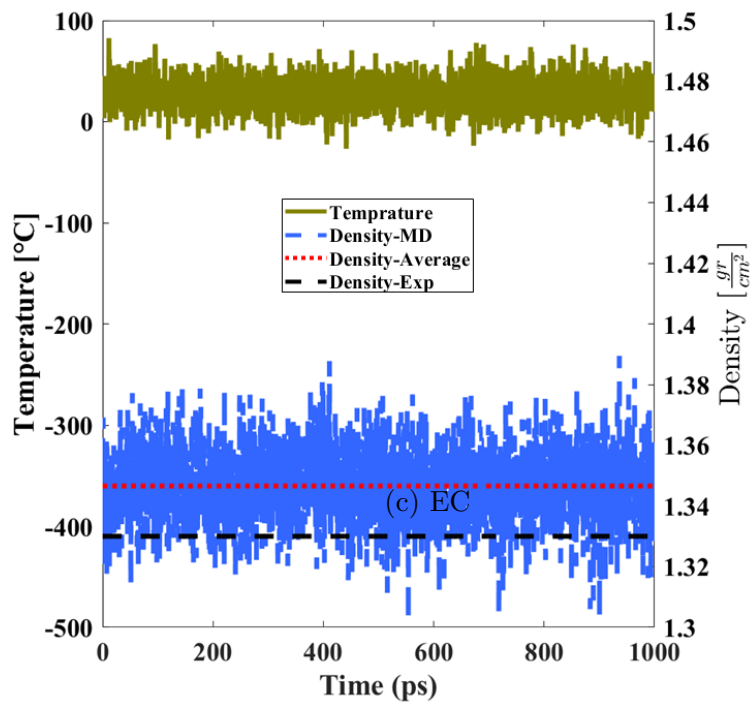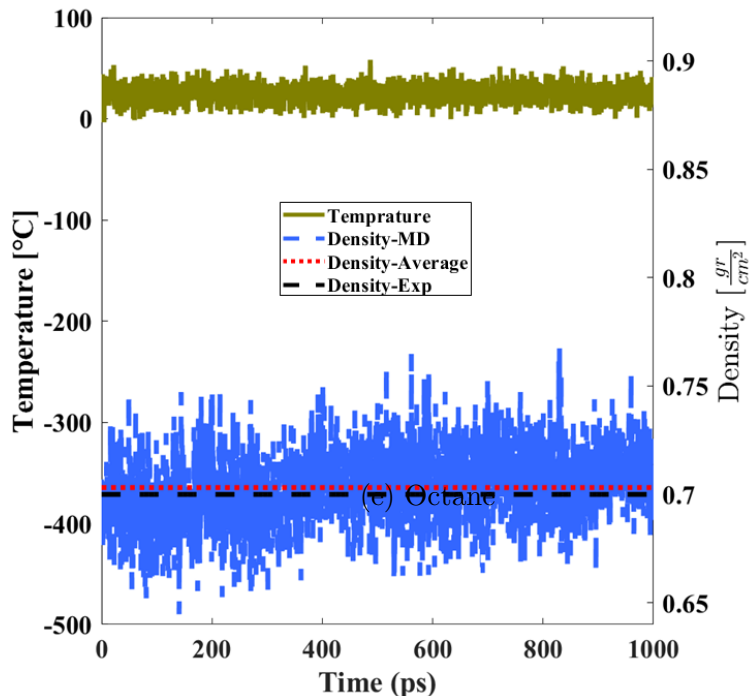
(d) Ethanol

Figure 3.5: The estimated density of H_2O, $LiPF_6$, EC, Ethanol, and Octane molecules, estimated using the enhanced algorithm proposed in this work [44–48].

Melting point is another system property that is governed by the nonbonded interactions. While density only depends on the location of the energy well, melting point is defined by the location and the *depth* of the energy well. The location of the energy well dictates the system's phase whereas the depth of this well defines the energy required for each atom/molecule to escape from this well and overcome some of the nonbonded interactions to undergo a phase transition. Therefore, an accurate estimation of the well's depth, defining the specific amount of energy required for breaking the inter-molecular nonbonded interactions, leads to predicting the exact melting point for the system.

MSD analysis elucidates the atomic/molecular displacement as a function of time

and is one of the conventional methods to study the phase transition using MD simulations. The phase transition from liquid to gas and solid to liquid phase drastically reduce the inter-molecular nonbonded interactions. Therefore, a transition from a solid to a liquid phase or from a liquid to a gas phase will be characterized by a leap in the MSD in MD simulations.

To investigate the melting behaviour of all the systems (except $LiPF_6$), the main step of the MD simulations was run for 50 ns during which the temperature was varied linearly from several degrees higher to several degrees lower than the experimental melting point of that system. In the case of the $LiPF_6$ system, since the melting point of this system is significantly high, it would be easier to stabilize the system at a lower temperature and increase the temperature during the simulation. Therefore, the MD simulation of the $LiPF_6$ system was run from a few degrees below its melting point to a few degrees higher than its melting point. The systems' temperature and MSD of all atoms/molecules are shown in Figures 3.6.

(a) H_2O

(b) $LiPF_6$

(c) EC
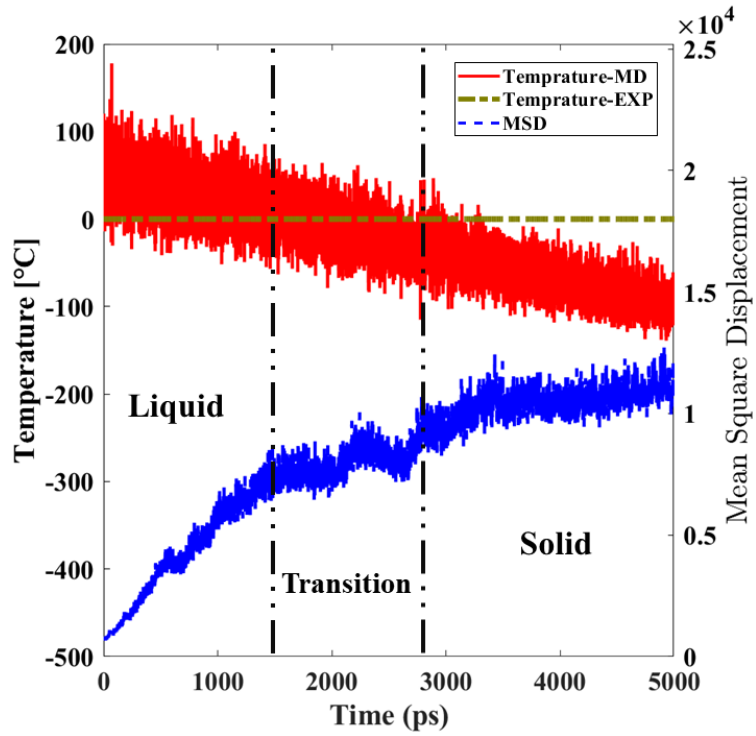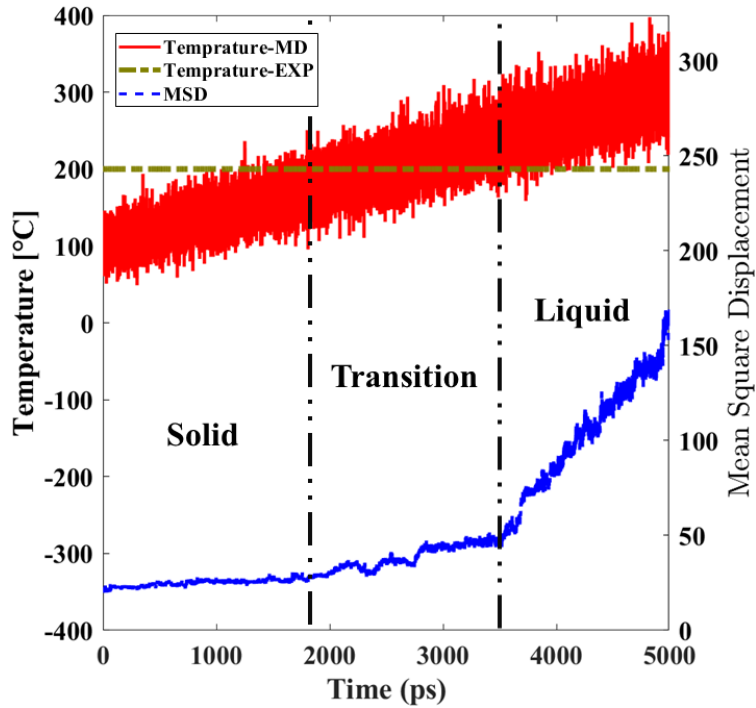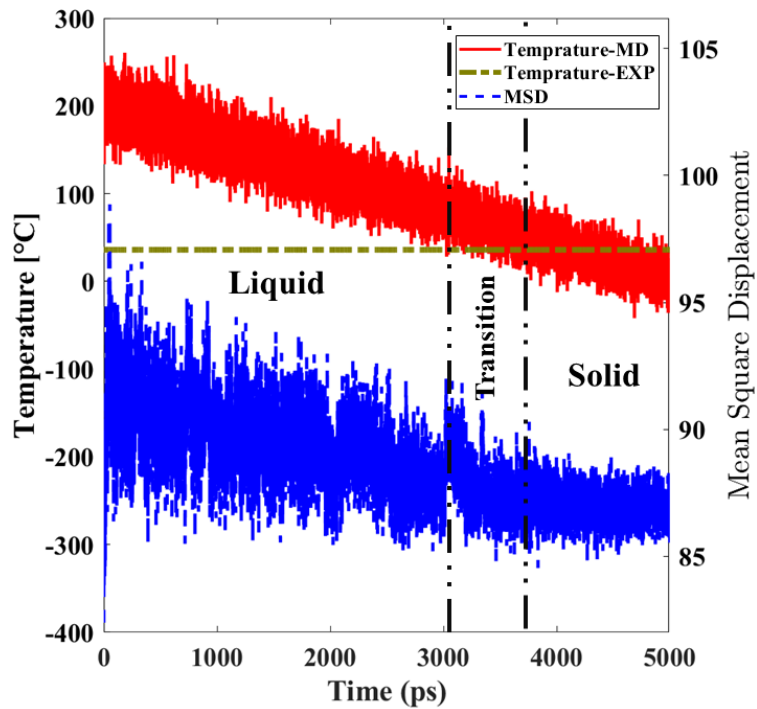
(d) Ethanol
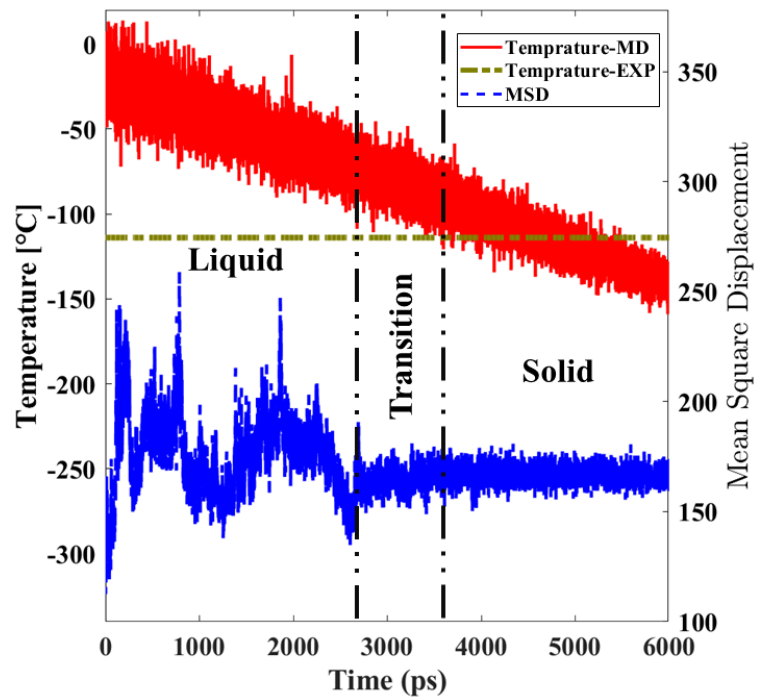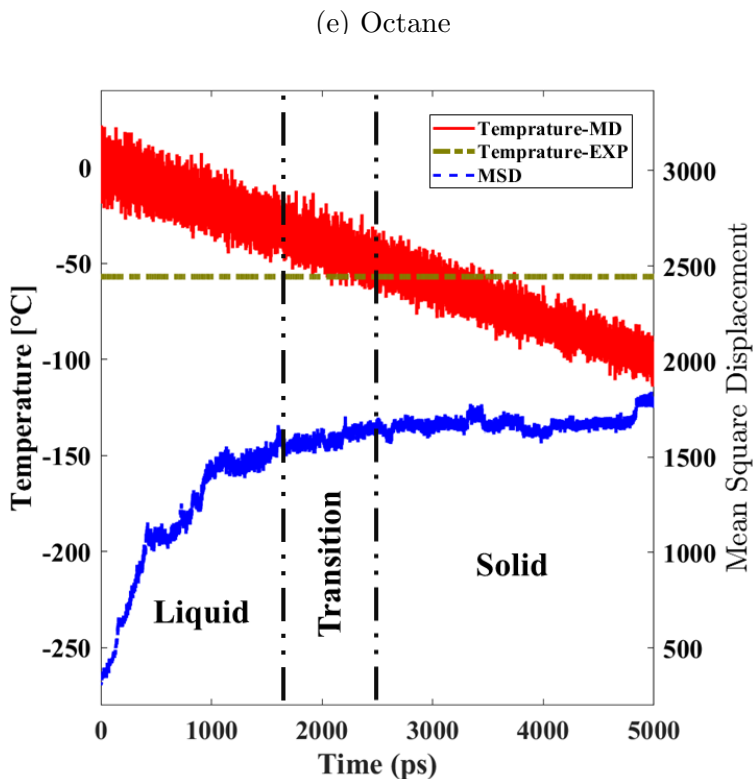
(e) Octane

Figure 3.6: The estimated melting point of H_2O, $LiPF_6$, EC, Ethanol, and Octane molecules, obtained from the algorithm proposed in this work [44–48].

As a natural characteristic of the MD simulations, there is a continuous fluctuation in the temperature of the systems, which makes it difficult to allocate a specific temperature value for them during the simulation. The system temperature can fluctuate around the phase transition temperature several times before completely crossing that point for a stable phase transition. In other words, there is a transition zone (as seen in Figure 3.6) in which the temperature fluctuates across the phase transition temperature for a molecule.

It must be noted that as soon as the temperature fluctuations reach the freezing value, the fluctuations in the MSD values are largely subdued. Similarly, in the case of $LiPF_6$, as we reach the melting point, there is a sharp increase in the MSD value,

and we also observe larger fluctuations. The phase change processes for H_2O, $LiPF_6$, EC, Ethanol, and Octane molecules are evaluated for the systems with the predicted nonboned potential parameters from the enhanced and pristine algorithms, and the results are summarized in Table 3.5.

Table 3.5: Melting Point [°C] of EC, Ethanol, H_2O, $LiPF_6$, and Octane predicted by pristine and enhanced algorithm, compared with the experimental data from the literature.

Molecule	Enhanced Algorithm (This work)		Pristine Algorithm [13] (previous work)		Experimental Data*
	Value	Error	Value	Error	
EC	50	35%	100	170%	37[44]
Ethanol	-100	13%	NA	-	-115[45]
H_2O	0	0%	NA	-	0[46]
$LiPF_6$	200	0%	NA	-	200[47]
Octane	-50	17%	NA	-	-60[48]

*The reference for each experimental value is in the brackets.

The melting points of various molecular systems can be accurately estimated using the methodology introduced in this study, as evidenced by the results for H2O and LiPF6 (Figure 3.6). The results for Ethanol and Octane molecular systems, although not as accurate, are still reasonable. It is noteworthy that the pristine framework is unable to determine the melting points of these molecules.

This framework is able to predict the melting temperature reasonably well (except for EC) because of its ability to determine the depth of the energy well. In the case of the EC molecule, it has the most complex structure, including an atomic ring and 6 different atom types. As a result, it has the lowest accuracy among all molecular

systems since these characteristics and complexities are not explicitly accounted for in this framework.

Boiling point, like the melting point, is governed by the depth and distance of the energy well in the nonbonded interactions. To establish the superiority of the framework presented in this work, MSD analysis of the boiling/dew point calculations for all five systems have been carried out. The results from the framework are shown in Figure 3.7.

(a) H_2O
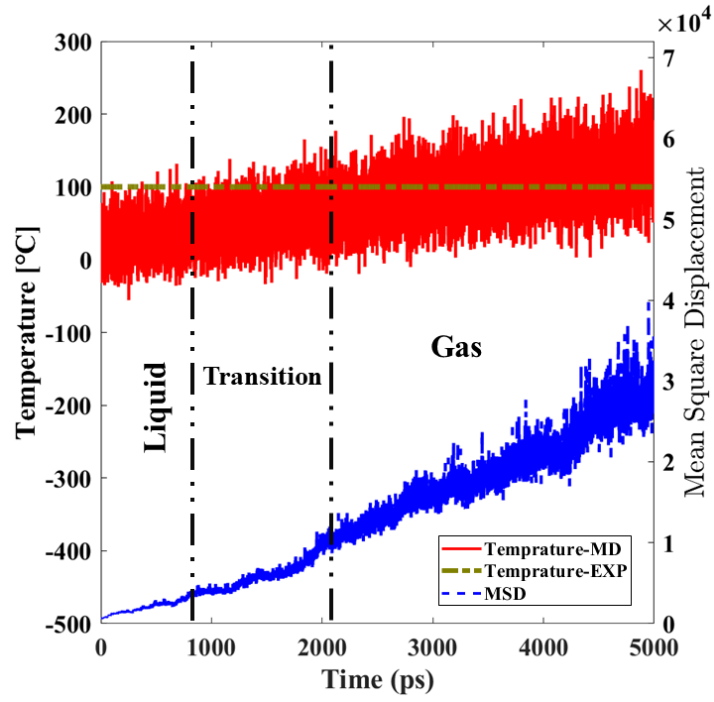
(b) EC
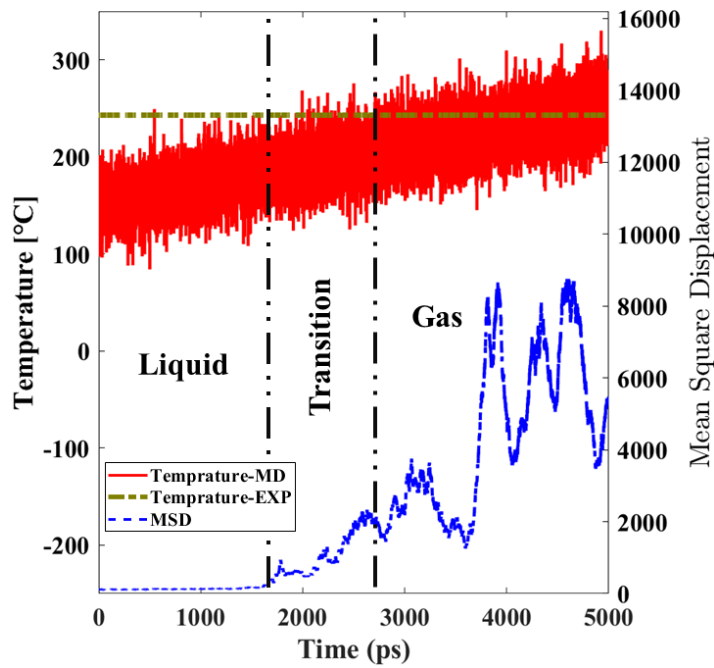
(c) Ethanol
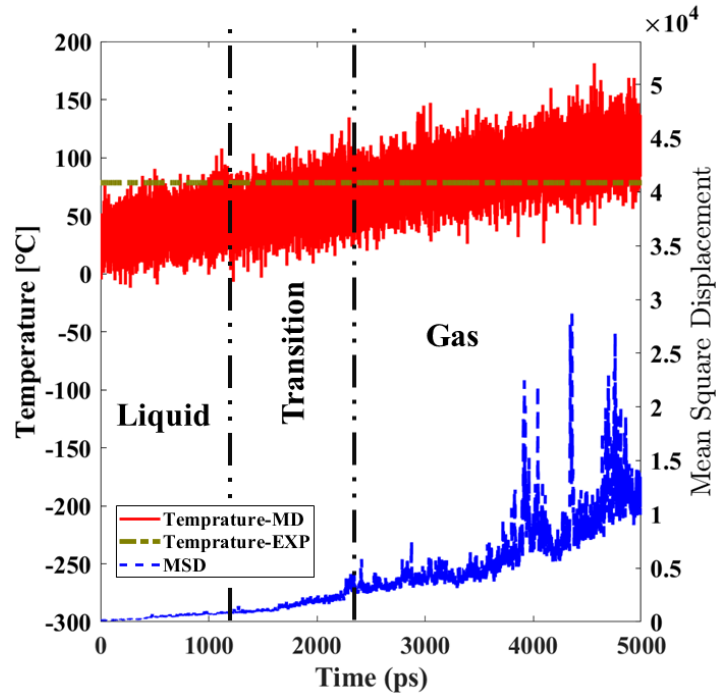
(d) Octane
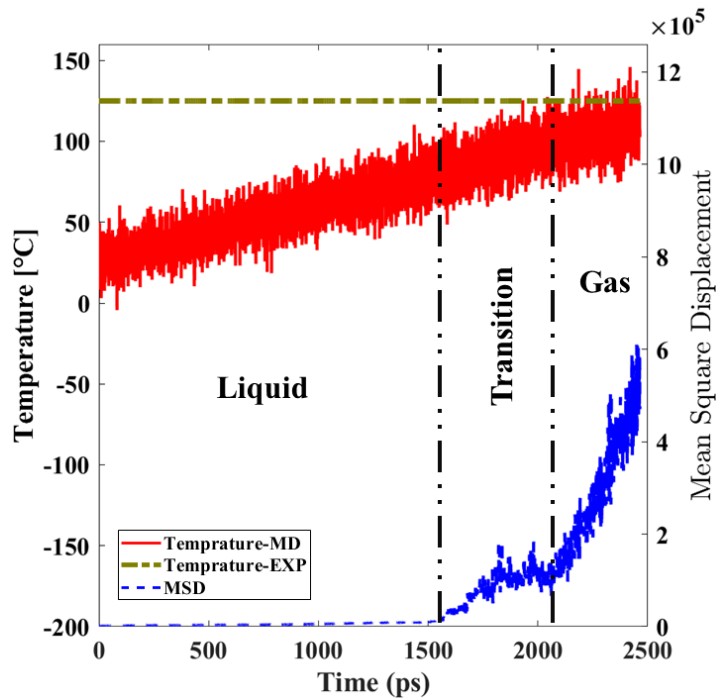
Figure 3.7: The estimated boiling point of H_2O, EC, Ethanol, and Octane molecules, obtained by the algorithm proposed in this work [44–46, 48].

The algorithm has demonstrated remarkable accuracy in estimating the boiling points of EC, Ethanol, H_2O, and Octane systems, with an accuracy of 91%, 96%, 90%, and 80%, respectively. This result aligns with the experimental data reported in Table 3.6, thereby validating the proposed framework presented in this study. Contrary to this, the previous algorithm was unable to predict boiling points for any of these molecules except H_2O which has the simplest structure.

Table 3.6: Boiling Point [°C] of EC, Ethanol, H_2O, and Octane predicted by pristine and enhanced algorithm, compared with the experimental data from the literature.

Molecule	Enhanced Algorithm		Pristine Algorithm		Experimental Data*
	Value	Error	Value	Error	
EC	220	9%	NA	-	240[44]
Ethanol	75	4%	NA	-	78[45]
H_2O	90	10%	90	10%	100[46]
Octane	100	20%	NA	-	125[48]

*The reference for each experimental value is mentioned as a superscript.

In summary, by evaluating nonbonded, bonded, angle, dihedral, and improper interactions employing quantum mechanics, and combining it with the nonbonded potential parameters predicted by the DNN model, in MD simulations, we can accurately predict several intrinsic properties in a variety of molecules. This clearly establishes the validity and the performance of the suite of algorithms presented in this study in determining the potential parameters of any molecule, enabling us to study new and novel materials using MD simulations. This is while, the utilization of conventional mathematical techniques in previous frameworks to evaluate nonbonded potential parameters has been based on simplifying assumptions, leading to

a substantial discrepancy in determining the energy well depth in particle-particle interactions.

3.4   Conclusion

The key to an accurate MD simulation is the use of appropriate and accurate potential parameters. In a recent study, we presented a suite of algorithms for evaluating the potential parameters for the nonbonded, bonded, angle, dihedral, and improper interactions [13]. However, due to the complexity of nonbonded interactions and the mentioned restriction of conventional mathematical methods, we introduced several simplifications that impact the accuracy of the results.

Addressing this issue, in this work, we have proposed a new coordinate generator algorithm and used a combination of neuro-computing techniques and QM calculations to present an enhanced framework with better accuracy. By simulating five different molecular systems using this enhanced suite of algorithms, we have successfully demonstrated the excellent accuracy of this framework in predicting nonbonded interaction-related phenomena such as phase transitions.

Our enhanced computational tool, in conjunction with the algorithms for evaluating the Bonded, Angle, Dihedral, and Improper interactions, presents a unique and novel computational framework in this field that can be used for finding the potential parameters of new and novel compounds in the absence of experimental data. This will help researchers design and develop novel materials for next-generation applications by integrating this new approach with MD simulations to study molecular and nanoscale systems and phenomena.

3.5   Acknowledgments

This work was funded by Natural Sciences and Engineering Research Council of Canada's Discovery Grants program. AL acknowledges the additional financial assistance from the Department of Mechanical Engineering. The authors are also grateful to the reviewers for their valuable comments to improve this manuscript.

Bibliography

[1] Shan Jiang, Junyeob Song, Yujing Zhang, Meitong Nie, Jongwoon Kim, Ana Lopez Marcano, Kelly Kadlec, William A Mills III, Xiaodong Yan, Hefei Liu, et al. Nano-optoelectrodes integrated with flexible multifunctional fiber probes by high-throughput scalable fabrication. *ACS Applied Materials & Interfaces*, 13(7):9156–9165, 2021.

[2] Shan Yan, Dong K Dinh, Guojung Shang, Shan Wang, Wei Zhao, Xin Liu, Richard Robinson, Jack P Lombardi III, Ning He, Susan Lu, et al. Nano-filamented textile sensor platform with high structure sensitivity. *ACS applied materials & interfaces*, 14(13):15391–15400, 2022.

[3] Wei Hong, Yining Zhao, Yuru Guo, Chengcheng Huang, Peng Qiu, Jia Zhu, Chun Chu, Hong Shi, and Mingchun Liu. Pegylated self-assembled nano-bacitracin a: probing the antibacterial mechanism and real-time tracing of target delivery in vivo. *ACS applied materials & interfaces*, 10(13):10688–10705, 2018.

[4] Simran Sandhu, Ramavtar Tyagi, Elahe Talaie, and Seshasai Srinivasan. Using

neurocomputing techniques to determine microstructural properties in a li-ion battery. *Neural Computing and Applications*, 34(12):9983–9999, 2022.

[5] Ramavtar Tyagi and Seshasai Srinivasan. Co-doping studies to enhance the life and electro-chemo-mechanical properties of the limn 2 o 4 cathode using multiscale modeling and neuro-computing techniques. *Physical Chemistry Chemical Physics*, 24(31):18645–18666, 2022.

[6] Thomas F Kelly and Michael K Miller. Atom probe tomography. *Review of scientific instruments*, 78(3):031101, 2007.

[7] John Melngailis. Focused ion beam technology and applications. *Journal of Vacuum Science & Technology B: Microelectronics Processing and Phenomena*, 5(2):469–495, 1987.

[8] David B Williams and C Barry Carter. The transmission electron microscope. In *Transmission electron microscopy*, pages 3–17. Springer, 1996.

[9] Amirmasoud Lanjan and Seshasai Srinivasan. An enhanced battery aging model based on a detailed diffusing mechanism in the sei layer. *ECS Advances*, 1(3):030504, 2022.

[10] Zahra Moradi, Amirmasoud Lanjan, and Seshasai Srinivasan. Enhancement of electrochemical properties of lithium rich li2ruo3 cathode material. *Journal of The Electrochemical Society*, 167(11):110537, 2020.

[11] Amirmasoud Lanjan, Behnam Ghalami Choobar, and Sepideh Amjad-Iranagh. First principle study on the application of crystalline cathodes li2mn0. 5tm0. 5o3

for promoting the performance of lithium-ion batteries. *Computational Materials Science*, 173:109417, 2020.

[12] Ramavtar Tyagi, Amirmasoud Lanjan, and Seshasai Srinivasan. Co-doping strategies to improve the electrochemical properties of lixmn2o4 cathodes for li-ion batteries. *ChemElectroChem*, 9(3):e202101626, 2022.

[13] Amirmasoud Lanjan, Zahra Moradi, and Seshasai Srinivasan. A computational framework for evaluating molecular dynamics potential parameters employing quantum mechanics. *Mol. Syst. Des. Eng.*, pages –, 2023.

[14] Zahra Moradi, Amirmasoud Lanjan, and Seshasai Srinivasan. Multiscale investigation into the co-doping strategy on the electrochemical properties of li2ruo3 cathodes for li-ion batteries. *ChemElectroChem*, 8(1):112–124, 2021.

[15] Amirmasoud Lanjan, Zahra Moradi, and Seshasai Srinivasan. Multiscale investigation of the diffusion mechanism within the solid–electrolyte interface layer: Coupling quantum mechanics, molecular dynamics, and macroscale mathematical modeling. *ACS Applied Materials & Interfaces*, 13(35):42220–42229, 2021.

[16] Amirmasoud Lanjan, Behnam Ghalami Choobar, and Sepideh Amjad-Iranagh. Promoting lithium-ion battery performance by application of crystalline cathodes lixmn1- zfezpo4. *Journal of Solid State Electrochemistry*, 24(1):157–171, 2020.

[17] Hao Hu, Zhenyu Lu, and Weitao Yang. Fitting molecular electrostatic potentials from quantum mechanical calculations. *Journal of chemical theory and computation*, 3(3):1004–1013, 2007.

[18] Simone Di Micco, Maria Giovanna Chini, Raffaele Riccio, and Giuseppe Bifulco. Quantum mechanical calculation of nmr parameters in the stereostructural determination of natural products. *European Journal of Organic Chemistry*, 2010(8):1411–1434, 2010.

[19] Chuan Tian, Koushik Kasavajhala, Kellon AA Belfon, Lauren Raguette, He Huang, Angela N Migues, John Bickel, Yuzhang Wang, Jorge Pincay, Qin Wu, et al. ff19sb: Amino-acid-specific protein backbone parameters trained against quantum mechanics energy surfaces in solution. *Journal of chemical theory and computation*, 16(1):528–552, 2019.

[20] Chengwen Liu, Jean-Philip Piquemal, and Pengyu Ren. Amoeba+ classical potential for modeling molecular interactions. *Journal of chemical theory and computation*, 15(7):4122–4139, 2019.

[21] Yudong Cao, Jhonathan Romero, and Alán Aspuru-Guzik. Potential of quantum computing for drug discovery. *IBM Journal of Research and Development*, 62(6):6–1, 2018.

[22] Giannozzi, P.; Baroni, S.; Bonini, N.; Calandra, M.; Car, R.; Cavazzoni, C.; Ceresoli, D.; Chiarotti, G. L.; Cococcioni, M.; Dabo, I.; Corso, A. D.; Gironcoli, S. D.; Fabris, S.; Fratesi, G.; Gebauer, R.; Gerstmann, U.; Gougoussis, C.; Kokalj, A.; Lazzeri, M.; Mauri, F.; Mazzarello, R.; Paolini, S.; Pasquarello, A.; Paulatto, L.; Sbraccia, C.; Scandolo, S.; Sclauzero, G.; Seitsonen, A. P.; Smogunov, A.; Umari, P.; Wentzcovitch, R. M. QUANTUM ESPRESSO: a modular and open-source software project for quantum simulations of materials. *Journal of Physics: Condensed Matter*, 21(39):395502, sep 2009.

[23] Giannozzi, P.; Andreussi, O.; Brumme, T.; Bunau, O.; Buongiorno Nardelli, M.; Calandra, M.; Car, R.; Cavazzoni, C.; Ceresoli, D.; Cococcioni, M.; Colonna, N.; Carnimeo, I.; Dal Corso, A.; De Gironcoli, S.; Delugas, P.; Distasio, R. A.; Ferretti, A.; Floris, A.; Fratesi, G.; Fugallo, G.; Gebauer, R.; Gerstmann, U.; Giustino, F.; Gorni, T.; Jia, J.; Kawamura, M.; Ko, H. Y.; Kokalj, A.; Kücükbenli, E.; Lazzeri, M. ; Marsili, M.; Marzari, N.; Mauri, F.; Nguyen, N. L.; Nguyen, H. V.; Otero-De-La-Roza, A.; Paulatto, L.; Poncé, S.; Rocca, D.; Sabatini, R.; Santra, B.; Schlipf, M.; Seitsonen, A. P.; Smogunov, A.; Timrov, I.; Thonhauser, T.; Umari, P.; Vast, N.; Wu, X.; Baroni, S., Advanced Capabilities for Materials Modelling with Quantum ESPRESSO. *Journal of Physics Condensed Matter*, 29(46), oct 2017.

[24] W. Kohn and L. J. Sham. Self-Consistent Equations Including Exchange and Correlation Effects. *Physical Review*, 140(4A):A1133, nov 1965.

[25] Ivan Novikov, Blazej Grabowski, Fritz Körmann, and Alexander Shapeev. Magnetic moment tensor potentials for collinear spin-polarized materials reproduce different magnetic states of bcc fe. *npj Computational Materials*, 8(1):1–6, 2022.

[26] Yang Zhang, Qiunan Xu, Klaus Koepernik, Roman Rezaev, Oleg Janson, Jakub Železný, Tomáš Jungwirth, Claudia Felser, Jeroen van den Brink, and Yan Sun. Different types of spin currents in the comprehensive materials database of non-magnetic spin hall effect. *npj Computational Materials*, 7(1):1–7, 2021.

[27] Anthony J Myles, Robert N Feudale, Yang Liu, Nathaniel A Woody, and Steven D Brown. An introduction to decision tree modeling. *Journal of Chemometrics: A Journal of the Chemometrics Society*, 18(6):275–285, 2004.

[28] Gérard Biau and Erwan Scornet. A random forest guided tour. *Test*, 25(2):197–227, 2016.

[29] Alex J Smola and Bernhard Schölkopf. A tutorial on support vector regression. *Statistics and computing*, 14(3):199–222, 2004.

[30] Risto Miikkulainen, Jason Liang, Elliot Meyerson, Aditya Rawal, Daniel Fink, Olivier Francon, Bala Raju, Hormoz Shahrzad, Arshak Navruzyan, Nigel Duffy, et al. Evolving deep neural networks. In *Artificial intelligence in the age of neural networks and brain computing*, pages 293–312. Elsevier, 2019.

[31] Vinod Nair and Geoffrey E Hinton. Rectified linear units improve restricted boltzmann machines. In *Icml*, 2010.

[32] Peng Li, Yang Liu, and Maosong Sun. Recursive autoencoders for itg-based translation. In *Proceedings of the 2013 Conference on Empirical Methods in Natural Language Processing*, pages 567–577, 2013.

[33] Fabian Pedregosa, Gaël Varoquaux, Alexandre Gramfort, Vincent Michel, Bertrand Thirion, Olivier Grisel, Mathieu Blondel, Peter Prettenhofer, Ron Weiss, Vincent Dubourg, et al. Scikit-learn: Machine learning in python. *the Journal of machine Learning research*, 12:2825–2830, 2011.

[34] Yann LeCun, Léon Bottou, Yoshua Bengio, and Patrick Haffner. Gradient-based learning applied to document recognition. *Proceedings of the IEEE*, 86(11):2278–2324, 1998.

[35] Kaiming He, Xiangyu Zhang, Shaoqing Ren, and Jian Sun. Delving deep into rectifiers: Surpassing human-level performance on imagenet classification. In *Proceedings of the IEEE international conference on computer vision*, pages 1026–1034, 2015.

[36] Xavier Glorot and Yoshua Bengio. Understanding the difficulty of training deep feedforward neural networks. In *Proceedings of the thirteenth international conference on artificial intelligence and statistics*, pages 249–256. JMLR Workshop and Conference Proceedings, 2010.

[37] Diederik P Kingma and Jimmy Ba. Adam: A method for stochastic optimization. arxiv: 14126980. 2014.

[38] Sashank J Reddi, Satyen Kale, and Sanjiv Kumar. On the convergence of adam and beyond. *arXiv preprint arXiv:1904.09237*, 2019.

[39] Steve Plimpton. Fast parallel algorithms for short-range molecular dynamics. *Journal of Computational Physics*, 117(1):1–19, 1995.

[40] Michele Parrinello and Aneesur Rahman. Polymorphic transitions in single crystals: A new molecular dynamics method. *Journal of Applied physics*, 52(12):7182–7190, 1981.

[41] William G Hoover. Canonical dynamics: Equilibrium phase-space distributions. *Physical review A*, 31(3):1695, 1985.

[42] Shuichi Nosé. A unified formulation of the constant temperature molecular dynamics methods. *The Journal of chemical physics*, 81(1):511–519, 1984.

[43] HJC Berendsen, B Hess, E Lindahl, D Van Der Spoel, AE Mark, and G Groenhof. Gromacs: fast, flexible, and free. *J. Comput. Chem*, 26(16):1701–1718, 2005.

[44] National center for biotechnology information (2022). pubchem compound summary for cid 7303, ethylene carbonate. retrieved october 18, 2022 from https://pubchem.ncbi.nlm.nih.gov/compound/ethylene-carbonate.

[45] National center for biotechnology information (2022). pubchem compound summary for cid 962, water. retrieved october 18, 2022 from https://pubchem.ncbi.nlm.nih.gov/compound/water.

[46] National center for biotechnology information (2022). pubchem compound summary for cid 962, water. retrieved october 18, 2022 from https://pubchem.ncbi.nlm.nih.gov/compound/water.

[47] National center for biotechnology information (2022). pubchem compound summary for cid 23688915, lithium hexafluorophosphate. retrieved october 18, 2022 from https://pubchem.ncbi.nlm.nih.gov/compound/lithium-hexafluorophosphate.

[48] National center for biotechnology information (2022). pubchem compound summary for cid 356, octane. retrieved october 18, 2022 from https://pubchem.ncbi.nlm.nih.gov/compound/octane.

Chapter 4

A Multi-Scale Investigation of Diffusion Mechanism Within the Solid-Electrolyte Interface Layer: Coupling Quantum Mechanics, Molecular Dynamics, and Macro-Scale Mathematical Modeling

Contributing Author: Amirmasoud Lanjan.

Abstract

The solid electrolyte interface (SEI) layer has a critical role in Li-ion batteries' (LIBs) lifespan. SEI layer, even in modern commercial LIBs, is responsible for more than 50% of capacity loss. Due to the inherent complexity in studying the SEI layer, many aspects of its performance and characteristics, including diffusion mechanisms in this layer, are unknown. As a result, most mathematical models use a constant value of diffusion coefficient, instead of a variable formulation, to predict LIBs' properties and performance such as capacity fading and SEI growth rate. In this work, by employing a multi-scale investigation using a combination of Quantum Mechanics, Molecular Dynamics and macro-scale mathematical modelling, some equations are presented to evaluate the energy barrier against diffusion, and the diffusion coefficient in different crystal structures in the inner section of the SEI layer. The equations are as a function of temperature and concentration, and can be used to study the diffusion mechanism in the SEI layer. They can also be integrated with other mathematical models of LIBs to increase the accuracy of the latter.

4.1   Introduction

After reaching a critical point with respect to the environmental issues and the consequent impact on human beings, a clean, efficient, and secure transportation network that was completely ignored until the 1990s is beginning to attract a lot of attention [1]. Industrial electrification, including that of transport systems, is the most promising approach to improve our energy efficiency. In the automotive sector, electric vehicles (EVs) faced challenges with their energy storage system solution, limiting

their practical utility. However, with their unique and superior properties, e.g., high energy and power density, and capacity, Li-Ion batteries (LIBs) have attracted much attention [2]. However, there is still room for considerable improvements to enhance their performance[3, 4], efficiency[5–8], and durability [9–11]. Since, almost half of the initial price of an EV is spent on its battery, long battery life is critical for using LIBs in EVs. Many investigations on different parts of the LIBs such as anode, cathode and electrolyte have been conducted in recent years. One of the main obstacles in developing high-quality and durable LIBs is the insufficient understanding of the electrode-electrolyte interface (SEI) layer in LIBs [12].

The SEI layer was introduced by Peled in 1979 [13]. When the lowest unoccupied molecular orbital (LUMO) of an electrolyte molecule is lower than the highest occupied molecular orbital (HOMO) of an electrode's molecule, electrons participate in a reduction reaction with electrolyte molecules [14]. Consequently, the electrolyte will be reduced and a layer on the electrode surface will be formed [14–16]. Based on the previous studies [17, 18], SEI has two layers: the first layer is an organic outer layer (near SEI-Electrolyte interface) which is porous and permeable to Li-ions and the electrolyte solvent. The second layer is an inorganic inner layer (near SEI-Electrode interface) which only allows the transport of Li-ions [14]. The SEI formation reactions consume the active Li-ions in the electrodes and electrolyte solvent molecules. SEI has a critical function in the batteries, and the lifetime of a LIB depends directly on its SEI layer. Even in the current commercial LIBs, the SEI is responsible for more than 50% of capacity loss [14, 19–21]. An intact well-engineered SEI layer can restrict the electron tunnelling, preventing further electrolyte reduction and suppress more capacity fading [14]. Consequently, research on the SEI layer and

understanding its properties is critical to improve LIB's electrochemical performance and durability[22, 23].

It is a challenge to directly capture the reaction at the SEI interface experimentally since some of the reactions could occur at the picosecond (ps) time scale. As a result, most experimental methods are incapable of accurately characterizing the SEI layer, particularly the thermodynamics and kinetic properties [14]. In the recent years, predictive modeling has been used to overcome the limitations of experimental research, and play an important role in understanding battery science for a wide range of length scales, namely, from a few electrons to the full battery system [24–27].

Due to the complexity of the SEI structure and the challenges in conducting experimental investigations, our understanding of the diffusion mechanism in this layer continues to remain unclear. The lack of precise knowledge of the diffusion coefficient results in the disagreement between the mathematical models that predict the SEI related properties, such as the capacity fading model of Christensen and Newman [28], and the experimental data. Christensen and Newman [28] presented a mathematical model to predict SEI growth rate, film resistance, and irreversible capacity loss due to the layer formation. In their work, due to the lack of knowledge about diffusion mechanisms in the SEI layer, they assumed that all the ions (Li^+ and PF_6) in all of the regions have the same diffusion coefficient in the SEI layer, i.e., $5.0 \times 10^{-14}(\frac{m^2}{s})$. Liu et al. [29] presented a model proposing a spatially dependent growth of the SEI layer in LIBs. They indicated that in the diffusion-limited condition, by doubling the diffusion coefficient of Li-ions in the SEI layer, the thickness of the layer will increase from 4 to 20 nm (500% increase) [29]. However, due to the lack of insight into the diffusion mechanisms, they continued using the constant diffusion coefficient from Christensen

and Newman [28], same as several other researchers (e.g., References [29–34]) that have suffered from unknown diffusion mechanisms in the SEI layer. This emphasizes the need for a more precise mathematical model to predict LIBs' performance with respect to SEI growth rate and capacity fading more accurately.

With the advent of Quantum Mechanics (QM) calculation, Molecular Dynamics (MD) simulation, and the modern computational capability, it is possible to develop a deeper understanding of the diffusion mechanisms in the SEI layer. To this end, QM calculations along with Density Functional Theory (DFT) approximation has become a valuable tool for investigating the LIBs' materials characteristics [2, 35–37]. In this work, QM calculations and MD simulations were employed to prescribe an equation for the diffusion coefficient as a function of temperature and Li-ions concentration for each crystal structure in the inner part of the SEI layer. Subsequently, a single equation for the diffusion coefficient was integrated with the macro-scale mathematical model to accurately model the physics within the SEI layers.

4.2 Theoretical Methods and Computational Details

In this work, QM calculations, MD simulations, and Macro-Scale Mathematical Modeling (MSMM) have been employed for a comprehensive multi-scale investigation into diffusion mechanisms in different materials in the SEI layer. The SEI layer is defined as a multi-layered structure with the following constituents: (I) an inorganic inner layer (near the electrode-SEI surface), consisting of Li_2CO_3, LiF, and Li_2O and (II) an organic outer layer (near electrolyte-SEI interface), consisting of dilithium ethylene

glycol decarbonate (Li_2EDC) and ROLi (where R depends on the solvent) [16, 18, 38–40]. While the outer layer is highly dependent on the electrolyte content, the inner layers mostly contain fixed materials (Li_2O and LiF) in the LIBs. The inorganic inner layer is permeable to Li-ions and prevents the passage of electrolyte solvent [14]. So, the diffusion mechanism in this layer is investigated for Li-Ions and the proposed diffusion equation is applied to calculate the diffusion coefficient as a function of concentration and temperature. This diffusion equation for the SEI layers can be integrated with the macro-scale mathematical models.

Creating the Crystal Structures Li_2CO_3, Li_2O, LiF are three main components of the inner section of the SEI layer [16, 18, 38–40] . As reported and supported by experimental evidences, Li_2CO_3 is a product of conversion reaction of $CoCO_3$ upon Li-ion insertion when the liquid electrolyte contains ethylene carbonate [41]. Tian et al. [42] and McShane et al. [43] established that Li_2CO_3 is themodynmically unstable and will further reduce to Li_2C_2 and Li_2O. Also, Li_2C_2 will participate in other reactions and produce Li^+, C_2H_2, and C [43]. Hence, Li_2CO_3 cannot be considered as a permanent ingeredient in the inner section of the SEI layer [41–43]. Consequently, they suggested that the only permanent components are Li_2O and LiF. Therefore, in this work, the materials in the inner layer, namely, LiF and Li_2O, are created individually based on the experimental data on the crystal structure (c.f. Table 4.1) [44–46].

Table 4.1: The primitive experimental lattice parameters data for LiF and Li_2O crystal structures [44–46].

LiF	Space Group	FM-3M		
a	4.030 $\mathring{A}$	α	90°
b	4.030 $\mathring{A}$	β	90°
c	4.030 $\mathring{A}$	γ	90°
Li_2O	Space Group	FM-3M		
a	4.573 $\mathring{A}$	α	90°
b	4.573 $\mathring{A}$	β	90°
c	4.573 $\mathring{A}$	γ	90°

A schematic of the crystal structures based on the data in Table 4.1 is shown in Figure 4.1. As seen in this figure, in Li_2O crystal structure, all of the diffusion paths have the same condition and they go through the bisects of the x, y, and z-axis (c.f. Figure 1a). Similar to Li_2O, due to the symmetry of the LiF crystal structure, all paths in this crystal have the same condition, and they are in direction of the x-, y-, and z-axis (c.f. Figure 1b).

(a) (b)
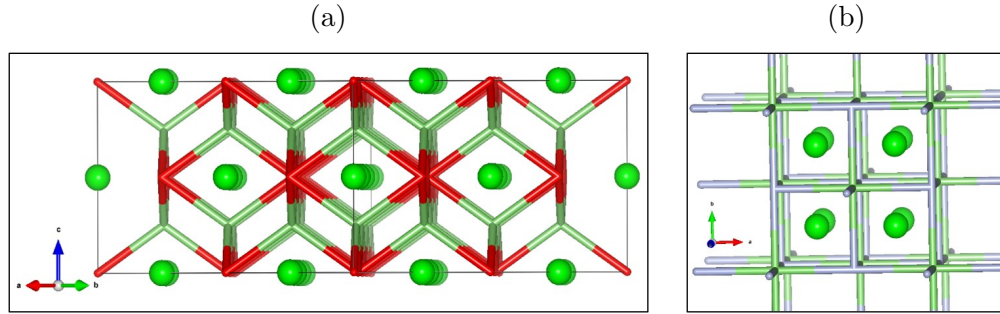
Figure 4.1: Schematic of crystal Structures of LiF and Li_2O, based on the experimental data in Table 4.1 using VESTA [47]. Additionally, the possible diffusion paths through each crystal structure are indicated. Due to the symmetry of the crystal structure, all paths in each crystal have the same condition and only one path type is considered per crystal structure. (a) Diffusion pathways in Li_2O crystal go through the bisects of the x, y, and z axis and (b) in LiF crystal, the diffusion pathways are in direction of the x, y, and z axis.

4.2.1   Quantum Mechanics Calculation

In this work, a spin-polarized density functional theory (SP-DFT) [48], one of the most promising approximations for relativity large systems, with Perdew-Burke-Ernzerhof (PBE) as its exchange correlation (XC) function has been employed for QM calculations. Further, Quantum Espresso [49, 50] package was used for QM calculations in this work. Other details of QM calculations are summarized in Table 4.A1 in Appendix 4.A.

Based on the other studies [14–16, 19, 38, 40, 51–53], the inner section of the SEI layer is only permeable for Li-ions. This section must prevent the diffusion of electrolyte's molecules (or ions) as well as electron transference. Hence, there are two types of ions in the SEI inner layer: (i) Li^+, F^-, and O^- ions, that create the crystal structures of SEI layer, indicated by sticks in Figure 4.1. The concentration of these ions is almost constant. (ii) Excess Li-ions that diffuse through the SEI layer via the

sites indicated by the green balls in Figure 4.1. These excess Li-ions are present in different concentrations in the SEI layer. The amount of excess Li-ion concentrations (C_{eLi}) in this layer is governed by the applied current and voltage values. Therefore, C_{eLi} is defined in this work as:

$$C_{eLi} = \frac{\text{Number of Excess Li}^+}{\text{Total number of sites available to be occupied by Li}^+}. \qquad (4.1)$$

It must be noted that in the above equation, $C_{eLi} = 0\%$ does not mean there is no Li-ion in the crystal structure. It only means that there are no diffusing (excess) Li-ions in it. Since the presence of large C_{eLi} in the SEI layer would create a large coulomb force and electrical field, high values for C_{eLi} would rarely be observed in the normal operational conditions of LIBs. Nevertheless, knowing that the QM and MD calculations make it possible to investigate a wide range of C_{eLi}, as a *theoretical* exercise, we have chosen to study large concentrations of Li-ions. Since the SEI inner layer prevents electrolytes and electrons transference, the concentration of the other charged species other than Li$^+$, F$^-$, and O$^-$ ions are assumed zero. Further, this will have a negligible effect on the crystal structure and energy barrier.

For this, after creating the primary crystal structures, using the data summarized in Table 4.1, different amounts (concentrations) of excess positive Li-ions were added to the crystals. A total of 5 different concentrations for each crystal structure were investigated. The inner layer's crystal structures are porous and have sites for Li-ions.

Next, the new crystal structures with the added Li-ions were optimized to obtain new lattice parameters and atomic positions. The geometry optimizations for LiF and Li_2O for each of five different C_{eLi}s were performed using QM calculation. After obtaining the optimized and stable crystals, QM was employed to define the energy

barrier (EB) against diffusion through the SEI crystal structures in the paths in Figure 4.1, for different concentrations of Li-ions. Since, both LiF and Li_2O have a symmetric crystal structure, only one kind of diffusion path was considered for each of them. A three-dimensional investigation on these paths through the crystal structures were undertaken by employing QM and MD calculations. The Nudged elastic band [54, 55] (NEB), which is a well-known method for finding saddle points and minimum energy paths for EB against diffusion, was utilized in this section.

4.2.2   Molecular Dynamics Simulation

MD simulations have been employed to evaluate the diffusion coefficient of excess Li-ions (eLi) in the studied crystal structures. For this, before running MD simulations, a geometry optimization task by means of QM calculation was performed to minimize the energy of the crystal structure and find the exact atomic position and lattice parameters. Subsequently, each MD simulation was run in the following three different stages: (I) NVT ensemble to stabilized the temperature and atomic velocity with a timestep size of 0.1 fs ; (II) NPT ensemble with a timestep size of 0.1 fs to stabilize the temperature; (III) after stabilizing the temperature and pressure, the main run under NVT or NPT ensemble with a timestep size of 1.0 fs, for $5.0{\times}10^6$ steps. Lammps package [56] was employed for MD simulations in this work.

Selecting an appropriate force field model for running an MD simulation is critical since the accuracy of results is directly dependent on it. Therefore, before running the MD for the crystal structures with different C_{eLi}, Li_2O and LiF crystal structures were simulated by the Buckingham [57], and the Embedded Ion Method (EIM) force field, respectively. The potential parameters utilized for Buck/Coul/Long and EIM

are summarized in Tables 4.A2 and 4.A3 in Appendix 4.A, respectively. The calculated density with these force fields and parameters for Li_2O and LiF are 2.05 g/cm^3 and 2.62 g/cm^3, respectively. These values represent a 2% and 0.7% deviation from the respective experimental data (2.01 g/cm^3 and 2.64 g/cm^3 for Li_2O and LiF, respectively [58]). Other key characteristics of the MD simulations are summarized in Table 4.A4 in Appendix 4.A. Finally, mean square displacement (MSD) analysis was also performed for the last 5 ns of the simulations.

Brownian motion is one of the modes of self-diffusion (diffusion in the absence of chemical potential gradient) at the molecular scale. Einstein's seminal research [59] introduced MSD as a powerful analysis to characterize the jetting motion at the molecular-scale. Based on this, self-diffusion is commonly estimated using the linear trend on the MSD vs time graph. Bullerjahn et al. [60] found that the diffusion coefficient obtained from the linear fit on the MSD curves is very sensitive to the time interval of the MD simulation. Specifically, when D_{Li^+} is estimated using the data spanning a short-time interval, it is compromised by possible non-diffusive dynamics. On the other hand, using data that spans very long-time intervals could result in significant statistical uncertainties. To address the latter, many published researches [61–64] have focused on precise diffusion coefficient estimation from MSD diagrams. In this work, Generalized Least Squares (GLS) estimator, a rigorous framework that combines the sophisticated estimators introduced by Bullerjahn et al. [60], is utilized to estimate D_{Li^+} from the evaluated MSD analysis. For this, MD simulations were used to find the MSD of the atoms using the following equation [60]:

$$MSD_i = \sum_{n=0}^{N-i} \frac{(X_{n+i} - X_n)^2 + (Y_{n+i} - Y_n)^2 + (Z_{n+i} - Z_n)^2}{N - i + 1}. \tag{4.2}$$

Equation 4.2 presents the correlation between MSD_i at different time lags $t_i = i\Delta t$ where i = 1, 2, ..., M ≤ N. Further, (X_i, Y_i, Z_i) represents the position of particle i at time t_i, and N is the number of steps. Following the proposition of Bullerjahn et al. [60] that is outlined in Appendix 4.B, D_{Li^+} is estimated as:

$$D_{Li^+} = \frac{\sigma_{GLS}^2}{6\Delta t}. \tag{4.3}$$

4.3   Diffusion Equation

A diffusion equation for Li-ions in the studied crystal materials can be calculated as a function of temperature based on the Arrhenius equation. For this, a modified form of the Arrhenius equation, which can model Li diffusion coefficient as a function of concentration (C) as well as temperature (T) can be written as [65]:

$$D_{Li^+}(C_{eLi}, T) = D_0 e^{\frac{-B_0 EB(C_{eLi})}{k_b T}}, \tag{4.1}$$

where k_b, EB, and T are Boltzmann constant, Energy Barrier, and temperature, respectively. B_0 and D_0 are constants that can be evaluated by writing Equation 4.1 as follows:

$$Ln(D_{Li^+}(C_{eLi}, T)) = Ln(D_0) - \frac{B_0 EB(C_{eLi})}{k_b T}. \tag{4.2}$$

In this equation, EB is evaluated by utilizing NEB method, and D_{Li^+} is obtained from the MD simulations. Subsequently, by employing linear curve fitting on Equation 4.2, the values for D_0 and B_0 can be calculated for LiF and Li_2O. In this, $EB(C_{eLi})$ is evaluated using Equation 4.1 that is constructed based on the data on the energy

barrier as a function of excess Li-ion concentration (C_{eLi}).

4.4   Macro-Scale Mathematical Modelling

Macro-Scale Mathematical Modelling (MSMM) has been used to obtain a single diffusion equation for the entire inner layer of the SEI based on the results of QM and MD studies. As mentioned earlier, the inner layer of SEI studied in this work is composed of randomly oriented crystals of Li_2O and LiF. Using Fick's second law to evaluate diffusion will require calculating the surface area of each crystal in the SEI layer. Based on Fick's second law, we can calculate the total diffusion coefficient of Li^+, in the SEI inner layer, based on the fraction of the surface area using the relation:

$$D_T = \epsilon_{LiF} D_{LiF} + \epsilon_{Li_2O} D_{Li_2O}. \qquad (4.1)$$

In the above equation, ϵ_i is the fraction of the surface area of the material i in the studied layer such that $\epsilon_{LiF} + \epsilon_{Li_2O} = 1$. A detailed formulation to calculate ϵ_i is presented in Appendix 4.C.

4.5   Results and Discussion

The EBs against diffusion through Li_2O and LiF crystal structures for different eLi concentrations are show in Figure 4.2. The peak EB for each concentration from these figures is plotted against the eLi concentrations for these crystals in Figure 4.3.

We find a quadratic trend on this graph and the coefficients of a second-degree polynomial behaviour are summarized in Table 4.2 with an R^2 higher than 93%. This quadratic trend can be explained as follows: Increasing eLi concentration from zero to about 25% results in an expansion of the crystal structure, resulting in a decrease in the EB against diffusion. On the other hand, after reaching a certain concentration, increasing eLi reduces vacancy sites, causing the EB to increase. Thus, we can represent the quadratic behaviour of EB as:

$$EB(C_{eLi}) = a_2 C_{eLi}^2 + a_1 C_{eLi}^1 + a_0. \tag{4.1}$$
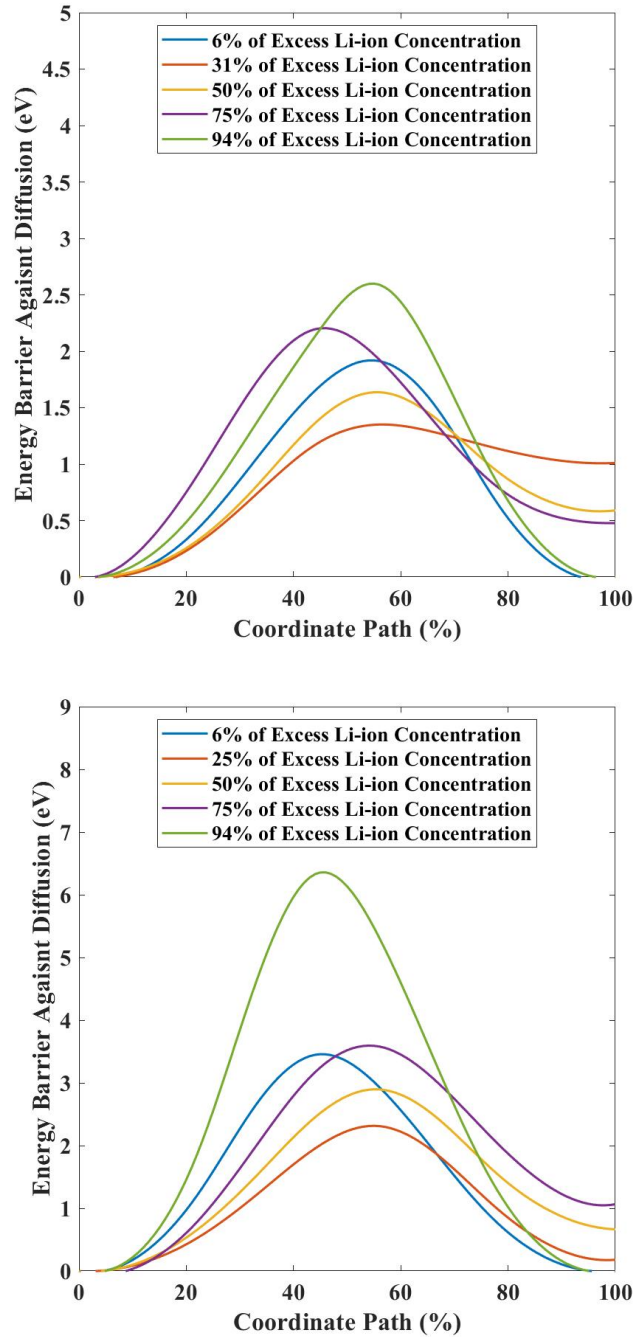
Figure 4.2: EB against diffusion through (a) LiF and (b) Li$_2$O crystal structure as a function of the coordinate path percentage, for five different excess Li-ion concentrations.
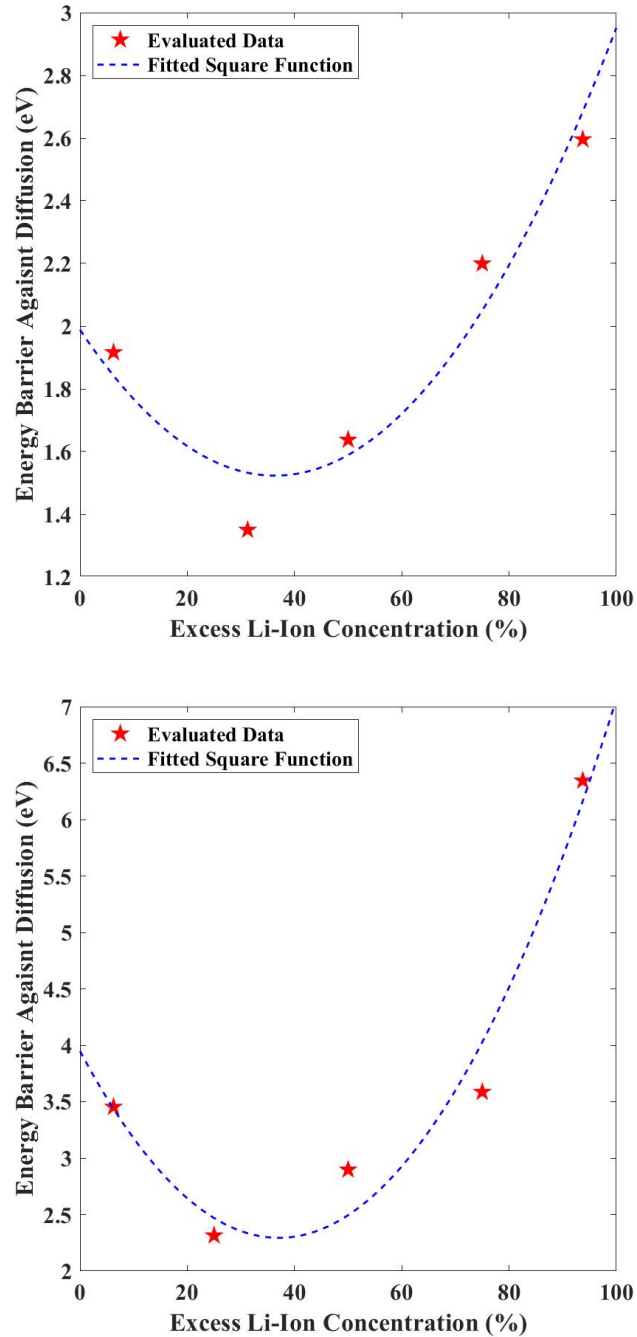
Figure 4.3: Energy barrier against diffusion as a function of excess Li-ion concentration for (a) LiF and (b) Li_2O.

Table 4.2: The coefficients of the second-degree polynomials
$EB = a_2 C_{eLi}^2 + a_1 C_{eLi}^1 + a_0$ (Equation 4.1), fitted on the EB versus C_{eLi} data for
Li$_2$O and LiF.

	a_2	a_1	a_0	R^2
Li$_2$O	12.0460	-8.9294	3.9488	0.96
LiF	3.5237	-2.5607	1.9886	0.93

The Li-ions diffusion coefficient $(D_{Li^+}$ $(\frac{m^2}{s}))$ for the studied crystal structures
and for each concentrations was calculated and is plotted in Figure 4.4. It must be
noted that since D_{Li^+} is an exponential function of EB, a small change in EB has
a remarkable impact on the diffusion coefficient, and thereby the SEI layer. The
MD simulation results in Figure 4.4 are consistent with the EB results. Specifically,
there is an initial increase in the diffusion coefficient because of a decrease in EB.
Beyond a certain critical eLi (approx. 40%), as the EB increases further, it impedes
the diffusion process, reflecting in a decrease in the values of the diffusion coefficient
in Figure 4.4.

The calculated values of EBs and D_{Li^+} are used in Equation 4.2 and the results
are plotted in Figure 4.5. Since EB and D_{Li^+} were obtained respectively by employing
QM and MD methods independently, small errors in the results produce significant
deviation from the linear trend during fitting data in Equation 4.2. As seen in this fig-
ure, an R^2 higher than 95% for both crystals clearly indicates the high accuracy of the
evaluated results. The calculated coefficients for Arrhenius equation (Equation 4.2)
are summarized in Table 4.3.
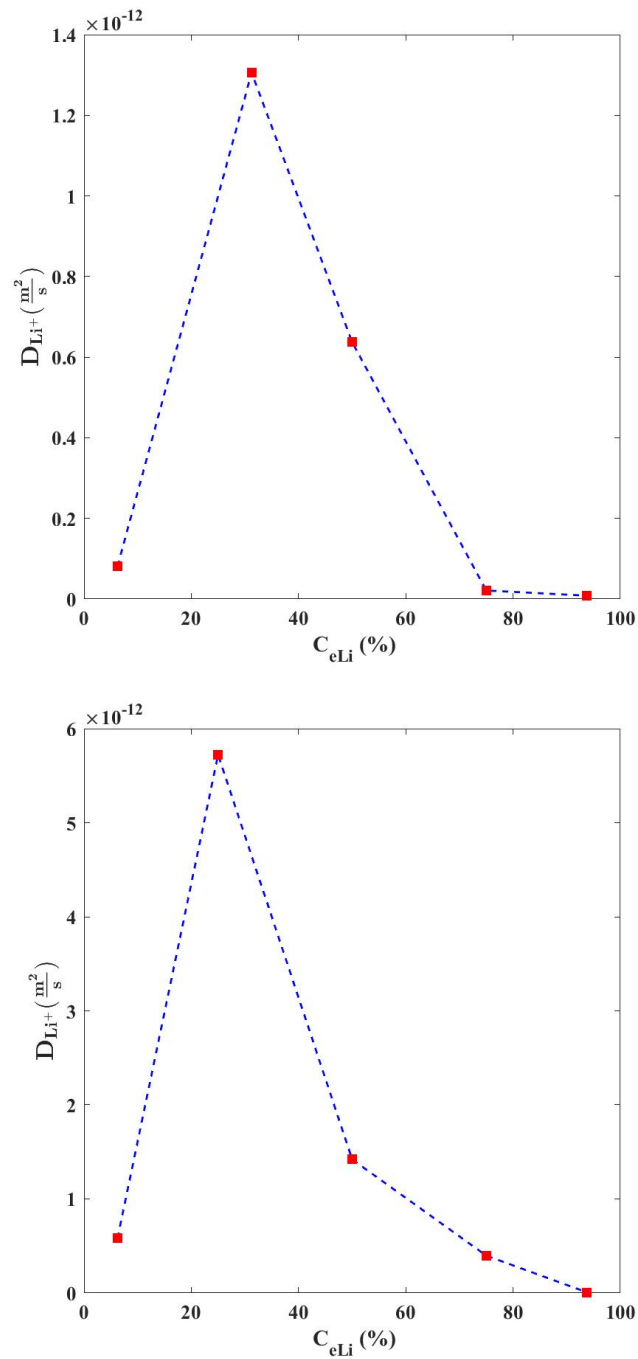
Figure 4.4: Li-ion diffusion coefficient (D_{Li^+}) as a function of excess Li-ion concentration for (a) LiF and (b) $\mathrm{Li_2O}$.
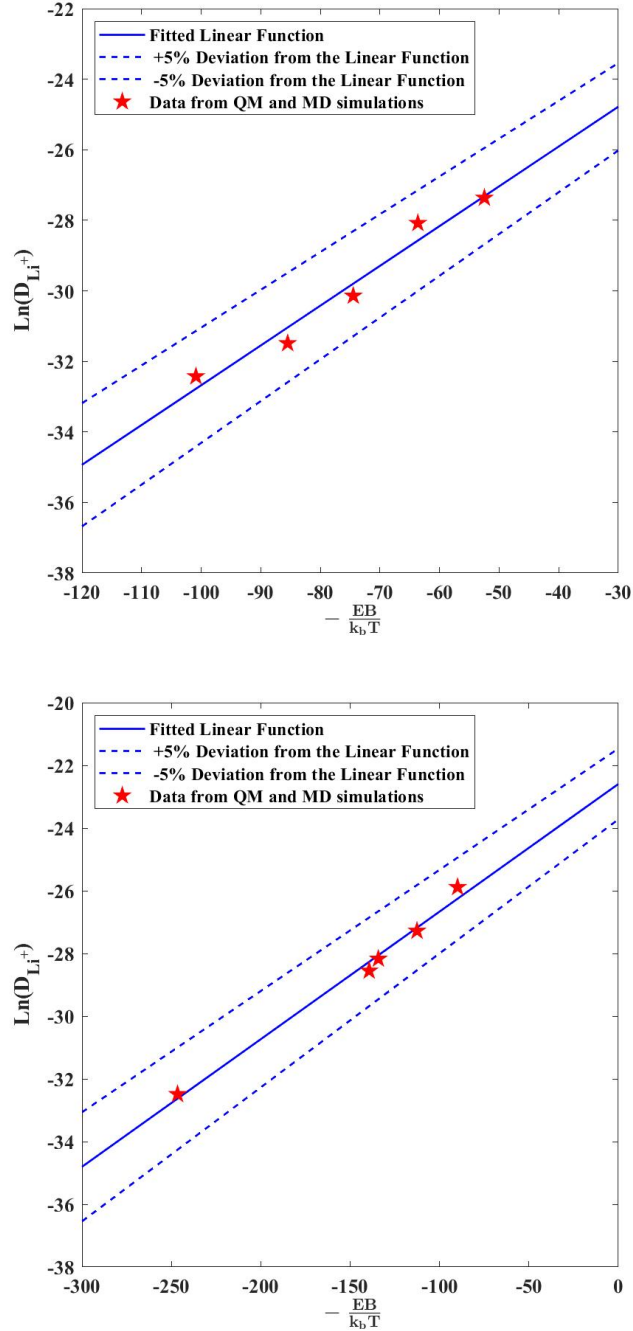
Figure 4.5: Ln (D_{Li^+}) for various eLi concentrations, evaluated using Equation 4.2, plotted against $-\frac{EB}{k_bT}$, and the corresponding linear trend for (a) LiF and (b) Li_2O. The obtained coefficients are summarized in Table 4.3.

Table 4.3: The constants in Equation 4.2 obtained from the curve fitting in Figure 4.5.

	B_0	D_0	R^2
Li_2O	4.07×10^{-2}	1.54×10^{-10}	0.98
LiF	1.128×10^{-1}	5.10×10^{-10}	0.96

Based on these results, we can write D_{Li^+} as a function of eLi concentration and temperature for Li_2O and LiF, respectively, as follows:

$$D_{Li^+_{Li_2O}}(C_{eLi}, T) = 1.54 \times 10^{-10} exp\left(-4.07 \times 10^{-2} \times \frac{12.0460C^2_{eLi} - 8.9294C^1_{eLi} + 3.9488}{k_b T}\right),$$
(4.2)

$$D_{Li^+_{LiF}}(C_{eLi}, T) = 5.10 \times 10^{-10} exp\left(-1.128 \times 10^{-1} \times \frac{3.5237C^2_{eLi} - 2.5607C^1_{eLi} + 1.9886}{k_b T}\right),$$
(4.3)

As mentioned in the Macro-Scale Mathematical Modelling section, the sum of the cross section areas of Li_2O and LiF is required, irrespective of their positions in the crystal structure. For the total LiF and Li_2O spread through the inner section of the SEI layer, we have:

$$D_T = \left[\left(\frac{\omega_{Li_2O}}{\omega_{Li_2O} + \frac{\rho_{Li_2O}}{\rho_{LiF}}\omega_{LiF}}\right) D_{Li^+_{Li_2O}} + \left(\frac{\omega_{LiF}}{\omega_{LiF} + \frac{\rho_{LiF}}{\rho_{Li_2O}}\omega_{Li_2O}}\right) D_{Li^+_{LiF}}\right].$$
(4.4)

where m_i, ρ_i, and L respectively are mass, density and length of component i. Also,

ω_i is the mass fraction of component i in the inner section of the SEI layer such that $\omega_1 + \omega_2 = 1$. A detailed derivation of Equation 4.4 is mentioned in Appendix 4.C.

Finally, a 3D surface plot along with a contour map of the diffusion coefficient (D_{Li+}), obtained from Equation 4.4, for a temperature range of 263.15 K to 358.15 K, and an excess Li-ion concentration (C_{eLi}) range of 0 to 1, with $\omega_1 = \omega_2 = 0.5$, is shown in Figure 4.6. Several observations can be made from this figure: (i) A C_{Li+} between 15% to 55% increases the diffusion coefficient significantly. (ii) The D_{Li+} function is more sensitive to C_{eLi} at relatively high temperatures. Therefore, defining the minimum and maximum SOC level should be done by considering the operating temperature conditions of the battery. (iii) Raising the temperature is not an effective method for increasing D_{Li+} at all concentrations.
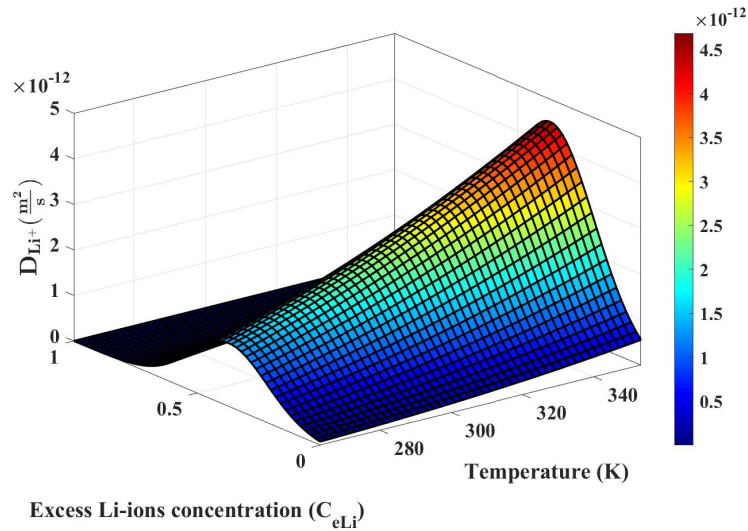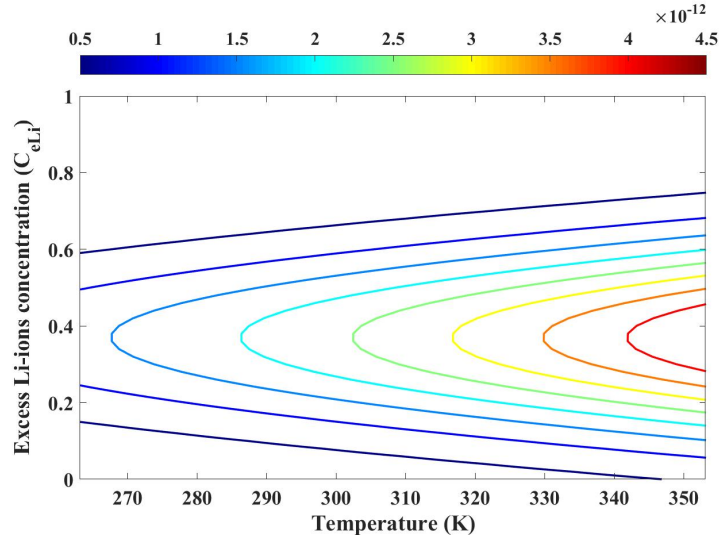
Figure 4.6: 3D surface plot and a contour map of the diffusion coefficient (D_{Li^+}), obtained from Equation 4.4 proposed in this work (with $\omega_1 = \omega_2 = 0.5$), as a function of temperature (263.15 K to 358.15 K) and excess Li-ion concentration (0% to 100%).

4.6   Summary and Conclusions

In this work, we have investigated the diffusion in the inner section of the SEI layer using a combination of quantum mechanics, molecular dynamics, and macro-scale mathematical modeling. The following are the key findings and propositions from this research: Quantum mechanics calculations have shown that the energy barrier (EB) has a quadratic relationship with the concentration of excess Li-ion concentration (C_{eLi}) (c.f. Figure 4.3). Specifically, the EB is high for very low and very high C_{eLi}. Therefore, at low and high C_{eLi}, waste voltage and electron leakage will increase, leading to a lower efficiency. Also, since EB is a function of C_{eLi}, D_{Li^+} is more sensitive to temperature at very low and very high excess Li-ion concentration. Hence, at a very low and very high concentration of excess Li-ions, raising the

130

temperature to increase D_{Li^+} is not very effective.

Next, the diffusion coefficient for different C_{eLi} values have been evaluated using molecular dynamics (MD) simulations. D_{Li^+} from MD, and EBs from QM calculations have been cast into an Arrhenius's formulation (Equations 4.2). The R^2 value of this resulting equation is higher than 0.95, confirming the accuracy as well as validity of the formulation. The formulation is rewritten for LiF and Li_2O by casting EB as a function of C_{eLi} (c.f. Equations 4.2 and 4.3).

Finally, as a highlight of this work and the main outcome of this investigation, we have combined the results from QM, MD and macro-scale mathematical modeling to present a single unified diffusion coefficient equation (Equation 4.4) that is a function of temperature and concentration.

4.7 Appendix 4.A: Settings and Parameters for QM and MD

All settings and parameters for the MD and QM calculations are summarized in the following tables:

Table 4.A1: The summary of the settings for QM calculations in this work.

Properties	Value or Method
XC Functional	PBE
Convergence tolerance	1.0×10^{-6} Ry
W.F. Cutoff	1.0×10^{2}
Charge Cutoff	1.0×10^{2} Ry
Maximum force	1.0×10^{-3} Ry/Bohr
Smearing factor	1.0×10^{-2} Ry

Table 4.A2: Force field parameters for primary Li_2O crystal structure for EIM force field [66].

	$Li^+ - Li^+$	$Li^+ - F^-$	$F^- - F^-$
E_{bij}(eV)	-0.2533	-1.2681	-0.1332
$r_{e,ij}$ (Å)	3.6176	1.9644	4.0026
$r_{c\Phi,ij}$(Å)	6.0490	4.5000	6.0090
α_{ij}	7.5536	13.467	7.7698
β_{ij}	3.5017	5.2272	2.9898
$A_{\phi,ij}$(eV)	0.3327	0.6998	0.1003
ζ_{ij}	0.6000	0.6000	0.6000
$r_{s\phi,ij}$(Å)	2.0000	2.0000	2.0000
$r_{c\phi,ij}$(Å)	7.0637	5.4840	7.0273
$A_{\eta,ij}$	0.0000	0.2177	0.0000
$r_{s\eta,ij}$(Å)	0.0000	2.0090	0.0000
$r_{c\eta,ij}$(Å)	0.0000	5.4300	0.0000

Table 4.A3: Force field parameters for primary Li_2O crystal structure for Buck/Coul/Long force field [67, 68].

	$A_{i,j}(eV)$	$\rho_{i,j}(\text{Å})$	$C_{i,j}(eV \text{ Å}^6)$
$Li^+ - Li^+$	0.0000	1.0000	0.0000
$Li^+ - O^{-2}$	653.83979	0.2857	0.0000
$O^{-2} - O^{-2}$	9022.8245	0.2650	85.092

Table 4.A4: A summary of the parameters and methods in the MD simulations in this work.

Property	Methods and specifications
Temperature	298.15 K
Frame output every	Every 10,000 steps
Force field	Buck/Coul/Long and EIM
Van der Waals	Ewald
Cutoff	10 Å

4.8   Appendix 4.B: The Generalized Least Squares (GLS)

Generalized Least Squares (GLS) estimator, a rigorous framework that combines the sophisticated estimators introduced by Bullerjahn et al. [60], has been employed to evaluate the diffusion coefficient from the MSD analysis as follows:

We can define the parameters a and σ as:

$$a^2 = \frac{\beta\gamma - \alpha\delta}{M\beta - *\alpha^2}, \quad \sigma^2 = \frac{M\delta - \alpha\gamma}{M\beta - *\alpha^2}, \tag{4.B1}$$

where α, β, γ and δ are given as:

$$\alpha = \frac{M(M+1)}{2}, \quad \beta = \alpha\frac{2M+1}{3}, \quad \gamma = \sum_{i=1}^{M} MSD_i, \quad \delta = \sum_{i=1}^{M} iMSD_i. \tag{4.B2}$$

σ^2 and a^2 calculated with Equation 4.B1 are used in the following [60]:

$$a_{GLS}^2 = \frac{\mu\nu - \lambda\zeta}{\kappa\mu - \lambda^2}, \quad \sigma_{GLS}^2 = \frac{\kappa\zeta - \lambda\nu}{\kappa\mu - \lambda^2}, \tag{4.B3}$$

$$\kappa = \sum_{i,j=1}^{M} (\sum_{i,j}(a_{GLS}^2, \sigma_{GLS}^2))^{-1}, \tag{4.B4}$$

$$\lambda = \sum_{i,j=1}^{M} i(\sum_{i,j}(a_{GLS}^2, \sigma_{GLS}^2))^{-1}, \quad \mu = \sum_{i,j=1}^{M} ij(\sum_{i,j}(a_{GLS}^2, \sigma_{GLS}^2))^{-1}, \tag{4.B5}$$

$$\nu = \sum_{i,j=1}^{M} MSD_i(\sum_{i,j}(a_{GLS}^2, \sigma_{GLS}^2))^{-1}, \quad \zeta = \sum_{i,j=1}^{M} iMSD_j(\sum_{i,j}(a_{GLS}^2, \sigma_{GLS}^2))^{-1},$$

where $\sum_{i,j}\left(a_{GLS}^2, \sigma_{GLS}^2\right)$ can be calculated employing following equations [60]:

$$\sum_{i,j}\left(a_{GLS}^2, \sigma_{GLS}^2\right) = \sum_{i,j}\left(0, \sigma_{GLS}^2\right) + \frac{a^4(1+\delta_{i,j}) + 4a^2\sigma^2 min(i,j)}{N - min(i,j) + 1} + \frac{a^4 max(0, N-i-j+1)}{(N-i+1)(N-j+1)},$$

(4.B6)

$$\sum_{i,j}\left(0, \sigma_{GLS}^2\right) = \frac{a^4}{3}\left[\frac{2min(i,j)[1+3ij - min(i,j)^2]}{N - min(i,j) + 1} + \frac{min(i,j)^2 - min(i,j)^4}{(N-i+1)(N-j+1)} + \Theta(i+j-N-2)\right.$$
$$\left. \times \frac{(N+1-i-j)^4 - (N+1-i-j)^2}{(N-i+1)(N-j+1)}\right],$$

(4.B7)

where Θ indicates Heaviside function.

4.9   Appendix 4.C: Formulation of Total Diffusion Coefficient

The inner layer of SEI consist of two crystal structures, including LiF and Li$_2$O. So, the total diffusion coefficient in this layer, D_T, based on sum of the surface area fraction, ϵ, of each crystal can be derived as follows:

Writing Fick's second law on each crystal structures in the SEI inner layer:

$$\begin{cases} A_T = A_{LiF} + A_{Li_2O} \\ A_T J_T = -A_T D_T \frac{dc}{dx} \end{cases} \Rightarrow A_i J_i = -A_i D_i \frac{dc}{dx}$$

(4.C1)

By considering ϵ_i as the surface area fraction of component i, the total diffusion

coefficient (D_T) in the SEI's inner layer could be calculated as:

$$\begin{cases} D_T = \frac{D_1 A_1 + D_2 A_2}{A_1 + A_2} \\ \\ \epsilon_i = \frac{A_i}{A_1 + A_2} \end{cases} \Rightarrow D_T = \epsilon_{LiF} D_{LiF} + \epsilon_{Li_2O} D_{Li_2O}. \tag{4.C2}$$

Since evaluating the surface area fraction for crystal structure in the inner layer of SEI is too difficult, the surface fraction could be defined as a function of the mass fraction by expanding A_i and ω_i:

$$\begin{cases} A_i = \frac{m_i}{\rho_i L} \\ \\ \omega_i = \frac{m_i}{m_{Li_2O} + m_{LiF}} \end{cases} \Rightarrow \begin{cases} \epsilon_{Li_2O} = \frac{\omega_{Li_2O}}{\omega_{Li_2O} + \frac{\rho_{Li_2O}}{\rho_{LiF}} \omega_{LiF}} \\ \\ \epsilon_{LiF} = \frac{\omega_{LiF}}{\omega_{LiF} + \frac{\rho_{LiF}}{\rho_{Li_2O}} \omega_{Li_2O}}, \end{cases} \tag{4.C3}$$

4.10   Nomenclature

The used symbols and indexes in the modified MSMM model in this work

Symbol	Unit	Description
a	1	GLS Parameter
a_0, a_1, a_2	1	Constant coefficient in Equation 4.1
A_i	m^2	Surface area of i crystal
B_0, D_0	$\frac{mol}{m^3}$	Constant coefficient in Equation 4.2
C_{eLi}	%	Excess Li-ion concentration
D_i	$\frac{m^2}{s}$	Diffusion coefficient in i crystal
EB	eV	Energy barrier against diffusion
k_b	$\frac{eV}{K}$	Boltzmann constant
m_i	g	Mass of i component

M, N	1	Number of the MD simulation steps
T	K	Temperature
X_n, Y_n, Z_n	Å	x,y,z positions of an atom in nth step
$\alpha, \beta, \gamma, \delta, \epsilon, \kappa, \lambda, \mu, \nu, \sigma, \zeta$	1	GLS estimator's parameters
ϵ	1	Surface area fraction
ω	1	Mass fraction
ρ	$\frac{g}{cm^3}$	Density

Bibliography

[1] A. Emadi. *Advanced Electric Drive Vehicles.* Energy, Power Electronics, and Machines. Taylor & Francis, 2014.

[2] Ajaykrishna Ramasubramanian, Vitaliy Yurkiv, Tara Foroozan, Marco Ragone, Reza Shahbazian-Yassar, and Farzad Mashayek. Lithium Diffusion Mechanism Through Solid-Electrolyte Interphase in Rechargeable Lithium Batteries. *Journal of Physical Chemistry C*, 123(16):10237–10245, apr 2019.

[3] Dina Becker, Markus Börner, Roman Nölle, Marcel Diehl, Sven Klein, Uta Rodehorst, Richard Schmuch, Martin Winter, and Tobias Placke. Surface modification of ni-rich $lini_{0.8}co_{0.1}mn_{0.1}o_2$ cathode material by tungsten oxide coating for

improved electrochemical performance in lithium-ion batteries. *ACS Applied Materials & Interfaces*, 11(20):18404–18414, 2019.

[4] Sui Gu, Zhaoyin Wen, Rong Qian, Jun Jin, Qingsong Wang, Meifen Wu, and Shangjun Zhuo. Carbon disulfide cosolvent electrolytes for high-performance lithium sulfur batteries. *ACS Applied Materials & Interfaces*, 8(50):34379–34386, 2016. PMID: 27998100.

[5] Alexander T. Tesfaye, Roberto Gonzalez, Jeffery L. Coffer, and Thierry Djenizian. Porous silicon nanotube arrays as anode material for li-ion batteries. *ACS Applied Materials & Interfaces*, 7(37):20495–20498, 2015. PMID: 26352212.

[6] Xiuling Zhang, Xinyu Du, Yingying Yin, Nian-Wu Li, Wei Fan, Ran Cao, Weihua Xu, Chi Zhang, and Congju Li. Lithium-ion batteries: Charged by triboelectric nanogenerators with pulsed output based on the enhanced cycling stability. *ACS Applied Materials & Interfaces*, 10(10):8676–8684, 2018. PMID: 29446611.

[7] Yibo Zhang, Rujun Chen, Ting Liu, Yang Shen, Yuanhua Lin, and Ce-Wen Nan. High capacity, superior cyclic performances in all-solid-state lithium-ion batteries based on 78li2s-22p2s5 glass-ceramic electrolytes prepared via simple heat treatment. *ACS Applied Materials & Interfaces*, 9(34):28542–28548, 2017. PMID: 28776981.

[8] Zahra Moradi, Amir Heydarinasab, and Farshid Pajoum Shariati. First-principle study of doping effects (ti, cu, and zn) on electrochemical performance of li2mno3 cathode materials for lithium-ion batteries. *International Journal of Quantum Chemistry*, 121(4):e26458, 2021.

[9] Tomooki Hosaka, Tatsuo Matsuyama, Kei Kubota, Satoshi Yasuno, and Shinichi Komaba. Development of kpf$_6$/kfsa binary-salt solutions for long-life and high-voltage k-ion batteries. *ACS Applied Materials & Interfaces*, 12(31):34873–34881, 2020. PMID: 32697073.

[10] Cao Cuong Nguyen, Taeho Yoon, Daniel M. Seo, Pradeep Guduru, and Brett L. Lucht. Systematic investigation of binders for silicon anodes: Interactions of binder with silicon particles and electrolytes and effects of binders on solid electrolyte interphase formation. *ACS Applied Materials & Interfaces*, 8(19):12211–12220, 2016. PMID: 27135935.

[11] Tianyu Feng, Youlong Xu, Zhengwei Zhang, Xianfeng Du, Xiaofei Sun, Lilong Xiong, Raul Rodriguez, and Rudolf Holze. Low-cost al$_2$o$_3$ coating layer as a preformed sei on natural graphite powder to improve coulombic efficiency and high-rate cycling stability of lithium-ion batteries. *ACS Applied Materials & Interfaces*, 8(10):6512–6519, 2016. PMID: 26913475.

[12] Fernando A. Soto, Asma Marzouk, Fedwa El-Mellouhi, and Perla B. Balbuena. Understanding Ionic Diffusion through SEI Components for Lithium-Ion and Sodium-Ion Batteries: Insights from First-Principles Calculations. *Chemistry of Materials*, 30(10):3315–3322, 2018.

[13] E. Peled. The electrochemical behavior of alkali and alkaline earth metals in nonaqueous battery systems—the solid electrolyte interphase model. *Journal of The Electrochemical Society*, 126(12):2047–2051, dec 1979.

[14] Aiping Wang, Sanket Kadam, Hong Li, Siqi Shi, and Yue Qi. Review on Modeling

of the Anode Solid Electrolyte Interphase (SEI) for Lithium-Ion Batteries. *npj Computational Materials*, 4(1):1–26, mar 2018.

[15] Kang Xu. Nonaqueous Liquid Electrolytes for Lithium-based Rechargeable Batteries. *Chemical Reviews*, 104(10):4303–4417, oct 2004.

[16] Kang Xu. Electrolytes and Interphases in Li-Ion Batteries and Beyond. *Chemical Reviews*, 114(23):11503–11618, dec 2014.

[17] Arthur V. Cresce, Selena M. Russell, David R. Baker, Karen J. Gaskell, and Kang Xu. In Situ and Quantitative Characterization of Solid Electrolyte Interphases. *Nano Letters*, 14(3):1405–1412, mar 2014.

[18] Siqi Shi, Peng Lu, Zhongyi Liu, Yue Qi, Louis G. Hector, Hong Li, and Stephen J. Harris. Direct Calculation of Li-ion Transport in the Solid Electrolyte Interphase. *Journal of the American Chemical Society*, 134(37):15476–15487, sep 2012.

[19] Petr Novák, Felix Joho, Roman Imhof, Jan Christoph Panitz, and Otto Haas. In Situ Investigation of the Interaction Between Graphite and Electrolyte Solutions. *Journal of Power Sources*, 81-82:212–216, sep 1999.

[20] A. Naji, J. Ghanbaja, B. Humbert, P. Willmann, and D. Billaud. Electroreduction of Graphite in $LiClO_4$-Ethylene Carbonate Electrolyte. Characterization of the Passivating Layer by Transmission Electron Microscopy and Fourier-Transform Infrared Spectroscopy. *Journal of Power Sources*, 63(1):33–39, nov 1996.

[21] Rosamaría Fong, Ulrich von Sacken, and J. R. Dahn. Studies of Lithium Intercalation into Carbons Using Nonaqueous Electrochemical Cells. *Journal of The Electrochemical Society*, 137(7):2009–2013, 1990.

[22] Franz Dinkelacker, Philipp Marzak, Jeongsik Yun, Yunchang Liang, and Aliaksandr S. Bandarenka. Multistage mechanism of lithium intercalation into graphite anodes in the presence of the solid electrolyte interface. *ACS Applied Materials & Interfaces*, 10(16):14063–14069, 2018. PMID: 29539259.

[23] Dong Zheng, Xiao-Qing Yang, and Deyang Qu. Stability of the solid electrolyte interface on the li electrode in li–s batteries. *ACS Applied Materials & Interfaces*, 8(16):10360–10366, 2016. PMID: 27045986.

[24] V. Prakash Reddy, Mario Blanco, and Ratnakumar Bugga. Boron-based anion receptors in lithium-ion and metal-air batteries. *Journal of Power Sources*, 247:813–820, 2014.

[25] Chu Ying Ouyang and Li Quan Chen. Physics Towards Next Generation Li Secondary Batteries Materials: A Short Review from Computational Materials Design Perspective. *Science China: Physics, Mechanics and Astronomy*, 56(12):2278–2292, nov 2013.

[26] D. Grazioli, M. Magri, and A. Salvadori. Computational Modeling of Li-ion Batteries. *Computational Mechanics 2016 58:6*, 58(6):889–909, aug 2016.

[27] Ying Shirley Meng and M. Elena Arroyo-de Dompablo. First principles computational materials design for energy storage materials in lithium ion batteries. *Energy Environ. Sci.*, 2:589–609, 2009.

[28] John Christensen and John Newman. A Mathematical Model for the Lithium-Ion Negative Electrode Solid Electrolyte Interphase. *Proceedings - Electrochemical Society*, 20:85–94, 2003.

[29] Lin Liu, Jonghyun Park, Xianke Lin, Ann Marie Sastry, and Wei Lu. A Thermal-Electrochemical Model that Gives Spatial-Dependent Growth of Solid Electrolyte Interphase in a Li-Ion Battery. *Journal of Power Sources*, 268:482–490, 2014.

[30] Xiankun Huang, Shaoyong Ke, Haichao Lv, and Yongzhong Liu. A Dynamic Capacity Fading Model with Thermal Evolution Considering Variable Electrode Thickness for Lithium-Ion Batteries. *Ionics*, 24(11):3439–3450, 2018.

[31] Andrew M. Colclasure, Kandler A. Smith, and Robert J. Kee. Modeling Detailed Chemistry and Transport for Solid-Electrolyte-Interface (SEI) Films in Li-Ion Batteries. *Electrochimica Acta*, 58(1):33–43, 2011.

[32] Githin K. Prasad and Christopher D. Rahn. Model Based Identification of Aging Parameters in Lithium Ion Batteries. *Journal of Power Sources*, 232:79–85, 2013.

[33] Saksham Phul, Abhishek Deshpande, and Balaji Krishnamurthy. A Mathematical Model to Study the Effect of Potential Drop Across the SEI Layer on the Capacity Fading of a Lithium Ion Battery. *Electrochimica Acta*, 164:281–287, 2015.

[34] Birger Horstmann, Fabian Single, and Arnulf Latz. Review on Multi-Scale Models of Solid-Electrolyte Interphase Formation. *Current Opinion in Electrochemistry*, 13:61–69, 2019.

[35] Amirmasoud Lanjan, Behnam Ghalami Choobar, and Sepideh Amjad-Iranagh. Promoting Lithium-Ion Battery Performance by Application of Crystalline Cathodes $Li_xMn_{1-z}Fe_zPO_4$. *Journal of Solid State Electrochemistry*, 24(1):157–171, jan 2020.

[36] Zahra Moradi, Amirmasoud Lanjan, and Seshasai Srinivasan. Enhancement of Electrochemical Properties of Lithium Rich Li_2RuO_3 Cathode Material. *Journal of The Electrochemical Society*, 167(11):110537, jul 2020.

[37] Zahra Moradi, Amirmasoud Lanjan, and Seshasai Srinivasan. Multiscale investigation into the co-doping strategy on the electrochemical properties of li_2ruo_3 cathodes for li-ion batteries. *ChemElectroChem*, 8(1):112–124, 2021.

[38] E. Peled, D. Golodnitsky, and G. Ardel. Advanced Model for Solid Electrolyte Interphase Electrodes in Liquid and Polymer Electrolytes. *Journal of The Electrochemical Society*, 144(8):L208–L210, dec 1997.

[39] Victor A. Agubra and Jeffrey W. Fergus. The formation and stability of the solid electrolyte interface on the graphite anode. *Journal of Power Sources*, 268:153–162, 2014.

[40] D. Aurbach, B. Markovsky, M. D. Levi, E. Levi, A. Schechter, M. Moshkovich, and Y. Cohen. New Insights into the Interactions Between Electrode Materials and Electrolyte Solutions for Advanced Nonaqueous Batteries. *Journal of Power Sources*, 81-82:95–111, sep 1999.

[41] Kevin Leung, Fernando Soto, Kie Hankins, Perla B. Balbuena, and Katharine L. Harrison. Stability of Solid Electrolyte Interphase Components on Lithium

Metal and Reactive Anode Material Surfaces. *Journal of Physical Chemistry C*, 120(12):6302–6313, mar 2016.

[42] Na Tian, Chunxiu Hua, Zhaoxiang Wang, and Liquan Chen. Reversible reduction of li$_2$co$_3$. *J. Mater. Chem. A*, 3:14173–14177, 2015.

[43] Eric J. McShane, Andrew M. Colclasure, David E. Brown, Zachary M. Konz, Kandler Smith, and Bryan D. McCloskey. Quantification of inactive lithium and solid–electrolyte interphase species on graphite electrodes after fast charging. *ACS Energy Letters*, 5(6):2045–2051, 2020.

[44] Mazharul M. Islam, Thomas Bredow, and Christian Minot. Theoretical Analysis of Structural, Energetic, Electronic, and Defect Properties of Li$_2$O. *Journal of Physical Chemistry B*, 110(19):9413–9420, may 2006.

[45] Linda Pastero, Francesco Roberto Massaro, and Dino Aquilano. Experimental and Theoretical Morphology of Single and Twinned Crystals of Li$_2$CO$_3$ (zabuyelite). *Crystal Growth and Design*, 7(12):2749–2755, dec 2007.

[46] Yongning Zhou, Wenyuan Liu, Mingzhe Xue, Le Yu, Changliang Wu, Xiaojing Wu, and Zhengwen Fu. LiF/Co Nanocomposite as a New Li Storage Material. *Electrochemical and Solid-State Letters*, 9(3):A147, jan 2006.

[47] Koichi Momma and Fujio Izumi. *VESTA3* for Three-Dimensional Visualization of Crystal, Volumetric and Morphology Data. *Journal of Applied Crystallography*, 44(6):1272–1276, Dec 2011.

[48] W. Kohn and L. J. Sham. Self-Consistent Equations Including Exchange and Correlation Effects. *Physical Review*, 140(4A):A1133, nov 1965.

[49] Giannozzi, P.; Baroni, S.; Bonini, N.; Calandra, M.; Car, R.; Cavazzoni, C.; Ceresoli, D.; Chiarotti, G. L.; Cococcioni, M.; Dabo, I.; Corso, A. D.; Gironcoli, S. D.; Fabris, S.; Fratesi, G.; Gebauer, R.; Gerstmann, U.; Gougoussis, C.; Kokalj, A.; Lazzeri, M.; Mauri, F.; Mazzarello, R.; Paolini, S.; Pasquarello, A.; Paulatto, L.; Sbraccia, C.; Scandolo, S.; Sclauzero, G.; Seitsonen, A. P.; Smogunov, A.; Umari, P.; Wentzcovitch, R. M. QUANTUM ESPRESSO: A modular and open-source software project for quantum simulations of materials. *Journal of Physics: Condensed Matter*, 21(39):395502, sep 2009.

[50] Giannozzi, P.; Andreussi, O.; Brumme, T.; Bunau, O.; Buongiorno Nardelli, M.; Calandra, M.; Car, R.; Cavazzoni, C.; Ceresoli, D.; Cococcioni, M.; Colonna, N.; Carnimeo, I.; Dal Corso, A.; De Gironcoli, S.; Delugas, P.; Distasio, R. A.; Ferretti, A.; Floris, A.; Fratesi, G.; Fugallo, G.; Gebauer, R.; Gerstmann, U.; Giustino, F.; Gorni, T.; Jia, J.; Kawamura, M.; Ko, H. Y.; Kokalj, A.; Kücükbenli, E.; Lazzeri, M. ; Marsili, M.; Marzari, N.; Mauri, F.; Nguyen, N. L.; Nguyen, H. V.; Otero-De-La-Roza, A.; Paulatto, L.; Poncé, S.; Rocca, D.; Sabatini, R.; Santra, B.; Schlipf, M.; Seitsonen, A. P.; Smogunov, A.; Timrov, I.; Thonhauser, T.; Umari, P.; Vast, N.; Wu, X.; Baroni, S., Advanced Capabilities for Materials Modelling with Quantum ESPRESSO. *Journal of Physics Condensed Matter*, 29(46), oct 2017.

[51] Siqi Shi, Hua Zhang, Xuezhi Ke, Chuying Ouyang, Minsheng Lei, and Liquan Chen. First-Principles Study of Lattice Dynamics of LiFePO$_4$. *Physics Letters, Section A: General, Atomic and Solid State Physics*, 373(44):4096–4100, oct 2009.

[52] Peng Lu and Stephen J. Harris. Lithium transport within the solid electrolyte interphase. *Electrochemistry Communications*, 13(10):1035–1037, 2011.

[53] Martin Winter. The solid electrolyte interphase – the most important and the least understood solid electrolyte in rechargeable li batteries. *Zeitschrift für Physikalische Chemie*, 223(10-11):1395–1406, 2009.

[54] HANNES JÓNSSON, GREG MILLS, and KARSTEN W. JACOBSEN. Nudged Elastic Band Method for Finding Minimum Energy Paths of Transitions. In *Classical and Quantum Dynamics in Condensed Phase Simulations*, pages 385–404. WORLD SCIENTIFIC, jun 1998.

[55] Graeme Henkelman, Gísli Jóhannesson, and Hannes Jónsson. Methods for Finding Saddle Points and Minimum Energy Paths. In *Theoretical Methods in Condensed Phase Chemistry*, pages 269–302. Kluwer Academic Publishers, dec 2005.

[56] Steve Plimpton. Fast Parallel Algorithms for Short-Range Molecular Dynamics. *Journal of Computational Physics*, 117(1):1–19, mar 1995.

[57] N Swindells and C Sykes. The Classical Equation of State of Gaseous Helium, Neon and Argon. *Proceedings of the Royal Society of London. Series A. Mathematical and Physical Sciences*, 168(933):264–283, oct 1938.

[58] Rasoul Sarraf-Mamoory, Saman Nadery, and Nastaran Riahi-Noori. The effect of precipitation parameters on preparation of lithium fluoride (lif) nano-powder. *Chemical Engineering Communications*, 194(8):1022–1028, 2007.

[59] A. Einstein. Über Die Von Der Molekularkinetischen Theorie der Wärme

Geforderte Bewegung Von in Ruhenden Flüssigkeiten Suspendierten Teilchen. *Annalen der Physik*, 322(8):549–560, 1905.

[60] Jakob Tómas Bullerjahn, Sören Von Bülow, and Gerhard Hummer. Optimal Estimates of Self-Diffusion Coefficients from Molecular Dynamics Simulations. *Journal of Chemical Physics*, 153(2):024116, jul 2020.

[61] Xavier Michalet and Andrew J. Berglund. Optimal Diffusion Coefficient Estimation in Single-Particle Tracking. *Physical Review E - Statistical, Nonlinear, and Soft Matter Physics*, 85(6):061916, jun 2012.

[62] Andrew J. Berglund. Statistics of Camera-Based Single-Particle Tracking. *Physical Review E - Statistical, Nonlinear, and Soft Matter Physics*, 82(1):011917, jul 2010.

[63] Christian L. Vestergaard, Paul C. Blainey, and Henrik Flyvbjerg. Optimal Estimation of Diffusion Coefficients from Single-Particle Trajectories. *Physical Review E - Statistical, Nonlinear, and Soft Matter Physics*, 89(2):022726, feb 2014.

[64] Xavier Michalet. Mean Square Displacement Analysis of Single-Particle Trajectories with Localization Error: Brownian Motion in an Isotropic Medium. *Physical Review E - Statistical, Nonlinear, and Soft Matter Physics*, 82(4):041914, oct 2010.

[65] Y. Du, A. V. Mamishev, B. C. Lesieutre, and M. Zahn. Measurement of Moisture Diffusion as a Function of Temperature and Moisture Concentration in Transformer Pressboard. *Conference on Electrical Insulation and Dielectric Phenomena (CEIDP), Annual Report*, 1:341–344, 1998.

[66] X. W. Zhou, F. P. Doty, and P. Yang. Atomistic Simulation Study of Atomic Size Effects on B1 (NaCl), B2 (CsCl), and B3 (Zinc-Blende) Crystal Stability of Binary Ionic Compounds. *Computational Materials Science*, 50(8):2470–2481, 2011.

[67] Youngjae Kim and Jungshin Kang. Viscosity of Molten MgF_2-LiF-MgO System and Structure Investigation Using Classical Molecular Dynamics Simulations. *Journal of Non-Crystalline Solids*, 552(August 2020):120377, 2021.

[68] Thorsten Stechert. *Glasses for Energy Applications : Atomic Scale Network Structure and Properties*. Materials phd theses, Imperial College London, 2013.

Chapter 5

Analysis of the Solid-Electrolyte Interface Layer in Li-ion Batteries Using Multi-Scale Modeling Techniques

PRELUDE: This chapter is been re-produced from the following manuscript which is under review in the "ACS Applied Materials Interfaces" journal: *A. Lanjan, Z. Moradi, S. Srinivasan, "Analysis of the Solid-Electrolyte Interface Layer in Li-ion Batteries Using Multi-Scale Modeling Techniques", ACS Applied Materials Interfaces.*

Contributing Author: Amirmasoud Lanjan.

Abstract

A comprehensive understanding of the various electrochemical processes at different time and length scales within the solid electrolyte interface (SEI) layer is critical to understanding the ageing and internal resistance. This task has not been actively

pursued for a long time due to the inherent complexity of the processes inherent to this layer. Filling this void in the literature, herein, a computational framework is employed to evaluate potential parameters for different components in this layer using quantum mechanics (QM) calculations. The *potential parameters* obtained from the QM calculations are employed as the inputs for molecular dynamics (MD) simulations to estimate the diffusion coefficient, Young's modulus, Poisson's ratio, and thermal conductivity in the SEI layer. Additionally, an enhanced macro-scale mathematical model, which considers SEI effects on the internal resistance and operating voltage in addition to the cathode, anode, and electrolyte, is developed. Finally, the obtained SEI properties were employed in the macro-scale model to evaluate the operating voltage for a Li-ion battery and the results are compared with the previous models in the literature and experimental data to stablish the validity and the superiority of our framework that accounts for the impact of the SEI layer in a Li-ion battery that is subject to a current of 0.2 to 60 C-rates.

5.1   Introduction

The massive amount of CO_2 emissions from the different sectors are raising serious concerns about the emerging environmental issues. Green technologies for harvesting clean energies are naturally being developed and researched at an accelerated pace. An important aspect of this exercise is the energy storage technology, that is also being actively researched and developed. To this end, the development of the next generation Lithium-ion batteries (LIBs) is being seen as one of the most promising energy storage system solutions due to their low self-discharge rate, high power and energy densities, and widespread application, including portable electronics and

electric vehicles (EVs) [3, 15, 17]. However, there is still room for considerable improvements to enhance the current state of LIBs in terms of their performance[1, 11], efficiency[23, 38, 44, 45], and their durability [5, 14, 27]. A prolonged battery lifespan is crucial for making the use of LIBs in EVs practical, given that nearly fifty percent of the EV's original cost is devoted to the battery. Consequently, in recent years, various studies have been carried out on distinct components of LIBs, including the anode, cathode, and electrolyte [18, 19, 22, 24, 25, 39]. One of the main obstacles in developing high-quality and durable LIBs is the insufficient understanding of the electrode-electrolyte interface (SEI) layer in LIBs that is one of the main reasons for the degradation of the batteries [20, 37].

SEI layer is formed when the anode electrode potential (μ) is larger than the lowest unoccupied molecular orbital (LUMO) of the electrolyte, leading to the reduction of the electrolyte molecules, forming a solid layer on the electrode/electrolyte interface called the "SEI Layer" [9, 33]. SEI layer formation consumes Li-ions, vitally affecting the battery's lifetime. Even in a well-engineered LIB, the SEI formation is the main source (more than 50%) of capacity loss [16, 26, 46]. However, SEI layer is not completely undesirable since it reduces electron tunnelling that prevents further contact between electrons and electrolyte molecules, suppressing a further fade in the battery's capacity [46]. Therefore, understanding SEI formation reactions, Li-ions diffusion mechanisms, and material characterization in this layer are critical for enhancing the electrochemical performance and durability of LIBs [2, 48]. The SEI layer has two subsections including (I) an organic outer sub-layer (near the Electrolyte interface), which allows the transfer of both Li-ions and the electrolyte solvent molecules, and (II) an inorganic inner sub-layer (near the Electrode interface), which only allows the

permeability of the Li-ions [20, 42]. The outer sub-layer consists of the well-known crystal structures including Li_2O, LiF, and Li_2CO_3. On the other hand, the crystal structures of the inner sub-layer including $Li_2C_2O_4$, Li_2EDC, $LiOCO_2CH_3$, and $LiOCO_2C_2H_5$ are mostly unknown. Since most of the SEI formation reactions occur at an extremely small time (pico-second) and length (nano-meter) scales, conventional experimental methods are not a feasible approach for capturing and characterizing them, especially the thermodynamics and kinetic aspects [20, 46].

Due to the lack of precise understanding of the diffusion mechanism in the SEI layer, there is a significant deviation from experimental data in mathematical models for SEI-related properties such as internal resistance, voltage drop, cycling efficiency, capacity fading, and aging. Hariharan et al. [12] and Nyman et al. [30] presented mathematical models for predicting the electrochemical performance and internal resistance of LIBs. However, their model largely ignored the role of SEI layer in the functioning of a battery, resulting in predictions that are not in good agreement with the experimental data.

On the other hand, Ekström and Lindbergh [4] derived a macro-scale mathematical continuum model to estimate the effect of SEI layer formation on the aging in LIBs. Their model uses three lumped fitting parameters, instead of the fundamental properties, to match the experimental data. While these fitting parameters improve the accuracy of the model, the model itself is now dependent on the experimental data for adjusting these parameters.

Such shortcomings have led to an active exploration of multi-scale computational tools such as Quantum Mechanics (QM), Molecular Dynamics (MD), and Macro-Scale modelling, to overcome the limitations of experimental approaches. Collectively,

these computational tools play an important role in advancing the battery technology by allowing researchers to investigate the battery architecture and the multitude of electrochemical processes therein over a wide range of time and length scales [6, 10, 35, 40]. For example, Lanjan et al. [20, 22] investigated the SEI layer employing the multi-scale predictive modeling and presented a diffusion coefficient equation for Li-ions in the SEI's outer sub-layer and used this equation to develop an enhanced version of the Ekström model with just two lumped fitting parameters, reducing the model dependency on the experimental data. However, they did not investigate the diffusion mechanism in the inner layer of the SEI due to the lack of knowledge on the crystal structures in this part of the SEIs, and instead focused on elucidating the diffusion mechanism in the outer sub-layer of the SEI.

It must be noted that the extremely short time scale of the processes in the SEI layer makes it almost impossible to use conventional experimental techniques to study the electrochemical processes in the SEI layer. The consequent lack of experimental data and thereby the absence of any information on the potential parameters for crystal structures in the inner sub-layer render MD simulations inapplicable to it. Also, due to the multi-component multi-layer structure of the SEI, commonly the smallest system representing an SEI layer is too large for the QM system size limits. With these constraints, Lanjan et al. [21] recently developed a computational framework coupling QM and MD techniques to determine the potential parameters for MD simulations, independent of the experimental data. This framework was validated with respect to the experimental data of a wide variety of molecules. In this work, we have employed this computational framework for characterizing crystal structures in the inner section of the SEI layer. Herein, the QM calculation is employed to evaluate particle-particle

interactions in the system. Afterward, these data were used to estimate nonbonded, bonded, angle, dihedral, and improper potential parameters for running MD simulations. Then, the MD simulation utilized these potential parameters to predict the SEI's crystal properties including density, Young's Modules, Poisson's Ratio, thermal conductivity, and diffusion coefficient. Employing SEI layer characteristics, a new macro-scale mathematical model has been developed to evaluate the electrochemical performance of LIBs. This model, as opposed to the previous conventional models, considers the SEI layer section in addition to the anode, cathode, and electrolyte. Finally, all these models were validated respective to the experimental data from the literature.

5.2   Methodology

The inner section of the SEI layer consists of $Li_2C_2O_4$, $C_4H_4Li_2O_6$ (Li_2EDC), $LiOCO_2CH_3$, and $LiOCO_2C_2H_5$ crystal structures [20]. Unlike the crystal structures in the outer section, i.e. Li_2O and LiF, these crystal structures are almost unknown [20]. Hence, potential parameters for running MD simulations on them are not available in the literature. Therefore, the first step is to evaluate the potential parameters of the crystal structures using QM calculation.

5.2.1   Potential Parameters

To determine the potential parameters, all crystal structures were created and relaxed using QM calculations. Afterwards, five main types of particle-particle interactions,

including nonbonded[1], bonded[2], angle[3], dihedral[4], and improper[5], were determined in the system. The seven algorithms developed by Lanjan et al. [21] were employed to create a series of crystal structures for each interaction in the system as a function of its distance/angle (x). IN doing this parametric variation, other effective parameters are maintained at their minimum energy level. For instance, for investigating a bond interaction, different crystal structures are created with different bond lengths while other bonds, angles, dihedrals, and impropers are relaxed at their minimum energy level. Then, the QM calculation is used to evaluate the system's energy (U) for these crystal structures as a function of their distance/angle (x). The data is eventually fitted on the potential equations (e.g., $U = k(x - x_0)^2$) to obtain the potential parameters (e.g., k and x_0).

5.2.2   Quantum Mechanics

Since QM calculation is only applicable to systems with a few electrons, the density functional theory (DFT) [29, 36, 47] approximation with Perdew Burke Ernzerhof (PBE) as its exchange-correlation function has been employed in this work. Also, all QM calculations were run using the "Quantum Espresso" software package [7, 8] using settings summarized in Table 5.1.

---

[1]*Nonbonded:* Refers to the forces of attraction or repulsion between atoms or molecules that do not involve the formation or breaking of chemical bonds such as Van der Waals, Coulombic, and polarization.

[2]*Bonded:* Refers to the attractive and repulsive forces that hold atoms together in a molecule or compound, such as covalent bonds or ionic bonds.

[3]*Angle:* Refers to the forces that determine the spatial arrangement of atoms in a molecule or compound, based on the bond angles between them.

[4]*Dihedral:* Refers to the forces that determine the orientation of two connected bonds in a molecule, based on the angle between them.

[5]*Improper:* Refers to the forces that help maintain the correct orientation of a functional group or a specific atom in a molecule, by preventing unwanted rotation or inversion.

Table 5.1: The summary of the settings for QM calculations in this work.

Properties	Value/Method
XC Functional	PBE
Convergence tolerance	1.0×10^{-6} Ry
W.F. Cutoff	1.0×10^{2}
Charge Cutoff	1.0×10^{2} Ry
Maximum force	1.0×10^{-3} Ry/Bohr
Smearing factor	1.0×10^{-2} Ry

Systems A to D, corresponding to the molecules $Li_2C_2O_4$, $C_4H_4Li_2O_6$ (Li_2EDC), $LiOCO_2CH_3$, and $LiOCO_2C_2H_5$, respectively, were created. Each system had a single molecule. System E is a random combination of systems A-D, representing the inner section of the SEI layer. A schematic diagram for each molecule is shown in Figure 5.1.
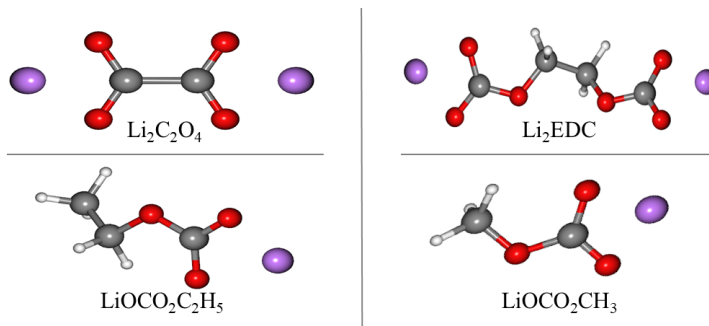
Figure 5.1: Schematic diagram for $Li_2C_2O_4$, $C_4H_4Li_2O_6$ (Li_2EDC), $LiOCO_2CH_3$, and $LiOCO_2C_2H_5$ molecules.

5.2.3   Molecular Dynamics

The potential parameters derived from the QM simulations were employed to run MD simulations on these systems. The "LAMMPS" software package [34] with the

potential styles summarized in Table 5.2 were used in this work. The summation of Buckingham and Coulombs' potentials is considered for the nonbonded interactions. Also, the "Ewald" long-range solver is employed to compute long-range Coulombic interactions.

Table 5.2: The potential styles utilized in the MD simulations using the LAMMPS software package.

Interaction type	Potential Style	Equation
Nonbonded	Buckingham/Coulombic	$E = Ae^{-\frac{r}{B}} - \frac{C}{r^6}$
Bonded	harmonic	$E = K(r - r_0)^2$
Angle	harmonic	$E = K(\theta - \theta_0)^2$
Dihedral	quadratic	$E = K(\phi - \phi_0)^2$
Improper	harmonic	$E = K(\chi - \chi_0)^2$

Eliminating the close contacts between particles and stabilizing the velocity, pressure, and temperature of the system, the energy is minimized in 20,000 steps over two stages of MD calculations under the NVT and NPT ensemble, each for 1 ns and 10 ns, respectively. Parrinello Rahman barostat [31] and Nosé Hoover thermostat [13, 28] were used to fix the simulations' pressure and temperature with damping relaxation times of 0.1 ps and 1 ps, respectively. The integration of Newton's equations of motion was accomplished using a Stoermer-Verlet integrator with a time step size of 1 femtosecond. To reduce the execution time and resolve any imbalances on the CPU, dynamic load balancing techniques were implemented. To obtain the time-averaged results for transport and structural properties, the data on trajectories were saved at intervals of 1,000 time steps. A detailed information on the characteristics of the MD simulations is summarized in Table 5.3. These three simulation stages, namely, energy

minimization, equilibrium gain, and property estimation, required approximately 16 hours to complete. The simulations were conducted using an 11th Generation Intel i7-11700K processor and 16 GB of RAM.

Table 5.3: The summary of the settings for MD simulations in this work.

Properties	Descriptions and specifications
Energy minimization	conjugate gradient for 2×10^4 steps
Production run	10 ns
Equilibrium	1 ns NVT run and 10 ns NPT run
Motions integrator	Stoermer-Verlet, 1 fs time-step
Pressure coupling	1 bar, Parrinello-Rahman barostat
Temperature coupling	25^oC, Nose-Hoover thermostat
Constraint solver	Constraining all bonds
Long-range interactions	Ewald summation with 1.0×10^{-5} accuracy
Periodic Boundary	x, y and z directions
Trajectory output	Every 1,000 time step (fs)
Neighbor list updating	Every 10 fs
Dynamic load balance	Yes

Diffusion Coefficients were calculated employing mean square displacement (MSD) analysis. For this, the particles in the system are allowed to move and interact with each other over a defined period of time. Over the course of the simulation, the positions of the particles at regular intervals are recorded to calculate the MSD of

each particle type as follows [20, 41]:

$$MSD = \frac{1}{N}\sum_{i=1}^{N}|r^{(i)}(t) - r^{(i)}(0)|^2, \qquad (5.1)$$

where N is the total number of particles, $r^{(i)}(t)$ is position vector of ith particle at time t. The diffusion coefficient is then calculated using the MSD by fitting it to the equation of MSD:

$$D = \frac{MSD}{2nt} \qquad (5.2)$$

where $n = 3$ is the dimensionality of the system and t is the time.

Young's Modulus and Poisson's ratio were calculated using the elastic constant calculation method. For this, we applied small strains (ϵ) to the simulation box, by subjecting the box to small a deformation along x-axes and measuring the stress (σ) response by determining the forces on the atoms and dividing it by the volume of the simulation cell. Subsequently, the Young's modulus and Poisson's ratio were obtained from the stress-strain relationship. More precisely, the Young's modulus can be calculated from the ratio of stress to strain along a specific axis as:

$$\sigma = \frac{F}{A}, \qquad (5.3)$$

$$\epsilon_x = \frac{L_{x_0} - L_x}{L_{x_0}}, \qquad (5.4)$$

$$E = \frac{\sigma}{\epsilon_x}. \qquad (5.5)$$

Poisson's ratio was obtained from the ratio of strains along orthogonal axes as:

$$\nu = \frac{\epsilon_x}{\epsilon_z} \tag{5.6}$$

Thermal Conductivity was calculated by performing a steady-state heat conduction MD simulation. In this simulation, a temperature gradient was applied to the system, and the heat flow was monitored over time. The simulation was run for a sufficient amount of time so that the heat flow reaches a steady state. After the simulation is complete, the thermal conductivity was extracted by calculating the heat flux and dividing it by the temperature gradient. Note that the heat flux can be obtained from the time derivative of the total heat energy in the system, while the temperature gradient can be obtained from the difference in temperature between the two ends of the system. Thus, the thermal conductivity is given as:

$$\kappa = \frac{J}{V \Delta T}, \tag{5.7}$$

where κ and $V = A\Delta x$ are thermal conductivity and volume, respectively. Also, J is the total heat passing through the system with a cross-section area A and a length of Δx.

5.2.4   Macro-Scale Model

With a detailed characterization of the SEI layer, we have adequate data to model the effect of the SEI layer on the electrochemical performance of the battery. Specifically, with this data, we have developed an enhanced mathematical model that considers the effect of the electrochemical processes within the SEI layer in addition to the

cathode, anode, and separators sections for a LIB system. This is a major evolution from the models of Hariharan et al. [12] and Nyman et al. [30] models, that do not account for the physics within the SEI layer. The key equations of our model can be summarized as follows:

Negative Electrode - Mass Balance:

$$\frac{d\bar{c}_{cn}}{dt} = -\frac{j_n}{r_n},$$
(5.8)

$$\frac{d\bar{c}_{srn}}{dt} = -\frac{30D_{sn}\bar{c}_{srn}}{r_n^2} - \frac{45j_n}{2r_n^2},$$
(5.9)

$$C_{sur,n} = \bar{c}_{sn} + \frac{8r_n}{35}\bar{c}_{srn} - \frac{r_n}{35D_{sn}}j_n.$$
(5.10)

Negative Electrode - Charge Transfer Reaction:

$$j_n = \frac{I}{a_n L_n F}.$$
(5.11)

Positive Electrode - Mass Balance:

$$\frac{d\bar{c}_{cp}}{dt} = -\frac{j_p}{r_p},$$
(5.12)

$$\frac{d\bar{c}_{srp}}{dt} = -\frac{30D_{sp}\bar{c}_{srp}}{r_p^2} - \frac{45j_p}{2r_p^2},$$
(5.13)

$$C_{sur,p} = \bar{c}_{sp} + \frac{8r_p}{35}\bar{c}_{srp} - \frac{r_p}{35D_{sp}}j_p.$$
(5.14)

Positive Electrode - Charge Transfer Reaction:

$$j_p = -\frac{I}{a_p L_p F}. \tag{5.15}$$

Electrolyte Potential:

$$A_1 = (L_n \epsilon_{ln} \alpha_n + \frac{L_s L_n \epsilon_{ln}}{2 D_{sn}} + \frac{l_n^2 \epsilon_{ln}}{3 D_{sn}}), \tag{5.16}$$

$$A_2 = (L_n \epsilon_{ln} \alpha_p + \frac{L_s L_n \epsilon_{ln}}{2 D_{sn}}), \tag{5.17}$$

$$A_3 = (1 - t_+) a_n L_n, \tag{5.18}$$

$$B_1 = (L_P \epsilon_{lp} \alpha_n), \tag{5.19}$$

$$B2 = \left(L_p \epsilon_{lp} \alpha_p - \frac{l_p^2 \epsilon_{ln}}{3 D_p} \right), \tag{5.20}$$

$$B3 = (1 - t_+) a_p L_p, \tag{5.21}$$

$$D = A_1 B_2 - A_2 B_1, \tag{5.22}$$

$$c_{lmid} = c_{lin} - \frac{3 L_s q_{lin}}{8 D_l} - \frac{L_s q_{lip}}{8 D_l}, \tag{5.23}$$

$$\alpha_n = -\frac{\frac{L_n L_s \epsilon_{sn}}{2D_l} + \frac{L_s^2 \epsilon_{sn}}{6D_l} + \frac{L_n^2 \epsilon_{sn}}{3D_l}}{L_n \epsilon_{sn} + L_s \epsilon_s + L_p \epsilon_{sp}}, \tag{5.24}$$

$$\alpha_p = -\frac{\frac{L_p L_s \epsilon_{sp}}{2D_l} + \frac{L_s^2 \epsilon_{sp}}{6D_l} + \frac{L_p^2 \epsilon_{sp}}{3D_l}}{L_n \epsilon_{sn} + L_s \epsilon_s + L_p \epsilon_{sp}}, \tag{5.25}$$

$$\Delta c_{SEI} = -\frac{j_n L_{SEI}}{D_{SEI}}, \tag{5.26}$$

$$c_{lip} = c_{l0} + \alpha_n q_{lin} + \alpha_p q_{lip} + \Delta c_{SEI}, \tag{5.27}$$

$$c_{lin} = c_{lip} + \frac{L_s(q_{lin} + q_{lip})}{2D_l}, \tag{5.28}$$

$$c_{lp} = c_{lip} - \frac{q_{lip} L_p}{2D_p}, \tag{5.29}$$

$$c_{ln} = c_{lin} + \frac{q_{lin} L_n}{2D_n}, \tag{5.30}$$

$$\frac{dq_{lin}}{dt} = -\frac{B_2}{D}q_{lin} - \frac{A_2}{D}q_{lip} + \frac{A_3 B_2}{D}j_n - \frac{A_2 B_3}{D}j_p, \tag{5.31}$$

$$\frac{dq_{lip}}{dt} = \frac{B_1}{D}q_{lin} + \frac{A_1}{D}q_{lip} - \frac{A_3 B_1}{D}j_n + \frac{A_1 B_3}{D}j_p, \tag{5.32}$$

$$\Phi_{lin} = 2\theta Ln\left(\frac{c_{lin}}{c_{lmid}}\right) + \frac{IL_s}{2\kappa_n}, \tag{5.33}$$

$$\Phi_{lip} = 2\theta Ln\left(\frac{c_{lip}}{c_{lmid}}\right) + \frac{IL_s}{2\kappa_n}, \tag{5.34}$$

$$V_{eln} = \Phi_{lin} + 2\theta Ln\left(\frac{c_{ln}}{c_{lin}}\right) + \frac{IL_n}{2\kappa_n}, \tag{5.35}$$

$$V_{elp} = \Phi_{lip} + 2\theta Ln\left(\frac{c_{lp}}{c_{lip}}\right) + \frac{IL_p}{2\kappa_p}, \tag{5.36}$$

$$V_{rdn} = \frac{2R_g T}{F} sinh^{-1}\left(\frac{j_n}{2k_n c_{surn}^{0.5}(c_{smaxn} - c_{surn})^{0.5}c_{ln}^{0.5}}\right), \tag{5.37}$$

$$V_{rdp} = \frac{2R_g T}{F} sinh^{-1}\left(\frac{j_p}{2k_p c_{surp}^{0.5}(c_{smaxp} - c_{surp})^{0.5}c_{lp}^{0.5}}\right). \tag{5.38}$$

Cell Voltage:

Open Circuit Voltage:

$$U_{cell} = U_p - U_n. \tag{5.39}$$

Electrolyte Voltage Drop:

$$V_{el} = V_{elp} - V_{eln}. \tag{5.40}$$

Reaction/Diffusion Voltage Drop:

$$V_{rd} = V_{rdp} - V_{rdn}. \tag{5.41}$$

Operating Voltage:

$$V_{cell} = U_{cell} + V_{el} + V_{rd}. \tag{5.42}$$

5.3   Results and Discussion

MSD analysis is one of the most common techniques in evaluating diffusion coefficients. The MSD values for the in x, y, z, and 3D directions are calculated for two types of systems: (i) four single molecule type systems that contain $Li_2C_2O_4$, $C_4H_4Li_2O_6$ (Li_2EDC), $LiOCO_2CH_3$, and $LiOCO_2C_2H_5$, respectively, and (ii) a fifth system containing all of these crystal structures in a random configuration represents the inner section of the SEI layer. The results are shown in Figure 5.2. For the system representing the SEI's inner layer, the MSD slope in the x and z directions are almost the same and almost eight times larger in the y direction.
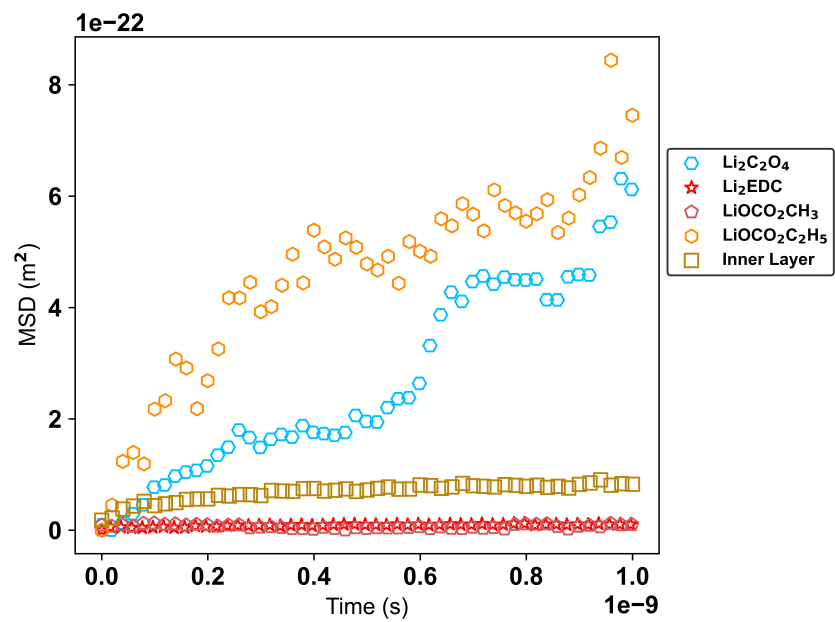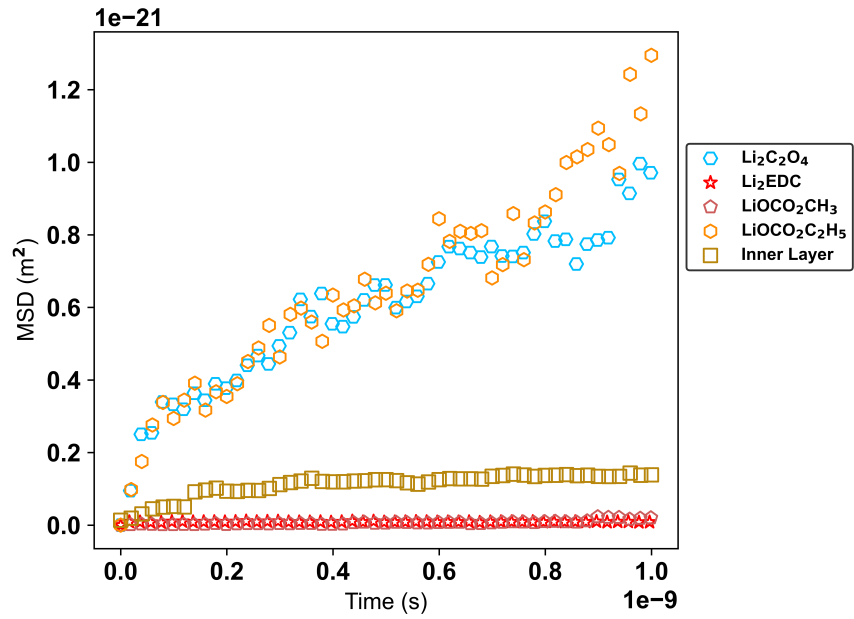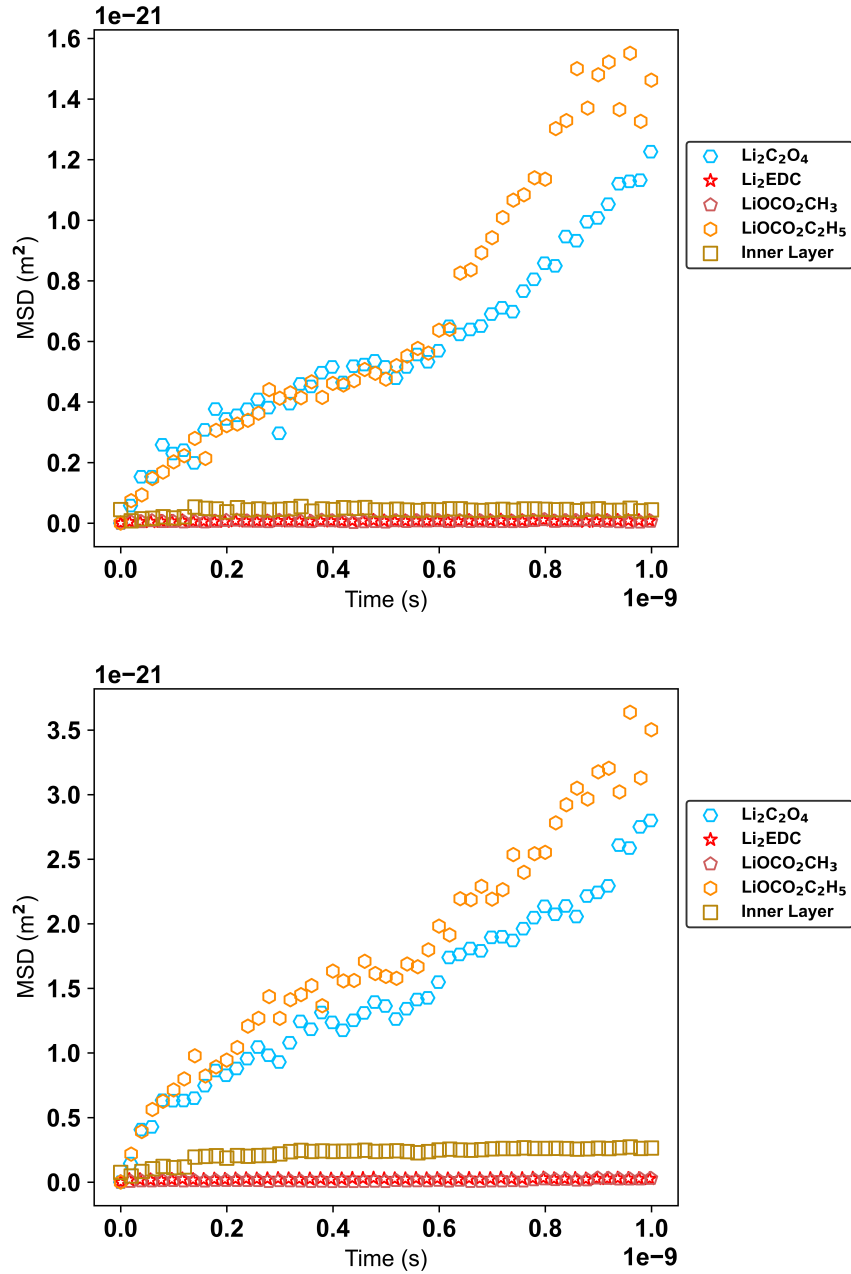
Figure 5.2: MSD analysis in (a) x, (b) y, (c) z, (d) 3D directions for $Li_2C_2O_4$, $C_4H_4Li_2O_6$ (Li_2EDC), $LiOCO_2CH_3$, $LiOCO_2C_2H_5$, and Inner Layer systems.

The diffusion coefficients for the studied materials in x, y, z, and 3D directions

were obtained by the linear regression on the MSD data points, and are summarized in Table 5.4. However, due to the lack of information in the literature regarding the orientation of the crystal growth in the SEI layer, we have used the 3D diffusion coefficient $(D_{Li^+}^{(3D)})$ for our calculations to study Li-ion migrations in this layer.

Crystal	$D_{Li^+}^{(x)}$ $(\frac{m^2}{s})$	$D_{Li^+}^{(y)}$ $(\frac{m^2}{s})$	$D_{Li^+}^{(z)}$ $(\frac{m^2}{s})$	$D_{Li^+}^{(3D)}$ $(\frac{m^2}{s})$
$Li_2C_2O_4$	3.48×10^{-13}	2.82×10^{-13}	4.80×10^{-13}	3.70×10^{-13}
Li_2EDC	2.56×10^{-17}	3.10×10^{-15}	1.53×10^{-15}	1.55×10^{-15}
$LiOCO_2CH_3$	7.66×10^{-15}	6.21×10^{-16}	2.94×10^{-16}	2.45×10^{-15}
$LiOCO_2C_2H_5$	4.82×10^{-13}	2.77×10^{-13}	7.56×10^{-13}	5.06×10^{-13}
Inner Layer	4.73×10^{-14}	2.18×10^{-14}	9.44×10^{-15}	2.62×10^{-14}

Table 5.4: Diffusion coefficient for the studied crystal structures including $Li_2C_2O_4$, $C_4H_4Li_2O_6$ (Li_2EDC), $LiOCO_2CH_3$, $LiOCO_2C_2H_5$, and the system representing the SEI inner layer in x, y, z, and 3D directions.

Almost any physical crack or damage in the SEI layer increases the electron tunnelling and solvent molecule diffusion, resulting in more electrolyte reduction and active Li-ion consumption. Shrinkage/expansion during the charge and discharge cycles in graphite anodes is one of the main reasons for SEI cracking and capacity loss. However, this can be reduced by increasing the crystal's roughness factors such as Young's modulus. Hence, the Young's modulus and Poisson's ratio are critical factors in LIBs durability. These values for the studied crystal structures are calculated and shown in Figure 5.3 and 5.4, respectively.
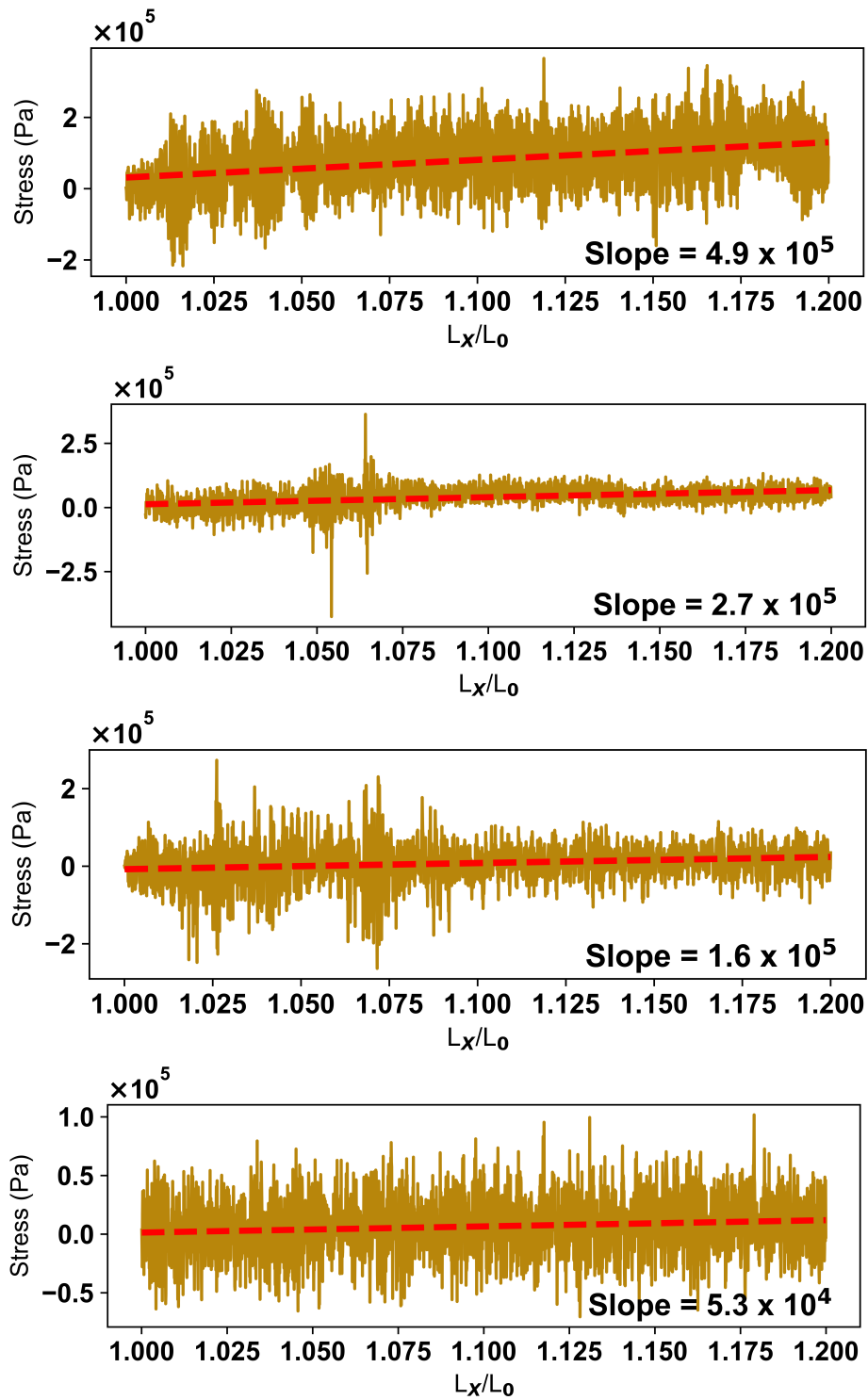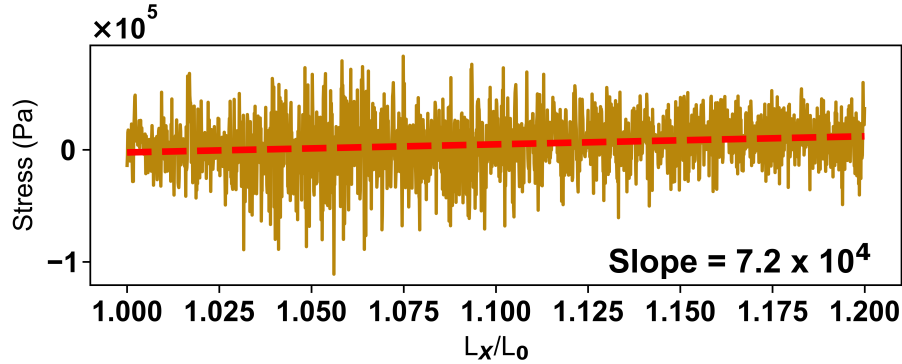
Figure 5.3: Predicted stress (σ) versus strain in x direction (ϵ_x) for $Li_2C_2O_4$, $C_4H_4Li_2O_6$ (Li_2EDC), $LiOCO_2CH_3$, $LiOCO_2C_2H_5$, and Inner Layer systems.

As expected, Young's modulus for the studied crystal structures, and thereby the system representing the inner section of the SEI layer, is relatively small. On comparing the different crystals, we find that the $LiOCO_2C_2H_5$ system with the smallest Young's modulus has the highest potential to be damaged and undergo capacity fading. Also, $LiOCO_2C_2H_5$ and Li_2EDC crystal structures have the largest and smallest Poisson's ratio, respectively.

Therefore, $LiOCO_2C_2H_5$ material has the least resistance to cracking during the expansion of the electrode in charge-discharge cycling. This can be addressed by adding electrolyte additives that reduce or even prevent the formation of $LiOCO_2C_2H_5$ crystals, resulting in a higher durability and longer lifetime for LIBs. Also, SEI cracking, the most common source of battery spoiling after a physical shock, can be reduced by employing chemistries and materials that will produce rough crystal structures in the SEI layer, resulting in durable LIBs in tough operational conditions.
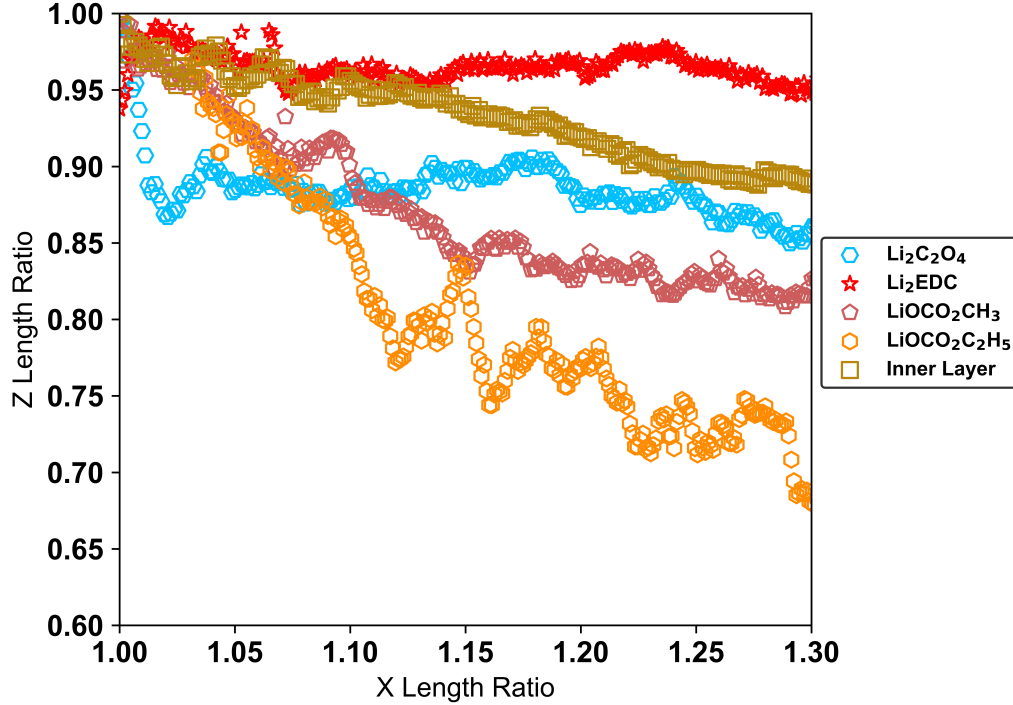
Figure 5.4: Strain in z direction (ϵ_z) versus strain in x direction (ϵ_x) for $Li_2C_2O_4$, $C_4H_4Li_2O_6$ (Li_2EDC), $LiOCO_2CH_3$, $LiOCO_2C_2H_5$, and Inner Layer systems.

In general, the crystal structures investigated in this work have much smaller thermal conductivity (see Figure 5.5) than graphite anode materials ($50\frac{W}{mK}$ [32]) which makes the SEI layer a thermal insulator on the surface of electrode particles. This allows us to operate the battery at higher temperatures and a smaller maximum allowable current for LIBs, increasing the charging time and lowering the discharging power. Again $LiOCO_2C_2H_5$ along with $Li_2C_2O_4$ has the worst performance in terms of thermal conductivity. However, the combination of these crystal structures in the SEI layer increases the particle-particle interactions, increasing the thermal conductivity to values that are larger than that of any other system with just a single component.
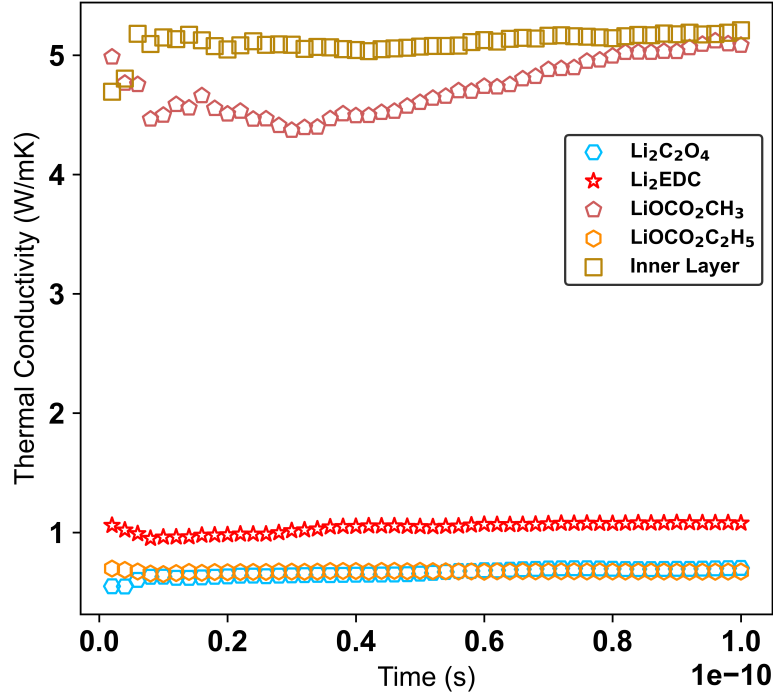
Figure 5.5: Predicted thermal conductivity (κ) for $Li_2C_2O_4$, $C_4H_4Li_2O_6$ (Li_2EDC), $LiOCO_2CH_3$, $LiOCO_2C_2H_5$, and Inner Layer systems.

After characterizing the SEI layer, the results obtained from MD simulations were employed in the enhanced macro-scale model introduced in the previous section to forecast operating voltage versus SOC for a battery under 0.2, 1.0, 10.0, 20.0, and 60.0 C-rate discharging current. The results from our enhanced macro-scale model, the conventional model in the literature, and the corresponding experimental data [43] are shown in Figure 5.6.
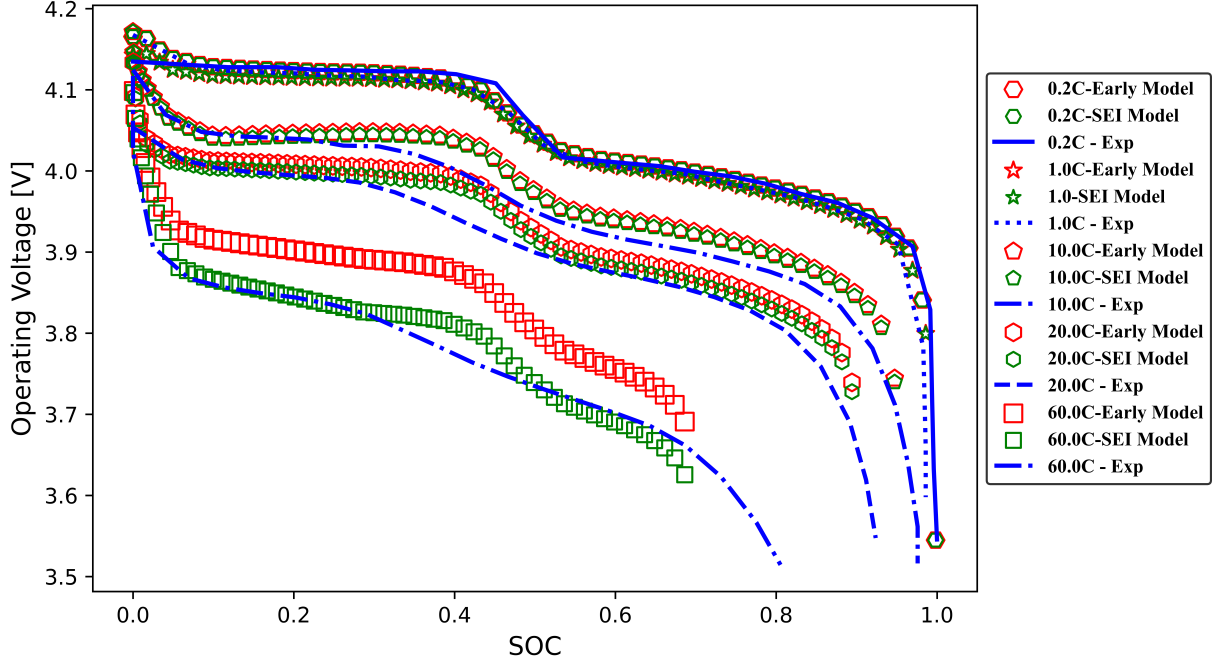
Figure 5.6: Operating voltage versus the state of charge (SOC) evaluated employing (I) Experimental data [43], (II) Pristine Hariharan et al. [12] and Nyman et al. [30] models, (III) Enhanced macro-scale model introduced in this work under 0.2, 1.0, 10.0, 20.0, and 60.0 C-rate discharging current.

Since this battery is not aged significantly, it only has a thin ($\approx$20 nm in thickness) SEI layer. The effect of this thin SEI layer on the Li-ion concentration gradient on the anode surface is negligible under a small current density. As seen in Figure 5.6, the accuracy of the enhanced and pristine models is almost the same ($\approx$99%) for 0.2 and 1.0 C-rate discharging current, respectively (see Table 5.5). However, upon increasing the applied current to 10.0 C and subsequently to 20.0 C, the pristine model begins to deviate from the experimental data by about 8 and 13% with respect to the experimental data, respectively. Additionally, in modelling the operating voltage under 60.0 C applied current, the pristine model deviates by more than 70% with

respect to the experimental data, which is not acceptable for any application. On the other hand, by including the SEI layer and its effect on the internal resistance in the enhanced model, the accuracy of the results are higher than 90% even for very high C-rates such as 60.0 C (see Table 5.5).

C-Rate	Pristine Model	Enhanced Model
0.2	99%	99%
1.0	99%	99%
10	92%	94%
20	87%	93%
60	31%	92%

Table 5.5: R^2 value obtained for (I) pristine and (II) enhanced models with respect to the experimental data [43] in Figure 5.6.

It must be noted that the need to include the SEI layer in the battery modelling for aged batteries are even more than a healthy battery, due to the thicker SEI layer and larger internal resistance. Our results clearly establish that coupling the enhanced model introduced in this work with battery ageing and SEI growth rate models such as the one proposed in Reference [22] can significantly increase the accuracy in simultaneously predicting the battery's performance and ageing.

5.4   Conclusions

Herein, we have employed a computational framework coupling QM and MD calculations to characterize the crystal structures in the SEI layer including $Li_2C_2O_4$, $C_4H_4Li_2O_6$ (Li_2EDC), $LiOCO_2CH_3$, and $LiOCO_2C_2H_5$. Afterwards, a macro-scale

mathematical model was developed that integrates the effects of the SEI layer on the internal resistance and LIBs performance using the properties obtained from QM and MD calculations. In evaluating this model, it was found that by increasing the applied current from 0.1 to 60 C-rate, the accuracy of the model remained in the range of $99\% - 93\%$ with respect to the experimental data. This is a far higher accuracy than that of the pristine model which ignores the impact of the SEI layer in their calculations, resulting in a sharp decline in the accuracy of the model (down to about 30% at 60 C-rate). Our findings highlight the crucial role of the SEI layer in the battery's performance and aging. It also emphasizes the need to consider the SEI layer in studying the battery's performance and ageing. This is particularly important for batteries operating under high-current conditions, or for an aged cell with a thicker SEI layer.

Bibliography

[1] D. Becker, M. Börner, R. Nölle, M. Diehl, S. Klein, U. Rodehorst, R. Schmuch, M. Winter, and T. Placke. Surface modification of ni-rich lini$_{0.8}$co$_{0.1}$mn$_{0.1}$o$_2$ cathode material by tungsten oxide coating for improved electrochemical performance in lithium-ion batteries. *ACS Applied Materials & Interfaces*, 11(20):18404–18414, 2019.

[2] F. Dinkelacker, P. Marzak, J. Yun, Y. Liang, and A. S. Bandarenka. Multistage mechanism of lithium intercalation into graphite anodes in the presence of the solid electrolyte interface. *ACS Applied Materials & Interfaces*, 10(16):14063–14069, 2018. PMID: 29539259.

[3] Y.-T. Du, X. Kan, F. Yang, L.-Y. Gan, and U. Schwingenschlögl. Mxene/graphene heterostructures as high-performance electrodes for li-ion batteries. *ACS Applied Materials & Interfaces*, 10(38):32867–32873, 2018. PMID: 30160474.

[4] H. Ekström and G. Lindbergh. A model for predicting capacity fade due to sei formation in a commercial graphite/lifepo4 cell. *Journal of The Electrochemical Society*, 162(6):A1003, 2015.

[5] T. Feng, Y. Xu, Z. Zhang, X. Du, X. Sun, L. Xiong, R. Rodriguez, and R. Holze. Low-cost al$_2$o$_3$ coating layer as a preformed sei on natural graphite powder to improve coulombic efficiency and high-rate cycling stability of lithium-ion batteries. *ACS Applied Materials & Interfaces*, 8(10):6512–6519, 2016. PMID: 26913475.

[6] D. E. Galvez-Aranda, V. Ponce, and J. M. Seminario. Molecular dynamics simulations of the first charge of a li-ion—si-anode nanobattery. *Journal of molecular modeling*, 23:1–16, 2017.

[7] P. Giannozzi, S. Baroni, N. Bonini, M. Calandra, R. Car, C. Cavazzoni, and D. Ceresoli. Chiarotti, glm cococcioni, i. dabo, et al. *J. Phys. Condens. Matter*, 21:395502, 2009.

[8] P. Giannozzi et al. J. of physics: Condens. *Matt*, 29:465901, 2017.

[9] J. B. Goodenough and Y. Kim. Challenges for rechargeable li batteries. *Chemistry of Materials*, 22(3):587–603, 2010.

[10] D. Grazioli, M. Magri, and A. Salvadori. Computational modeling of li-ion batteries. *Computational Mechanics*, 58:889–909, 2016.

[11] S. Gu, Z. Wen, R. Qian, J. Jin, Q. Wang, M. Wu, and S. Zhuo. Carbon disulfide cosolvent electrolytes for high-performance lithium sulfur batteries. *ACS Applied Materials & Interfaces*, 8(50):34379–34386, 2016. PMID: 27998100.

[12] K. S. Hariharan, P. Tagade, and S. Ramachandran. *Mathematical Modeling of Lithium Batteries: From Electrochemical Models to State Estimator Algorithms*. Springer, 2018.

[13] W. G. Hoover. Canonical dynamics: Equilibrium phase-space distributions. *Physical review A*, 31(3):1695, 1985.

[14] T. Hosaka, T. Matsuyama, K. Kubota, S. Yasuno, and S. Komaba. Development of kpf_6/kfsa binary-salt solutions for long-life and high-voltage k-ion batteries. *ACS Applied Materials & Interfaces*, 12(31):34873–34881, 2020. PMID: 32697073.

[15] J. Jia, C. Tan, M. Liu, D. Li, and Y. Chen. Relaxation-induced memory effect of lifepo4 electrodes in li-ion batteries. *ACS Applied Materials & Interfaces*, 9(29):24561–24567, 2017. PMID: 28657290.

[16] F. Joho, B. Rykart, R. Imhof, P. Novák, M. E. Spahr, and A. Monnier. Key factors for the cycling stability of graphite intercalation electrodes for lithium-ion batteries. *Journal of power sources*, 81:243–247, 1999.

[17] S. Kim, B. Seo, H. V. Ramasamy, Z. Shang, H. Wang, B. M. Savoie, and V. G. Pol. Ion–solvent interplay in concentrated electrolytes enables subzero temperature li-ion battery operations. *ACS Applied Materials & Interfaces*, 14(37):41934–41944, 2022. PMID: 36084339.

[18] A. Lanjan, B. G. Choobar, and S. Amjad-Iranagh. First principle study on the application of crystalline cathodes li2mn0. 5tm0. 5o3 for promoting the performance of lithium-ion batteries. *Computational Materials Science*, 173:109417, 2020.

[19] A. Lanjan, B. Ghalami Choobar, and S. Amjad-Iranagh. Promoting lithium-ion battery performance by application of crystalline cathodes lixmn1- zfezpo4. *Journal of Solid State Electrochemistry*, 24(1):157–171, 2020.

[20] A. Lanjan, Z. Moradi, and S. Srinivasan. Multiscale investigation of the diffusion mechanism within the solid–electrolyte interface layer: Coupling quantum mechanics, molecular dynamics, and macroscale mathematical modeling. *ACS Applied Materials & Interfaces*, 13(35):42220–42229, 2021. PMID: 34436850.

[21] A. Lanjan, Z. Moradi, and S. Srinivasan. A computational framework for evaluating molecular dynamics potential parameters employing quantum mechanics. *Mol. Syst. Des. Eng.*, pages –, 2023.

[22] A. Lanjan and S. Srinivasan. An enhanced battery aging model based on a detailed diffusing mechanism in the sei layer. *ECS Advances*, 1(3):030504, 2022.

[23] Z. Moradi, A. Heydarinasab, and F. Pajoum Shariati. First-principle study of doping effects (ti, cu, and zn) on electrochemical performance of li2mno3 cathode

materials for lithium-ion batteries. *International Journal of Quantum Chemistry*, 121(4):e26458, 2021.

[24] Z. Moradi, A. Lanjan, and S. Srinivasan. Enhancement of electrochemical properties of lithium rich li2ruo3 cathode material. *Journal of The Electrochemical Society*, 167(11):110537, 2020.

[25] Z. Moradi, A. Lanjan, and S. Srinivasan. Multiscale investigation into the co-doping strategy on the electrochemical properties of li2ruo3 cathodes for li-ion batteries. *ChemElectroChem*, 8(1):112–124, 2021.

[26] A. Naji, J. Ghanbaja, B. Humbert, P. Willmann, and D. Billaud. Electrore-duction of graphite in liclo4-ethylene carbonate electrolyte. characterization of the passivating layer by transmission electron microscopy and fourier-transform infrared spectroscopy. *Journal of power sources*, 63(1):33–39, 1996.

[27] C. C. Nguyen, T. Yoon, D. M. Seo, P. Guduru, and B. L. Lucht. Systematic investigation of binders for silicon anodes: Interactions of binder with silicon particles and electrolytes and effects of binders on solid electrolyte interphase formation. *ACS Applied Materials & Interfaces*, 8(19):12211–12220, 2016. PMID: 27135935.

[28] S. Nosé. A unified formulation of the constant temperature molecular dynamics methods. *The Journal of chemical physics*, 81(1):511–519, 1984.

[29] I. Novikov, B. Grabowski, F. Körmann, and A. Shapeev. Magnetic moment tensor potentials for collinear spin-polarized materials reproduce different magnetic states of bcc fe. *npj Computational Materials*, 8(1):1–6, 2022.

[30] A. Nyman, T. G. Zavalis, R. Elger, M. Behm, and G. Lindbergh. Analysis of the polarization in a li-ion battery cell by numerical simulations. *Journal of The Electrochemical Society*, 157(11):A1236, 2010.

[31] M. Parrinello and A. Rahman. Polymorphic transitions in single crystals: A new molecular dynamics method. *Journal of Applied physics*, 52(12):7182–7190, 1981.

[32] T. Pavlov, L. Vlahovic, D. Staicu, R. Konings, M. Wenman, P. Van Uffelen, and R. Grimes. A new numerical method and modified apparatus for the simultaneous evaluation of thermo-physical properties above 1500k: A case study on isostatically pressed graphite. *Thermochimica Acta*, 652:39–52, 2017.

[33] E. Peled. The electrochemical behavior of alkali and alkaline earth metals in nonaqueous battery systems—the solid electrolyte interphase model. *Journal of The Electrochemical Society*, 126(12):2047–2051, dec 1979.

[34] S. Plimpton. Fast parallel algorithms for short-range molecular dynamics. *Journal of Computational Physics*, 117(1):1–19, 1995.

[35] V. P. Reddy, M. Blanco, and R. Bugga. Boron-based anion receptors in lithium-ion and metal-air batteries. *Journal of Power Sources*, 247:813–820, 2014.

[36] L. J. Sham and W. Kohn. One-particle properties of an inhomogeneous interacting electron gas. *Physical Review*, 145(2):561, 1966.

[37] F. A. Soto, A. Marzouk, F. El-Mellouhi, and P. B. Balbuena. Understanding ionic diffusion through sei components for lithium-ion and sodium-ion batteries:

Insights from first-principles calculations. *Chemistry of Materials*, 30(10):3315–3322, 2018.

[38] A. T. Tesfaye, R. Gonzalez, J. L. Coffer, and T. Djenizian. Porous silicon nanotube arrays as anode material for li-ion batteries. *ACS Applied Materials & Interfaces*, 7(37):20495–20498, 2015. PMID: 26352212.

[39] R. Tyagi, A. Lanjan, and S. Srinivasan. Co-doping strategies to improve the electrochemical properties of lixmn2o4 cathodes for li-ion batteries. *ChemElectroChem*, 9(3):e202101626, 2022.

[40] R. Tyagi and S. Srinivasan. Molecular dynamics modeling of lithium ion intercalation induced change in the mechanical properties of lixmn2o4. *The Journal of Chemical Physics*, 153(16):164712, 2020.

[41] R. Tyagi and S. Srinivasan. Co-doping studies to enhance the life and electro-chemo-mechanical properties of the limn 2 o 4 cathode using multi-scale modeling and neuro-computing techniques. *Physical Chemistry Chemical Physics*, 24(31):18645–18666, 2022.

[42] A. Wang, S. Kadam, H. Li, S. Shi, and Y. Qi. Review on modeling of the anode solid electrolyte interphase (sei) for lithium-ion batteries. *npj Computational Materials*, 4(1):15, 2018.

[43] H. Xia, Z. Luo, and J. Xie. Nanostructured limn2o4 and their composites as high-performance cathodes for lithium-ion batteries. *Progress in Natural Science: Materials International*, 22(6):572–584, 2012.

[44] X. Zhang, X. Du, Y. Yin, N.-W. Li, W. Fan, R. Cao, W. Xu, C. Zhang, and C. Li. Lithium-ion batteries: Charged by triboelectric nanogenerators with pulsed output based on the enhanced cycling stability. *ACS Applied Materials & Interfaces*, 10(10):8676–8684, 2018. PMID: 29446611.

[45] Y. Zhang, R. Chen, T. Liu, Y. Shen, Y. Lin, and C.-W. Nan. High capacity, superior cyclic performances in all-solid-state lithium-ion batteries based on 78li2s-22p2s5 glass-ceramic electrolytes prepared via simple heat treatment. *ACS Applied Materials & Interfaces*, 9(34):28542–28548, 2017. PMID: 28776981.

[46] Y. Zhang, D. A. Kitchaev, J. Yang, T. Chen, S. T. Dacek, R. A. Sarmiento-Pérez, M. A. Marques, H. Peng, G. Ceder, J. P. Perdew, et al. Efficient first-principles prediction of solid stability: Towards chemical accuracy. *npj Computational Materials*, 4(1):1–6, 2018.

[47] Y. Zhang, Q. Xu, K. Koepernik, R. Rezaev, O. Janson, J. Železný, T. Jungwirth, C. Felser, J. van den Brink, and Y. Sun. Different types of spin currents in the comprehensive materials database of nonmagnetic spin hall effect. *npj Computational Materials*, 7(1):1–7, 2021.

[48] D. Zheng, X.-Q. Yang, and D. Qu. Stability of the solid electrolyte interface on the li electrode in li–s batteries. *ACS Applied Materials & Interfaces*, 8(16):10360–10366, 2016. PMID: 27045986.

Chapter 6

An Enhanced Battery Aging Model Based on a Detailed Diffusing Mechanism in the SEI layer

Contributing Author: Amirmasoud Lanjan.

6.1 Abstract

The impetus for this study is the lack of a detailed knowledge on the formation mechanism of the solid electrolyte interface (SEI) layer and the diffusion mechanisms within this layer that impacts the predictive abilities of the current mathematical models. Specifically, most models continue to employ a constant value of diffusion coefficient

along with several lumped fitting parameters, instead of a variable formulation that is dependent on the temperature and concentration of Li-ions, to characterize Li-ion batteries (LIBs). As a result, the current models fail in predicting the capacity fading accurately. In overcoming this gap, we have employed a previously proposed temperature and concentration-dependent diffusion equation to present a modified mathematical model that is capable of accurately predicting the capacity fading and SEI growth rate as a function of temperature, concentration, and time, with just two significantly simplified temperature dependent fitting parameters. Further, these parameters need to be adjusted only for new temperatures. Our enhanced model is validated with respect to the experimental data for different operational conditions, including open circuit condition with different initial state of charges (SOCs) as well as cycling with a constant current.

6.2   Introduction

In the transportation sector, a high proportion of the emissions of greenhouse gases (GHG) ($\sim$50%) and energy consumption ($\sim$50%) are contributing significantly to environmental issues. Therefore, transport electrification is critical to address the current environmental issues, and has attracted a lot of political and social attention. This receives further impetus from the fact that a typical electric motor (EM) utilized in electric vehicles (EVs) has a significantly higher efficiency ($>$90%) than internal combustion engines (ICEs) ($<$15%). Still, one of the biggest barriers in adopting this transformation of the transport sector is the limited lifespan of Li-ion batteries (LIBs). In addition to the costs, LIBs' short lifetime will produce a lot of waste materials which is beginning to pose a new environmental problem. Therefore, extending a battery's

lifespan is critical for transport electrification and mitigating environmental issues.

The main parts of LIBs, i.e., the electrolyte, the cathode, and the anode have been well investigated in recent years [1–6]. While these studies have improved the LIBs' performance parameters (e.g., capacity, power, voltage), precise aging mechanisms are still largely unknown. Moreover, even in the recent well-engineered LIBs, over 50% of capacity loss is due to the solid electrolyte interface (SEI) layer [7–10].

The SEI layer was first observed and reported by Peled in 1979 [11]. This layer is formed through some reduction and oxidation reactions on the electrode surface. When the cathode's potential is lower and/or the anode's potential is higher than the electrolyte's oxidation and/or reduction potentials, the electrolyte molecules are oxidized and/or reduced on the electrode surface, respectively. The products of these oxidation and reduction reactions will accumulate on the surface, forming the SEI layer [7, 12]. These oxidation and reduction potentials of the electrolyte directly depend on the highest occupied molecular orbital (HOMO) and the lowest unoccupied molecular orbital (LUMO) energy level, respectively [12, 13]. It must be noted that the operating conditions of a battery, such as the loaded voltage, current and temperature, affect these potential window. The SEI formation reactions decompose the electrolyte's molecules and consume active Li-ions resulting in a capacity loss [14].

An intact and well-designed SEI layer reduces electron tunneling and electrolyte diffusion at the electrode-electrolyte interface. This further decreases the SEI formation and reduction reactions, and thereby the rate of capacity fading [7]. A typical SEI layer comprises the following: (I) An inorganic inner layer which is closer to the electrode interface and is only permeable for Li-ions. (II) An organic porous outer

layer which is closer to the electrolyte interface and that allows the transport of electrolyte solvent molecules as well as Li-ions [15, 16]. Therefore, characterizing and understanding the SEI layer transportation and formation mechanisms is the key to improving LIBs' durability [17, 18].

Since some of the SEI formation reactions occur at picosesond (ps) timescales, experimental investigations are very challenging. Therefore, multi-scale multi-physics modelling including Quantum Mechanics (QM) calculations, Molecular Dynamics (MD) simulations, and Macro-Scale mathematical modelling are often employed by researchers to understand the mechanisms at various time and length scales that cause the aging in LIBs, overcoming the constraints and limitations of the experimental methods [19–24].

Christensen and Newman [25] developed a model to estimate the rate of SEI growth and irreversible capacity loss. However, due to the lack of information on the diffusion coefficient equation in the SEI layer, they assumed a constant diffusion coefficient of $5.0 \times 10^{-14} (\frac{m^2}{s})$ for all the ions (Li^+ and PF_6^-) in every region. Thus, a lack of clarity on the diffusion mechanism in the SEI layer and the complexity of this structure results in the discrepancies between predictions from the mathematical models such as the ones by Christensen and Newman [25] and the actual aging behaviour of LIBs. This claim is further supported by the work of Deng et al. [26] who have shown that the SEI formation is a diffusion-limited phenomenon which is governed by the value of the diffusion coefficient in this layer. Liu et al. [27] developed a model indicating a spatial dependence of the SEI layer formation in LIBs. They found that in a diffusion-limited system, the thickness of the SEI layer can increase from 4 nm to 20 nm (500%) if the diffusion coefficient in the SEI layer is

doubled [27]. However, as with the other researchers [27–32], with an insufficient understanding of the diffusion mechanisms, resulting in the lack of a temperature and concentration-dependent equation for the diffusion coefficient, they used the constant value proposed by Christensen and Newman [25]. In summary, to develop a good understanding of the aging mechanisms in a LIB, we need an accurate mathematical model to estimate LIBs' lifespan that accounts for the capacity fade due to the SEI growth rate.

In 2015, Ekström and Lindbergh [33] derived a macro-scale mathematical continuum model to estimate the effect of SEI layer formation on the aging of LIBs that use a graphite anode material. The model is a combination of kinetic and transport control systems and uses a constant diffusion coefficient. In their model, the authors proposed three lumped fitting parameters which are substituted in the equations instead of variables such as a diffusion coefficient. Using these parameters improves the accuracy of the model with respect to the experimental data for a range of temperature and concentration values. However, the problem with these fitting parameters is that they need to be adjusted experimentally before we can employ the model. Further, the fitting parameters will vary with the material of the LIBs, prohibiting us from a computational exploration of new and novel materials in LIBs.

In our previous work [14], we used a combination of QM calculations and MD simulations to prescribe a temperature and Li-ion concentration-dependent equation for the diffusion coefficient for every crystal structure in the inner part of the SEI layer. Subsequently, to accurately model the physics within the SEI layer, the macro-scale mathematical model was equipped with a single equation for the diffusion coefficient. Specifically, the diffusion coefficient equation in our previous work [14] was

integrated into a popular macro-scale mathematical model (MSMM) from Ekström and Lindbergh [33] that is used in commercialized engineering software, i.e., Comsol Multiphysics, to investigate SEI growth and capacity fading. The results obtained from our proposed formulation are validated with respect to the experimental data and compared with the results obtained by using a model with constant diffusion coefficient to highlight the accuracy and impact of our new formulation. In other words, as the outcome of this work, a modified version of the Ekström and Lindbergh MSMM is proposed in which only two simplified fitting parameters are used, eliminating the most complicated parameter in the original model. Our revised formulation accounts for the effect of temperature and concentration on ageing. We use this model to study SEI growth and capacity fading as a function of time and initial SOC for a wide range of temperatures and concentrations.

6.3   The Theoretical Method and Computational Details

SEI Components

The inner section of the SEI layer is made of three main components, namely, Li_2CO_3, LiF, and Li_2O [13, 16, 34–36]. Experimental and theoretical studies indicated that Li_2CO_3 is a component in the SEI layer, produced by a reaction of $CoCO_3$ and Li-ion in presence of the ethylene carbonate (EC) [37]. Several studies [38, 39] found that the thermodynamically unstable Li_2CO_3 will reduce to Li_2O and Li_2C_2. Li_2C_2 will further decompose to Li^+, C_2H_2, and C [39]. Consequently, Li_2CO_3 cannot be considered as a permanent component in a SEI layer's inner section [37–39]. Therefore, in this work,

only LiF and Li_2O are assumed as the constant components in this part.

Diffusion Equation

Li-ion diffusion coefficient in the SEI layer (D_T) are calculated as [14]:

$$D_T = \delta_{LiF} \, D_{LiF} + \delta_{Li_2O} \, D_{Li_2O}, \tag{6.1}$$

where δ_i and D_i is the surface area fraction and diffusion coefficient of component i, respectively. Further, the diffusion coefficient of each component can be calculated as a function of temperature and concentration as:

$$D_i(C,T) = D_0 \, exp\left(\frac{-A_0 \, EB(C)}{k_b \, T}\right), \tag{6.2}$$

where D_0 and A_0 are SEI component dependent constants that are reported in Table 6.1 [14]. In the above equation, EB is the energy barrier which can be calculated as a function of concentration via:

$$EB(C_{Li^+}) = a_2 C_{Li^+}^2 + a_1 C_{Li^+}^1 + a_0, \tag{6.3}$$

where the SEI component dependent constants a_0, a_1, and a_2 are summarized in Table 6.2 [14].

Table 6.1: The constants in Equation 6.2 for the SEI components Li_2O and LiF.

	A_0	$D_0 \ [\frac{m^2}{s}]$	R^2
Li_2O	4.07×10^{-2}	1.54×10^{-10}	0.98
LiF	1.128×10^{-1}	5.10×10^{-10}	0.96

Table 6.2: The coefficients of the second-degree polynomial
$EB = a_2 C_{Li^+}^2 + a_1 C_{Li^+}^1 + a_0$ (Equation 6.3) for Li$_2$O and LiF.

	a$_0$ [eV]	a$_1$ [eV]	a$_2$ [eV]	R^2
Li$_2$O	3.9488	-8.9294	12.0460	0.96
LiF	1.9886	-2.5607	3.5237	0.93

Since it would be difficult to directly measure the fraction of the surface area of different components in the SEI layer, δ_i can be obtained as follow:

$$\omega_i = \frac{m_i}{m_{Li_2O} + m_{LiF}}, \tag{6.4}$$

$$\delta_{Li_2O} = \frac{\omega_{Li_2O}}{\omega_{Li_2O} + \frac{\rho_{Li_2O}}{\rho_{LiF}}\omega_{LiF}} \quad \text{and} \quad \delta_{LiF} = \frac{\omega_{LiF}}{\omega_{LiF} + \frac{\rho_{LiF}}{\rho_{Li_2O}}\omega_{Li_2O}}, \tag{6.5}$$

where m, L, ω and ρ, are mass, thickness, mass fraction, and density of the material i, either LiF or Li$_2$O, in the SEI layer, respectively.

A Mathematical Model for Aging

In this work, we present a modified version of the Ekström and Lindbergh [33] model. Specifically, the enhanced model uses only two simplified fitting parameters and uses a temperature and Li-ion concentration-dependent diffusion coefficient equation proposed in our previous work [14]. The resulting model uses the information on SEI growth rate more precisely to estimate the aging of the battery and helps enhance the accuracy of the model. We establish the superior performance of this enhanced model by comparing it with the original model that uses three complex fitting parameters instead of a diffusion coefficient value. Specifically, we present a zero-dimensional

model which uses a galvanostatic mode in battery cycling and therefore does not require the definition of a positive electrode or the electrolyte.

In this model, the accumulated charge (Q_{SEI} (C)), which is lost in LIBs due to the SEI formation reactions, is calculated as follows [33]:

$$\frac{dQ_{SEI}}{dt} = -I_{SEI}, \tag{6.6}$$

where I_{SEI} is the sum of the current distribution passing through the surfaces that are fully covered by the intact or cracked SEI layer. The derivation of I_{SEI}, outlined in the Appendix 6.A, yields the following expression:

$$I_{SEI} = -(1 + HK_{crd})\frac{JI_{1C}}{exp(\frac{\alpha F\eta_{SEI}}{RT}) + \frac{fJQ_{SEI}}{I_{1C}}}, \tag{6.7}$$

where I_{1C} are the currents through the cracked parts and 1 C-rate charging current, respectively. Additionally, J, H, and f are three lumped fitting parameters to compensate for the lack of knowledge regarding SEI and aging phenomena which need to be fitted for each new battery cell and/or operational condition. In the original Ekström and Lindbergh model [33], these fitting parameters are defined as:

$$J = \frac{\epsilon_{cov}I_0}{I_{1C}}, \tag{6.8}$$

$$f = \frac{\tau_{cov}VI_{1C}^2}{\epsilon_{cov}(1 - \epsilon_{cov})CDFA^2}, \tag{6.9}$$

$$H = \frac{a_{crd}}{\epsilon_{cov}}. \tag{6.10}$$

The parameters in these equations are described in the nomenclature. A detailed

description of the derivation of the equations in this model are presented in Appendix 6.A.

As mentioned earlier, the SEI layer is made of different materials and crystal structures, namely, Li_2O and LiF. Also, different particles diffuse through these crystal structures including electrolyte solvent molecules and Li-ions with different sizes and charge values. Therefore, the diffusion coefficient values would vary widely for different particles in these various structures, and will be impacted by the operating temperatures and concentrations. Due to the lack of data for the complex diffusion and reaction mechanisms, J, f, and H (Equation 6.8-6.10) are employed to increase the accuracy of the model and reduce the deviation from experimental data.

Since the accumulation of Li-ions increases the charge profile gradient in the SEI layer, it raises the electron leakage, increasing I_0. On the other hand, reducing the diffusion coefficient increases the Li-ions gradient. This clearly indicates that I_0 is inversely proportional to D_T. Consequently, I_0 can be reversely proportional to the D_T. Therefore, in this work, modifying Equation (6.8), we employed the following expression for J that uses a material constant (J_0) and D_T.:

$$J = \frac{J_0}{D_T} \tag{6.11}$$

In the above equation, D_T is the expression given in Equation (6.1). Also, J_0 is $1.49 \times 10^{-16} [\frac{m^2}{s}]$, a material constant that is dependent on the solvent molecules.

Thus, with the introduction of this equation, the first lumped fitting parameter (J) is no longer required. In other words, we have eliminated the fitting parameter J in the modified model and reduced the number of lumped fitting parameters to two.

Simplified expressions for the remaining two fitting parameters, i.e., f and H,

were developed as follows: We obtained experimental data from the literature for the following three aging conditions at two different temperatures (25°C and 45°C)[33, 40]:

1. charge/discharge cycling with 1 C-rate load current

2. open circuit at 50% SOC

3. open circuit at 100% SOC

The Ekström and Lindbergh model with the updated expression for J (Equation 6.11) was applied to these data and the model was tuned for the values of f and H to reflect the highest possible accuracy. The tuned values of these parameters are summarized in Table 6.4. Finally, with these tuned values of f and H for a temperature range of [25°C, 45°C], a linear profile of these parameters as a function of temperature was defined as follows:

$$f(T) = f_0\, T + f_1, \tag{6.12}$$

$$H(T) = H_0\, T + H_1. \tag{6.13}$$

Table 6.3: The constants in Equation 6.12.

$f_0\ [\frac{1}{K}]$	f_1	$H_0\ [\frac{1}{K}]$	H_1
-1.9×10^5	6.1×10^7	-0.14	49.5

Thus, the modified Ekström and Lindbergh model presented in this work uses simpler revised expressions for J, f and H, that collectively account for the temperature and concentration of the Li-ions.

Table 6.4: Employed parameters for the modified MSMM aging model introduced in this work.

Parameter	25°C	45°C
f	4.5×10^6	7.0×10^5
H	6.8	3.9

While this diffusion coefficient equation (Equation 6.1) employs the same formulation for all diffusing particles, contributing to the deviation from experimental results, it adequately accounts for the effects of different concentrations, temperatures and crystal structures on diffusion coefficient and SEI formation. In the ensuing section, we demonstrate that our modified model is able to predict the experimental data with high accuracy, justifying the new formulation that limits the number of fitting parameters to two.

Additionally, accounting for the capacity fade due to the loss of Li-ions during the SEI formation, the Relative capacity (RC) can be calculated as:

$$\text{RC} = \frac{Q_{batt,0} - Q_{SEI}}{Q_{batt,0}}, \tag{6.14}$$

where $Q_{batt,0}$ is the initial battery capacity. Moreover, the SEI thickness can be estimated as:

$$s = \frac{Q_{SEI}V}{(1 - \epsilon_{cov})A}. \tag{6.15}$$

In our calculations, the initial charge accumulation (Q_{SEI}) is set to zero at $t = 0$, and the initial relative capacity (RC) is 100%. All the indices and symbols used in this model are defined in the nomenclature. The relative capacity during 400

days at the three different aging conditions described earlier, each at two different temperatures (25°C and 45°C), were evaluated employing the pristine and modified Ekström and Lindbergh model presented in this work, and the results are compared with the experimental data.

6.4   Results and Discussion

We investigated capacity fading as a function of time at two different temperatures using the modified MSMM model that is equipped with a temperature and concentration-dependent diffusion equation (Equation 6.1) for D_T. As mentioned earlier, the experimental data from the three different battery aging conditions, each at two different temperatures, were used for validating the model.

The results obtained from this investigation are presented in Figure 6.1. As seen in this figure, the results from the pristine model and the modified MSMM model that use three and two lumped fitting parameters, respectively. To facilitate the comparison of the models, experimental data is also included for all the simulated conditions. The results show that both models, i.e., the pristine and the modified MSMM model, produce results that are in good agreement with the experimental data.
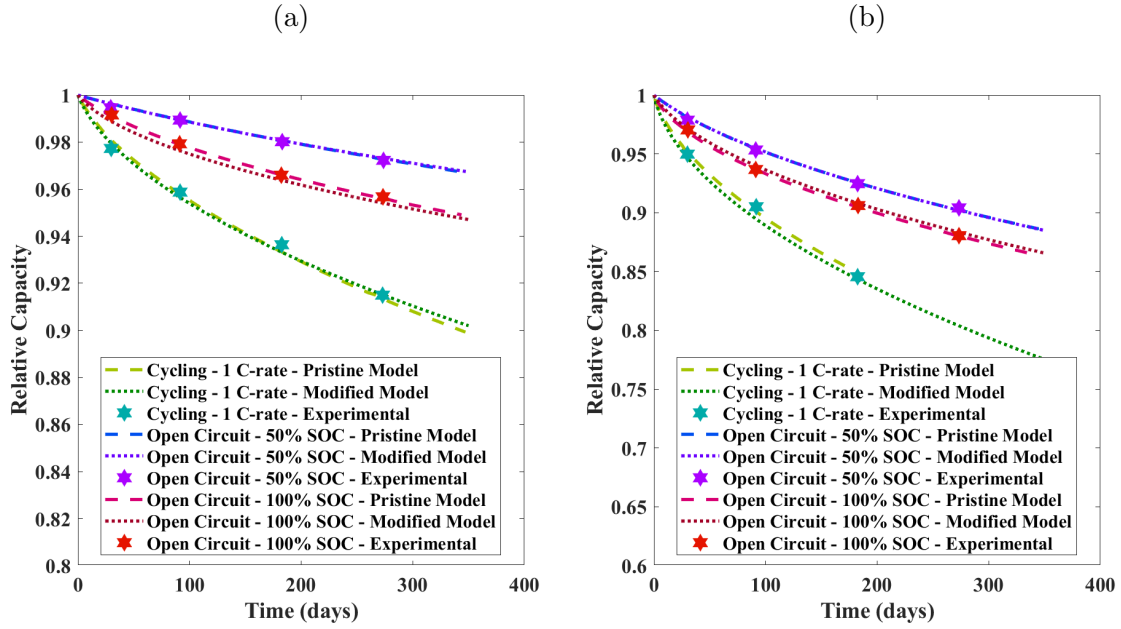
Figure 6.1: Relative capacity versus time for a duration of 350 days: Markers, dashed, and dotted lines are for the experimental data [33], pristine model and the modified model, respectively at (a) 25°C and (b) 45°C. At each temperature, the relative capacity has been obtained for open circuit condition with 50% and 100% initial capacity as well as for the cycling operation with I_{1C} (1 C-rate) current.

The R^2 for the pristine and modified MSMM model with respect to the experimental data is summarized in Table 6.5. Therefore, substituting the diffusion coefficient in Equation 6.11 and calculating the value of J directly for a specific temperature and operating condition not only reduces the number of required parameters, revealing the effects of the diffusion coefficient in the SEI layer on the capacity fading, but also increase the accuracy of the model for a wide range of SOC values.

Table 6.5: R^2 values of the estimated relative capacity using the pristine and the modified MSMM models with respect to the experimental data.

Temperature	Operational Condition	Pristine	Modified
25°C	Open Circuit - 50% SOC	0.99	0.99
25°C	Open Circuit - 100% SOC	0.99	0.97
25°C	Cycling - 1 C-rate	0.99	0.98
45°C	Open Circuit - 50% SOC	0.99	0.99
45°C	Open Circuit - 100% SOC	0.99	0.98
45°C	Cycling - 1 C-rate	0.99	0.98

As seen in Table 6.5, the accuracy of the pristine model is higher than 99% which is either equal to or marginally better than the modified model. However, the pristine model needs re-tuning of the three fitting parameters for each SOC and employing the same values of the parameters for a wide range of SOC will reduce the model's accuracy to lower than 10%. On the other hand, the modified model does not require any parameter adjustment for the entire range of SOCs (from 0% to 100%). In this model, two fitting parameters (f and H) are a function of temperature and instead of the third parameter (J), we directly employ the diffusion coefficient, collectively accounting for the impact of other variables. By employing such fixed parameters in the modified model for a variety of operating conditions, the accuracy is still as high as 98% (c.f. Table 6.5).

The relative capacity was also calculated for a wide range of initial SOC and two temperatures, and the results are shown in Figure 6.2. As seen in this figure, as the temperature increases, the capacity fading rate increases significantly. This is while the relation between SOC and capacity fading is not linear and follows a quadratic

trend in a way that the highest capacity fading occurs at the highest as well as the lowest SOC. Also, the slowest aging rate observed was at around 50% SOC. These results are in good agreement with the experimental data in the literature [40].

(a)   (b)
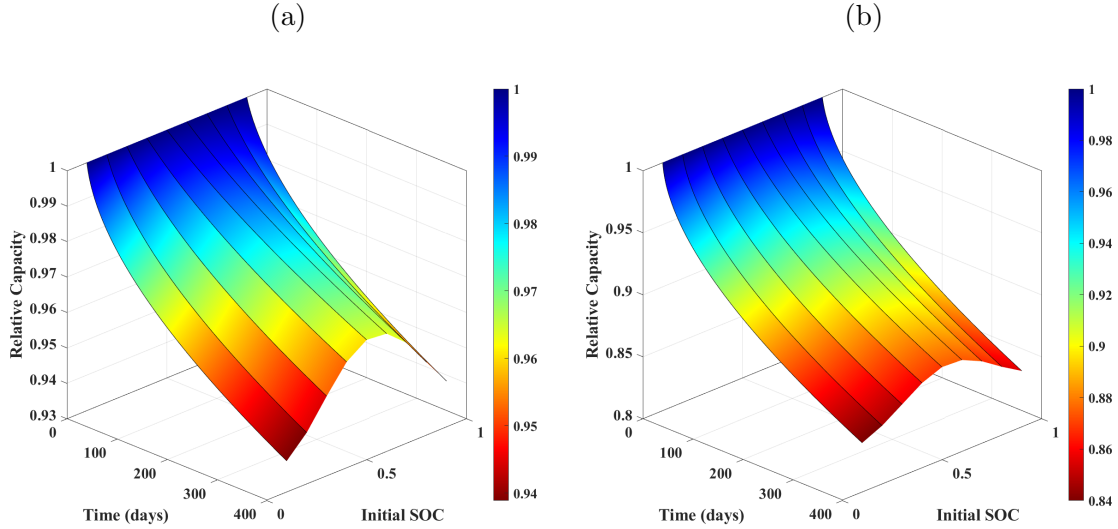
Figure 6.2: Relative capacity for different operating conditions for a duration of 350 days in (a) 25°C and (b) 45°C.

The SEI thickness as a function of time and initial SOC is shown in Figure 6.3. It is seen that the SEI growth is highly sensitive to temperature and it increases from around 11 nm to 30 nm when the temperature increases from 25°C to 45°C. Also, SEI thickness is more sensitive to the initial SOC in lower temperatures and grows from 8 nm to 11 nm as we move far from 50% initial SOC. Overall, the range of the SEI thickness and its relation with the initial SOC and temperature are in good agreement with the experimental data in the literature [40].
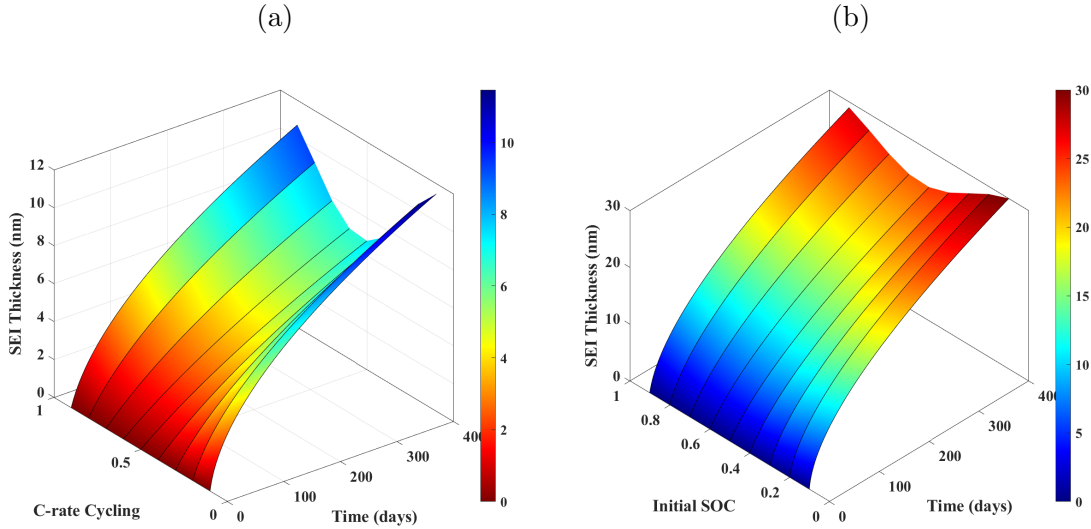
Figure 6.3: The SEI thickness for different operating conditions for a duration of 350 days in (a) 25°C and (b) 45°C.

6.5   Further Investigation

We have presented the validity of an enhanced model that uses fewer fitting parameters, with respect to experimental data from diverse operating conditions. However, in the Macro-scale simulations, we have assumed the same diffusion behaviour through the entire SEI layer for all particles. This approximation is one of the probable reasons for the deviations of the model predictions from the experimental data. On the other hand, the outer section of SEI constitutes a wide variety of components and is directly dependent on the electrolyte of LIBs. So, the diffusion equation will vary depending upon the type of electrolyte used. Hence, further investigations are required to reveal additional details on the diffusion mechanisms in the SEI layer and provide a diffusion equation which includes the effects of charge and size of different particles, and the outer section of the SEI layer, on the diffusion coefficient and SEI formation

reactions.

6.6   Conclusions

SEI formation reactions consume active Li-ions and electrolyte molecules in the LIBs, resulting in a capacity fade. Being directly dictated by the SEI growth rate, the capacity fading rate has the highest value at t = 0 and will decrease with time, and is sensitive to LIB's operating temperature. Overall, capacity fading and SEI growth rate are governed by the temperature and concentration-dependent diffusion processes inside the SEI layer.

Incorporating this into the macro-scale mathematical model, we have presented an enhanced version of the Ekström and Lindbergh [33] model using just two modified lumped fitting parameters as well as the equation of D_T (Equation 6.1) [14] which are adequately capable of predicting the decay in the relative capacity of a LIB as a function of time. This is validated with respect to the experimental data at two different temperatures during the following aging conditions: (I) charge/discharging cycling with 1 C-rate load current, (II) open circuit condition at 50% SOC, and (III) open circuit condition at 100% SOC (c.f. Figure 6.1a). Further, the enhanced model is also capable of predicting the SEI growth rate as a function of temperature and Li-ion concentration.

It must be noted that not only does the modified MSMM model have just two fitting parameters with simpler temperature dependent formulations but it can also accurately predict the capacity fading and the SEI growth rate for different operational condition and initial SOCs with fixed parameters. In other words, the fitting parameters must be evaluated only for each different operational temperature in the

modified model.

6.7 Appendix 6.A: Derivation of $\mathbf{I}_{SEI}$

The total current through a SEI layer can be written as:

$$I_{SEI} = I_{cov} + I_{crd}, \tag{6.A1}$$

where I_{cov} and I_{crd} are the currents through the covered and cracked parts, respectively.

Further, $\mathrm{I}_{cov\,(or\,crd)}$ can be written based on a first-order mass transfer restricting current through a Nernst boundary layer as:

$$I_{cov\,(or\,crd)} = \frac{I_{kin,cov\,(or\,crd)}}{1 + \frac{I_{kin,cov\,(or\,crd)}}{I_{lim.cov\,(or\,crd)}}}. \tag{6.A2}$$

In this equation, $\mathrm{I}_{kin.cov(or\;crd)}$ (A) is the kinetic current, and I_{lim} is the highest current of the SEI formation, restricted by the mass transport. These currents can be calculated as:

$$I_{kin.cov\,(or\,crd)} = -\epsilon_{cov\,(or\,crd)} I_0\,exp\left(-\frac{\alpha \eta_{SEI} F}{RT}\right), \tag{6.A3}$$

where I_0 and η_{SEI} are the exchange current and the over potential of the SEI formation reaction, respectively. All other symbols and notations are defined in the nomenclature section. Also, ϵ_{crd} and ϵ_{cov} are calculated as:

$$\epsilon_{crd} = a_{crd} K_{crd}, \tag{6.A4}$$

$$\epsilon_{cov} = 1 - \epsilon_{crd}, \tag{6.A5}$$

where K_{crd} and a_{crd} are the expansion factor and a dimensionless proportionality factor, respectively. Further, for K_{crd}, we have:

$$K_{crd} = \begin{cases} -2\frac{I_{ical}}{I_{1C}} & I_{ical} < 0 \text{ and } x < 0.3 \\[2mm] 0 & I_{ical} < 0 \text{ and } 0.3 \leq x \leq 0.7 \\[2mm] -\frac{I_{ical}}{I_{1C}} & I_{ical} < 0 \text{ and } 0.7 \leq x \\[2mm] 0 & I_{ical} \geq 0 \end{cases} \tag{6.A6}$$

The over potential of the SEI formation reaction can be calculated by setting the SEI reaction equilibrium potential ($E_{qe,SEI}$) to zero and evaluating the difference between the electrode potential (Φ_s) and electrolyte potential (Φ_l) as follows:

$$\eta_{SEI} = \Phi_s - \Phi_l - E_{qe,SEI}. \tag{6.A7}$$

It must be noted that the liquid phase potential is directly related to the intercalation reaction's equilibrium potential ($E_{qe,ical}$) and the corresponding over potential, η_{ical}, and can be expressed as:

$$\Phi_l = -(E_{qe,ical} + \eta_{ical}). \tag{6.A8}$$

By inverting the Butler-Volmer equation, the relationship between the over potential

and the intercalation current can be written as:

$$\eta_{ical} = \frac{RT}{0.5F} \operatorname{arcsinh}\left(\frac{I_{ical}}{2k_{ical}I_{1C}((1-x)x)^{0.5}}\right), \qquad (6.A9)$$

where x and I_{ical} are the SOC and intercalation current of the anode, respectively. I_{1C} is the battery's nominal 1C charge, and k_{ical} is the proportionality constant chosen to render the over potential. In the Nernst boundary layer, the limiting current density and the accumulated SEI layer thickness are inversely related:

$$I_{lim.cov\ (or\ crd)} = -\frac{\epsilon_{cov\ (or\ crd)}CD_{cov(orcord)}FA}{s}, \qquad (6.A10)$$

where C, F, and A are the concentration, Faraday's constant, and electrode surface area, respectively. $D_{cov(orcord)}$ is inversely related to the tortuosity of the layer as:

$$D_{cov(orcord)} = \frac{D_T}{\tau_{cov}}. \qquad (6.A11)$$

Finally, to minimize the error and improve the accuracy of the model, Ekström and Lindbergh [33] proposed the following three lumped fitting parameters as:

$$J = \frac{\epsilon_{cov}I_0}{I_{1C}}, \qquad (6.A12)$$

$$f = \frac{\tau_{cov}VI_{1C}^2}{\epsilon_{cov}(1-\epsilon_{cov})CDFA^2}, \qquad (6.A13)$$

$$H = \frac{a_{crd}}{\epsilon_{cov}}. \qquad (6.A14)$$

6.8   Nomenclature

Symbol	Unit	Description
a_{crd}	1	Proportionality factor
A	m^2	Electrode surface area
C	$\frac{mol}{m^3}$	Reactant concentration of SEI formation
C_{batt}	1	Relative capacity
D_i	$\frac{m^2}{s}$	Diffusion coefficient
$E_{eq,i}$	V	Equilibrium potential
f	1	Lumped fitting parameter
F	$\frac{C}{mol}$	Faraday's constant, 96485
I_0	A	Exchange current
I_{1C}	A	1C charge/discharge current, 2.3
I_{kin}	A	Kinetic current
I_{lim}	A	Limiting current
I_{load}	A	Applied current on the battery
J	1	Lumped fitting parameter
H	1	Lumped fitting parameter
$Q_{batt.0}$	C	Initial battery capacity, 2.3
Q_{neg}	C	Charge stored in the negative electrode
Q_{SEI}	C	Charge lost to SEI forming reactions
R	$\frac{J}{molK}$	Molar gas constant, 8.3145
s	m	SEI layer thickness
T	k	Temperature
V	$\frac{m^3}{C}$	Coulombic volume for forming the SEI

x	1	Stoichiometric coefficient in Li_xC_6
α	1	Transfer coefficient
ϵ_i	1	Porosity
η_i	V	Over-potential
Φ_i	V	Potential of i phase
τ_i	1	Tortuosity

Index	Description
cov	Areas covered by an microporous SEI layer
crd	Areas where the SEI layer has cracked
ical	Intercalating reaction
neg	negative electrode
SEI	SEI layer or SEI layer forming reaction
s	Solid (Electrode) phase
l	Liquid (Electrolyte) phase

Bibliography

[1] Ramavtar Tyagi, Amirmasoud Lanjan, and Seshasai Srinivasan. Co-doping strategies to improve the electrochemical properties of lixmn2o4 cathodes for li-ion batteries. *ChemElectroChem*, 9(3):e202101626, 2022.

[2] Zahra Moradi, Amirmasoud Lanjan, and Seshasai Srinivasan. Enhancement of

electrochemical properties of lithium rich li2ruo3 cathode material. *Journal of The Electrochemical Society*, 167(11):110537, 2020.

[3] Amber Mace, Senja Barthel, and Berend Smit. Automated multiscale approach to predict self-diffusion from a potential energy field. *Journal of chemical theory and computation*, 15(4):2127–2141, 2019.

[4] Niko Prasetyo, Philippe H Hunenberger, and Thomas S Hofer. Single-ion thermo-dynamics from first principles: Calculation of the absolute hydration free energy and single-electrode potential of aqueous li+ using ab initio quantum mechanical/molecular mechanical molecular dynamics simulations. *Journal of chemical theory and computation*, 14(12):6443–6459, 2018.

[5] P Ganesh, Jeongnim Kim, Changwon Park, Mina Yoon, Fernando A Reboredo, and Paul RC Kent. Binding and diffusion of lithium in graphite: quantum monte carlo benchmarks and validation of van der waals density functional methods. *Journal of Chemical Theory and Computation*, 10(12):5318–5323, 2014.

[6] Bo Wang, Shaohong L Li, and Donald G Truhlar. Modeling the partial atomic charges in inorganometallic molecules and solids and charge redistribution in lithium-ion cathodes. *Journal of chemical theory and computation*, 10(12):5640–5650, 2014.

[7] Aiping Wang, Sanket Kadam, Hong Li, Siqi Shi, and Yue Qi. Review on Modeling of the Anode Solid Electrolyte Interphase (SEI) for Lithium-Ion Batteries. *npj Computational Materials*, 4(1):1–26, mar 2018.

[8] Petr Novák, Felix Joho, Roman Imhof, Jan Christoph Panitz, and Otto Haas. In

Situ Investigation of the Interaction Between Graphite and Electrolyte Solutions. *Journal of Power Sources*, 81-82:212–216, sep 1999.

[9] A. Naji, J. Ghanbaja, B. Humbert, P. Willmann, and D. Billaud. Electroreduction of Graphite in LiClO4-Ethylene Carbonate Electrolyte. Characterization of the Passivating Layer by Transmission Electron Microscopy and Fourier-Transform Infrared Spectroscopy. *Journal of Power Sources*, 63(1):33–39, nov 1996.

[10] Rosamaría Fong, Ulrich von Sacken, and J. R. Dahn. Studies of Lithium Intercalation into Carbons Using Nonaqueous Electrochemical Cells. *Journal of The Electrochemical Society*, 137(7):2009–2013, 1990.

[11] E. Peled. The electrochemical behavior of alkali and alkaline earth metals in nonaqueous battery systems—the solid electrolyte interphase model. *Journal of The Electrochemical Society*, 126(12):2047–2051, dec 1979.

[12] Kang Xu. Nonaqueous Liquid Electrolytes for Lithium-based Rechargeable Batteries. *Chemical Reviews*, 104(10):4303–4417, oct 2004.

[13] Kang Xu. Electrolytes and Interphases in Li-Ion Batteries and Beyond. *Chemical Reviews*, 114(23):11503–11618, dec 2014.

[14] Amirmasoud Lanjan, Zahra Moradi, and Seshasai Srinivasan. Multiscale investigation of the diffusion mechanism within the solid–electrolyte interface layer: Coupling quantum mechanics, molecular dynamics, and macroscale mathematical modeling. *ACS Applied Materials & Interfaces*, 13(35):42220–42229, 2021.

[15] Arthur V. Cresce, Selena M. Russell, David R. Baker, Karen J. Gaskell, and Kang Xu. In Situ and Quantitative Characterization of Solid Electrolyte Interphases. *Nano Letters*, 14(3):1405–1412, mar 2014.

[16] Siqi Shi, Peng Lu, Zhongyi Liu, Yue Qi, Louis G. Hector, Hong Li, and Stephen J. Harris. Direct Calculation of Li-ion Transport in the Solid Electrolyte Interphase. *Journal of the American Chemical Society*, 134(37):15476–15487, sep 2012.

[17] Franz Dinkelacker, Philipp Marzak, Jeongsik Yun, Yunchang Liang, and Aliaksandr S. Bandarenka. Multistage mechanism of lithium intercalation into graphite anodes in the presence of the solid electrolyte interface. *ACS Applied Materials & Interfaces*, 10(16):14063–14069, 2018. PMID: 29539259.

[18] Dong Zheng, Xiao-Qing Yang, and Deyang Qu. Stability of the solid electrolyte interface on the li electrode in li–s batteries. *ACS Applied Materials & Interfaces*, 8(16):10360–10366, 2016. PMID: 27045986.

[19] Amirmasoud Lanjan, Behnam Ghalami Choobar, and Sepideh Amjad-Iranagh. First Principle Study on the Application of Crystalline Cathodes $Li_2Mn_{0.5}TM_{0.5}O_3$ for Promoting the Performance of Lithium-Ion Batteries. *Computational Materials Science*, 173:109417, feb 2020.

[20] Amirmasoud Lanjan, Behnam Ghalami Choobar, and Sepideh Amjad-Iranagh. Promoting Lithium-Ion Battery Performance by Application of Crystalline Cathodes $Li_xMn_{1z}Fe_zPO_4$. *Journal of Solid State Electrochemistry*, 24(1):157–171, jan 2020.

[21] Zahra Moradi, Amirmasoud Lanjan, and Seshasai Srinivasan. Multiscale investigation into the co-doping strategy on the electrochemical properties of li$_2$ruo$_3$ cathodes for li-ion batteries. *ChemElectroChem*, 8(1):112–124, 2021.

[22] Ying Shirley Meng and M. Elena Arroyo-de Dompablo. First principles computational materials design for energy storage materials in lithium ion batteries. *Energy Environ. Sci.*, 2:589–609, 2009.

[23] Diego E. Galvez-Aranda, Victor Ponce, and Jorge M. Seminario. Molecular Dynamics Simulations of the First Charge of a Li-Ion—Si-Anode Nanobattery. *Journal of Molecular Modeling*, 23(4):1–16, apr 2017.

[24] D. Grazioli, M. Magri, and A. Salvadori. Computational Modeling of Li-Ion Batteries. *Computational Mechanics 2016 58:6*, 58(6):889–909, aug 2016.

[25] John Christensen and John Newman. A Mathematical Model for the Lithium-Ion Negative Electrode Solid Electrolyte Interphase. *Proceedings - Electrochemical Society*, 20:85–94, 2003.

[26] Jie Deng, Gregory J. Wagner, and Richard P. Muller. Phase field modeling of solid electrolyte interface formation in lithium ion batteries. *Journal of The Electrochemical Society*, 160(3):A487–A496, 2013.

[27] Lin Liu, Jonghyun Park, Xianke Lin, Ann Marie Sastry, and Wei Lu. A Thermal-Electrochemical Model that Gives Spatial-Dependent Growth of Solid Electrolyte Interphase in a Li-Ion Battery. *Journal of Power Sources*, 268:482–490, 2014.

[28] Xiankun Huang, Shaoyong Ke, Haichao Lv, and Yongzhong Liu. A Dynamic

Capacity Fading Model with Thermal Evolution Considering Variable Electrode Thickness for Lithium-Ion Batteries. *Ionics*, 24(11):3439–3450, 2018.

[29] Andrew M. Colclasure, Kandler A. Smith, and Robert J. Kee. Modeling Detailed Chemistry and Transport for Solid-Electrolyte-Interface (SEI) Films in Li-Ion Batteries. *Electrochimica Acta*, 58(1):33–43, 2011.

[30] Githin K. Prasad and Christopher D. Rahn. Model based identification of aging parameters in lithium ion batteries. *Journal of Power Sources*, 232:79–85, 2013.

[31] Saksham Phul, Abhishek Deshpande, and Balaji Krishnamurthy. A Mathematical Model to Study the Effect of Potential Drop Across the SEI Layer on the Capacity Fading of a Lithium Ion Battery. *Electrochimica Acta*, 164:281–287, 2015.

[32] Birger Horstmann, Fabian Single, and Arnulf Latz. Review on multi-scale models of solid-electrolyte interphase formation. *Current Opinion in Electrochemistry*, 13:61–69, 2019.

[33] Henrik Ekström and Göran Lindbergh. A model for predicting capacity fade due to SEI formation in a commercial graphite/LiFePO4cell. *Journal of The Electrochemical Society*, 162(6):A1003–A1007, 2015.

[34] E. Peled, D. Golodnitsky, and G. Ardel. Advanced Model for Solid Electrolyte Interphase Electrodes in Liquid and Polymer Electrolytes. *Journal of The Electrochemical Society*, 144(8):L208–L210, dec 1997.

[35] Victor A. Agubra and Jeffrey W. Fergus. The formation and stability of the

solid electrolyte interface on the graphite anode. *Journal of Power Sources*, 268:153–162, 2014.

[36] D. Aurbach, B. Markovsky, M. D. Levi, E. Levi, A. Schechter, M. Moshkovich, and Y. Cohen. New Insights into the Interactions Between Electrode Materials and Electrolyte Solutions for Advanced Nonaqueous Batteries. *Journal of Power Sources*, 81-82:95–111, sep 1999.

[37] Kevin Leung, Fernando Soto, Kie Hankins, Perla B. Balbuena, and Katharine L. Harrison. Stability of Solid Electrolyte Interphase Components on Lithium Metal and Reactive Anode Material Surfaces. *Journal of Physical Chemistry C*, 120(12):6302–6313, mar 2016.

[38] Na Tian, Chunxiu Hua, Zhaoxiang Wang, and Liquan Chen. Reversible reduction of li_2co_3. *J. Mater. Chem. A*, 3:14173–14177, 2015.

[39] Eric J. McShane, Andrew M. Colclasure, David E. Brown, Zachary M. Konz, Kandler Smith, and Bryan D. McCloskey. Quantification of inactive lithium and solid–electrolyte interphase species on graphite electrodes after fast charging. *ACS Energy Letters*, 5(6):2045–2051, 2020.

[40] M Safari and C Delacourt. Aging of a commercial graphite/lifepo4 cell. *Journal of The Electrochemical Society*, 158(10):A1123, 2011.

Chapter 7

Summary, Conclusions, and Future Investigation

The main objective of this dissertation was to study the ageing issue in battery cells for the electric vehicle industry. This was accomplished in three stages:

7.1 Stage 1: Development and Validation of a Computational Framework

MD simulations are an increasingly popular computational method for investigating the behaviour of molecular systems, especially in the areas of nanotechnology and biomedical sciences. However, the success of an MD simulation relies heavily on the accuracy of the potential parameters used in the simulation. These potential parameters determine the interactions between atoms and molecules in the system, and inaccurate parameters can lead to incorrect predictions of the system's behaviour.

The traditional approach is to determining potential parameters for a given system via experimental measurements. However, this approach is too time-consuming and expensive, especially for novel materials and compounds. In recent years, computational methods have emerged as an alternative means of determining potential parameters, with the advantage of being faster and cheaper.

In a preliminary study, a suite of algorithms closely coupled with QM calculations was introduced to accurately determine the required potential parameters for any molecular configuration and thereby any material systems. These algorithms help obtain the potential parameters for the nonbonded, bonded, angle, dihedral, and improper interactions. However, due to the complexity of nonbonded interactions, the accuracy of the results obtained using this suite of algorithms was limited. To address this limitation, a new coordinate generator algorithm and a combination of neuro-computing techniques and QM calculations have been proposed in this thesis to enhance the accuracy of the potential parameters. The enhanced suite of algorithms has been successfully applied to simulate five different molecular systems, demonstrating its excellent accuracy in predicting nonbonded interaction-related phenomena such as phase transitions.

This novel computational framework presents a unique approach in the field of MD simulations, allowing researchers to design and develop novel materials for next-generation applications by integrating this new approach with MD simulations to study molecular and nanoscale systems and phenomena. The enhanced accuracy of the proposed suite of algorithms opens up new possibilities for investigating elusive nano-scale phenomena that occur at very rapid time scales. In conclusion, the development of this enhanced suite of algorithms for determining potential parameters

represents a significant advancement in the field of MD simulations, and its potential applications are vast. By providing accurate and reliable potential parameters, this approach will help researchers gain a better understanding of the behaviour of molecular systems and design novel materials with specific properties for various applications.

Finally, the computational framework has been successfully validated for various molecule types with respect to the experimental data of established materials such as H_2O (a polar molecule), $LiPF_6$ (an ionic compound), C_2H_5OH (ethanol), C_8H_{18} (a long chain molecule), and Ethylene Carbonate (EC) (a complex molecular system). The obtained results have an accuracy of over 90%.

7.2   Stage 2: Study the SEI Layer formation and Characterisation

In this stage, a comprehensive investigation into the diffusion properties and crystal structures of the SEI layer in lithium-ion batteries (LIBs) using a combination of quantum mechanics, molecular dynamics, and macro-scale mathematical modelling has been undertaken in this thesis.

The results reveal that the energy barrier (EB) for diffusion in the inner section of the SEI layer has a quadratic relationship with the concentration of excess Li-ion concentration ($CeLi$). Specifically, the EB is high for very low and very high $CeLi$, leading to lower efficiency, waste voltage, and electron leakage. Additionally, the diffusion coefficient of Li^+ (DLi^+) is more sensitive to temperature at very low and very high excess Li-ion concentrations. The diffusion coefficient for different $CeLi$

values is evaluated using molecular dynamics simulations and combined with the EB values to derive an Arrhenius formulation.

Furthermore, the macro-scale mathematical model shows that ignoring the SEI layer in LIB calculations results in a significant reduction in accuracy, especially under high-current conditions and/or for aged cells with a thicker SEI layer. In contrast, the enhanced model presented in this work results in higher accuracy, indicating the vital effects of the SEI layer on internal resistance and ageing in LIBs.

Overall, this stage modelled the diffusion mechanisms in the SEI layer and presents a unified diffusion coefficient equation as a function of temperature and concentration, and highlights the importance of considering the SEI layer in LIB calculations to accurately predict performance and ageing.

7.3 Stage 3: Employing SEI Characteristics for Developing New Mathematical Models

After characterizing the SEI layer using the introduced computational framework, an enhanced mathematical model was developed in this stage to forecast operating voltage versus SOC for a battery under different discharging currents, namely 0.2, 1.0, 10.0, 20.0, and 60.0 C-rates. The obtained data from the enhanced model and conventional models in the literature were compared with experimental data. The experimental data were obtained from a new battery cell which had a thin SEI layer with a thickness of 20 nm and was not significantly aged. Hence, the effect of it SEI layer on the Li-ion concentration gradient on the anode surface was negligible under low current density.

The results showed that the accuracy of the enhanced and pristine models was almost the same and equal to 99% for discharging currents of 0.2 and 1.0 C-rates, respectively. However, as the applied current increased to 10.0 C and then to 20.0 C, the deviation of the pristine model increased to 8% and 13%, respectively. Furthermore, the pristine model's deviation in modelling the operating voltage under a 60.0 C applied current exceeded 70%, which is not acceptable for any practical application. On the other hand, the enhanced model, which considers the SEI layer and its effect on the internal resistance, maintained an accuracy higher than 90% even under a 60.0 C applied current. These results demonstrate the crucial impact of the SEI layer on the internal resistance and ageing in LIBs and the importance of including its effects in the calculations, especially under high-current conditions and for aged cells with a thicker SEI layer.

The formation of SEI reactions in LIBs consumes active Li-ions and electrolyte molecules, resulting in a reduction in capacity. This capacity fade is primarily determined by the SEI growth rate, which is highest at t = 0 and decreases over time and is sensitive to the operating temperature of the battery. The diffusion processes inside the SEI layer, which are dependent on temperature and concentration, govern both capacity fading and SEI growth rate. After characterizing the SEI layer in the previous stage, we employed the diffusion mechanisms to develop an improved version of the Ekström and Lindbergh ageing model by incorporating the diffusion processes and using just two modified lumped fitting parameters and the equation of D_T (Equation 4.4). This model can accurately predict the decay in the relative capacity of a LIB as a function of time. This has been validated using experimental data obtained under various aging conditions, including charge/discharge cycling with a 1

C-rate load current and open circuit conditions at 50% and 100% SOC, as shown in Figure 6.1. Furthermore, the enhanced model can predict the SEI growth rate as a function of temperature and Li-ion concentration. Importantly, the modified MSMM model uses only two fitting parameters, with simpler temperature-dependent formulations, and can accurately predict capacity fading and SEI growth rate for different operational conditions and initial SOCs with fixed parameters.

7.4   Future Investigation

In this work, a computational multi-scale framework has been developed to combine Quantum Mechanics (QM), Molecular Dynamics (MD), and Artificial Intelligence (AI) to study and characterize novel materials/phenomena. This framework has been employed to thoroughly investigate the solid electrolyte interface (SEI) layer and battery ageing in Li-Ion Batteries (LIBs). The presented framework can be used to investigate next-gen solid-state batteries.

Reliance solely on high-voltage improved cathode materials to boost the energy density and durability of LIBs is not a viable solution due to the instability of the liquid electrolyte and separator at high voltages [1]. Moreover, the liquid electrolyte along with other additives are flammable and volatile which would compromise the safety of the battery [2, 3]. An effective alternative to achieve a higher energy density and safety rating is to replace the flammable liquid electrolytes with high-performance solid-state electrolytes (SE) which can overcome most issues of LIBs. Most of the SEs exhibit high thermal stability even at temperatures over 200°C [4]. On the other hand, some liquid electrolytes evaporate at temperatures higher than 70°C, creating safety issues. Additionally, SEs have no leakage and have a wider electrochemical

window compared to the liquid electrolytes. The latter have a lower electrochemical window (under 4.5 V) [5–7]. Furthermore, issues such as capacity fading and internal short circuits can be suppressed with the rigid structure of SEs [8]. With respect to charge transference, SEs have considerably high ionic conduction as well as low electronic conductivity. High ionic conductivity of 10^{-2} $\frac{S}{cm}$ [9, 10] has enabled fast-charging in SEs [8], and in general, there is ample scope to develop novel battery chemistries [11, 12].

While there are distinct advantages of SEs, there are still some challenges that impede the practical application of SEs. For instance, current solid-state batteries (SSBs) usually show insufficient cycling performance because of material degradation of anodes, cathodes, and electrolytes. Longer durability and stability are critical for the applicability of SSBs, and in fact, the United States Council for Automotive Researches has set a battery life target of 10 years lifetime for 1000 cycles with an 80% depth of discharge [13, 14]. The major shortcomings stem from failures in the interfaces via various mechanisms at the interfaces [8]. For instance, the poor wetability of the cathode-electrolyte interface and formation of the space-charge layer are related to slow interfacial kinetics and high impedance [6, 15]. Dendrite growth, an unwanted phenomenon, results in short-circuiting, and this not only negatively impacts the lifetime of SSBs but is also a safety issue [16, 17]. Thus, the commercialization of high-energy-density SSBs requires several enhancements. For example, for fast-charging SSBs, power density is very important. Introducing SEs with high ionic conductivity characteristics requires investigation into the ion transport at interfaces and interface modification [14].

Recent articles have extensively debated the issues related to LIBs ranging from

experimental studies [18] to computational studies [19]. In SSB-related articles, most of the investigations have focused on either introducing a variety of solid-state electrolytes [20–24] or discussing one or more issues that must be addressed. For example, Kerman et al. [25] underlined the kinetic limitations of processes at interfaces and outlined the main challenges in processing SSBs. Lim et al. [8] highlighted the types of interfaces and the problems related to the contact point. The review article by Kim et al. [4] focused on dendrite formation and degradation of cathode materials containing lithium. Manthiram et al. [11] discussed the main mechanisms and challenges of SSBs.

While these studies are valuable resources for research areas in SSBs, most of the SSBs' challenges originate from a combination of several parameters/factors that operate simultaneously at various time and length scales. The lack of comprehensive knowledge that covers the entire gamut of multi-scale phenomena and their impact on the operation of a battery indicates the necessity of not only highlighting the major difficulties faced by these types of batteries but also showcasing our frameworks and algorithms that can be utilized to study these challenges, serving as the foundation for future multi-scale research in this field. For instance:

This framework can be employed to calculate Nudged Elastic Band (NEB). NEB is one of the most promising methods for predicting the activation energy of a physical or chemical process. The lowest possible energy path for a physical or chemical reaction can be achieved by employing the NEB method. Utilizing SEs in the batteries as one of the most promising solutions for suppressing Li-dendrite growth, significantly impacts the diffusion of Li-ions in the separator section. SEs with low diffusion coefficients raise the diffusion polarization in the SSBs and consequently the internal

resistance increases. As a result, there is a decline in the cycling efficiency. Therefore, one of the most important characterizations which should be investigated in a new SEs is the diffusion mechanisms in it. Subsequently, different diffusion pathways in this crystal structure can be studied using the NEB method. Moreover, the NEB technique can be used to evaluate temperature dependency of the diffusion by obtaining the energy barrier and Arrhenius equation as follows [26]:

$$D = D_0 \times \exp(-\frac{EB}{RT}), \tag{7.1}$$

where D and EB are the diffusion coefficient and energy barrier against diffusion, respectively. D_0 is a coefficient of the equation. Also, R and T are the Gas constant and Temperature, respectively.

Also, this framework can be used to study the atomic- or molecular- properties of the systems. The activation energy (energy barrier) in Equation 7.1 can *only* be calculated by QM calculations with NEB analysis. However, the other parameter, D_0 is evaluated by a linear regression using the following relation:

$$Ln(D) = Ln(D_0) - \frac{EB}{RT}. \tag{7.2}$$

For a linear regression, some D in a range of T along with their corresponding EB points are required. The diffusion coefficient (D) values can be obtained using the MD simulation and the Mean Square Displacement (MSD) analysis as follows:

$$MSD = \frac{1}{N}(\sum_{i=1}^{N} |r_i(t) - r_i(0)|^2), \tag{7.3}$$

where $r_i(t)$ represents the position of particle i at time t and N is the total number

of particles in the system. More precisely, calculating the MSD values of the particle type j (MSD_j), the diffusion coefficient of this particle type (D_j) can be calculated as:

$$D_j = \frac{1}{2 \times \text{(Dimension No.)}} \lim_{t \to \infty} \frac{1}{t} MSD_j. \tag{7.4}$$

Many other SE properties such as lattice parameters, Intrinsic Defects, Elastic Modules, Density of State, and ion conductivity can be obtained by employing this framework on next-gen solid-state batteries.

Bibliography

[1] Liping Yue, Jun Ma, Jianjun Zhang, Jingwen Zhao, Shanmu Dong, Zhihong Liu, Guanglei Cui, and Liquan Chen. All solid-state polymer electrolytes for high-performance lithium ion batteries. *Energy Storage Materials*, 5:139–164, 2016.

[2] Miguel A. González, Oleg Borodin, Maiko Kofu, Kaoru Shibata, Takeshi Yamada, Osamu Yamamuro, Kang Xu, David L. Price, and Marie-Louise Saboungi. Nanoscale relaxation in "water-in-salt" and "water-in-bisalt" electrolytes. *The Journal of Physical Chemistry Letters*, 11(17):7279–7284, 2020. PMID: 32787289.

[3] Kang Xu. Electrolytes and interphases in li-ion batteries and beyond. *Chemical Reviews*, 114(23):11503–11618, 2014. PMID: 25351820.

[4] Joo Gon Kim, Byungrak Son, Santanu Mukherjee, Nicholas Schuppert, Alex Bates, Osung Kwon, Moon Jong Choi, Hyun Yeol Chung, and Sam Park. A

review of lithium and non-lithium based solid state batteries. *Journal of Power Sources*, 282:299–322, 2015.

[5] Long Zhang, Kun Yang, Jianli Mi, Lei Lu, Linran Zhao, Limin Wang, Yueming Li, and Hong Zeng. Na3pse4: A novel chalcogenide solid electrolyte with high ionic conductivity. *Advanced Energy Materials*, 5(24):1501294, 2015.

[6] Kun Kelvin Fu, Yunhui Gong, Boyang Liu, Yizhou Zhu, Shaomao Xu, Yonggang Yao, Wei Luo, Chengwei Wang, Steven D Lacey, Jiaqi Dai, et al. Toward garnet electrolyte–based li metal batteries: An ultrathin, highly effective, artificial solid-state electrolyte/metallic li interface. *Science Advances*, 3(4):e1601659, 2017.

[7] Philippe Knauth. Inorganic solid li ion conductors: An overview. *Solid State Ionics*, 180(14-16):911–916, 2009.

[8] Hee-Dae Lim, Jae-Ho Park, Hyeon-Ji Shin, Jiwon Jeong, Jun Tae Kim, Kyung-Wan Nam, Hun-Gi Jung, and Kyung Yoon Chung. A review of challenges and issues concerning interfaces for all-solid-state batteries. *Energy Storage Materials*, 25:224–250, 2020.

[9] Fudong Han, Yizhou Zhu, Xingfeng He, Yifei Mo, and Chunsheng Wang. Electrochemical stability of li10gep2s12 and li7la3zr2o12 solid electrolytes. *Advanced Energy Materials*, 6(8):1501590, 2016.

[10] Sebastian Wenzel, Simon Randau, Thomas Leichtweiß, Dominik A Weber, Joachim Sann, Wolfgang G Zeier, and Jürgen Janek. Direct observation of the interfacial instability of the fast ionic conductor li10gep2s12 at the lithium metal anode. *Chemistry of Materials*, 28(7):2400–2407, 2016.

[11] A. Manthiram, X. Yu, and S. Wang. Lithium battery chemistries enabled by solid-state electrolytes. *nature reviews materials*, 2(2):16103, 2017.

[12] John B. Goodenough and Kyu-Sung Park. The li-ion rechargeable battery: A perspective. *Journal of the American Chemical Society*, 135(4):1167–1176, 2013. PMID: 23294028.

[13] Amin Mahmoudzadeh Andwari, Apostolos Pesiridis, Srithar Rajoo, Ricardo Martinez-Botas, and Vahid Esfahanian. A review of battery electric vehicle technology and readiness levels. *Renewable and Sustainable Energy Reviews*, 78:414–430, 2017.

[14] Jun Ma, Bingbing Chen, Longlong Wang, and Guanglei Cui. Progress and prospect on failure mechanisms of solid-state lithium batteries. *Journal of Power Sources*, 392:94–115, 2018.

[15] Lin Xu, Shun Tang, Yu Cheng, Kangyan Wang, Jiyuan Liang, Cui Liu, Yuan-Cheng Cao, Feng Wei, and Liqiang Mai. Interfaces in solid-state lithium batteries. *Joule*, 2(10):1991–2015, 2018.

[16] Lukas Porz, Tushar Swamy, Brian W Sheldon, Daniel Rettenwander, Till Frömling, Henry L Thaman, Stefan Berendts, Reinhard Uecker, W Craig Carter, and Yet-Ming Chiang. Mechanism of lithium metal penetration through inorganic solid electrolytes. *Advanced Energy Materials*, 7(20):1701003, 2017.

[17] Asma Sharafi, Harry M Meyer, Jagjit Nanda, Jeff Wolfenstine, and Jeff Sakamoto. Characterizing the li–li7la3zr2o12 interface stability and kinetics as a

function of temperature and current density. *Journal of Power Sources*, 302:135–139, 2016.

[18] Ximing Cheng and Michael Pecht. In situ stress measurement techniques on li-ion battery electrodes: A review. *Energies*, 10(5):591, 2017.

[19] Ying Zhao, Peter Stein, Yang Bai, Mamun Al-Siraj, Yangyiwei Yang, and Bai-Xiang Xu. A review on modeling of electro-chemo-mechanics in lithium-ion batteries. *Journal of Power Sources*, 413:259–283, 2019.

[20] Xiaoyan Liu, Xinru Li, Hexing Li, and Hao Bin Wu. Recent progress of hybrid solid-state electrolytes for lithium batteries. *Chemistry–A European Journal*, 24(69):18293–18306, 2018.

[21] Lu Han, Michelle L Lehmann, Jiadeng Zhu, Tianyi Liu, Zhengping Zhou, Xiaomin Tang, Chien-Te Heish, Alexei P Sokolov, Pengfei Cao, Xi Chelsea Chen, et al. Recent developments and challenges in hybrid solid electrolytes for lithium-ion batteries. *Frontiers in Energy Research*, 8:202, 2020.

[22] RC Agrawal and GP Pandey. Solid polymer electrolytes: materials designing and all-solid-state battery applications: an overview. *Journal of Physics D: Applied Physics*, 41(22):223001, 2008.

[23] Xiaoqi Zhu, Kai Wang, Yanan Xu, Gefei Zhang, Shengqiang Li, Chen Li, Xiong Zhang, Xianzhong Sun, Xingbo Ge, and Yanwei Ma. Strategies to boost ionic conductivity and interface compatibility of inorganic-organic solid composite electrolytes. *Energy Storage Materials*, 2021.

[24] Yoon Seok Jung, Dae Yang Oh, Young Jin Nam, and Kern Ho Park. Issues and challenges for bulk-type all-solid-state rechargeable lithium batteries using sulfide solid electrolytes. *Israel Journal of Chemistry*, 55(5):472–485, 2015.

[25] Kian Kerman, Alan Luntz, Venkatasubramanian Viswanathan, Yet-Ming Chiang, and Zhebo Chen. practical challenges hindering the development of solid state li ion batteries. *Journal of The Electrochemical Society*, 164(7):A1731, 2017.

[26] Amirmasoud Lanjan, Zahra Moradi, and Seshasai Srinivasan. Multiscale investigation of the diffusion mechanism within the solid–electrolyte interface layer: Coupling quantum mechanics, molecular dynamics, and macroscale mathematical modeling. *ACS Applied Materials & Interfaces*, 13(35):42220–42229, 2021. PMID: 34436850.

Appendix A

Supporting Information of Chapter 2

A.1 Pseudo Code of the Algorithms

Algorithm A1 Nonbonded

```
0: Start
0: Create a list of different atom types present in the system
0: Define the list of different distances value between two atoms as:
   [0.05, 1.0] (in steps of 0.05) and [1.0-3.5] (in steps of 0.5)
0: for p_i in the list of elements do
0:   for D_j in the list of distances do
0:     Set the distance between two atoms equal to D_j
0:     Set the system's charge based on the atom types
0:     Run QM simulation to evaluate the total system energy, E_j
0:     r_j = D_j × √3
0:     Store the pair of (E_j, r_j)
0:     Fit the nonbonded force field equation on the (E,D) data
0:     Save the parameters
0:   end for
0: end for
0: Use mixing rules defined in Equations 2.2-2.4 to obtain the
   potential parameters between dissimilar atom types
0: Finish =0
```

Algorithm A2 Bonded

```
0: Start
0: Create a "Bond-Type" list that contains the different bond types
   in the molecular system
0: Create a "Length" list:  [-0.6, 0.6] (in steps of 0.05), to vary
   the bond length
0: Create a "Bond" list that contains the pairs of atoms for each
   bond in the system
```

0: for $(n_1, n_2)_i$ Bond in "Bond-Type" list do

0:   Create a "Moving Atoms" list containing all atoms except the
     group that should be kept fix

0:   Define a mover vector from atom n_1 to n_2, named $\vec{MV}$

0:   for C_l in "Length" list. do

0:     $\vec{MV}_l$ is equal to C_l percent of $\vec{MV}$

0:     Move all atoms in the "Moving Atoms" list by $\vec{MV}_l$ vector

0:     Run the QM Simulation to evaluate total system energy (E_l) at
       Bonded length (l_l)

0:     Store the pair of (E_l, r_l)

0:   end for

0:   Fit an appropriate bonded interaction force field equation to
     the (E, r) data to evaluate the potential parameters of ith
     Bond type

0: end for

0: Finish =0

Algorithm A3 Angle

```
0: Start
0: Create the "Angle-Type" list for the different angle types that
   exist in the system
0: Define a "Rotation" list containing different rotation angle
   values in the range [-15, 15]
```
0: for $(n_1, n_2, n_3)_i$ in "Angle-Type" list do
0:     Determine the two leg vectors $\vec{V_1}$ and $\vec{V_2}$
0:     Calculate the cross product of the leg vectors
0:     θ_P is the primary angel
0:     for θ_j in "Rotation" list do
0:         Rotate the leg vectors about $\vec{V_r}$ based on the θ_j value
0:         Evaluate new system energy (E_j), employing QM calculations
0:         Store $(E_j,\ \theta_j + \theta_P)$
0:     end for
0:     Fit an appropriate angle interaction equation to the (E, θ)
       data
0: end for
0: Finish =0

Algorithm A4 Rotator

0: Start
0: Input $\vec{V}$, θ, and $\vec{V_r}$
0: Create a unite vector from $\vec{V_r}$
0: Define the rotational matrix $\vec{R} =$ as per Equation 2.5
0: Return $\vec{V}_{new} = \vec{V} \cdot \vec{R}$
0: Finish =0

Algorithm A5 Angle Finder

0: Start
0: Input the positions of the four atoms (n_1, n_2, n_3, and n_4)
   participating in the dihedral
0: Find a plane equation which is perpendicular to the bond between n_2
   and n_3
0: Find the equation of two lines passing n_1 and n_4 and perpendicular
   to the plane
0: Find incident points of these lines on the plane
0: Calculate the angle created by these three points as the Dihedral
   angle
0: Finish =0

Algorithm A6 Dihedral

```
0: Start
0: Create a "Dihedral-Type" list containing different dihedral types
   that exist in the system
0: Define a "Rotation Angel" list of different rotation angle values
   in the range [-15, 15]
0: for (n₁, n₂, n₃, n₄)ᵢ in "Dihedral-Type" list do
0:    Calculate the primarily dihedral's angle (φₚ)
0:    Define the two leg vectors of the dihedral
0:    Define the normal vector of the plane perpendicular to the bond
      between n₂ and n₃
0:    for φⱼ in "Rotation Angel" list do
0:       Rotate the leg vectors equal to φⱼ
0:       Evaluate new system energy (Eⱼ), employing QM calculations
0:       Store (Eⱼ, φⱼ + φₚ)
0:    end for
0:    Fit and appropriate Dihedral interaction equation to the (E, φ)
      data
0: end for
0: Finish =0
```

Algorithm A7 Improper

```
0: Start
0: Create the "Improper-Type" list containing the different improper
   types that exist in the system
0: Define the "Rotation Angle" list containing the different rotation
   angle values in the range [-15, 15]
0: for (n₁, n₂, n₃, n₄)ᵢ in "Improper-Type" list do
0:    Find the two planes containing n₁, n₂, n₃ and n₂, n₃, n₄
0:    Find the primarily improper angle as χₚ
0:    for χⱼ in "Rotation Angle" list do
0:       Rotate the two planes equal to χⱼ
0:       Evaluate new system energy (Eⱼ), employing QM calculations
0:       Store (Eⱼ, χⱼ + χₚ)
0:    end for
0:    Fit an appropriate Improper interaction force field equation to
      the (E, χ) data
0: end for
0: Finish =0
```

A.2   Potential Energy Figures

(a) H_2O

(b) $LiPF_6$

(c) EC
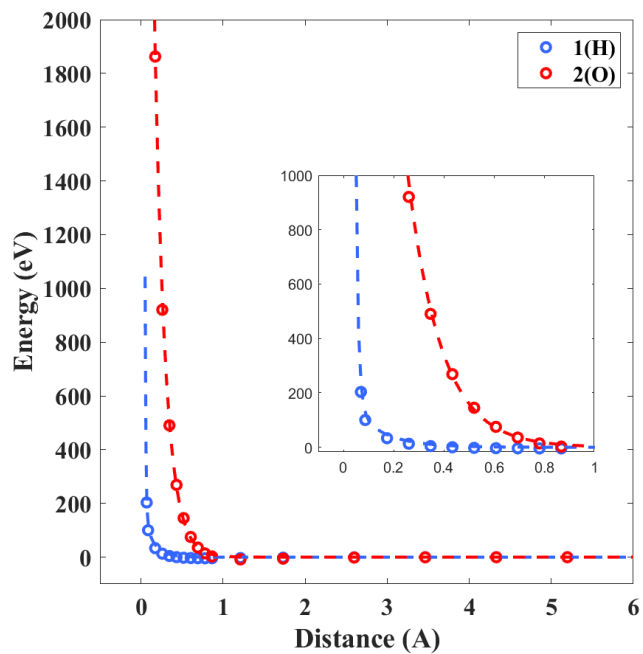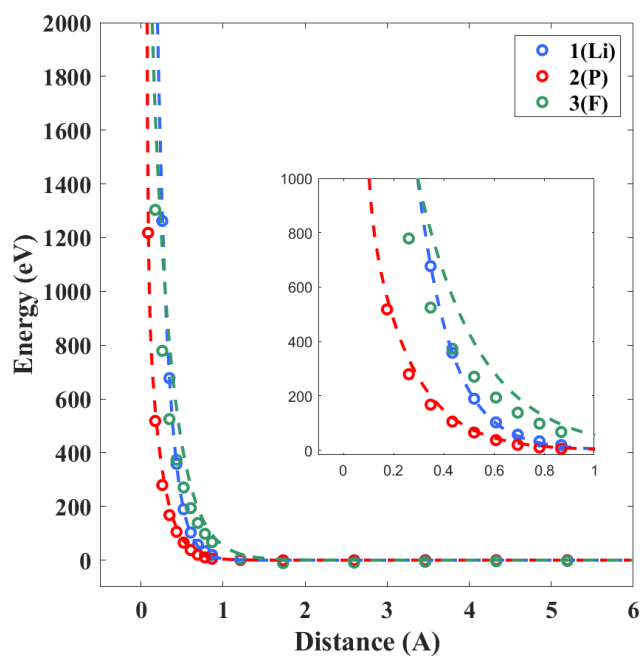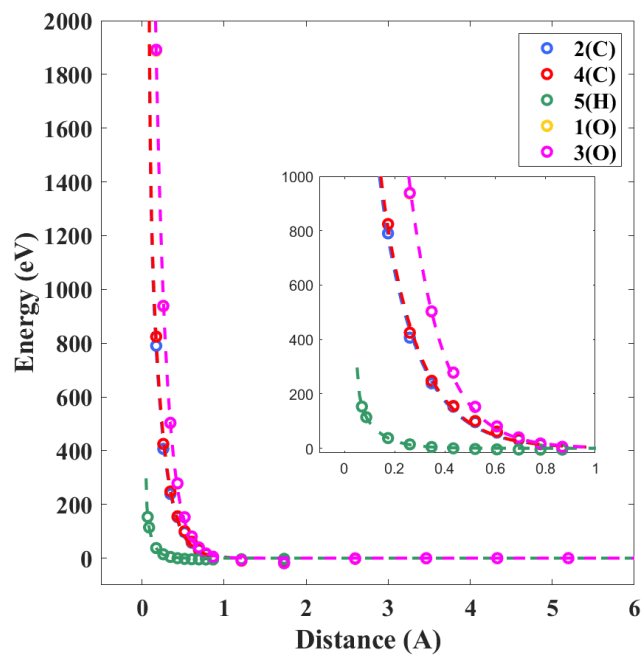
(d) Ethanol
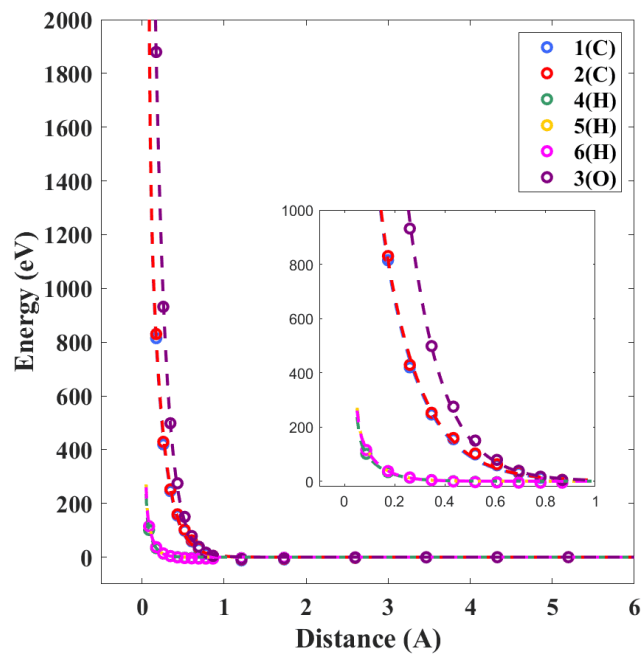
(e) Octane
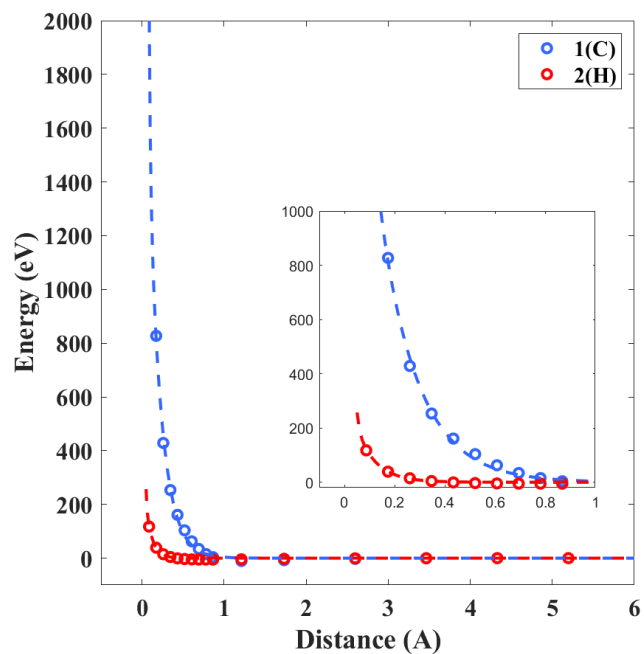
Figure A1: Data of nonbonded interactions energy as a function of the distance between two atoms of each type using a combination of our algorithms and QM calculation (indicated by symbols). The Buckingham potential equation $(E = Aexp(-\frac{r}{B}) - \frac{C}{r^6})$ (indicated by the dashed lines) has been fitted to this data.

(a) H_2O

(b) $LiPF_6$

(c) EC

(d) Ethanol
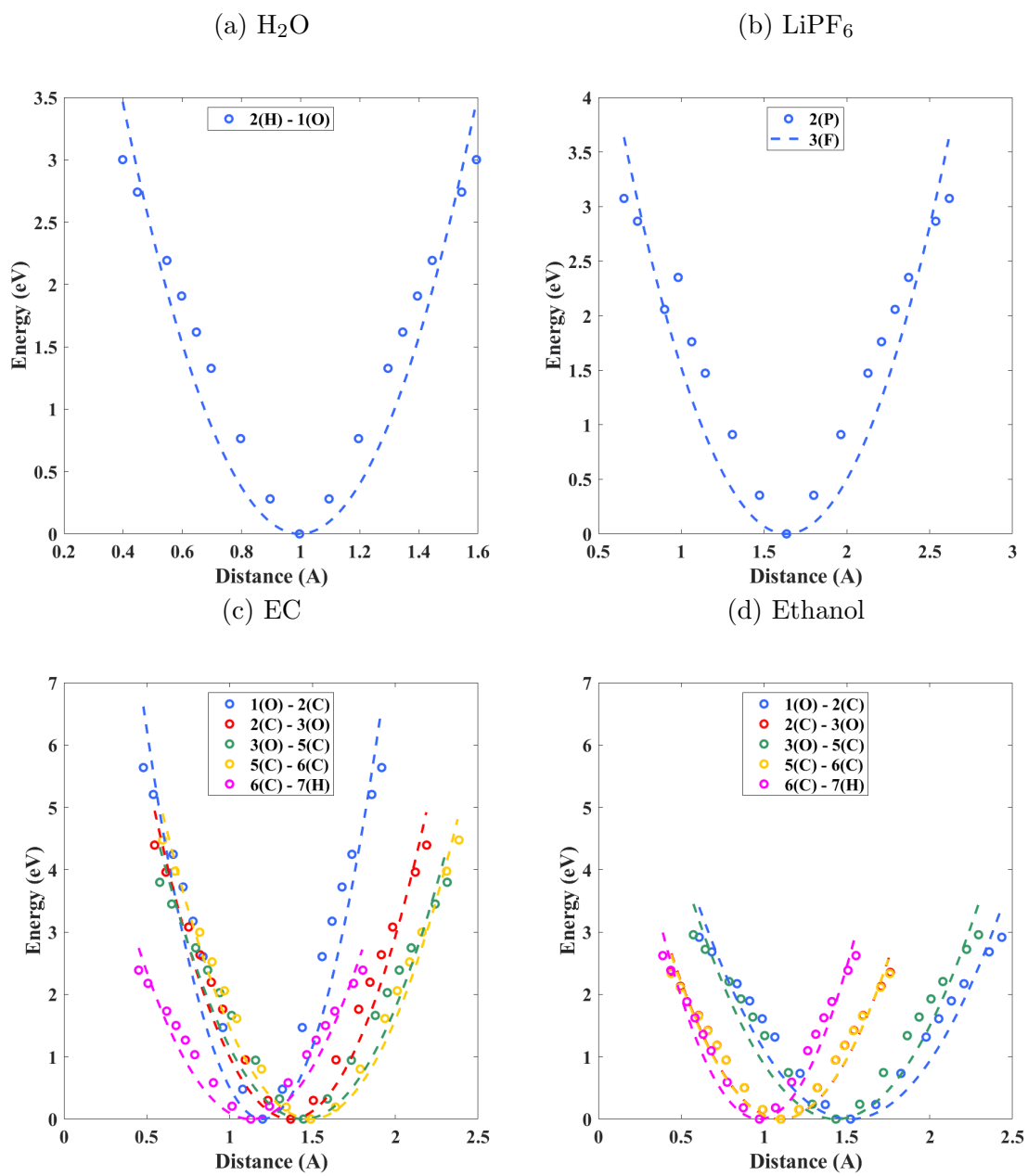
(e) Octane
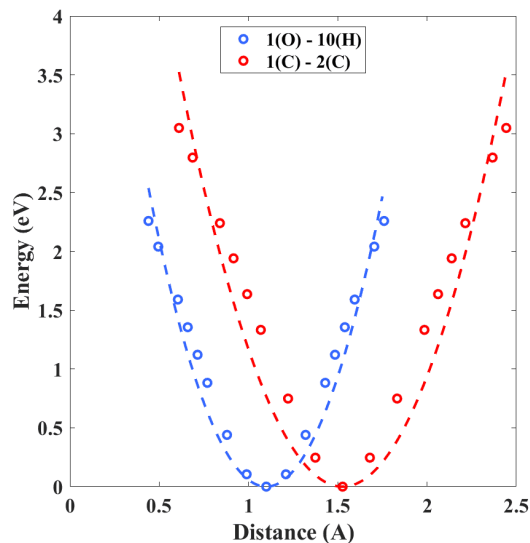
Figure A2: Estimated bonded interaction energy as a function of the bond length for different bond types in the three molecules. The Harmonic Bonded interaction equation (Table 2.2) has been fitted on the obtained data points.

(a) H_2O (b) $LiPF_6$

(c) EC

(d) Ethanol

(e) Octane
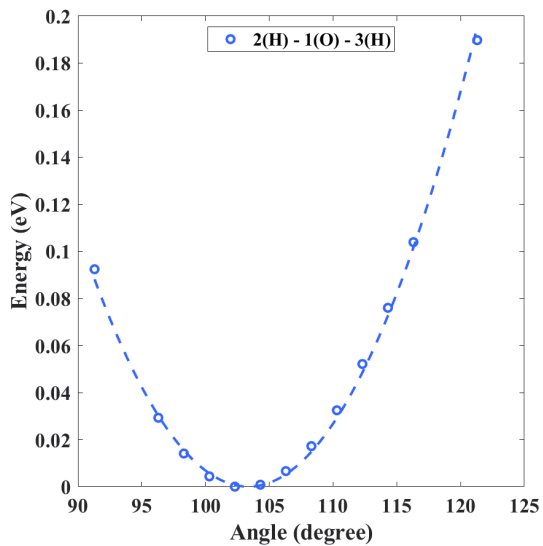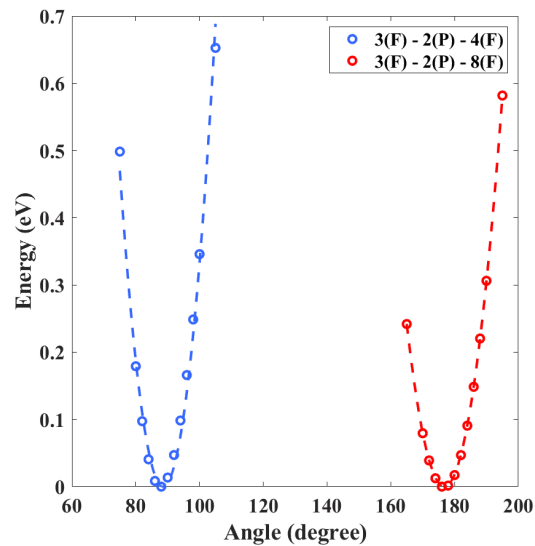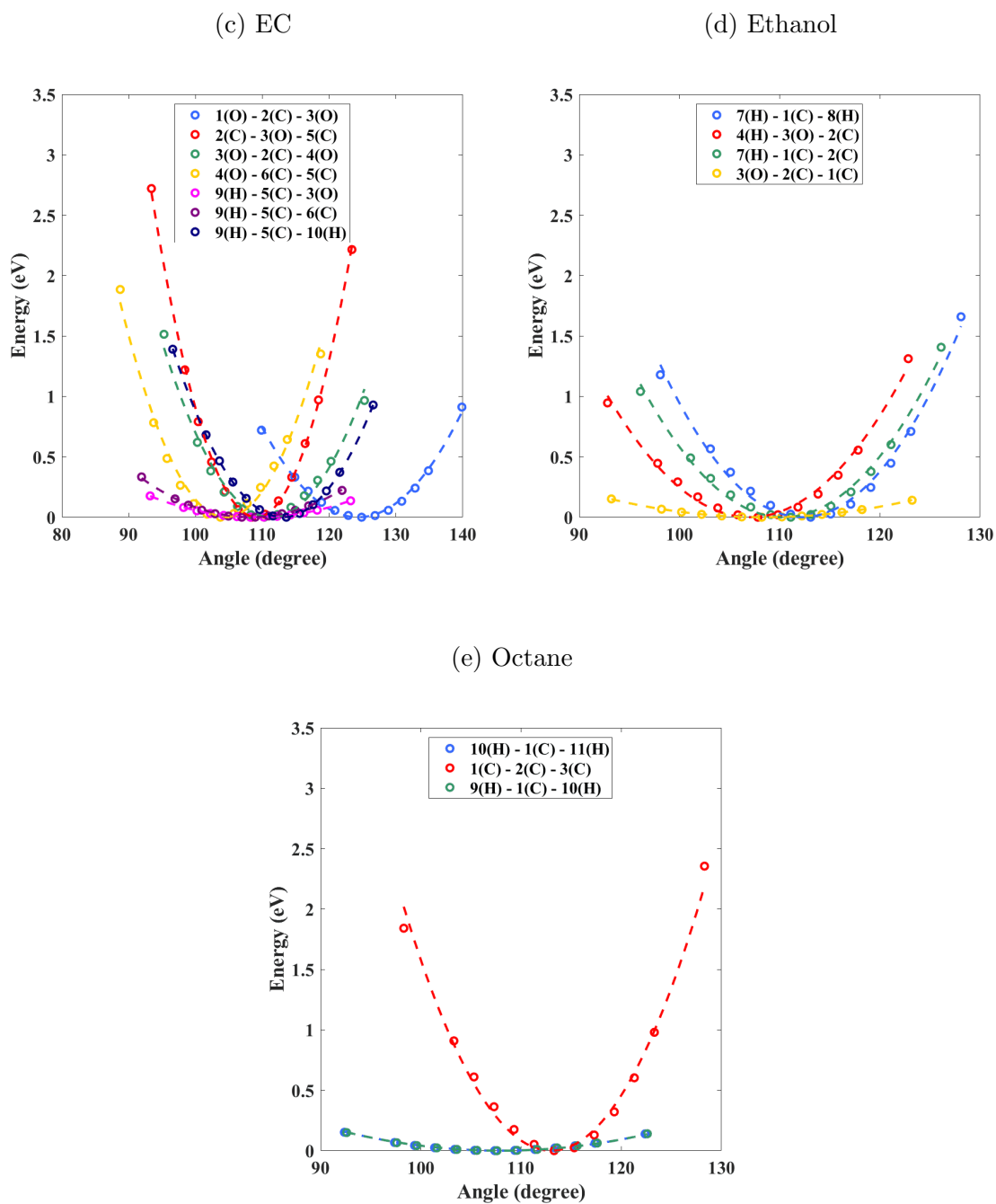
Figure A3: The data points for the *angle* interaction energy as a function of θ, for the studied molecules, using a combination of Algorithms 3, 4 and QM calculation. The Harmonic Angle style equation (Table 2.2) is fitted on these data points.

(a) Dihedral - EC
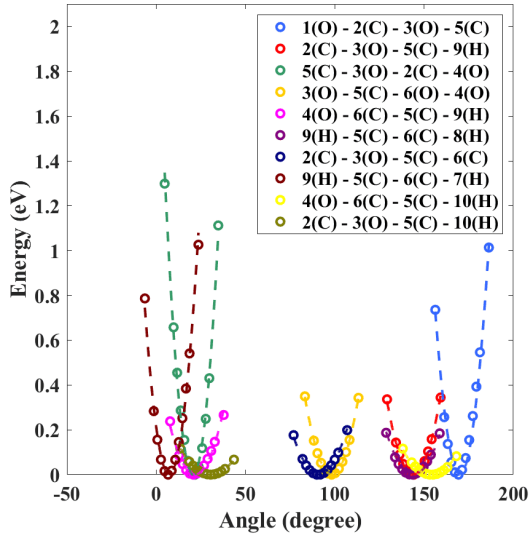
(b) Improper - EC
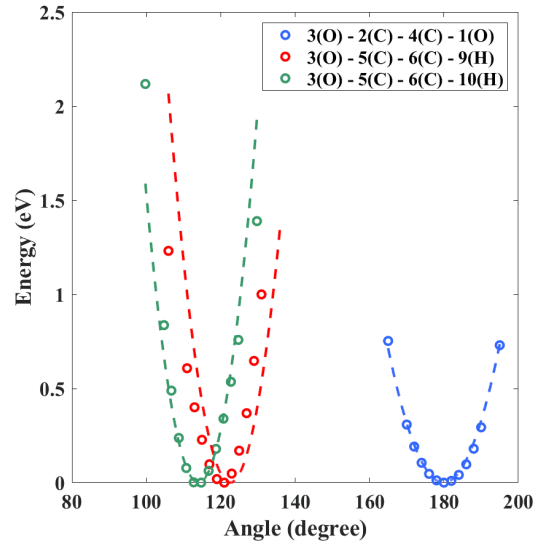
(c) Dihedral - Ethanol

(d) Improper - Ethanol

(e) Dihedral - Octane   (f) Improper - Octane
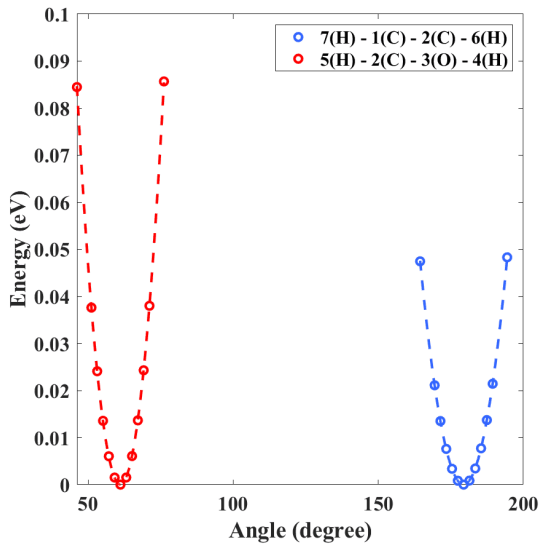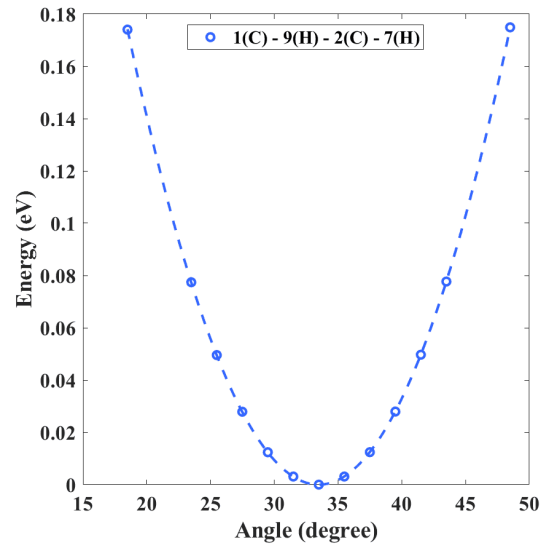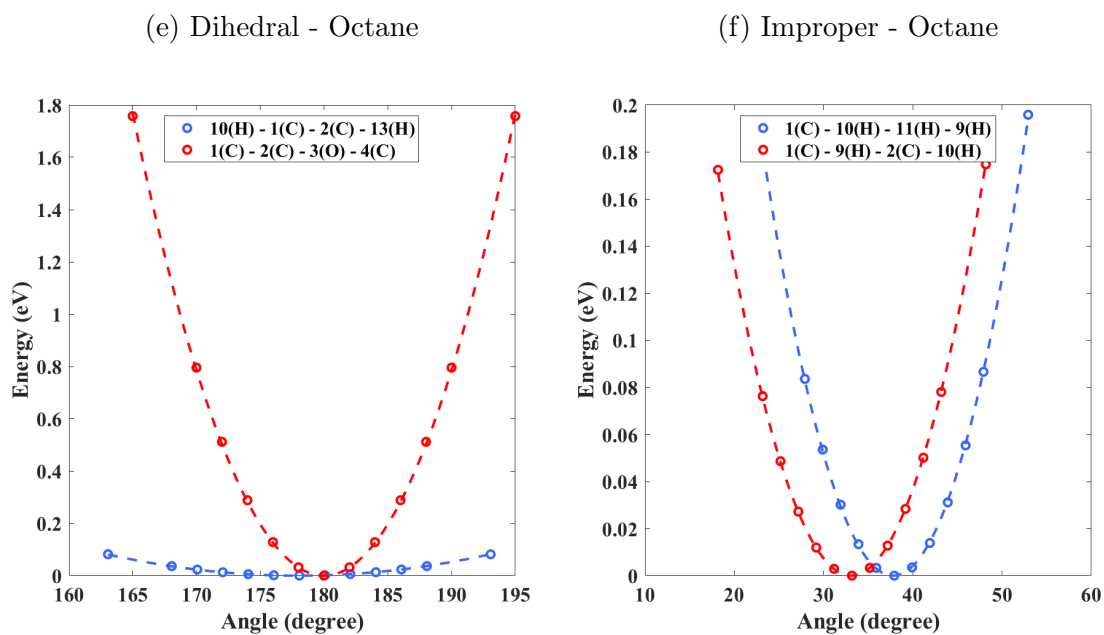
Figure A4: The data points for the *dihedral* and *improper* interaction energy as a function of ϕ and χ, for EC and Ethanol molecules, have been obtained by employing our algorithms in conjunction with the QM calculation. The Quadric and Harmonic Dihedral and Improper style equations (Table 2.2), are fitted on these data points.

A.3   Potential Parameters Values

Table A1: Nonbonded potential parameters for the Buckingham potential equation $(E = A exp(-\frac{r}{B}) - \frac{C}{r^6})$, using the suite of algorithms for the studied molecules.

Type	A	B(Å)	C(Å^6)	R^2
H_2O				
1(O) - 1(O)	$5.65E+3$	$1.43E-1$	$-5.50E-3$	0.99
2(H) - 2(H)	$1.81E+2$	$1.12E-1$	$-1.39E-5$	0.99
LiPF$_6$				
1(Li) - 1(Li)	$1.67E+3$	$1.71E-1$	$-8.72E-2$	0.99
2(P) - 2(P)	$1.71E+3$	$3.21E-1$	$-1.97E-6$	0.99
3(F) - 3(F)	$4.82E+3$	$1.58E-1$	$-7.25E-6$	0.99
EC				
1(O) - 1(O)	$3.37E+4$	$1.12E-1$	$3.59E+0$	0.99
2(C) - 2(C)	$4.37E+3$	$1.47E-1$	$0.46E+0$	0.99
3(O) - 3(O)	$3.66E+4$	$1.11E-1$	$3.88E+0$	0.99
4(C) - 4(C)	$6.93E+3$	$1.33E-1$	$7.66E-1$	0.99
5(H) - 5(H)	$3.89E+2$	$7.56E-2$	$1.61E-6$	0.99
Ethanol				
1(C) - 1(C)	$2.49E+3$	$1.56E-1$	$-3.09E-4$	0.99
2(C) - 2(C)	$2.50E+3$	$1.53E-1$	$-2.99E-4$	0.99
3(O) - 3(O)	$6.85E+3$	$1.35E-1$	$-5.49E-4$	0.99
4(H) - 4(H)	$1.96E+2$	$1.44E-1$	$-2.01E-5$	0.99
5(H) - 5(H)	$3.06E+2$	$8.87E-2$	$-4.97E-6$	0.98

6(H) - 6(H)	$3.00E + 2$	$8.99E - 2$	$-5.47E - 6$	0.98

<center>Octane</center>

1(C) - 1(C)	$7.95E + 3$	$1.31E - 1$	$8.58E - 1$	0.99
2(H) - 2(H)	$3.55E + 2$	$8.01E - 2$	$2.03E - 6$	0.99

Table A2: Bonded potential parameters for the Harmonic style equation $(E = K(r - r_0)^2)$ for the five molecules.

Type	K $(\frac{eV}{\overset{\circ}{A}})$	$r_0(\overset{\circ}{A})$	R^2
	H_2O		
1(O) - 2(H)	$+9.7002E + 0$	$+9.9642E - 1$	0.86
	$LiPF_6$		
2(P) - 3(F)	$+3.7769E + 0$	$+1.6359E + 0$	0.78
	EC		
1(O) - 2(C)	$+1.2795E + 1$	$+1.1988E + 0$	0.84
2(C) - 3(O)	$+7.3383E + 0$	$+1.3684E + 0$	0.92
3(O) - 5(C)	$+5.7992E + 0$	$+1.4457E + 0$	0.87
5(C) - 6(C)	$+5.9967E + 0$	$+1.1275E + 0$	0.88
6(C) - 7(H)	$+6.1310E + 0$	$+1.4903E + 0$	0.96
	Ethanol		
1(C) - 7(H)	$+6.0882E + 1$	$+1.1012E + 0$	0.92
2(C) - 5(H)	$+6.0685E + 0$	$+1.0994E + 0$	0.92
1(C) - 2(C)	$+4.0770E + 0$	$+1.5220E + 0$	0.86
2(C) - 3(O)	$+4.6610E + 0$	$+1.4342E + 0$	0.85

3(O) - 4(H)	$+8.7982E+0$	$+9.7215E-1$	0.90

Octane

1(C) - 2(C)	$+4.1993E+1$	$+1.5271E+0$	0.87
1(C) - 9(H)	$+5.8337E+0$	$+1.0996E+0$	0.93

Table A3: Angle potential parameters for the Harmonic style equation $(E = K(\theta - \theta_0)^2)$ for the five molecules.

Type	K $(\frac{eV}{rad})$	θ_0(deg)	R^2
	H$_2$O		
2(H) - 1(O) - 3(H)	$+1.9910E+0$	$+1.0336E+2$	0.99
	LiPF$_6$		
3(F) - 2(P) - 4(F)	$+8.3750E+0$	$+8.8599E+1$	0.99
3(F) - 2(P) - 8(F)	$+5.7379E+0$	$+1.7677E+2$	0.99
	EC		
1(O) - 2(C) - 3(O)	$+1.1835E+1$	$+1.2433E+2$	0.99
2(C) - 3(O) - 5(C)	$+3.5900E+1$	$+1.0908E+2$	0.99
3(O) - 2(C) - 4(O)	$+1.7875E+1$	$+1.1132E+2$	0.98
4(O) - 6(C) - 5(C)	$+2.3454E+1$	$+1.0451E+2$	0.99
9(H) - 5(C) - 3(O)	$+2.2683E+0$	$+1.0910E+2$	0.99
9(H) - 5(C) - 6(C)	$+3.9920E+0$	$+1.0823E+2$	0.99
9(H) - 5(C) - 10(H)	$+1.6783E+1$	$+1.1310E+2$	0.99
	Ethanol		
7(H) - 1(C) - 8(H)	$+2.1289E+1$	$+1.0840E+2$	0.99

4(H) - 3(O) - 2(C)	$+1.6393E+1$	$+1.0702E+2$	0.99
7(H) - 1(C) - 2(C)	$+1.7807E+1$	$+1.1036E+2$	0.98
3(O) - 2(C) - 1(C)	$+2.0673E+0$	$+1.1225E+2$	0.99

Octane

1(C) - 2(C) - 3(C)	$+3.0673E+1$	$+1.1283E+2$	0.99
10(H) - 1(C) - 11(H)	$+2.1239E+0$	$+1.0764E+2$	0.99
9(H) - 1(C) - 10(H)	$+2.1117E+0$	$+1.0777E+2$	0.99

Table A4: Dihedral and Improper potential parameters of EC, Ethanol and Octane molecules for Quadratic and Harmonic potential style ($E = K(\phi - \phi_0)^2$, $E = K(\chi - \chi_0)^2$).

EC

Dihedral

Type	K $(\frac{eV}{rad})$	ϕ_0(deg)	R^2
1(O)-2(C)-3(O)-5(C)	$+1.268E+1$	$+1.696E+2$	0.99
2(C)-3(O)-5(C)-9(H)	$+5.047E+0$	$+9.830E+1$	0.99
5(C)-3(O)-2(C)-4(O)	$+1.317E+1$	$+7.270E+0$	0.99
3(O)-5(C)-6(O)-4(O)	$+3.690E+0$	$+2.168E+1$	0.99
4(O)-6(C)-5(C)-9(H)	$+2.729E+0$	$+9.116E+1$	0.99
9(H)-5(C)-6(C)-8(H)	$+1.312E+0$	$+3.060E+1$	0.99
2(C)-3(O)-5(C)-6(C)	$+1.758E+1$	$+2.062E+1$	0.99
9(H)-5(C)-6(C)-7(H)	$+1.433E+0$	$+1.543E+2$	0.99
4(O)-6(C)-5(C)-10(H)	$+2.700E+0$	$+1.435E+2$	0.99

2(C)-3(O)-5(C)-10(H)	$+4.958E+0$	$+1.441E+2$	0.99

Improper

Type	K ($\frac{eV}{rad}$)	χ_0(deg)	R^2
2(C)-3(O)-4(C)-1(O)	$+2.509E+0$	$-2.383E-1$	0.99
3(O)-2(C)-4(C)-1(O)	$+1.057E+1$	$+1.798E+2$	0.99
5(C)-3(O)-6(C)-9(H)	$+3.068E+0$	$+3.299E+1$	0.99

Ethanol

Dihedral

Type	K ($\frac{eV}{rad}$)	ϕ_0(deg)	R^2
7(H)-1(C)-2(C)-6(H)	$+1.241E0$	$+6.110E+1$	0.99
5(H)-2(C)-3(O)-4(H)	$+6.985E-1$	$+1.793E+2$	0.99

Improper

Type	K ($\frac{eV}{rad}$)	χ_0(deg)	R^2
1(C)-9(H)-2(C)-7(H)	$+2.545E+0$	$+3.348E+1$	1.00

Octane

Dihedral

Type	K ($\frac{eV}{rad}$)	ϕ_0(deg)	R^2
1(C)-2(C)-3(C)-4(C)	$+2.577E1$	$+1.800E+2$	1.0
10(H)-1(C)-2(C)-13(H)	$+1.192E0$	$+1.780E+2$	1.0

Improper

Type	K ($\frac{eV}{rad}$)	χ_0(deg)	R^2
1(C)-10(H)-11(H)-9(H)	$+2.793E+0$	$+3.779E+1$	1.00
1(C)-9(H)-2(C)-10(H)	$+2.533E+0$	$+3.313E+1$	1.00

Appendix B

Supporting Information of Chapter 3

Table B1: Nonbonded potential parameters for the Buckingham potential equation ($E = A exp(-\frac{r}{B}) - \frac{C}{r^6}$), using the suite of algorithms for the studied molecules.

Type	A	B(Å)	C(Å^6)	R^2
		H$_2$O		
1(O) - 1(O)	$6.82 \times 10^{+3}$	1.36×10^{-1}	-1.54×10^{-4}	0.99
2(H) - 2(H)	$2.26 \times 10^{+2}$	1.35×10^{-1}	-5.60×10^{-5}	0.99
		LiPF$_6$		
1(Li) - 1(Li)	$1.57 \times 10^{+3}$	1.80×10^{-1}	-1.93×10^{-4}	0.99
2(P) - 2(P)	$3.97 \times 10^{+3}$	2.63×10^{-1}	-7.86×10^{-4}	0.99
3(F) - 3(F)	$8.85 \times 10^{+3}$	1.36×10^{-1}	-7.49×10^{-4}	0.99
		EC		
1(O) - 1(O)	$6.68 \times 10^{+3}$	1.37×10^{-1}	-5.63×10^{-4}	0.99
2(C) - 2(C)	$2.29 \times 10^{+3}$	1.74×10^{-1}	-3.51×10^{-4}	0.99
3(O) - 3(O)	$6.69 \times 10^{+3}$	1.36×10^{-1}	-5.59×10^{-4}	0.99
4(C) - 4(C)	$2.41 \times 10^{+3}$	1.58×10^{-1}	-3.11×10^{-4}	0.99

5(H) - 5(H)	$3.09 \times 10^{+2}$	9.48×10^{-2}	-2.92×10^{-6}	0.99

<div align="center">Ethanol</div>

1(C) - 1(C)	$2.49 \times 10^{+3}$	1.56×10^{-1}	-3.09×10^{-4}	0.99
2(C) - 2(C)	$2.50 \times 10^{+3}$	1.53×10^{-1}	-2.99×10^{-4}	0.99
3(O) - 3(O)	$6.85 \times 10^{+3}$	1.35×10^{-1}	-5.49×10^{-4}	0.99
4(H) - 4(H)	$1.96 \times 10^{+2}$	1.44×10^{-1}	-2.01×10^{-5}	0.99
5(H) - 5(H)	$3.06 \times 10^{+2}$	8.87×10^{-2}	-4.97×10^{-6}	0.98
6(H) - 6(H)	$3.00 \times 10^{+2}$	8.99×10^{-2}	-5.47×10^{-6}	0.98

<div align="center">Octane</div>

1(C) - 1(C)	$2.48 \times 10^{+3}$	1.56×10^{-1}	-3.07×10^{-4}	0.99
2(H) - 2(H)	$3.13 \times 10^{+2}$	8.86×10^{-2}	-4.32×10^{-6}	0.99

Table B2: Bonded potential parameters for the Harmonic style equation $(E = K(r - r_0)^2)$ for the five molecules.

Type	K $(\frac{eV}{\mathring{A}})$	$r_0(\mathring{A})$	R^2

<div align="center">H_2O</div>

1(O) - 2(H)	$+9.7002 \times 10^{+0}$	$+9.9642 \times 10^{-1}$	0.86

<div align="center">$LiPF_6$</div>

2(P) - 3(F)	$+3.7769 \times 10^{+0}$	$+1.6359 \times 10^{+0}$	0.78

<div align="center">EC</div>

1(O) - 2(C)	$+1.2795 \times 10^{+1}$	$+1.1988 \times 10^{+0}$	0.84
2(C) - 3(O)	$+7.3383 \times 10^{+0}$	$+1.3684 \times 10^{+0}$	0.92
3(O) - 5(C)	$+5.7992 \times 10^{+0}$	$+1.4457 \times 10^{+0}$	0.87

5(C) - 6(C)	$+5.9967 \times 10^{+0}$	$+1.1275 \times 10^{+0}$	0.88
6(C) - 7(H)	$+6.1310 \times 10^{+0}$	$+1.4903 \times 10^{+0}$	0.96

Ethanol

1(C) - 7(H)	$+6.0882 \times 10^{+1}$	$+1.1012 \times 10^{+0}$	0.92
2(C) - 5(H)	$+6.0685 \times 10^{+0}$	$+1.0994 \times 10^{+0}$	0.92
1(C) - 2(C)	$+4.0770 \times 10^{+0}$	$+1.5220 \times 10^{+0}$	0.86
2(C) - 3(O)	$+4.6610 \times 10^{+0}$	$+1.4342 \times 10^{+0}$	0.85
3(O) - 4(H)	$+8.7982 \times 10^{+0}$	$+9.7215 \times 10^{-1}$	0.90

Octane

1(C) - 2(C)	$+4.1993 \times 10^{+1}$	$+1.5271 \times 10^{+0}$	0.87
1(C) - 9(H)	$+5.8337 \times 10^{+0}$	$+1.0996 \times 10^{+0}$	0.93

Table B3: Angle potential parameters for the Harmonic style equation $(E = K(\theta - \theta_0)^2)$ for the five molecules.

Type	K $(\frac{eV}{rad})$	θ_0(deg)	R^2
	H_2O		
2(H) - 1(O) - 3(H)	$+1.9910 \times 10^{+0}$	$+1.0336 \times 10^{+2}$	0.99
	$LiPF_6$		
3(F) - 2(P) - 4(F)	$+8.3750 \times 10^{+0}$	$+8.8599 \times 10^{+1}$	0.99
3(F) - 2(P) - 8(F)	$+5.7379 \times 10^{+0}$	$+1.7677 \times 10^{+2}$	0.99
	EC		
1(O) - 2(C) - 3(O)	$+1.1835 \times 10^{+1}$	$+1.2433 \times 10^{+2}$	0.99
2(C) - 3(O) - 5(C)	$+3.5900 \times 10^{+1}$	$+1.0908 \times 10^{+2}$	0.99

3(O) - 2(C) - 4(O)	$+1.7875 \times 10^{+1}$	$+1.1132 \times 10^{+2}$	0.98
4(O) - 6(C) - 5(C)	$+2.3454 \times 10^{+1}$	$+1.0451 \times 10^{+2}$	0.99
9(H) - 5(C) - 3(O)	$+2.2683 \times 10^{+0}$	$+1.0910 \times 10^{+2}$	0.99
9(H) - 5(C) - 6(C)	$+3.9920 \times 10^{+0}$	$+1.0823 \times 10^{+2}$	0.99
9(H) - 5(C) - 10(H)	$+1.6783 \times 10^{+1}$	$+1.1310 \times 10^{+2}$	0.99

Ethanol

7(H) - 1(C) - 8(H)	$+2.1289 \times 10^{+1}$	$+1.0840 \times 10^{+2}$	0.99
4(H) - 3(O) - 2(C)	$+1.6393 \times 10^{+1}$	$+1.0702 \times 10^{+2}$	0.99
7(H) - 1(C) - 2(C)	$+1.7807 \times 10^{+1}$	$+1.1036 \times 10^{+2}$	0.98
3(O) - 2(C) - 1(C)	$+2.0673 \times 10^{+0}$	$+1.1225 \times 10^{+2}$	0.99

Octane

1(C) - 2(C) - 3(C)	$+3.0673 \times 10^{+1}$	$+1.1283 \times 10^{+2}$	0.99
10(H) - 1(C) - 11(H)	$+2.1239 \times 10^{+0}$	$+1.0764 \times 10^{+2}$	0.99
9(H) - 1(C) - 10(H)	$+2.1117 \times 10^{+0}$	$+1.0777 \times 10^{+2}$	0.99

Table B4: Dihedral and Improper potential parameters of EC, Ethanol and Octane molecules for Quadratic and Harmonic potential style ($E = K(\phi - \phi_0)^2$, $E = K(\chi - \chi_0)^2$).

EC

Dihedral

Type	K $(\frac{eV}{rad})$	ϕ_0(deg)	R^2
1(O) - 2(C) - 3(O) - 5(C)	$+1.2685 \times 10^{+1}$	$+1.6965 \times 10^{+2}$	0.99
2(C) - 3(O) - 5(C) - 9(H)	$+5.0472 \times 10^{+0}$	$+9.8307 \times 10^{+1}$	0.99

5(C) - 3(O) - 2(C) - 4(O)	$+1.3173 \times 10^{+1}$	$+7.2704 \times 10^{+0}$	0.99
3(O) - 5(C) - 6(O) - 4(O)	$+3.6904 \times 10^{+0}$	$+2.1683 \times 10^{+1}$	0.99
4(O) - 6(C) - 5(C) - 9(H)	$+2.7294 \times 10^{+0}$	$+9.1166 \times 10^{+1}$	0.99
9(H) - 5(C) - 6(C) - 8(H)	$+1.3124 \times 10^{+0}$	$+3.0604 \times 10^{+1}$	0.99
2(C) - 3(O) - 5(C) - 6(C)	$+1.7585 \times 10^{+1}$	$+2.0626 \times 10^{+1}$	0.99
9(H) - 5(C) - 6(C) - 7(H)	$+1.4332 \times 10^{+0}$	$+1.5430 \times 10^{+2}$	0.99
4(O) - 6(C) - 5(C) - 10(H)	$+2.7008 \times 10^{+0}$	$+1.4352 \times 10^{+2}$	0.99
2(C) - 3(O) - 5(C) - 10(H)	$+4.9580 \times 10^{+0}$	$+1.4412 \times 10^{+2}$	0.99

Improper

Type	K $(\frac{eV}{rad})$	χ_0(deg)	R^2
2(C) - 3(O) - 4(C) - 1(O)	$+2.5091 \times 10^{+0}$	-2.3835×10^{-1}	0.99
3(O) - 2(C) - 4(C) - 1(O)	$+1.0579 \times 10^{+1}$	$+1.7989 \times 10^{+2}$	0.99
5(C) - 3(O) - 6(C) - 9(H)	$+3.0682 \times 10^{+0}$	$+3.2992 \times 10^{+1}$	0.99

Ethanol

Dihedral

Type	K $(\frac{eV}{rad})$	ϕ_0(deg)	R^2
7(H) - 1(C) - 2(C) - 6(H)	$+1.2413 \times 10^{0}$	$+6.1107 \times 10^{+1}$	0.99
5(H) - 2(C) - 3(O) - 4(H)	$+6.9854 \times 10^{-1}$	$+1.7938 \times 10^{+2}$	0.99

Improper

Type	K $(\frac{eV}{rad})$	χ_0(deg)	R^2
1(C) - 9(H) - 2(C) - 7(H)	$+2.5458 \times 10^{+0}$	$+3.3482 \times 10^{+1}$	1.00

Octane

Dihedral

Type	K ($\frac{eV}{rad}$)	ϕ_0(deg)	R^2
1(C) - 2(C) - 3(C) - 4(C)	$+2.5770 \times 10^1$	$+1.8000 \times 10^{+2}$	1.0
10(H) - 1(C) - 2(C) - 13(H)	$+1.1921 \times 10^0$	$+1.7806 \times 10^{+2}$	1.0

Improper

Type	K ($\frac{eV}{rad}$)	χ_0(deg)	R^2
1(C) - 10(H) - 11(H) - 9(H)	$+2.7938 \times 10^{+0}$	$+3.7799 \times 10^{+1}$	1.00
1(C) - 9(H) - 2(C) - 10(H)	$+2.5333 \times 10^{+0}$	$+3.3132 \times 10^{+1}$	1.00